SYMBOLIC DYNAMICS IN CHAOTIC SYSTEMS

Kai T. Hansen
Physics Department,
University of Oslo,
Box 1048, Blindern, N-0316 Oslo, Norway.
e-mail: k.hansen@fys.uio.no

Thesis presented for the degree Dr. Philos.
at the University of Oslo

September, 1993

Contents

Acknowledgments

I am very grateful for all inspiring help from Predrag Cvitanović which has been important for me, both professionally and personally. I want to thank all the people in the chaos group at the Niels Bohr Institute and Nordita where I have experienced a very good professional and social environment. For interesting discussions here where I learned a lot I thank Vivianne Baladi, Tomas Bohr, Hans Henrik Rugh, Freddy Christiansen, Stephen Creagh, Per Dahlqvist, Peter Dimon, Hans Frisk, Mogens Høgh Jensen, Zoltan Kaufmann, Ronnie Mainieri, Mads Nordahl, Agata Pavone, Gunnar Russberg, Per Rosenqvist, Thomas Schreiber, Gabor Vattay and many others. I want to thank many of the people I have met at a number of conferences and other places for many inspiring discussions. I also would like to thank Jan Frøyland for introducing me to the world of chaos, and to all friends at the physics department in Oslo. I am grateful for the help I got with some of my drawings from Elisabeth Grothe.

I thank NAVF (The Norwegian Research Council) for the grant making this project possible.

I am grateful to Sidsel Hoelsæter for great patience with me moving around all the time, and to my parents, Inger and Ronald Hansen, for all their help and encouragement throughout the years. I will also thank my grandparents, Helmine and Paul Paulsberg, and dedicate this work to the memory of my grandfather.

Introduction

After calculus was invented by Newton and Leibniz 300 years ago, the main goal of mechanics has been to find an analytic solution describing the exact dynamics of a given mechanical system. If an analytic solution could not be obtained, then one tried to find a perturbation solution close to an exact solution. Problems which could not be solved this way were usually left untouched by mathematicians and physicists. Newton obtained the exact solution of the gravitational two body problem while for the three body problem he could obtain only perturbation solutions in some limits. The way we attack these kinds of mechanical problems (and other dynamical problems) from the chaos-theory point of view is different. We try to explain the dynamics not as one analytically describable path, but as a collection of different possible paths from which one can calculate average quantities of the system. The questions we ask and can answer are closer to the theory of statistical mechanics and quantum mechanics than to the traditional mechanics.

The first to emphasize that one should study the global dynamics in the phase space of the system in a qualitative way was Poincaré who introduced several of the ideas and methods we use today. He discussed stable and unstable manifolds, defined the surface of section (today called the Poincaré map), and stressed the importance of the periodic orbits. By the end of the 19th century Poincaré and others proved that the three body problem did not have the analytic solutions which Newton hoped to find. The ideas of Poincaré were developed by other mathematicians in the beginning of the 20th century, but received scant given little attention in physics and applied mathematics. Birkoff continued Poincaré's work on discrete mappings and stable and unstable manifolds. In the middle of this century the digital computer was developed, and use of computers to numerically solve problems which do not have analytic solutions became a very important part of the study of dynamical systems. The interplay between the numerical simulations and development of the theory has been fruitful, with many examples of numerical experiments giving new theoretical insights, such as the Fermi-Pasta-Ulam coupled oscillator chains, the Lorenz attractor, the integrable Toda lattice, the chaotic Hénon-Heile problem, the Feigenbaum period doubling, and the Hénon attractor. These results gave new insights in the structure of the problems without a traditional analytic solution. Important theoretical results were obtained by mathematicians like Kolmogorov, Arnold, Moser, Sinai, Smale, Newhouse, Ruelle and many others. These "strange" problems are now usually referred to as *chaotic systems*. There is no agreement on the ultimate definition of a chaotic system, but this may be unimportant since in practice there is general agreement on what the interesting questions

are. In the last 20 years there has been a huge interest in chaotic systems and many new results have been obtained. The work giving the background for this thesis will be discussed in the text where we use these results. We build on the results concerning symbolic dynamics obtained by Sharkovskii, Smale, Metropolis, Stein, Stein, Milnor, Thurston, Grassberger, Cvitanović and many others.

"Quantum-chaos" is the youngest of the theories in the "chaos family" and at the moment maybe the one with fastest progress. The problem of quantum mechanics and chaos is discussed from many different points of view, all the way from philosophical discussions to the real experiments. The semi-classical theory of chaotic systems is of most interest to us since this theory gives a close relation between the study of a classical system and the corresponding quantum systems, and for both the quantum system and the classical systems description of periodic orbits of the classical system plays an essential role.

In this thesis we will study the structure of orbits in classical chaotic systems and a major tool will be the concept of symbolic dynamics. As much of the work in chaos theory, this work is a mix of theoretical results, computer simulations and applications to physical systems. We do not claim that the theoretical results here are rigorously proven; they are mostly based on numerics and conjectures. Some of the theoretical results may easily be turned into theorems while other conjectures will need a lot of work to be proven, falsified or improved. We have obtained descriptions of the orbits existing in chaotic systems and these descriptions can be used in calculations of quantities like the energy levels of a quantum system. In this thesis we work out a method for obtaining this description. Most applications of this are left as future work.

A number of new results connected to the symbolic description of chaotic systems are presented here. Bifurcation diagrams for three-modal one-dimensional maps are drawn in a symbolic parameter plane, topologically equivalent to a usual parameter plane. A global bifurcation diagram for this map has not been shown before. We obtain similar bifurcation diagrams for the general once-folding two-dimensional maps; the Hénon map is one two-parameter realization of such once-folding map. These bifurcation diagrams are obtained by an approximation procedure which orders the infinite-dimensional parameter space in a hierarchical manner. This yields in a rather complicated description of bifurcations which agrees with numerics for the Hénon map worked out in detail by Mira [153] and with other numerical examples of once-folding maps. We think that this description presented here for the first time is the correct way to describe these bifurcations. There are many questions not yet settled concerning the correctness of the assumptions underlying this theory.

The important question of a unique partition of the folding map is addressed and we propose a method that should yield a unique partition. Generalization of these results to an n-folding two-dimensional map is also discussed. For a number of billiard systems; 3-disk, 4-disk, 7-disk, hyperbola billiard, stadium billiard and wedge billiard, we define a well ordered symbolic dynamics description and obtain a pruning front. The pruning front distinguishes between symbol strings corresponding to the admissible and the forbidden orbits. This can be used to construct an approximate Markov partition. Finding the topological entropy is the simplest application of the theory. These results are the first systematical description of admissible orbits for the billiard systems and this is the first implementation of a construction of approximate Markov partitions in billiard systems. We also investigate in some detail the bifurcation of orbits in billiard systems as the parameters change. This yield singular bifurcations which we show can be described by symbolic dynamics. We compare the singular bifurcations of billiards with bifurcations found in smooth Hamiltonian potentials, and find families of orbits bifurcating together described by the same symbolic dynamics in both systems. This relation between symbolic description of orbits in billiards and in smooth systems, apparantly not investigated before, offers a better understanding of bifurcation of orbits in smooth Hamiltonian systems.

The pruning front for dispersive billiards and some of the results for bifurcations in billiards and smooth potentials are published in refs. [108, 109, 110]. One result concerning the change of symbolic description of unstable orbits in the Hénon map is also published in ref. [107].

Part I

One-dimensional maps

Chapter 1

Unimodal map

1.1 Bifurcations in the unimodal map

A curious feature of chaotic systems is that the description of most phenomena observed in many different chaotic systems is greatly aided by a proper understanding of the simple one-dimensional unimodal map, so we will devote a considerable amount of space to the review of this well known and much studied map.

A unimodal map is a continuous one-dimensional function $\mathbb{R} \to \mathbb{R}$ with a monotonously increasing (or decreasing) branch, a critical point x_c as the maximum (minimum) point, and a monotonously decreasing (respectively increasing) branch. We assume in this section that the critical point is a maximum point. The dynamics of the point x is given by the iteration

$$x_{t+1} = f(x_t, a) \tag{1.1}$$

and some simple examples of unimodal maps are the logistic map

$$x_{t+1} = a x_t (1 - x_t) \tag{1.2}$$

drawn in figure 1.1 for $a = 3.92$ and the tent map

$$x_{t+1} = \begin{cases} a x_t & x_t \leq 1/2 \\ a(1 - x_t) & x_t > 1/2 \end{cases} . \tag{1.3}$$

drawn in figure 1.2 for $a = 1.75$. For convenience we assume $a \geq 0$, because $a < 0$ gives a function with a minimum point and with the same dynamics. Both the logistic map and the tent map are unimodal and have similar topological properties, while metric properties are very different. The tent map is a singular map, while the logistic map is typical for smooth maps with a critical point $f'(x_c) = 0$ with

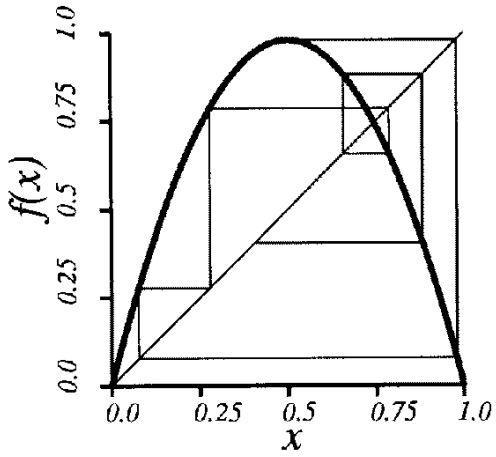

Figure 1.1: The logistic map $f(x) = ax(1-x)$ with $a = 3.92$ and the orbit starting at the point $x = 0.5$.

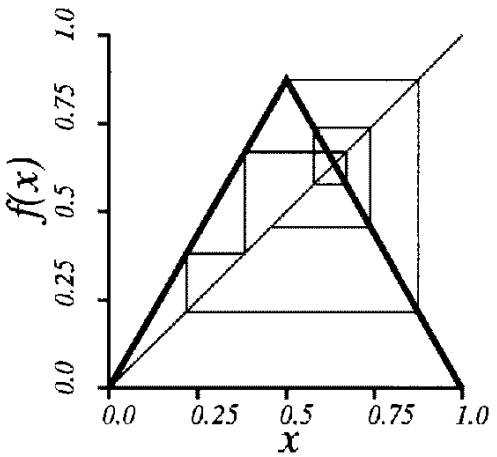

Figure 1.2: The tent map $f(x) = ax$ if $x \leq 0.5$ and $f(x) = a(1-x)$ if $x > 0.5$ and the orbit starting at the point $x = 0.5$.

$f''(x_c) \neq 0$. We will find that two-dimensional systems often have bifurcations similar to those we find in one of these two simple maps.

The iteration of points x is illustrated graphically in the figures 1.1 and 1.2. We draw a horizontal line from the point $x = x_t$ on the function f to a point on the diagonal $y = x$ and then we draw a vertical line from this point on the diagonal to a point on the function f. This point has $x = x_{t+1}$ and we find the time series

$$x_1 x_2 x_3 \ldots \tag{1.4}$$

from the starting point x_0. It is this time series we want to study – its convergence to an asymptotic attractor and the transient dynamics.

The first numerical experiment we do on the computer is to find the attractor $\lim_{t\to\infty} x_t$ and plot the attractor as a function of the parameter a. This picture is the well known bifurcation tree for the logistic map in figure 1.3 [144, 72]. The tent map also has an attractor, and the bifurcation tree for the tent map is drawn in figure 1.4.

The symbolic sequence of an orbit given by the time series (1.4) is defined as follows. In a smooth map the critical point x_c is the x-value giving $f'(x) = 0$ and for the logistic map $x_c = 1/2$. The tent map has a special point which we also may call a critical point at $x_c = 1/2$ where $f(x)$ has a maximum point and $f'(x)$ is discontinuous. Let [152] the binary symbols be defined as

$$s_t = \begin{cases} 1 & \text{if } x_t > x_c \\ 0 & \text{if } x_t < x_c \end{cases} . \tag{1.5}$$

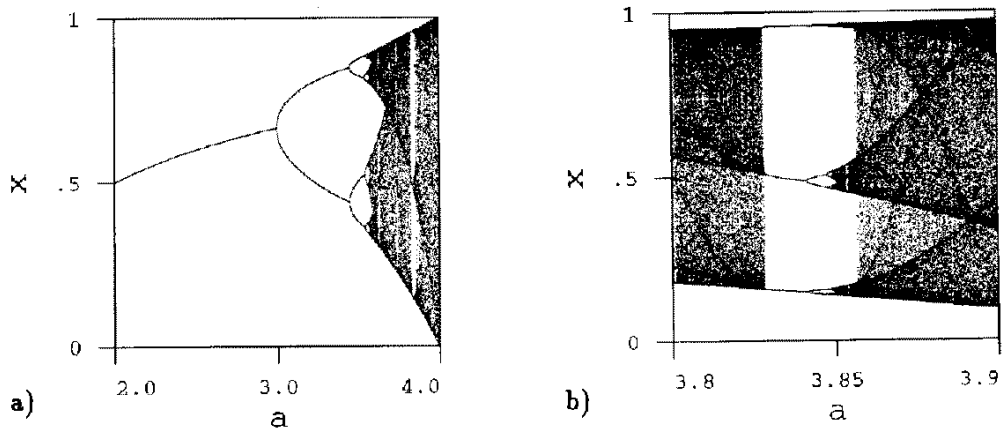

Figure 1.3: The bifurcation tree of the logistic map. a) The whole tree, b) magnification around the period 3 resonance.

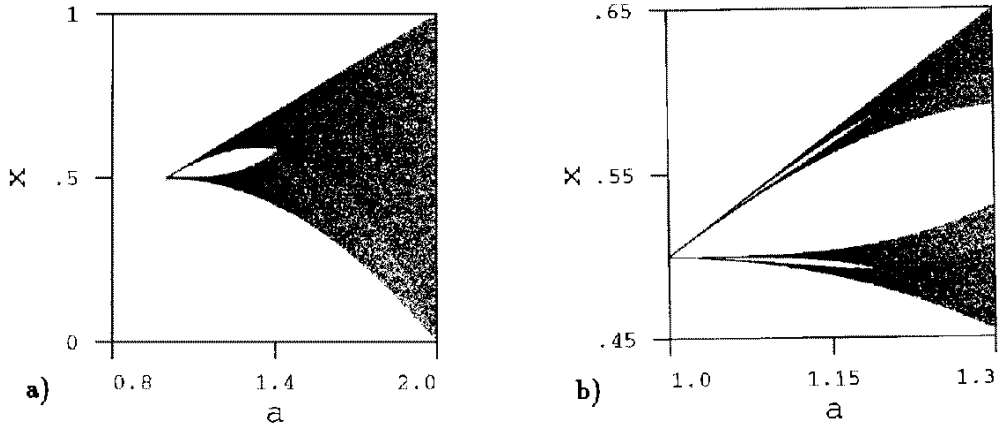

Figure 1.4: The bifurcation tree of the tent map. b) magnification around the creation of the fixed point.

The symbol string $S = s_1 s_2 s_3 \ldots$ with $s_t \in \{0, 1\}$ is the *forward itinerary* of point x_0. Symbols L and R are often used [147] instead of 0 and 1 so the symbols indicate if the point x_t is on the left side (L) or the right side (R) of the critical point. If $x_t = x_c$ the symbol $s_t = C$ is often used but we will investigate separately these special orbit.

Figure 1.1 shows the trajectory of the point $x_0 = x_c = 0.5$ in the logistic map and we read the symbol sequence from the figure

$$s_1 s_2 s_3 s_4 s_5 s_6 \ldots = 100111 \ldots \tag{1.6}$$

The tent map in figure 1.2 gives the same first 6 symbols when we start with $x_0 = x_c = 0.5$. The symbol string obtained by choosing $x_0 = x_c$ is of special interest and this string is called the kneading sequence of the unimodal map.

A periodic orbit of length n is a real solution of

$$f^{(n)}(x) = f(f(\ldots f(x)\ldots)) = x \tag{1.7}$$

The unimodal map, eq. (1.7), has 2^n solutions in the complex plane, and we will therefore have 2^n or less period n orbits for the map.

A periodic orbit of length n is described by an infinite repetition of a length n symbol string, indicated by the line over the string:

$$\overline{S} = (s_1 s_2 s_3 \ldots s_n)^\infty = \overline{s_1 s_2 s_3 \ldots s_n} \tag{1.8}$$

Each point x_t in a periodic orbit can be associated with one of the 2^n possible symbolic strings $\overline{s_1 s_2 \ldots s_n}$. A cyclic permutation of the symbolic string $\overline{s_1 s_2 \ldots s_n}$ to a new string $\overline{s_k s_{k+1} \ldots s_n s_1 \ldots s_{k-1}}$ is the description of the point x_{t+k-1} in the same periodic orbit.

A periodic orbit is stable if

$$\left| \frac{df^{(n)}(x)}{dx} \right| = |f'(x) \cdot f'(f(x)) \cdot \ldots \cdot f'(f(f(\ldots f(x)\ldots)))| < 1 \tag{1.9}$$

If we draw the function $f^{(n)}(x)$ then for a stable periodic orbit the slope of this function at the fixed point is between -1 and 1. The interval on the parameter axis where a periodic orbit is stable is called the stable window of the periodic orbit.

1.1.1 Fixed point and period doubling

Both fixed points (period 1 orbits) $x = 0$, $x = 1 - 1/a$ of the logistic map (1.2) exist for all $a > 0$. The first solution $x = 0$ is stable for $0 < a < 1$ and unstable for $a > 1$. This solution has $x < x_c$ for all parameter values and we denote this orbit

as $\overline{0}$ and the point as $x_{\overline{0}}$ where the index gives the symbolic description of the orbit. To avoid a too cumbersome notation we don't use the line over the symbols if it is clear from the context that we refer to a periodic orbit. We then write x_0 and 0 which should be understood as $x_{\overline{0}}$ and $\overline{0}$.

The other fixed point $x = 1 - 1/a$ is unstable for $0 < a < 1$, stable for $1 < a < 3$ and unstable for $a > 3$. This fixed point has $x < x_c$ for $0 < a < 2$ and $x > x_c$ for $a > 2$. As the interesting dynamics take place for $a > 2$ it is tempting to identify this orbit by $\overline{1}$ and denote the point $x_{\overline{1}}$ for all values of the parameter a, but this has to be done with care. It is typical that a stable orbit change symbolic description somewhere within the stable window. In one-dimensional smooth maps this is always at the parameter value where the orbit is super-stable $df^{(n)}(x)/dx = 0$, i.e. where one of the points in the orbit is identical to x_c. In a unimodal map there is only one of the n points in a period n orbit that can cross the critical point and the symbolic description of the orbit can only change in one symbol

$$\overline{s_1 s_2 \dots s_{n-1} s_n} \to \overline{s_1 s_2 \dots s_{n-1}(1 - s_n)} \tag{1.10}$$

In the multimodal maps discussed in chapter 2 there are several points in the periodic orbit that can cross a critical point and the symbolic description can change in different ways. We choose to call this second fixed point $\overline{1}$ but we should always remember that when an orbit is stable , its symbolic dynamics may change and is not unique. In the unimodal map an unstable orbit has a unique symbolic description.

The stability of the fixed point $\overline{1}$ changes from $f'(x_{\overline{1}}) = 1$ at $a = 1$ to $f'(x_{\overline{1}}) = 0$ at $a = 2$ and to $f'(x_{\overline{1}}) = -1$ at $a = 3$. When $f'(x_{\overline{1}}) < 0$ the fixed point has the unique symbolic description $\overline{1}$. The interval $a \in (1, 3)$ is the stable window for the fixed point.

The tent map has a fixed point $x_0 = 0$ for all $a > 0$ and a fixed point $x_1 = a/(a + 1)$ that exists for $a > 1$ and this fixed point is unstable for all $a > 1$. The fixed point x_1 does not have any stable window such as the fixed point in the logistic map and the fixed point is uniquely described by the symbolic description $\overline{1}$.

At $a = 3$ the fixed point x_1 of the logistic map has a period doubling bifurcation where the fixed point becomes unstable and a period 2 orbit

$$x_{01} = \frac{a+1}{2a} + \frac{1}{2a}\sqrt{(a+1)(a-3)} \tag{1.11}$$

$$x_{10} = \frac{a+1}{2a} - \frac{1}{2a}\sqrt{(a+1)(a-3)} \tag{1.12}$$

is created and exists for all $a > 3$. The stability $df^{(2)}(x)/dx$ is 1 at $a = 3$, it is 0 at $a = 1 + \sqrt{5} \approx 3.2361$ and it is -1 at $a = 1 + \sqrt{6} \approx 3.4495$. For larger values of a the orbit is unstable. Close to the bifurcation point at $a = 3$ both points in the

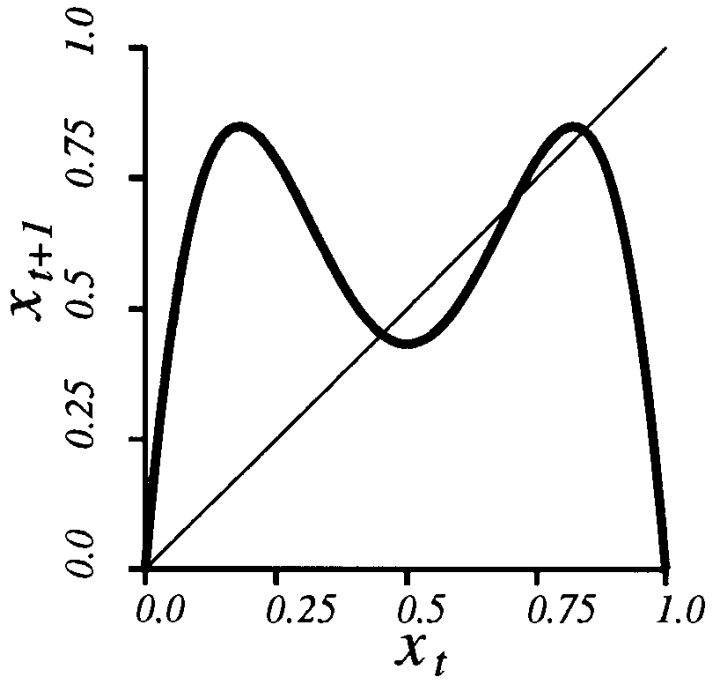

Figure 1.5: The second iterated function $f^{(2)}(x)$ for $a = 3.4$. The four fixed points of this function is the two fixed point $\overline{0}$ and $\overline{1}$ and the two points in the orbit $\overline{10}$.

period 2 orbit are close to the fixed point on the right side of x_c, but for $a > 1-\sqrt{5}$ there is one point on each side of x_c. We denote the orbit by $\overline{10}$ and its points $x_{\overline{01}}$ and $x_{\overline{10}}$ ($x_{\overline{01}} > x_{\overline{10}}$). In figure 1.5 the function $f^{(2)}(x)$ is drawn and the period 2 orbit appears as two fixed points in this drawing.

At $a = 1+\sqrt{6}$ the period 2 orbit becomes unstable and a period 4 orbit is born. After this orbit has passed the super-stable point its symbolic description is $\overline{1011}$ with the four points $x_{\overline{1110}} < x_{\overline{1011}} < x_{\overline{1101}} < x_{\overline{0111}}$. Notice that the map of one of this points give another of the points where the index is a cyclic permutation of the symbolic string $x_{\overline{0111}} = f(x_{\overline{1011}})$, $x_{\overline{1110}} = f(x_{\overline{0111}})$, $x_{\overline{1101}} = f(x_{\overline{1110}})$ and $x_{\overline{1011}} = f(x_{\overline{1101}})$.

We can generalize the period doubling bifurcations. Each periodic orbit bifurcates into an orbit with twice the length and for one parameter value $a_\infty = 3.5714\ldots$ there is an accumulation point where the length of the orbit goes to infinity. It has been shown by Feigenbaum [72, 73, 74] that there is a universal scaling law for all maps which have a quadratic critical point. The universality follows from the Cvitanović–Feigenbaum functional equation $g(x) = -\alpha g(g(-x/\alpha))$.

The symbolic description of the period doubling orbits is given by Metropolis, Stein and Stein (MSS) [147]. The symbolic description of the new orbit is obtained

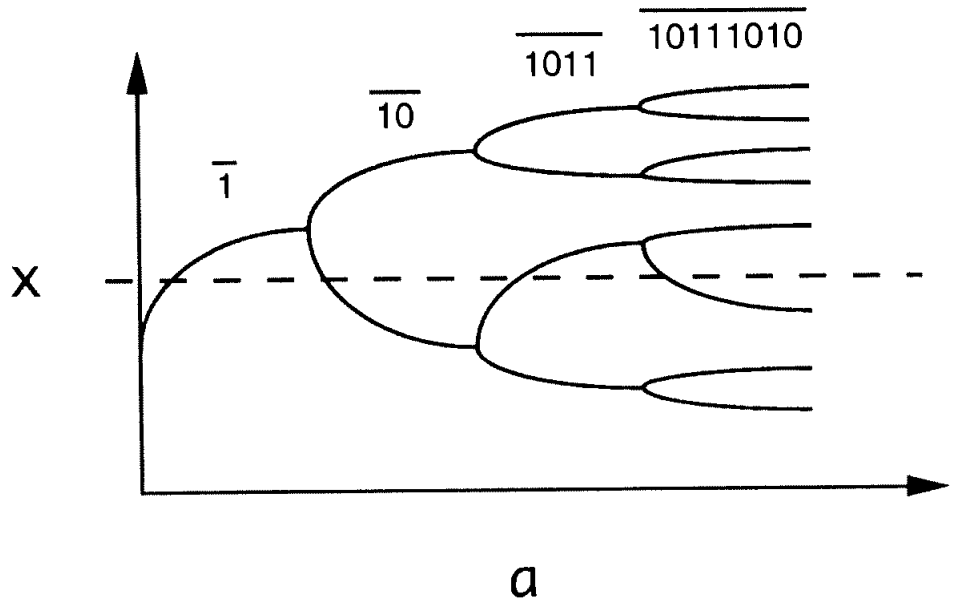

Figure 1.6: The bifurcations of the fixed point and the symbolic description of the periodic orbits.

by writing the old symbol sequence twice and changing the last symbol:

$$\overline{s_1 s_2 \dots s_n} \to \overline{s_1 s_2 \dots s_n s_1 s_2 \dots s_{n-1}(1-s_n)} \tag{1.13}$$

which is called a harmonic by MSS. The period 4 orbit $\overline{1011}$ bifurcates to the period 8 orbit $\overline{10111010}$ etc. Figure 1.6 shows the bifurcation of the fixed point and the symbolic description of the orbits. We should also observe that the number of symbols 1 in these symbol strings is always odd because only orbits with an odd number of 1s can have stability -1 and become unstable in a period doubling bifurcation.

At a parameter $a < a_\infty$ the attractor is a period n orbit and the repellor is the union of shorter unstable periodic orbits. A point x is a *non-wandering point* if for any neighborhood U of x there is a time t such that $U \cap f^{(t)}(U) \neq \emptyset$. The union of all non-wandering points are the *non-wandering set* of the map. For such a parameter the non-wandering set is the union of the periodic orbits.

The periodic orbits have preimages on the x-axis. In figure 1.7 the preimages of the stable fixed point $\overline{1}$ are drawn as a function of the parameter a. For $a < 2$ there is one preimage of the fixed point while for $a > 2$ there is a infinite number of preimages. In figure 1.8 the preimages of the fixed point are drawn as horizontal lines in the (x_t, x_{t+1}) plane. The preimages converge geometrically to the fixed point $x_0 = 0$ and its preimage $x = 1$.

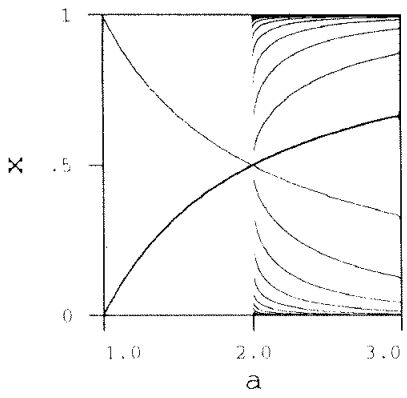

Figure 1.7: The stable fixed point $\overline{1}$ and its preimages as a function of the parameter for $1 < a < 3$.

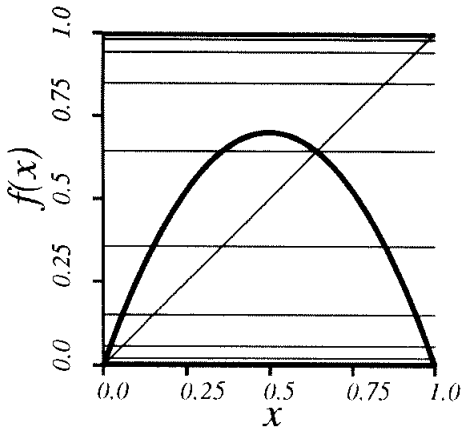

Figure 1.8: The preimages of the stable fixed point $\overline{1}$ drawn as horizontal lines in the (x_t, x_{t+1}) plane. $a = 2.8$

A complete description of the dynamics of the map in the symbolic dynamics language requires a description of both the repellor and the attractor. This can be done by the graphs in figure 1.9 a), b) and c) which gives the symbolic future of any point in the case of the stable orbits $\overline{1}$, $\overline{10}$ and $\overline{1011}$. Moving along a solid curve in the graph corresponds to a symbol 1, while a dashed curve corresponds to a symbol 0. The arrow shows in which direction to move. In figure 1.9 a) we see that there can be an arbitrary number of symbols 0 but after a symbol 1 there can only be symbols 1. For example, the sequence $0001111111\ldots$ is legal but the sequence $0001110111\ldots$ can not exist in the map for this parameter value. This is the description of the symbolic future $s_1 s_2 s_3 \ldots$ and is valid for all starting points, even if $x_0 > x_c$ ($s_0 = 1$).

The graphs are representations of Markov matrixes describing the dynamics in terms of symbols. The graph in figure 1.9 a) represents the matrix

$$\begin{array}{c} \\ 0 \\ 1 \end{array} \begin{array}{c} \begin{array}{cc} 0 & 1 \end{array} \\ \left[\begin{array}{cc} 1 & 1 \\ 0 & 1 \end{array}\right] \end{array} \tag{1.14}$$

The rows are the symbol s_t and the columns are the symbol s_{t+1}. A number 1 in the matrix shows that the string $s_t s_{t+1}$ is legal and a 0 shows that the string $s_t s_{t+1}$ is forbidden.

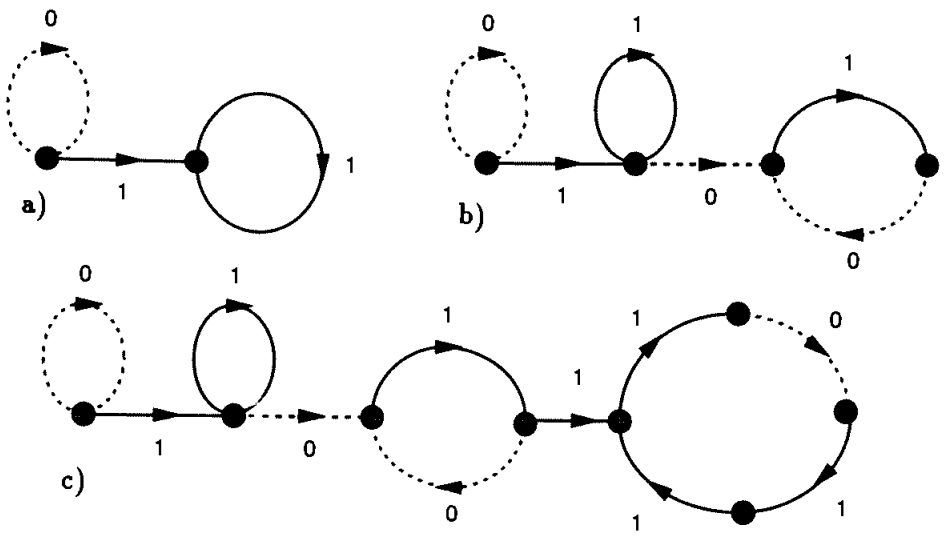

Figure 1.9: Graph representation of legal orbits for a parameter value that gives a stable a) fixed point $\overline{1}$, b) period 2 orbit $\overline{10}$, c) period 4 orbit $\overline{1011}$.

The graph in figure 1.9 b) represents the matrix

$$\begin{array}{c} \\ 000 \\ 011 \\ 111 \\ 001 \\ 110 \\ 010 \\ 101 \end{array} \begin{array}{c} \begin{array}{ccccccc} 000 & 011 & 111 & 001 & 110 & 010 & 101 \end{array} \\ \left[\begin{array}{ccccccc} 1 & 0 & 0 & 1 & 0 & 0 & 0 \\ 0 & 0 & 1 & 0 & 1 & 0 & 0 \\ 0 & 0 & 1 & 0 & 1 & 0 & 0 \\ 0 & 1 & 0 & 0 & 0 & 1 & 0 \\ 0 & 0 & 0 & 0 & 0 & 0 & 1 \\ 0 & 0 & 0 & 0 & 0 & 0 & 1 \\ 0 & 0 & 0 & 0 & 0 & 1 & 0 \end{array}\right] \end{array} \tag{1.15}$$

A row in this matrix is a 3 symbol string $s_{t-2}s_{t-1}s_t$ and a column is a 3 symbol string $s_{t-1}s_ts_{t+1}$. A number 0 in the corresponding matrix element means that the combination giving the 4 symbol string $s_{t-2}s_{t-1}s_ts_{t+1}$ is illegal. The graph representation is much simpler and intuitively understandable that the full matrix. We show later than the construction of a graph is relatively simple and in addition it is simple to find the characteristic polynomial of the matrix from the graph representation [40]. In the ζ-function formalism in chapter 11 this is shown to be useful.

If there exists a finite graph there also exists a corresponding finite Markov matrix and a finite Markov partition of the non-wandering set. A system with a finite Markov partition is a system with finite memory in the sense that we only have to know a finite length symbol string of the past to know which choices we

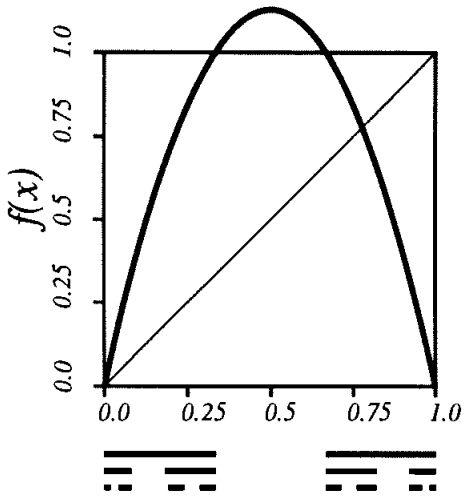

Figure 1.10: The logistic map with $a = 4.5$ and the remaining intervals after 1, 2 and 3 iterations.

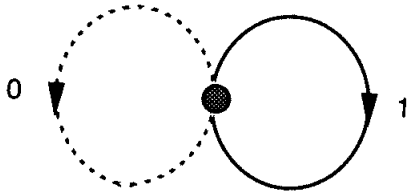

Figure 1.11: The symbolic graph for the complete Cantor set repellor and the attractor for $a = 4$, where all symbol sequences are legal.

have for the next symbol. It is shown by Grassberger [90] that the size of the symbolic graph goes to infinity as we converge to the accumulation point a_∞ of the period doubling bifurcations. At this point the system has infinite memory as defined above.

The tent map has a singular bifurcation for $a = 1$ where all period doubled orbits from the fixed point $\overline{1}$ start to exist and are unstable. The parameter $a = 1$ is then simultaneously the point where the fixed point is borne and the accumulation point a_∞ for the bifurcations of the fixed point.

1.1.2 Unimodal map with complete grammar

If the parameter in the logistic map is $a > 4$ then the critical point x_c diverges for $t \to \infty$ and $x = -\infty$ is the attractor. We will now describe the corresponding repellor. The repellor is a Cantor set and figure 1.10 shows that if we start with the unit interval $(0, 1)$ then at each iteration the middle segment of the remaining intervals escapes from the unit interval.

In symbolic dynamics the orbits in the repellor can be described by all possible combinations of the symbols 0 and 1. The symbols 0 and 1 are letters in a alphabet

$$\{0, 1\} \tag{1.16}$$

and the grammar for a string made from this alphabet is simply that any combination of letters gives a legal string. This grammar is given by the simple graph in

figure 1.11 which represents the Markov matrix

$$\begin{array}{c} \\ 0 \\ 1 \end{array} \begin{array}{c} \begin{array}{cc} 0 & 1 \end{array} \\ \left[\begin{array}{cc} 1 & 1 \\ 1 & 1 \end{array} \right] \end{array} \tag{1.17}$$

If $a = 4$ for the logistic map, x_c is mapped to the fixed point x_0 and we have a chaotic attractor. The symbolic description of the orbits in the attractor is the same complete binary alphabet as for the repellor.

The tent map for $a > 2$ also has a repellor that is described by the same binary symbolic alphabet and for $a = 2$ there is a chaotic attractor with the same description.

1.1.3 The symbolic interval and the kneading sequence

The description of the dynamics for the logistic map when $a_\infty < a < 4$ is complicated and the symbolic description is useful in describing these bifurcations. To make a simple theory for the bifurcations we redefine the symbolic description. The Cantor set in figure 1.10 can be mapped onto the real interval $[0, 1]$ by associating a real number, τ to each infinite symbolic sequence. To keep the ordering of the points on the x-axis we have to define new *well–ordered* symbols w_t.

An increasing function ($f'(x_t) > 0$) preserves the ordering between two points on the x-axis such that if $\hat{x}_t > x_t$ then $\hat{x}_{t+1} > x_{t+1}$. A decreasing function ($f'(x_t) < 0$) reverses the ordering; if $\hat{x}_t > x_t$ then $\hat{x}_{t+1} < x_{t+1}$. The symbol s_t as defined in (1.5) is 0 if the function increases and 1 if the function decreases. We associate with x_t a binary number $\tau(x_t) \in [0, 1]$ as follows

$$\begin{aligned} w_1 &= s_1 \\ w_{t+1} &= \begin{cases} w_t & \text{if } s_t = 0 \\ 1 - w_t & \text{if } s_t = 1 \end{cases} \\ \tau &= 0.w_1 w_2 w_3 \ldots = \sum_{t=1}^{\infty} \frac{w_t}{2^t}. \end{aligned} \tag{1.18}$$

The number $\tau(x_t)$ preserves the ordering of x_t in the sense that if $\hat{x}_{t+1} > x_{t+1}$ then $\tau(\hat{x}_t) > \tau(x_t)$. We call the symbols $w + t$ the well–ordered symbols and $\tau(x_t)$ the well–ordered symbolic future value of x_t or for brevity; the symbolic value.

As long as $a \geq 4$ for the logistic map any real number $0 < \tau < 1$ corresponds to a symbolic description of an orbit in the non-wandering set of the map. If $a < 4$ there is only a subset of the points in the interval $\tau \in [0, 1]$ of the interval that corresponds to the symbolic description of an orbit and the forbidden symbolic values can be

found using the following observation [152]. The largest possible x_t value (except a starting point x_0) is the image of the critical point $x_{\max} = f(x_c)$. An orbit described by a symbolic sequence S will have a point $x > f(x_c)$ if $\tau(S) > \tau(x_c)$ and cannot be an admissible orbit. We define

$$\kappa = \tau(x_c) \tag{1.19}$$

to be the *kneading value* [152] of the unimodal map and the interval

$$(\kappa, 1] \tag{1.20}$$

its *primary pruned interval.*

For the symbolic sequence S, the dynamics is a shift operation

$$S(f^k(x_0)) = \sigma^k S = \{s_{k+1}s_{k+2}s_{k+3}\ldots\} \tag{1.21}$$

and the orbit S is not admissible if τ of any shifted sequence of S falls into the primary pruned interval. For any orbit S there exists a supremum value $\tau^{\max}$ of the orbit and its images

$$\tau^{\max}(S) = \sup_k \tau(\sigma^k S) \tag{1.22}$$

From this it follows

Theorem 1[175, 147, 99, 152]: Let κ be the kneading value of the critical point as defined in (1.19) and $\tau^{\max}(S)$ be the supremum symbolic value of the orbit S as defined in (1.22). Then the orbit S is admissible if and only if $\tau^{\max}(S) \leq \kappa$.

1.1.4 Bifurcations and symbolic parameter space

We can make use of the kneading value when describing the bifurcations in the unimodal map.

The kneading value κ can be considered as a new topological parameter of the map. In figures 1.12 and 1.13 the value of κ is drawn as a function of a for the logistic map and the tent map. The plot is a staircase-like monotone increasing function. The jumps in κ correspond to symbolic values that are not allowed. Each jump in κ has a one to one correspondence to one window on the parameter axis with a stable periodic orbit for the smooth unimodal map. We can consider the kneading interval $\kappa \in [0, 1]$ to be a parameter space for the unimodal map and we will denote κ the symbolic parameter value when we take this point of view.

The tent map has larger jumps in κ in figure 1.13 than in the logistic map because the tent map does not have any windows, but if these two maps have the same kneading value then the same orbits exist for the parameter values a.

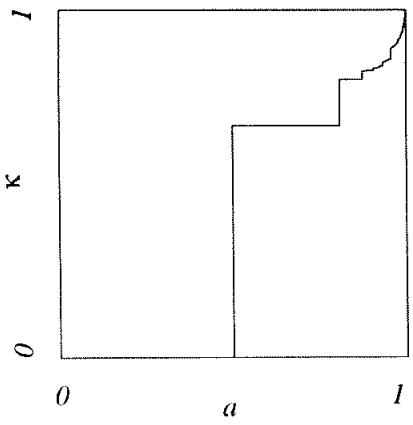

Figure 1.12: The kneading value κ as a function of the parameter a for the logistic map.

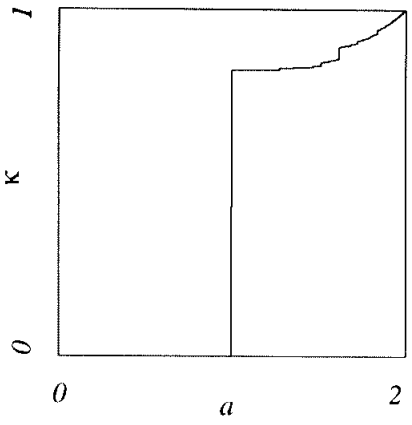

Figure 1.13: The kneading value κ as a function of the parameter a for the tent map.

1.1.5 Band merging bifurcations

One bifurcation in figure 1.3 is the *band merging* bifurcation where $n \cdot 2^{m+1}$ of chaotic bands merge into $n \cdot 2^m$ of chaotic bands. Between two chaotic bands there is an unstable period $n \cdot 2^m$ orbit with $df^{(n)}/dx < -1$ which is an isolated part of the repellor. At the band merging bifurcation this points starts to belong to the attractor when two and two of the $n \cdot 2^{m+1}$ bands join each other at the $n \cdot 2^m$ points of the periodic orbit. The boundaries of the chaotic bands are images of the critical point and the kneading sequence is preperiodic to the symbolic description of the unstable period n orbit.

The simplest example of a band merging bifurcation is the point where two bands merge into one band and the joining point is the fixed point $\overline{1}$. The kneading sequence is here

$$K = 10\overline{1}$$

giving the kneading value

$$\kappa = 0.1\overline{10} = 0.11010101010\ldots = 5/6 \tag{1.23}$$

which is the symbolic parameter value for the two band merging bifurcation for all unimodal maps. No orbits with $\tau^{\max}(S) > 0.1\overline{10}$ exist for this parameter value. In the logistic map the parameter value $a = 3.6785\ldots$ gives this band merging bifurcation and in figure 1.14 the map and the preimages of the fixed point is drawn showing that at this point the parabola is tangent to the closest of the

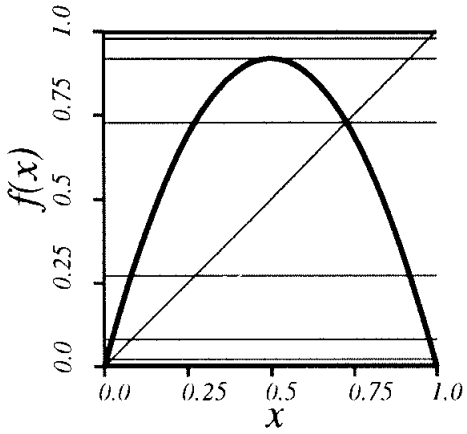

Figure 1.14: The logistic map at the band merging point when two bands merge to one band $a = 3.6785$ and the preimages of the fixed point drawn as horizontal lines.

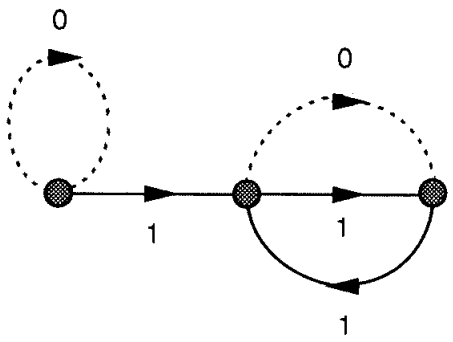

Figure 1.15: The symbolic graph for the band merging point $\kappa = 0.1\overline{10}$.

horizontal lines. There exists a finite grammar describing the non-wandering set and the Markov graph in figure 1.15 shows the rules giving the admissible symbol strings. Comparing with the graphs in figure 1.9 b) and c) we find that the fixed point $\overline{1}$ that used to be a transient orbit now is included in the last, attracting part of the graph. The attractor part of the Markov graph in figure 1.15 can be described by the new two letter alphabet

$$\{01, 11\}$$

All combinations of the two letters 01 and 11 give a symbol string which corresponds to an orbit in the chaotic attractor.

To each period doubling bifurcation there is a corresponding band merging bifurcation. The kneading sequence at a period doubling bifurcation is given by (1.13) and is

$$K = \overline{s_1 s_2 \dots s_n} \rightarrow K = \overline{s_1 s_2 \dots s_n s_1 s_2 \dots s_{n-1}(1 - s_n)} \tag{1.24}$$

The band merging bifurcation which corresponds to this is located at the the kneading sequence

$$K = s_1 s_2 \dots s_n s_1 s_2 \dots s_{n-1}(1 - s_n)\overline{s_1 s_2 \dots s_n} \tag{1.25}$$

with the same symbol string $s_1 s_2 \dots s_n$. The band merging bifurcations for the fixed point in the logistic map also converge to the accumulation parameter a_∞ with the same Feigenbaum scaling factor but with $a > a_\infty$.

The two kinds of bifurcations have the same kneading sequence at the accumulation point:

$$1011101010111011\ldots$$

and this gives the topological parameter value

$$\kappa_\infty = 0.1101001100101101\ldots \tag{1.26}$$

There are similarities between the period doubling and the band merging bifurcation but there are also important differences. The period doubling bifurcation is a local bifurcation depending only on the stability of one orbit. The band merging bifurcation is a global bifurcation involving the critical point and a large non-wandering set. We find that in the discussion of the two dimensional maps in chapter 5 this is analogue to a creation of a homoclinic tangency. Also the similar scaling property of the two kind of bifurcations that exists for the logistic map is not true for all unimodal maps. The tent map has a singular creation of periodic orbits but figure 1.4 shows that there are band merging bifurcations converging to $a_\infty = 1$. The description of the allowed symbol strings changes very differently around the two different bifurcations. The period doubling bifurcations create a new structure in the Markov graph which is a new attractor, leaving the old attractor as a transient loop. The Markov graph does not change from one period doubling bifurcation to the next. The Markov graph for the band merging bifurcation is valid only for this parameter value.

1.1.6 Resonances

In a chaotic band there are resonances where new orbits are created and there is a window with a stable orbit that goes through period doublings and band merging bifurcations and finally in a crisis bifurcation again gives a band attractor. We look in some detail at the simplest of these resonances which is the period 3 resonance in figure 1.3 b).

One stable and one unstable period 3 orbit are created at a tangent bifurcation in the logistic map at $a = 3.8284\ldots$. The symbolic description of both the two orbits are $S = \overline{101}$ at the parameter where they are created. At the super-stable point $a = 3.8319\ldots$ the stable orbit changes symbolic dynamics to $S = \overline{100}$. The symbolic parameter value of the bifurcation creating the two orbits is

$$\kappa = \tau^{\max}(\overline{101}) = 0.\overline{110} = 6/7 \tag{1.27}$$

The symbolic parameter value where the stable orbit crosses the super-stable point is

$$\kappa = \tau^{\max}(\overline{100}) = 0.\overline{111000} = 8/9. \tag{1.28}$$

The orbit $\overline{100}$ undergoes period doubling bifurcations to orbits with a symbolic description given by eq. (1.24) with the initial string $s_1 s_2 s_3 = 100$ and also band merging bifurcations with the kneading sequence given by eq. (1.25).

The *crisis* bifurcation of the period 3 resonance is the parameter value where the attractor changes from 3 chaotic bands to one chaotic band. This is the bifurcation when the critical point maps into the unstable period 3 orbit $\overline{101}$ which for the logistic map occurs for $a = 3.8568\ldots$. This bifurcation has the kneading sequence $100\overline{101}$ and the symbolic parameter value

$$\kappa = 0.111\overline{001} = 25/28. \tag{1.29}$$

In the general description of a resonance two orbits $\overline{s_1 s_2 \ldots s_n}$ and $\overline{s_1 s_2 \ldots s_{n-1}(1-s_n)}$ are born at a tangent bifurcation at the the symbolic parameter value

$$\kappa = \tau(\overline{s_1 s_2 \ldots s_{n-1}(1-s_n)}). \tag{1.30}$$

The string $s_1 s_2 \ldots s_n$ giving a resonance can not be of the form $s_1 s_2 (1 - s_{(n/2)}) s_1 s_2 \ldots s_{(n/2)}$ since this orbit would be born at a period doubling, the number of symbols '1' in $s_1 s_2 \ldots s_n$ is odd and the cyclic permutation $(\overline{s_1 s_2 \ldots s_n})$ is the permutation giving the largest value of τ. The resonance has period doubling and band merging bifurcations with $\overline{s_1 s_2 \ldots s_n}$ as the generating string and the crisis bifurcation takes place at

$$\kappa = \tau^{\max}(s_1 s_2 \ldots s_n \overline{s_1 s_2 \ldots s_{n-1}(1-s_n)}). \tag{1.31}$$

The ordering of resonances along the parameter axis follows the size of $\tau^{\max}(S)$ and this ordering of orbits is often called the MSS (Metropolis, Stein, Stein) sequence.

We can mark the values $\tau(\overline{S})$ on the κ axis for different periodic orbits $\overline{S}$ and this gives a picture analog to the bifurcation tree in figure 1.3. In figure 1.16 a) we have marked the symbolic value of some periodic orbits orbits and in figure 1.16 b) we have also drawn some of the intervals that corresponds to stable windows in the smooth unimodal map. The κ-axis may be considered as a topologic or symbolic parameter axis. The ordering of bifurcations is the same along κ as along the parameter a and therefore are these two axis topological equivalent but the metric properties (scaling etc.) is different.

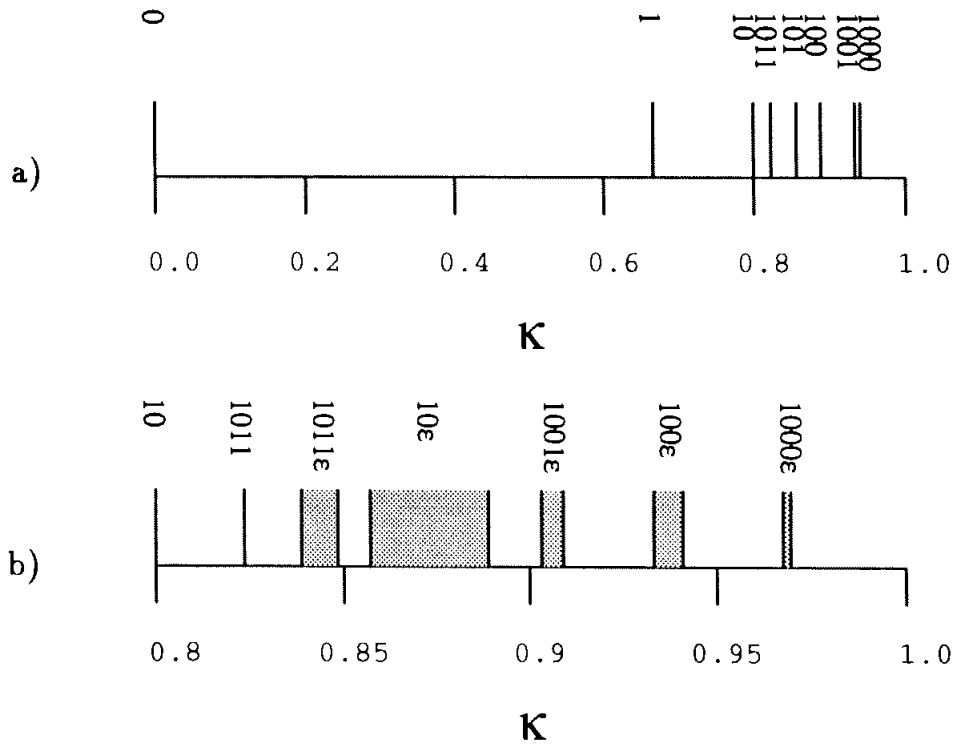

Figure 1.16: The bifurcation points of periodic orbits plotted at the symbolic parameter axis κ.

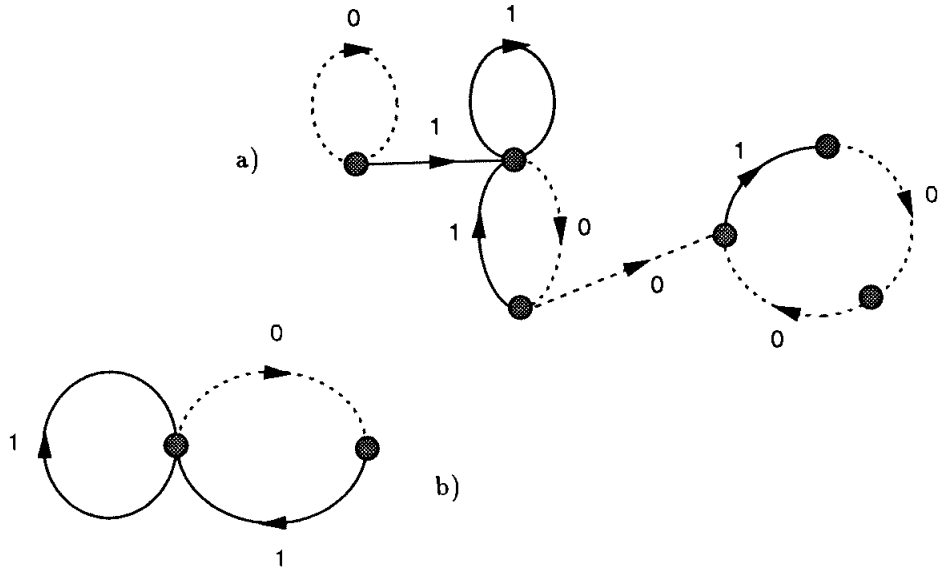

Figure 1.17: Graph representation of legal orbits for a parameter value that gives the stable period 3 orbit. a) The whole automaton. b) The Cantor set part of the automaton that follows after the 0–loop.

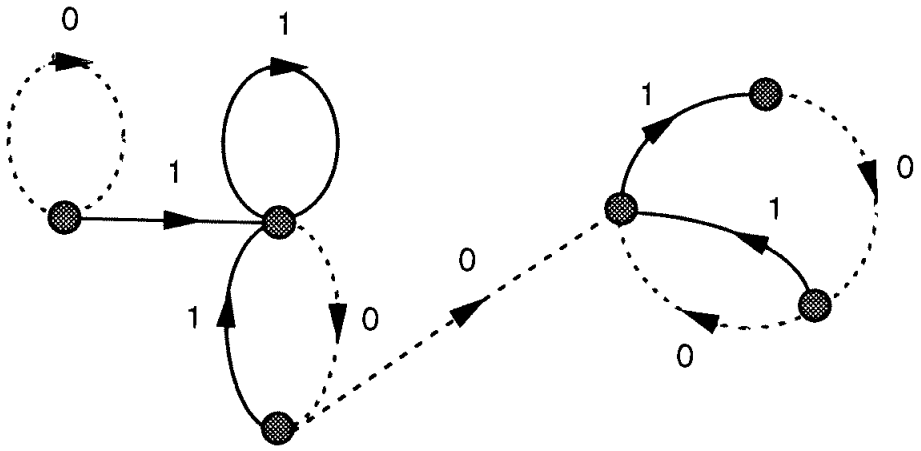

Figure 1.18: Graph representation of legal orbits for a parameter value that gives the crisis bifurcation of the period 3 resonance.

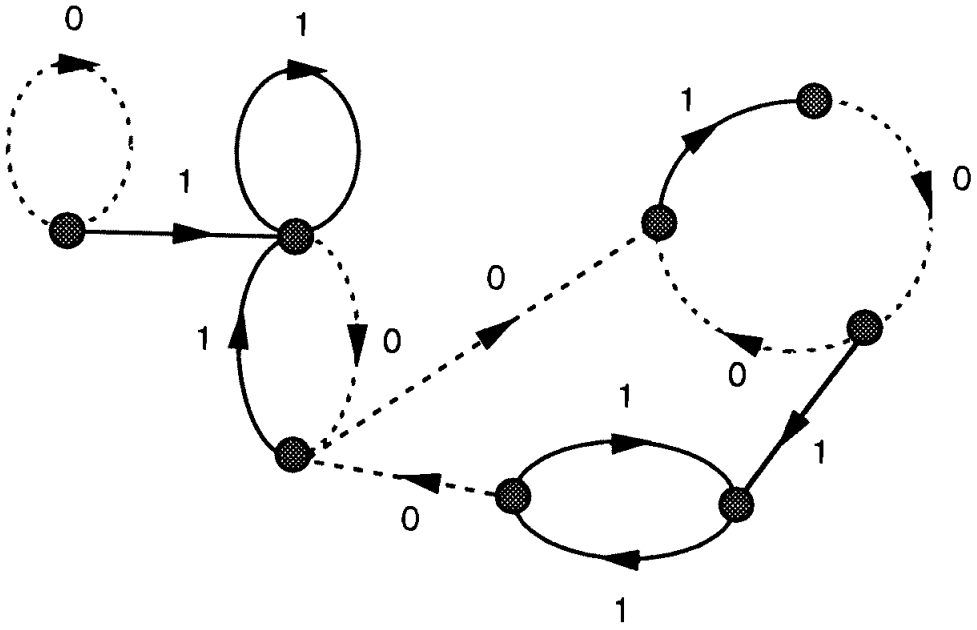

Figure 1.19: Graph representation for the kneading sequence $100101\overline{1}$.

The symbolic automaton graphs for the stable period 3 orbit $\overline{100}$ is drawn in figure 1.17 and the automaton at the band merging point is drawn in figure 1.18. In figure 1.17 a) the rightmost part of the graph is the stable orbit but of more interest is the middle part describing the fractal repellor. When removing the 0–loop to the left and the $\overline{100}$ attractor to the right, the remaining part is drawn in figure 1.17 b). This automaton gives the symbolic description of the Cantor set repellor consisting of all orbits created for a smaller parameter value except the isolated $\overline{0}$ fixed point. It can also be described by the alphabet

$$\{1, 01\} \tag{1.32}$$

The automaton for the kneading sequence $100\overline{101}$ in figure 1.19 shows that the fractal repellor $\{1, 01\}$ is still isolated and the attractor is the chaotic bands that can be described bye the alphabet

$$\{100, 101\} \tag{1.33}$$

with all combinations of symbols allowed. For any parameter value larger than the crisis bifurcation the $\{1, 01\}$ part is connected to the attractor giving one band attractor again. One example is given in figure 1.19 where the diagram for the kneading sequence $100101\overline{1}$ is drawn.

1.1.7 Resonances in the tent map

The tent map (1.3) has discontinuous $f'(x)$ and for $a > 1$ then $|f'(x)| = a > 1$ and there can not be a stable orbit as attractor. The fixed point $x_{\overline{0}} = 0$ is stable for $a < 1$ and unstable for $a > 1$. This does not prevent the map from having chaotic bands an in figure 1.4 we find that there are bands close to the bifurcation of the fixed point at $a = 1$ but no bands in a period 3 resonance or in any other resonance.

The band merging from $2n$ bands to n bands in figure 1.4 takes place when the slope of $f^{(2n)}(x)$ has absolute value 2. We have $|df^{(2n)}(x)/dx| = a^{2n}$ which gives a band merging for

$$a = 2^{\frac{1}{-2n}} \tag{1.34}$$

These values converges to $a = 1$ from above, not as a geometric series but much slower.

There exists no other band structure than the bands generated by the fixed point and a chaotic band has no internal resonance structure. This is easily shown because in the one band region $\sqrt{2} < a < 2$ the orbits of length n have slope $|df^{(2n)}(x)/dx| = a^{2n}$ and this is larger than 2 for all orbits $n \geq 2$ and then there are

no bands other than the period 1 band. The period 3 orbit is born, goes through all period doublings, band mergings and the crisis bifurcation at one singular parameter value $a = (1 + \sqrt{5})/2 = 1.6180\ldots$. This is one large jump in the plot of κ as a function of a in figure 1.13.

From the self similarity it follows that also the 2^n bands are without internal structure of bands. The slope is squared for each bifurcation and the shortest orbit born in the bands is twice as long and cannot have bands.

The plot of κ as a function of a in figure 1.13 has fewer steps and larger jumps for the tent map than for the logistic map because of the singular bifurcation points in the parameter a.

1.2 Construction of a finite automaton

There is a simple procedure giving the Markov graph or an automaton for the unimodal map when we know the kneading sequence K. We can also use the procedure to generate a Markov graph for other systems given a finite list of forbidden symbol strings.

In general there is no guarantee that the Markov graph for the unimodal map is finite. One example where the automaton is infinite is the accumulation point of the period doubling bifurcation [90]. If there exists a stable periodic orbit the automaton is finite and ends in a cycle with the symbols of the stable orbit. We may approximate the automaton for most parameter values with an automaton for a stable orbit at a parameter value close to the exact parameter value. We conjecture that the automaton converges to the correct automaton as we choose parameter values giving stable orbits closer and closer to the parameter value. The eigenvalue from the automatons converges to the limit also when the attractor is a chaotic orbit.

A different way to approximate the automaton is to approximate the kneading sequence by a string that after a finite number of symbols ends in a periodic orbit. This may be e.g. a band merging or a crisis bifurcations. This choice also gives a rational kneading value and a finite graph and we expect the eigenvalues will converge. The calculations are however more complicated and it is not so clear which part of the graph gives the largest eigenvalues.

The part of the automata which gives the eigenvalues we are interested in when there exist a stable orbit is a Cantor set repellor. We show how to find the topological entropy and other statistical measures from the automaton below. The repellor is the first loop structure that follows after the transient $\overline{0}$ loop and if they exist as

isolated transient loops, also after the $\overline{1}$ loop, $\overline{10}$ loop, $\overline{1011}$ loop, ... This is the period doubled loops of the fixed point. If the stable orbit is in the one-band region only $\overline{0}$ is a transient. If the stable orbit is in the two band region $\overline{0}$ is a transient followed by $\overline{1}$ as a transient and then followed by the repellor giving the largest eigenvalues. The four band region gives three transient loops etc.

One example is the stable orbit $\overline{100}$ in the one-band region for which the whole automaton is drawn in figure 1.17 a) while the Cantor set part is drawn in figure 1.17 b). We find in figure 1.18 that this Cantor set part is the same automaton also at the crisis bifurcation and it is the same graph all along the period 3 resonance.

The topological entropy (see section 1.3) for the transient repellor is here

$$h = \ln\left(\frac{2}{\sqrt{5}-1}\right) = \ln(1.618\ldots) \tag{1.35}$$

which is larger than the topological entropy for the three chaotic bands at the crisis bifurcation

$$h = \ln\left(2^{1/3}\right) = \ln(1.260\ldots). \tag{1.36}$$

The topological entropy for the chaotic bands at the crisis of a period n resonance is $1/n$-th of the topological entropy for the complete binary repellor $h = \ln 2$. The bands at the crisis of the period 3 resonance has the largest entropy in any resonance of the one band regime. The topological entropy at the band merging is given by the graph in figure 1.15 and gives $h = \ln\sqrt{2}$. The topological entropy is for the part of the graph following the 0 loop in the one band regime

$$\ln\sqrt{2} \leq h \leq \ln 2 \tag{1.37}$$

which is larger than any topological entropy in a resonance. By self similarity is the same true for the 2,4,8,...band regimes. We expect that the part of the Markov graph giving the largest topological entropy also gives the leading eigenvalues for other measures.

Since the repellor is constant from a tangent bifurcation to the crisis bifurcation we restrict ourself to choose stable periodic orbits born at a tangent bifurcation as other stable orbits inside a resonance do not give different leading eigenvalues.

The symbolic description of the possible orbits from a point x_0 in the unimodal map can be drawn as a path down a binary tree as drawn in figure 1.20. We refer to a node in the binary tree with the preceding symbol string and we refer to the top node as $\emptyset$. We first draw the kneading sequence $K = s_1 s_2 s_3 \ldots$ for the chosen parameter value as a path in the tree. From each node along this path there is a

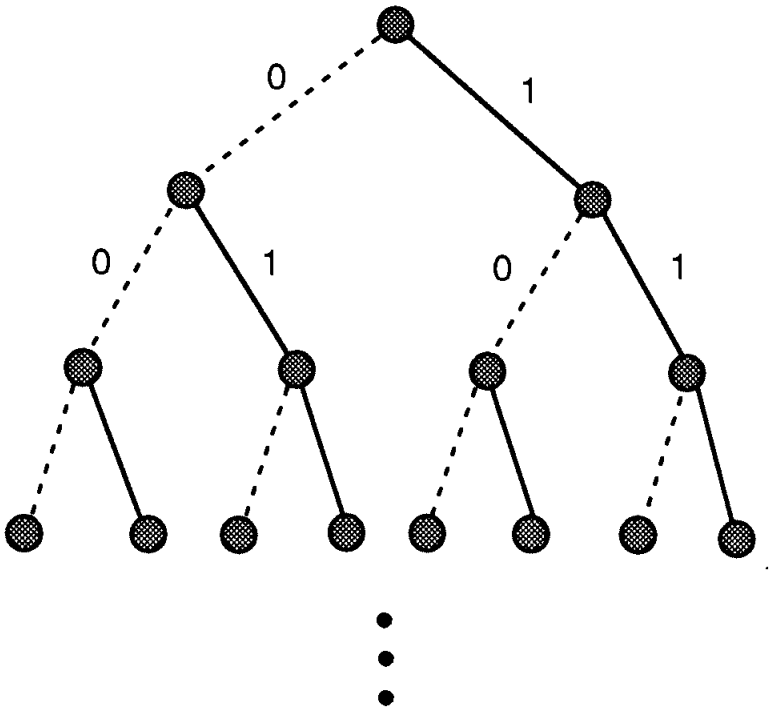

Figure 1.20: A binary tree.

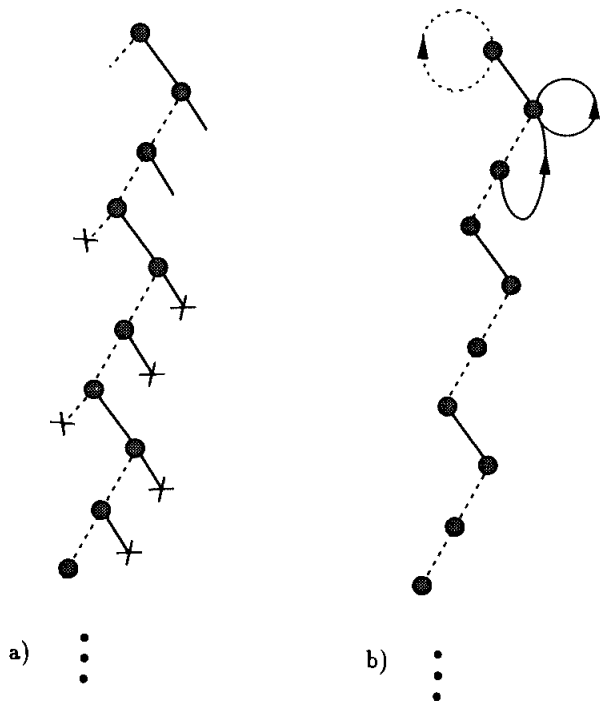

Figure 1.21: The construction of the stable period 3 automaton. In a) the forbidden side branches ends in a cross, and in b) the legal side branches are reconnected to the graph.

side branch and we have to decide if this is a legal branch. The side branch after the n–th node is $s_1 s_2 \ldots s_n(1 - s_{n+1})$ and this branch is legal if

$$\tau(s_i s_{i+1} \ldots s_n(1 - s_{n+1})) < \kappa \tag{1.38}$$

for all $i \in \{1, 2, \ldots n\}$. A side branch that is legal is connected to the node with the symbolic description $s_1 s_2 \ldots s_k$ where the symbol string is

$$s_1 s_2 \ldots s_k = s_{n-k+2} \ldots s_n(1 - s_{n+1}) \tag{1.39}$$

for the largest possible integer k. This procedure prevents that a legal side branch is followed by an illegal string. The automaton we obtain by this procedure can then be minimalized.

We give a few examples how to use this procedure. Figure 1.21 a) shows the path in the binary tree for the kneading sequence $K = \overline{100}$ with $\kappa = 0.\overline{111000}$. We

find the following legal side branches of the path

$$\begin{array}{rcrcrcl} 0 & \Rightarrow & \tau(0) & = & 0 & < & \kappa \\ 11 & \Rightarrow & \tau(11) & = & 0.10 & < & \kappa \\ 101 & \Rightarrow & \tau(101) & = & 0.110 & < & \kappa \\ & & \tau(01) & = & 0.01 & < & \kappa \\ & & \tau(1) & = & 0.1 & < & \kappa \end{array}$$

and the forbidden branches

$$\begin{array}{rcrcrcl} 1000 & \Rightarrow & \tau(1000) & = & 0.1111 & > & \kappa \\ 10011 & \Rightarrow & \tau(10011) & = & 0.11101 & > & \kappa \\ 100101 & \Rightarrow & \tau(100101) & = & 0.111001 & > & \kappa \\ 1001000 & \Rightarrow & \tau(1001000) & = & 0.1110000 & < & \kappa \\ & & \tau(001000) & = & 0.001111 & < & \kappa \\ & & \tau(01000) & = & 0.01111 & < & \kappa \\ & & \tau(1000) & = & 0.1111 & > & \kappa \\ & \vdots & & & & & \end{array}$$

The forbidden side branches is marked by a cross in figure 1.21. The reconnection of the legal branches to a node following (1.39) gives

$$\begin{array}{rcl} 0 & \to & \emptyset \\ 11 & \to & 1 \\ 101 & \to & 1 \end{array}$$

and are drawn in figure 1.21 b). In figure 1.21 b) we see that the node 100100 has the same infinite future as the node 100 and we identify these two nodes and then we have the finite automaton of figure 1.17.

In figure 1.22 the construction of the automaton for the kneading sequence $K = 100101\overline{1}$ is shown.

These rules except the final reduction of the graph are implemented on a computer and given a stable periodic orbit by its symbolic string it gives the automata. On the computer the stable period n orbit loop is removed by letting also the string $s_1 s_2 \dots s_n$ be forbidden. This procedure for constructing a Markov graph is easily generalized to a construction of a n-ary tree where the forbidden strings are given as a finite list of strings. We than draw the paths of all forbidden strings in the tree. Then all side branches are checked, not by (1.38) but with the list of forbidden strings and the side branch is marked illegal if the string $s_i s_{i+1} \dots s_n(1 - s_{n+1})$, $i \in \{1, \dots, n\}$ is in the list. The reconnection of side branches is done by (1.39). A finite list of forbidden strings gives a finite automaton.

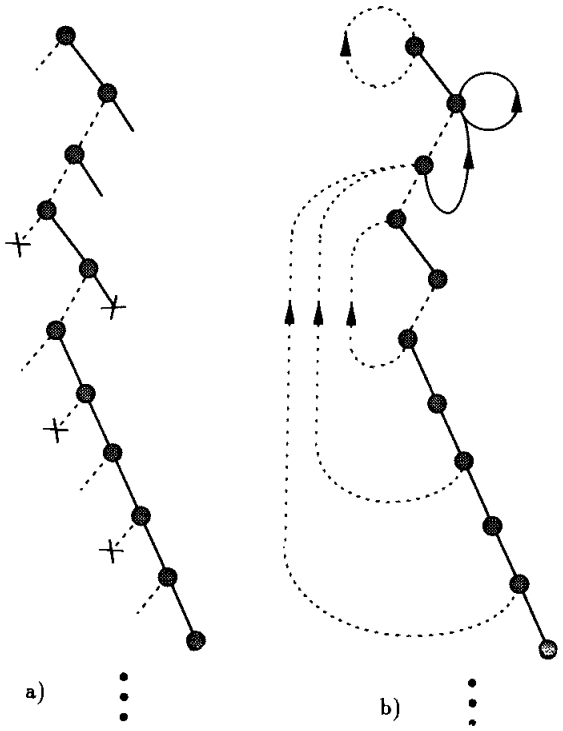

Figure 1.22: The construction of the automaton for kneading sequence $K = 100101\overline{1}$. In a) the forbidden side branches ends in a cross, and in b) the legal side branches are reconnected to the graph.

1.3 Topological entropy

The topological entropy h is a measure of the exponential growth of the number of periodic orbits with the length. This is the simplest of the average values one can find and it is the simplest application of the zeta-function formulation discussed in chapter 11 Let $N(n)$ be the number of periodic orbits of length n, then

$$N(n) \sim e^{hn} \tag{1.40}$$

in the limit $n \to \infty$. The number h can be obtained by calculating and counting periodic orbits, but if we know the symbolic description of the map h can be obtained in a much more effective way [45, 162, 40, 14].

The topological entropy is the negative logarithm of the leading (smallest and real) eigenvalue of the characteristic polynomial of the Markov matrix $h = -\ln z$. This polynomial

$$p(z) = 1 + a_1 z + a_2 z^2 + a_3 z^3 + \cdots = 0 \tag{1.41}$$

is obtained from the automaton by the following rules: a_i is initially 0; $a_i \to a_i - 1$ for each non self intersecting loop in the graph with i nodes; $a_i \to a_i \pm 1$ for each combination of non self intersecting loops that have no node in common and where the sum of the nodes is i. The sign $+$ is chosen when the number of loops in the combination is even and the sign $-$ if the number of loops is odd. This is applied for each part of the graph that is recursive; that is the part of the graph where one can get from any node in this part to any other node in the same part by some path. Each recursive part of the graph gives a eigenvalue and the smallest real eigenvalue gives the topological entropy.

$$h = -\ln z_0 \tag{1.42}$$

The simplest example is the complete binary map where the symbolic description of the repellor or the attractor is given by the automaton in figure 1.11. The automaton has two loops with length 1 and the loops can not be combined as they have one node in common. This give the polynomial

$$p(z) = 1 - 2z = 0$$

and from this $z = 1/2$ and

$$h = \ln 2$$

This result is of course easily obtained by just observe that since all combinations of the two symbols 0 and 1 are legal and most strings are not a repetition of shorter strings, then the number of periodic orbits grows as

$$N(n) \sim 2^n$$

The repellor in the period 3 resonance window in figure 1.17 b) gives one length 1 loop and one length 2 loop and topological entropy is then

$$\begin{aligned} 1 - z - z^2 &= 0 \\ z &= \frac{1+\sqrt{5}}{2} \\ h &= \ln\left(\frac{2}{1+\sqrt{5}}\right) \end{aligned}$$

A more interesting example is to choose a parameter value a that numerically gives a chaotic attractor and look at the convergence of h. If we choose $a = 3.8$ in the logistic map we find the kneading sequence

$$K = 10110111101101111010111101111 10\ldots$$

and we may e.g. find the automaton describing the repellor of the period 29 resonance close to the chaotic attractor. This gives a automaton with 29 nodes and the characteristic polynomial

$$\begin{aligned} p(z) \;=\; & 1 - z^1 - z^2 + z^3 - z^4 - z^5 + z^6 - z^7 + z^8 - z^9 - z^{10} \\ & + z^{11} - z^{12} - z^{13} + z^{14} - z^{15} + z^{16} - z^{17} - z^{18} + z^{19} + z^{20} \\ & - z^{21} + z^{22} - z^{23} + z^{24} + z^{25} - z^{26} + z^{27} - z^{28} \end{aligned}$$

and solving $p(z) = 0$ gives the smallest real root

$$z = 0.62616120\ldots$$

The error can be estimated to be of order $z^{29} \approx 10^{-6}$ because going from length 29 to a longer string typically for the unimodal map graphs or combination of loops with 29 and more nodes giving terms $\pm z^{29}$ and of higher order in the polynomial. Describing resonances of increasing length and with $a < 3.8$ we find polynomials with a better estimate for the topological entropy. For the closest stable period 90 orbit we find the topological entropy

$$\begin{aligned} h &= -\ln 0.62616130424685\ldots \\ &= \ln 1.59703257486152\ldots \\ &= 0.46814726655867\ldots. \end{aligned} \tag{1.43}$$

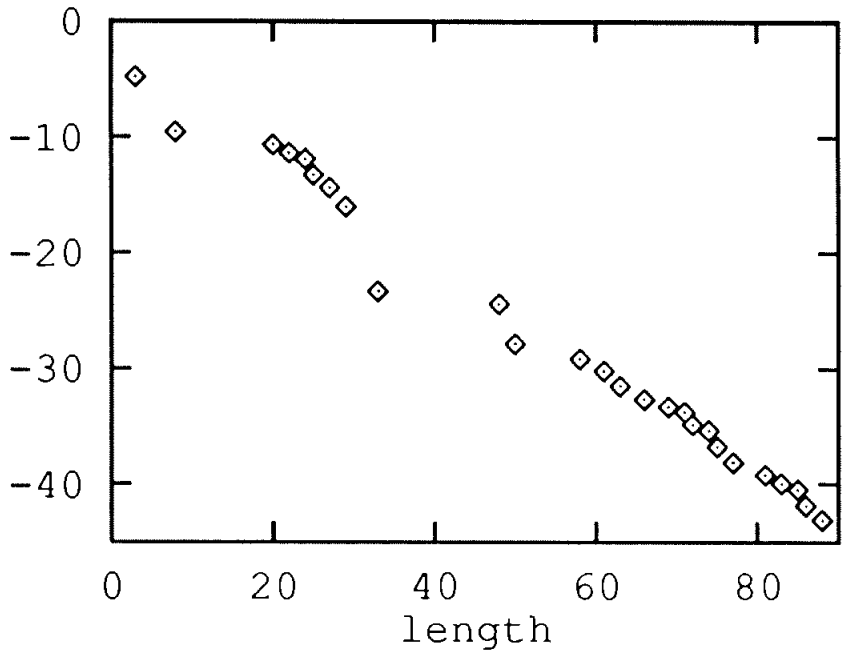

Figure 1.23: The logarithm of the difference between the leading zero of the characteristical polynomial and our best estimate as a function of the length for the logistic map $a = 3.8$.

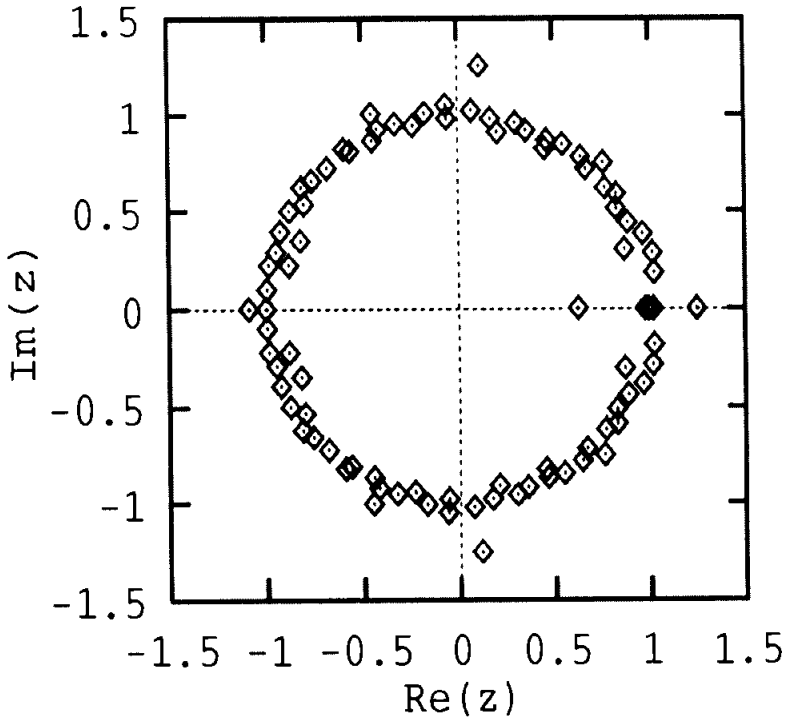

Figure 1.24: The zeroes of the characteristical polynomial for the logistic map $a = 3.8$ approximated up to length 90 symbolic strings.

We can find how fast this converges to our best estimate (1.43). In figure 1.23 is the logarithm of the difference between the zero of a polynomial and our best estimate plotted as a function of the length of the stable periodic orbit. The convergence is approximately linear with a slope of $-0.47 \approx h$.

We can find all real and complex zeroes of the characteristical polynomial and in figure 1.24 the zeroes of the polynomial obtained by including the forbidden strings of length 90 and less are plotted in the complex plane. The leading zero giving the topological entropy is the point closest to the origin while most of the other zeroes are close to the unit circle. This circle gives the radius of convergence.

All automatons for the unimodal map are simple because the automaton consists only of one long path of nodes and pointers back from a node to an earlier node.

Chapter 2

The n–modal map

Our motivation for studying multi-modal 1-dimensional maps is both because these maps are interesting chaotic systems and because as it will be shown below (chapter 4), the multi-modal maps are the approximations for the general 2-dimensional folding maps. The "finger print" of a n-modal map is the *swallowtail* bifurcation structure in the parameter space and to describe the organization of the swallowtails is one main result in this chapter. The swallowtails are also typical structures in the 2-dimensional folding maps and the methods used in this chapter will be applied for folding maps in chapter 4. We will also study here how a change of modality implies that the symbolic description may change for an unstable orbit followed adiabatically in the parameter space. This will also be the situation for the folding maps and is the main difficulty in the definition of symbolic dynamics as discussed in section 5.2.

A one dimensional continuous map $x_{t+1} = f(x_t)$ with n maximum and minimum points is called the n–modal map. This is a natural generalization of the study of unimodal maps with bifurcations and kneading sequences as the unimodal maps but with larger alphabets and more complicated bifurcations. Bifurcation diagrams for n-modal maps with $n > 2$ have not been systematically studied earlier. In chapter 4 we show that a restricted n-modal map gives the approximate description of the Hénon map, and we conjecture that such approximations are applicable to most folding flows in three dimensions.

The complete unimodal repellor, figure 1.10, has at l-th level 2^l intervals remaining in the interval $[0, 1]$. In a complete n–modal repellor a Cantor set with $(n+1)^l$ intervals remaining at each level l, so a $(n+1)$–ary alphabet labels uniquely the points in the Cantor set. For example figure 2.1 shows the bimodal function

$$f(x) = x^3 - ax + b \tag{2.1}$$

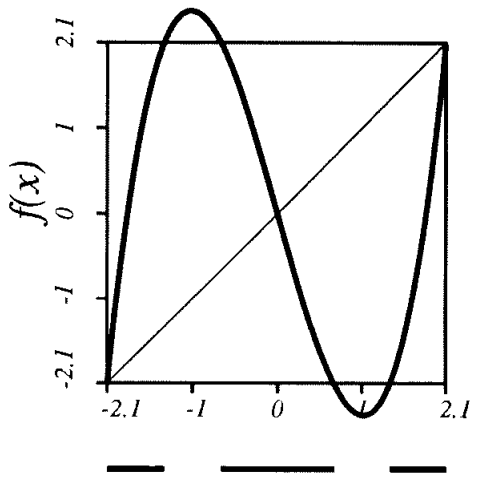

Figure 2.1: The bimodal map (2.1) with $a = 3.5$ and $b = 0$, and the intervals which have not escaped after 1 iteration.

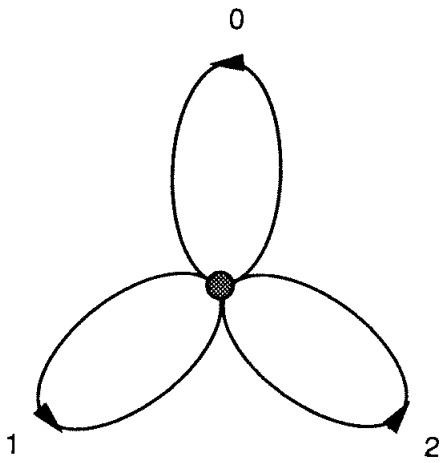

Figure 2.2: The automaton for the complete 3–ary Cantor set repellor; all symbol strings are legal.

with maximum at $x_{c1} = -\sqrt{a/3}$, and minimum at $x_{c2} = \sqrt{a/3}$, for parameter values $a = 3.5$ and $b = 0$. The 3 intervals are labeled by the alphabet $s \in \{0, 1, 2\}$ and the automaton graph in figure 2.2 generates all admissible strings of the three symbols.

One example of a trimodal map is given by the function

$$f(x) = cx^4 + x^3 - ax + b \tag{2.2}$$

drawn in figure 2.3 for $a = 5.85$, $b = 2.8$ and $c = 0.15$. The repellor is here a complete 4–interval Cantor set.

We shall enumerate the n–modal map critical points; $x_{c1}, x_{c2}, \ldots x_{cn}$ from left to right. The symbol corresponding to a point x_t is

$$s_t = \begin{cases} 0 & \text{if} \quad x_t < x_{c1} \\ i & \text{if} \quad x_{ci} < x_t < x_{c(i+1)} \\ n & \text{if} \quad x_t > x_{cn} \end{cases} \tag{2.3}$$

For convenience we choose $f'(x) > 0$ for $x_t < x_{c1}$. In that case $f'(x) > 0$ for s_t even and $f'(x) < 0$ for s_t odd, and x_{ci} is a maximum if i is odd and a minimum if i is even. Choosing $f'(x) < 0$ for $x_t < x_{c1}$ gives a map with slightly different bifurcation structure which can be studied by the same method. As for the unimodal map, the ordering of symbols has to be reversed when $f'(x) < 0$, *i.e.* for s_t odd. The well ordered symbolic value of the point x_0 with future symbol string $s_1 s_2 s_3 \ldots$ is

$$\tau = 0.w_1 w_2 w_3 \ldots = \sum_{t=1}^{\infty} \frac{w_t}{(n+1)^t} \tag{2.4}$$

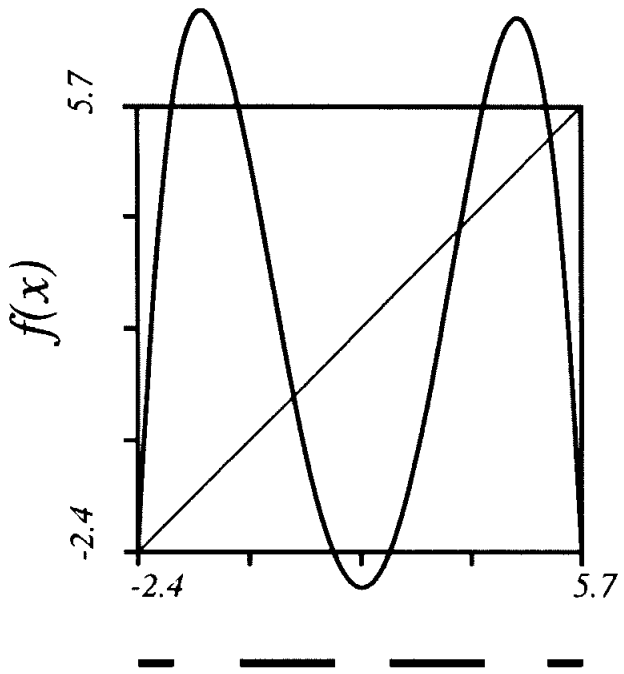

Figure 2.3: The 3–modal map (2.1 with $a = 5.85$, $b = 2.8$ and $c = 0.15$ and the remaining intervals after 1 iteration.

where w_t is given recursively by

$$\begin{aligned} w_1 &= s_1 \\ p_1 &= \begin{cases} 1 & \text{if } s_1 \text{ even} \\ -1 & \text{if } s_1 \text{ odd} \end{cases} \end{aligned}$$

$$\begin{aligned} w_t &= \begin{cases} s_t & \text{if } p_{t-1} = 1 \\ (n - s_t) & \text{if } p_{t-1} = -1 \end{cases} \\ p_t &= \begin{cases} p_{t-1} & \text{if } s_t \text{ even} \\ -p_{t-1} & \text{if } s_t \text{ odd} \end{cases} \end{aligned} \tag{2.5}$$

In the unimodal case is $n = 1$ and the algorithm (2.4) reduces to algorithm (1.18). If $f'(x) < 0$ for $x_t < x_{c1}$ we have the same algorithm but with the inverted values of p_t.

The n critical points $x_{c1}x_{c2}\ldots x_{cn}$ yield n different kneading sequences $K_1K_2\ldots K_n$, and n kneading values $\kappa_1\kappa_2\ldots\kappa_n$. As for the unimodal map, the critical points bound the extreme x values an orbit can have. The i-th critical point x_{ci} restricts the value $f(x)$ can take on the interval $x_{c(i-1)} < x < x_{c(i+1)}$. For a point x between two critical points, the value $f(x)$ is smaller than the closest maximum point and larger than the closest minimum point.

The admissibility (pruning) condition for orbit S is

$$\begin{aligned} \tau_i^{\max}(S) &\leq \kappa_i \quad \text{for} \quad i \quad \text{odd} \\ \tau_i^{\min}(S) &\geq \kappa_i \quad \text{for} \quad i \quad \text{even} \end{aligned} \tag{2.6}$$

The index i on τ restricts x_0 to the appropriate interval, $s_0 = i - 1$ or $s_0 = i$. If $s_0 = 0$ there is no explicit minimum restriction, and if $s_0 = n$ there is no explicit maximum (minimum) restriction if n is even (odd).

One complication is that as the parameters vary a map may lose some of the critical points. A maximum and a minimum point x_{ci} and $x_{c(i+1)}$ may merge, reducing the function $f(x)$ to have $(n-2)$ critical points and making the map $(n-2)$–modal. The symbol $s \in \{i-1, i, i+1\}$ are then indistinguishable and a symbol $i-1$ can be changed to $i+1$ by smoothly changing parameters. This bifurcation is important because it implies that orbits change symbolic description without becoming stable and this bifurcation is unavoidable in the description of two-dimensional maps. We will return to this in section 2.2 and in section 5.2.1.

2.1 Bimodal maps

The simplest example of a multimodal map is the bimodal map. The bifurcation structure of real bimodal maps has been investigated by MacKay, Tresser, van

Zeijts, Glass, Milnor, Fraser, Kapral and others [19, 78, 79, 86, 140, 141, 142, 151]. The complex bimodal map has also been studied by Branner, Douady, Hubbard and Milnor [30, 63, 150]. Scaling relations for bifurcations in these maps are obtained by MacKay and van Zeijts [142]. The bimodal bifurcation is a typical bifurcation inside an Arnold tongue and a general phenomena observable in most dissipative dynamical systems. In figures 2.4, 2.6 and 2.8 we show the parameter regions where some short orbits of the map (2.1) are stable and these are the typical bimodal swallowtails.

If we scan the parameter space of a bimodal map by varying only one parameter then we would find a sequence of bifurcations and inverse bifurcations which would be hard to make any sense of, while in a two dimension parameter space the bifurcation structures can be explained. A good way to represent bimodal maps is to use the kneading values as the topological parameters or symbolic parameters (see discussion below). In the topological parameter space (κ_1, κ_2) the bifurcations have a universal form common to all bimodal maps, in the same sense that the MSS ordering in the unimodal κ parameter is universal.

From 2.6 it follows that an orbit S is admissible in the bimodal map if

$$\tau^{\max}(S) < \kappa_1 \tag{2.7}$$

$$\tau^{\min}(S) > \kappa_2 \tag{2.8}$$

The area of the (κ_1, κ_2) parameter plane for which a given orbit S exists is given by the inequalities (2.7) and (2.8).

The shortest periodic orbits $\overline{1}$, $\overline{21}$, $\overline{20}$ and $\overline{10}$ exist for the kneading values

$$\begin{array}{lllll} \overline{1} & \text{exists if} & \kappa_1 \geq 0.\overline{1} = 1/2 & \text{and} & \kappa_2 \leq 0.\overline{1} = 1/2 \\ \overline{21} & \text{exists if} & \kappa_1 \geq 0.\overline{2101} = 4/5 & \text{and} & \kappa_2 \leq 0.\overline{1012} = 2/5 \\ \overline{20} & \text{exists if} & \kappa_1 \geq 0.\overline{20} = 3/4 & \text{and} & \kappa_2 \leq 0.\overline{02} = 1/4 \\ \overline{10} & \text{exists if} & \kappa_1 \geq 0.\overline{1210} = 3/5 & \text{and} & \kappa_2 \leq 0.\overline{0121} = 1/5 \end{array} \tag{2.9}$$

The regions in the topological parameter plane for which the periodic orbits $\overline{1}$, $\overline{21}$, $\overline{20}$ and $\overline{10}$ exist are the rectangles drawn in figure 2.5.

This pattern, which we call a swallow tail, should be compared with the stable period 2 orbit in the parameter plane (a, b) in figure 2.4. The diagonal $\kappa_2 = 1 - \kappa_1$ is a symmetry axis and corresponds to $b = 0$ in eq. (2.1).

The area in (κ_1, κ_2) for which the symbol string $\overline{1}$ is admissible corresponds to the values of κ_1 and κ_2 for which there exists a fixed point between x_{c1} and x_{c2}. But in addition, the symbol string $\overline{1}$ describes the stable period 2 orbit that bifurcates from the fixed point before it reaches the super stable value. This period 2 orbit may become super-stable if the left point in the orbit reaches the critical

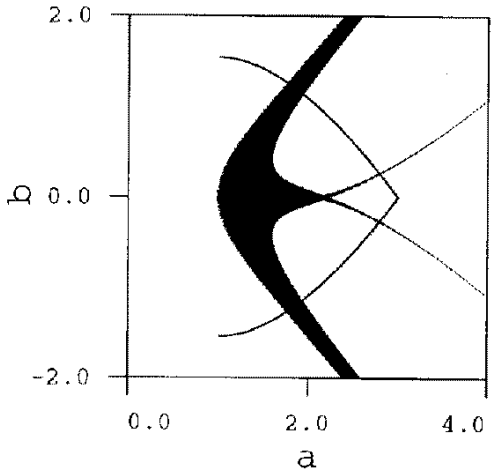

Figure 2.4: The area in parameter plane (a, b) of the bimodal map (2.1) where period 2 orbits are stable together with the curves corresponding to the "one Ulam" map.

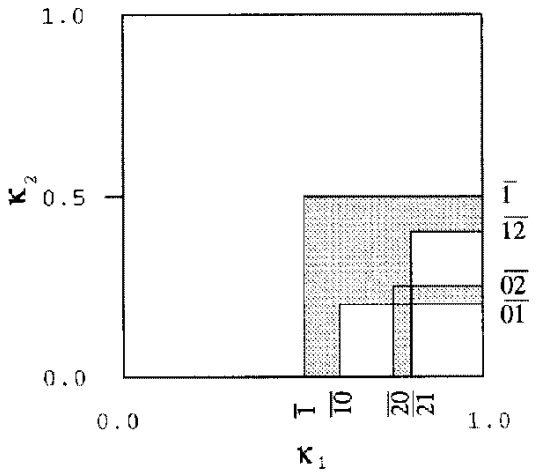

Figure 2.5: The areas in the topological parameter space of the bimodal map where the periodic orbits $\overline{1}$, $\overline{21}$, $\overline{20}$ and $\overline{10}$ exist.

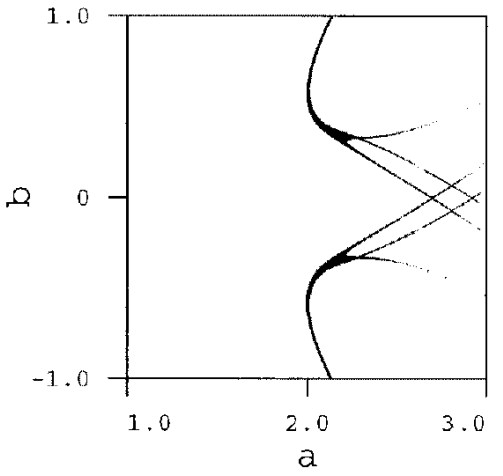

Figure 2.6: The area in the parameter plane (a, b) of the bimodal map (2.1) for which the period 3 orbits are stable.

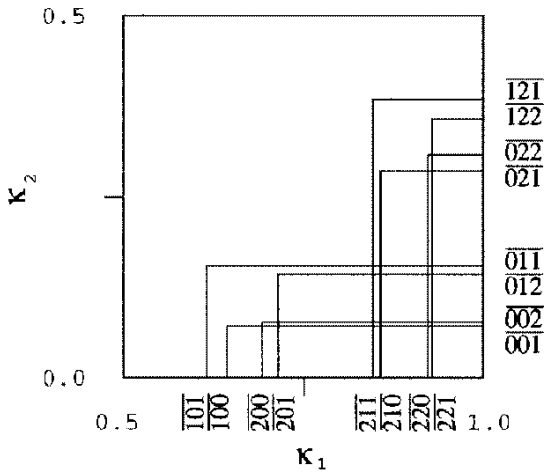

Figure 2.7: The areas in the topological parameter space of the bimodal map for which the period 3 orbits exist.

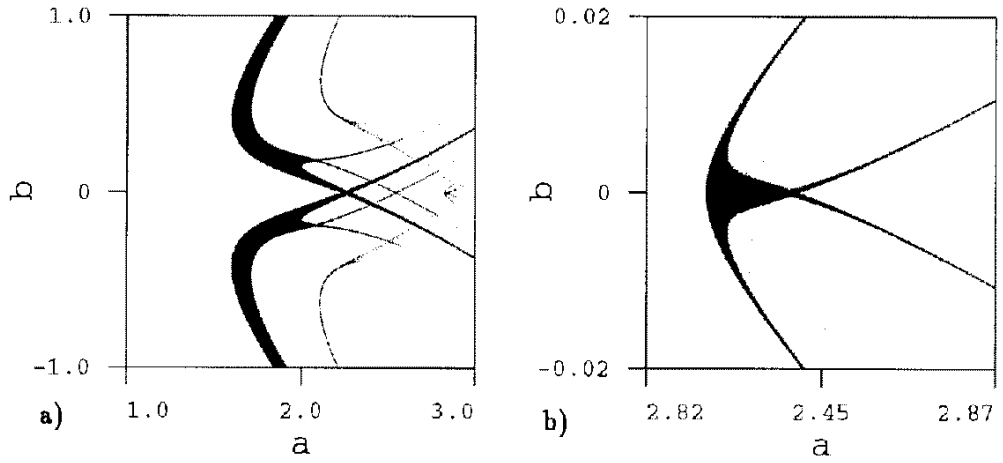

Figure 2.8: a) The area in the parameter plane (a, b) of the bimodal map (2.1) where period 4 orbits are stable. b) A magnification showing the smallest period 4 swallow tail.

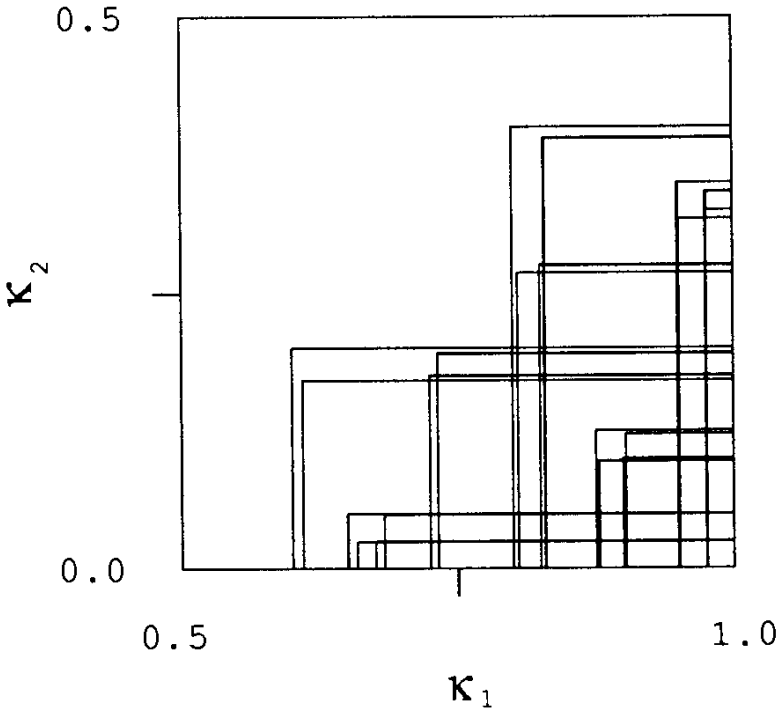

Figure 2.9: The areas in the topological parameter space of the bimodal map where the period 4 orbits exist.

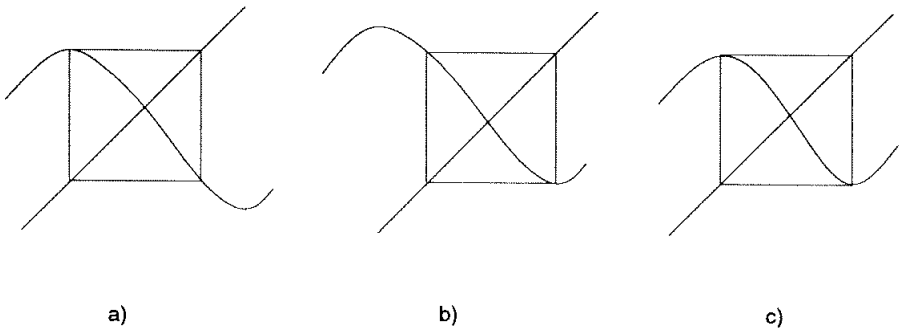

Figure 2.10: The possible super-stable period 2 orbits when the symbolic description of the orbit changes from $\overline{1}$ to a) $\overline{10}$ b) $\overline{21}$ c) $\overline{20}$.

point x_{c1} changing the symbols of the orbit to $\overline{10}$ as in figure 2.10 a), or if the right point in the orbit reaches x_{c2} changing the symbols to $\overline{21}$ as in figure 2.10 b), or if both points in the orbit reach the two critical points simultaneously changing the symbol string to $\overline{20}$ as drawn in figure 2.10 c). Up to 3 different stable orbits may be described with the symbol string $\overline{20}$. In figure 2.11 the curves in the parameter space where the orbits are super-stable are drawn as dashed curves and these curves will correspond topologically to the bifurcation lines in figure 2.5.

The figures 2.5, 2.7 and 2.9 may be interpreted in the following way. A kneading value κ jumps from κ_a to κ_b when the attracting stable orbit passes through a super stable point as showed in the unimodal map in figure 1.12. Values in the open interval $\langle \kappa_a, \kappa_b \rangle$ do not correspond to any kneading sequence, so this interval is "forbidden". In a smooth map we can identify this empty interval with the parameter interval where a period n orbit goes from the super-stable point through a period doubling bifurcation to the super-stable period $2n$ orbit. The period doubling corresponds to one point in this interval. The areas in parameter space where the period $2n$ orbit is stable have the same topological structure as the forbidden interval areas. In figure 2.5 the forbidden areas are colored gray and we identify this area with the black area in figure 2.4; the *swallowtail*. This topological identification between structures in the real parameter space (a, b) and the kneading value space (κ_1, κ_2) motivates us to call the space (κ_1, κ_2) the *topological parameter space*. Since the values κ are a representation of the symbolic dynamics we will also use the term *symbolic parameter space*.

If one of the critical points iterates into the fixed point $\overline{0}$ all bifurcations take place at the other critical point. The lines of parameter values (a, b) where this hap-

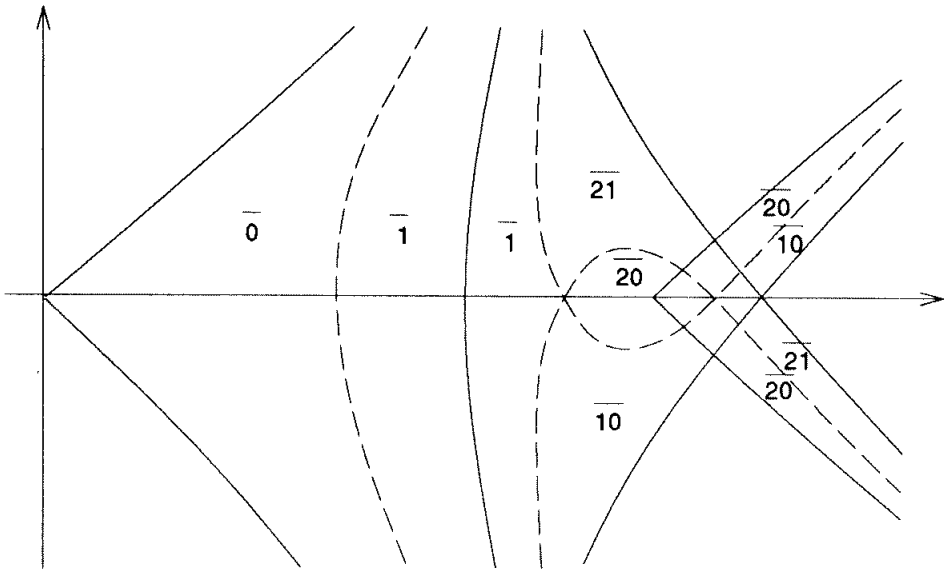

Figure 2.11: A sketch of the curves in parameter space giving bifurcations (solid curve) and super stable period 1 and period 2 orbits (dashed curve) in the bimodal map. The symbol strings for various orbits are indicated.

pens are drawn in figure 2.4; we call this a "one-Ulam" map case. For parameter values outside these Ulam curves at least one critical point iterates to infinity, and there is no swallowtail crossings, only non–crossing tails (codimension one bifurcations). The one-Ulam curves and all parameter values beyond these curves map in the topological parameter space into the two borders $\kappa_1 = 1$ and $\kappa_2 = 0$.

2.1.1 Markov graphs

The construction of the automaton graph of the bimodal map is similar to the unimodal case: the kneading sequences are drawn on a tree, forbidden branches are crossed out, and the admissible branches are reconnected into a closed graph. The bimodal case tree is more complicated than for the unimodal case tree, but there are no new important conceptual features brought in by the generalization to bimodal maps.

We work out one example, the case of two coexisting stable periodic orbits, with the repellor described by a Markov partition and a finite automaton graph. Assume that the orbits $\overline{21}$ and $\overline{100}$ are stable. From figures 2.5 and 2.7 we see that at the point $(\kappa_1, \kappa_2) = (0.\overline{2101}, 0.\overline{001221})$ the vertical line for $\overline{21}$ crosses the horizontal line for $\overline{001}$. This implies that there exists a parameter space (a, b) region for which

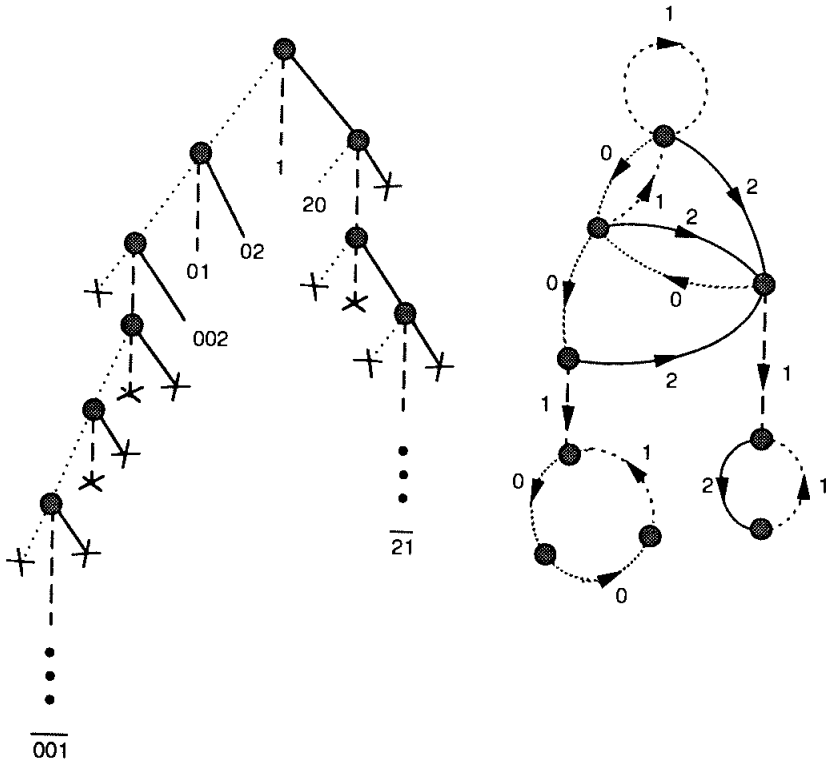

Figure 2.12: The construction of the automaton graph for the bimodal map with coexisting stable orbits $\overline{21}$ and $\overline{100}$.

both orbits are stable. Comparing figure 2.4 and figure 2.6 we see that the two tails where these orbits are stable indeed cross. Figure 2.12 shows the construction of the corresponding pruned tree and the automaton. The construction yields a transient repellor and the two attracting cycles. It misses the two loops $\overline{0}$ and $\overline{2}$ which is the two isolated unstable fixed points, and which can be drawn in the automaton as isolated transients before the transient repellor in figure 2.12. These loops will not contribute to calculations of average values like entropy (see below). Removing the two attracting cycles $\overline{100}$ and $\overline{21}$ yields the repellor automaton with the 5 loops

$$\{\overline{1}\}, \{\overline{01}\}, \{\overline{20}\}, \{\overline{201}\}, \{\overline{200}\} \tag{2.10}$$

and the 2 two combinations of loops without a common node

$$\{\overline{20}, \overline{1}\}, \{\overline{002}, \overline{1}\} \tag{2.11}$$

The topological polynomial is then

$$p(z) = 1 - z - 2z^2 - z^3 + z^4 \tag{2.12}$$

with the smallest root and the topological entropy

$$z = 0.480534, \qquad h = \ln 2.08102 = 0.732857 \tag{2.13}$$

slightly larger than for the complete unimodal map.

2.2 Trimodal maps

In the generalization from bimodal to trimodal maps some new phenomena appear. Trimodal maps have bifurcations of co-dimension three and we have to describe a rather complicated bifurcation structure in 3 dimensional parameter space.

The first important observation is that a map like (2.2) *does not* have three critical points for all parameter values (a, b, c). A minimum and a maximum point may merge, reducing the map to the unimodal case with a one-parameter bifurcation structure. Also the number of symbols changes from four symbols when the map is trimodal to two symbols when it is unimodal. This merging of critical points could be avoided by a restriction on the parameters, but that would exclude us from understanding the bifurcations that take place in maps of the Hénon type and therefore is it necessary to handle this problem.

The parameter space (a, b, c) looks rather complicated; figures 2.14, 2.18 and 2.22 are scans of the (a, b) plane at different constant c values, showing the parameter regions where a fixed point or a periodic orbit is stable. A simpler description of the bifurcation structures can be obtained by using the kneading value topological parameter space $(\kappa_1, \kappa_2, \kappa_3)$. The bifurcation parameter values for the fixed points and period 2 orbits are drawn as planes in this space in figure 2.17. The map is trimodal if $\kappa_1 > \kappa_2$ and $\kappa_3 > \kappa_2$. The border planes $\kappa_1 = \kappa_2$ and $\kappa_3 = \kappa_2$ are drawn in the figure; the trimodal bifurcations take place inside the skew-pyramidal region in this space. When the parameters of the function (a, b, c) change in such a way that we cross one border plane, we move into a one-dimensional unimodal parameter space and may reenter the three-dimensional parameter space again at a different point on a border plane. When we enter the unimodal region we can go through bifurcation of the MSS type and reenter at any point on the border planes of the trimodal map. The unimodal map will not have a negative Schwarzian close to the trimodal case so the stability of orbits may be different than for the logistic map.

The planes giving the bifurcations of orbits are obtained by determining the values $\tau_i^{\max}(S)$, $i \in \{1, 2, 3\}$, for a given orbit and drawing the planes $\kappa_i = \tau_i^{\max}(S)$. Table 2.1 gives the numerical values of $\tau_i^{\max}$ for the orbits of length 1, 2 and 3. Note

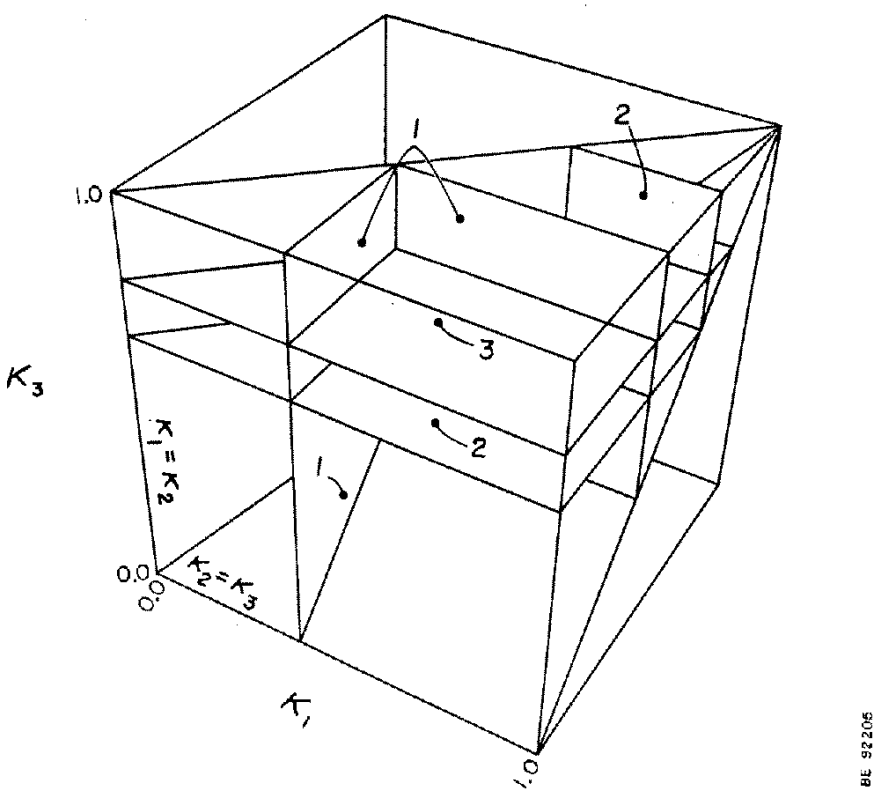

Figure 2.13: The bifurcation planes of fixed points in the trimodal map in the topological parameter space $(\kappa_1, \kappa_2, \kappa_3)$. The κ_2 axis is hidden behind the bifurcation planes.

that not all the orbits has all the three $\tau_i^{\max}$-values. The conditions for an orbit to be admissible in the trimodal map follows from (2.6):

$$\begin{aligned} \tau_1^{\max}(S) &\leq \kappa_1 \\ \tau_2^{\min}(S) &\geq \kappa_2 \\ \tau_3^{\max}(S) &\leq \kappa_3 . \end{aligned} \tag{2.14}$$

If these 3 conditions yield a box in the region within the border planes $\kappa_1 = \kappa_2$ and $\kappa_3 = \kappa_2$, the orbit always disappears in a bifurcation before the map gets unimodal, and the orbit can never change symbols without going through a super-stable value. If the box is only partly confined within the border planes, then the orbit exists and may be unstable also when the map is unimodal, and may change symbolic description without ever getting stable. The sign of the eigenvalue cannot change as long as the orbit remains unstable, so the sum of symbols which are either 1 or 3 has to remain odd or even.

S	$\tau_1^{\max}$	S	$\tau_2^{\min}$	S	$\tau_3^{\max}$
				$\overline{3}$	$.\overline{30}$
		$\overline{2}$	$.\overline{2}$	$\overline{2}$	$.\overline{2}$
$\overline{1}$	$.\overline{12}$	$\overline{1}$	$.\overline{12}$		
$\overline{0}$	$.\overline{0}$				
$\overline{30}$	$.\overline{3300}$			$\overline{03}$	$.\overline{0330}$
$\overline{31}$	$.\overline{32}$	$\overline{31}$	$.\overline{32}$	$\overline{13}$	$.\overline{10}$
		$\overline{32}$	$.\overline{3102}$	$\overline{32}$	$.\overline{3102}$
$\overline{21}$	$.\overline{2112}$	$\overline{12}$	$.\overline{1122}$	$\overline{12}$	$.\overline{1122}$
$\overline{20}$	$.\overline{20}$	$\overline{02}$	$.\overline{02}$	$\overline{02}$	$.\overline{02}$
$\overline{10}$	$.\overline{1320}$	$\overline{01}$	$.\overline{0132}$		

S	$\tau_1^{\max}$	S	$\tau_2^{\min}$	S	$\tau_3^{\max}$
$\overline{300}$	$.\overline{333000}$			$\overline{003}$	$.\overline{003330}$
$\overline{301}$	$.\overline{332}$	$\overline{301}$	$.\overline{332}$	$\overline{013}$	$.\overline{010}$
$\overline{230}$	$.\overline{233100}$	$\overline{302}$	$.\overline{331002}$	$\overline{302}$	$.\overline{331002}$
$\overline{330}$	$.\overline{300}$			$\overline{303}$	$.\overline{330}$
$\overline{331}$	$.\overline{301032}$	$\overline{331}$	$.\overline{301032}$	$\overline{313}$	$.\overline{323010}$
$\overline{231}$	$.\overline{232}$	$\overline{231}$	$.\overline{232}$	$\overline{312}$	$.\overline{322}$
$\overline{311}$	$.\overline{321012}$	$\overline{131}$	$.\overline{101232}$	$\overline{113}$	$.\overline{123210}$
$\overline{310}$	$.\overline{320}$	$\overline{031}$	$.\overline{032}$	$\overline{103}$	$.\overline{130}$
$\overline{320}$	$.\overline{313020}$	$\overline{032}$	$.\overline{031302}$	$\overline{203}$	$.\overline{2031130}$
$\overline{321}$	$.\overline{312}$	$\overline{132}$	$.\overline{102}$	$\overline{213}$	$.\overline{210}$
		$\overline{232}$	$.\overline{231102}$	$\overline{322}$	$.\overline{311022}$
		$\overline{332}$	$.\overline{302}$	$\overline{323}$	$.\overline{310}$
$\overline{221}$	$.\overline{221112}$	$\overline{122}$	$.\overline{111222}$	$\overline{212}$	$.\overline{211122}$
$\overline{220}$	$.\overline{220}$	$\overline{022}$	$.\overline{022}$	$\overline{202}$	$.\overline{202}$
$\overline{210}$	$.\overline{213120}$	$\overline{021}$	$.\overline{021312}$	$\overline{102}$	$.\overline{131202}$
$\overline{211}$	$.\overline{212}$	$\overline{121}$	$.\overline{112}$	$\overline{112}$	$.\overline{122}$
$\overline{201}$	$.\overline{201132}$	$\overline{012}$	$.\overline{011322}$	$\overline{012}$	$.\overline{011322}$
$\overline{200}$	$.\overline{200}$	$\overline{002}$	$.\overline{002}$	$\overline{002}$	$.\overline{002}$
$\overline{100}$	$.\overline{133200}$	$\overline{001}$	$.\overline{0011332}$		
$\overline{101}$	$.\overline{132}$	$\overline{011}$	$.\overline{012}$		

Table 2.1: The fixed points, period 2 and period 3 orbits in the trimodal map with the kneading values giving the topological bifurcation diagrams in figures 2.13, 2.17, 2.20 and 2.21.

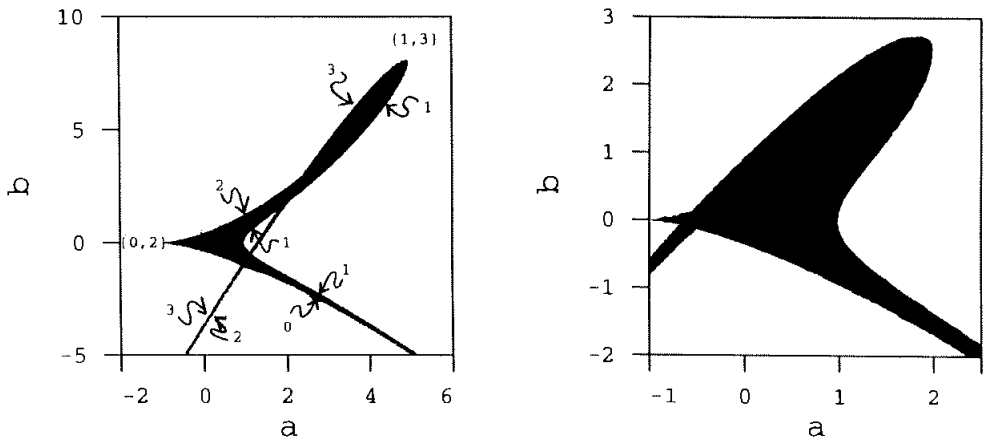

Figure 2.14: The area in parameter space (a, b) for the trimodal map where fixed points are stable, a) $c = 0.25$, b) $c = 0.5$.

2.2.1 Fixed points

In figure 2.13 the bifurcation diagram for the fixed points in $(\kappa_1, \kappa_2, \kappa_3)$ is drawn. The point $(1.0, 0.0, 1.0)$ corresponds to the complete trimodal repellor. This point is in figure 2.13 the corner closest to the viewer. Going downwards from this corner the figure can be read as follows; at the horizontal plane marked 3 the fixed point with symbolic description $\overline{3}$ becomes superstable and changes symbolic description to $\overline{2}$. When κ_3 decreases further, the two fixed points $\overline{2}$ disappear at the horizontal plane marked 2 in figure 2.13. The fixed point $\overline{1}$ disappears either at a plane with constant κ_1 or with constant κ_2. If we let κ_1 decrease, the fixed point $\overline{1}$ changes symbolic description to $\overline{0}$ and the two fixed points $\overline{0}$ disappear at $\kappa_1 = 0$. Another possibility is that we let κ_2 increase and then the fixed point $\overline{1}$ changes symbolic description to $\overline{2}$ and the two fixed points $\overline{2}$ disappear at the vertical plane marked 2 in figure 2.13.

If we try to follow a fixed point $\overline{3}$ while κ_1 decreases or κ_2 increases we can pass into the unimodal map regime through the plane $\kappa_1 = \kappa_2$, without any bifurcations of the fixed point. In figure 2.13 we see that it is possible to enter the trimodal region at the plane $\kappa_2 = \kappa_3$ where the fixed point $\overline{1}$ exists but not the fixed point $\overline{3}$. We may therefore change the symbolic description of the fixed point by smooth parameter changes without ever making the fixed point stable. Since the sign of the derivative cannot change, the fixed point $\overline{3}$ can change only into $\overline{1}$, and the fixed point $\overline{2}$ only into $\overline{0}$.

We now compare figure 2.13 with two scans of the parameter plane (a, b) with $c = 0.25$ and $a = 0.5$, figure 2.14 a) and b). These scans should be thought of

as topological equivalent to surfaces cutting through the symbolic parameter space of figure 2.13. In figure 2.14 symbols 0 and 2 indicates planes at which a tangent bifurcation creates the fixed points $\overline{0}$ or $\overline{2}$. Symbols 1 and 3 indicate the planes where the fixed point $\overline{1}$ or $\overline{3}$ becomes unstable. The area indicated by $\{1,3\}$ corresponds to parameter values for which the map is unimodal, and the fixed point with negative $f'(x)$ does not have a unique symbol but as one moves into the trimodal region the fixed point achieves either the symbolic description $\overline{1}$ or the symbolic description $\overline{3}$. For the area indicated by $\{0,2\}$ the fixed point with positive $f'(x)$ does not have a unique symbol in the 4 letter alphabet, but may become either $\overline{0}$ or $\overline{2}$. Moving in these two areas corresponds to move around the corners of the boxes $\overline{1}$ or $\overline{2}$ in figure 2.13. To get around the corners one has to cross a unimodal region and consequently some symbols may change.

In the (a,b) plane all regions with a stable fixed point are connected; and this can be read out of the picture of the topological parameter space, figure 2.13. The two horizontal planes $\overline{3}$ and $\overline{2}$ are associated with one tail of a stable fixed point. As κ_2 increases in figure 2.13, this tail connects to the tail associated with the planes for $\overline{2}$ and $\overline{1}$ with constant κ_2. Decreasing κ_1 in this tail gives the transition to the tail associated with the region between the constant κ_1 plane of $\overline{1}$ and the $\kappa_1 = 0$ line where $\overline{0}$ bifurcates. We see that this last region crosses the first region of the planes of $\overline{3}$ and $\overline{2}$, and this is also the case in the (a,b) plane in figure 2.14.

Figure 2.15 is a sketch of the (a,b) plane as in figure 2.14 but the sheets representing the different orbits are drawn in three dimensions to make the cusp bifurcations clearer. In this figure it is also clear that orbits may change symbols when moving around one of the cusp singularities.

In figure 2.16 the function $f(x)$ is drawn for a sequence of values for which the fixed point change symbol from $\overline{1}$ to $\overline{3}$.

2.2.2 Period 2 orbits

Figure 2.17 shows the planes in the topological parameter plane where both the fixed points and the period 2 orbits bifurcate. This figure is interpreted in a similar way as figure 2.13. We know from the bimodal map that period 2 orbits may exhibit a swallowtail crossing, and we do find swallowtails in figure 2.17. On the top plane, $\kappa_3 = 1$, we find the same swallowtail crossing as in the bimodal plane in figure 2.5. We adapt a convention to describe crossings such that $\overline{\{s_1,s_2\},\{s_3,s_4\}}$ is equivalent with the four symbol strings $\overline{s_1 s_3}$, $\overline{s_1 s_4}$, $\overline{s_2 s_3}$ $\overline{s_2 s_4}$ and the notation $\overline{s_1\{s_2,s_3,s_4\}}$ is short for the three orbits $\overline{s_1 s_2}$, $\overline{s_1 s_3}$ and $\overline{s_1 s_4}$. The symbols of the orbits in this crossing are $\overline{\{1,2\}\{0,1\}}$ (the orbits $\overline{10}$, $\overline{1}$, $\overline{20}$, $\overline{21}$) as in the bimodal case, and the

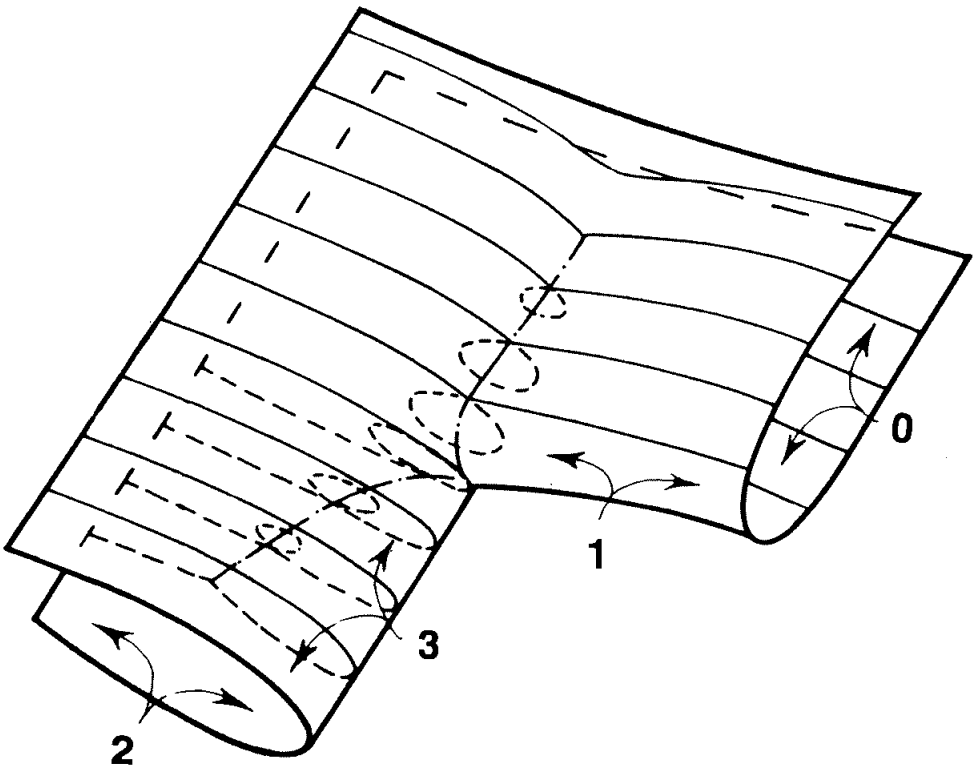

Figure 2.15: Coexistence of fixed points in the (a, b) plane with constant c for the trimodal map.

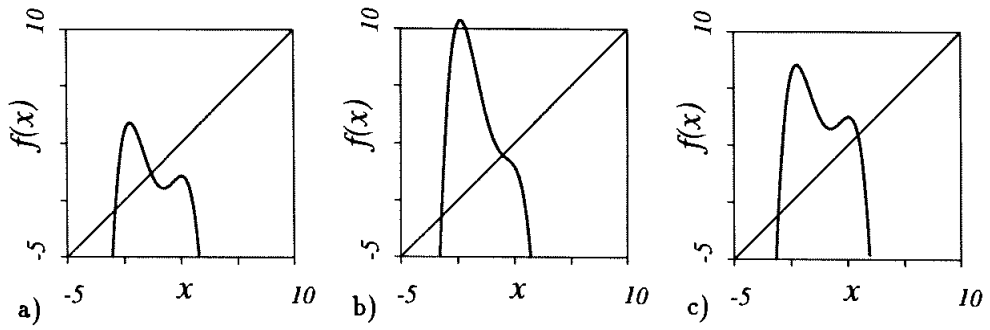

Figure 2.16: The function $f(x)$ for different parameter values in the region where a fixed point changes symbol from $\overline{1}$ to $\overline{3}$, $c = 0.25$, a) $a = 3$, $b = 2$ b) $a = 4.77$, $b = 7$ c) $a = 3$, $b = 6$.

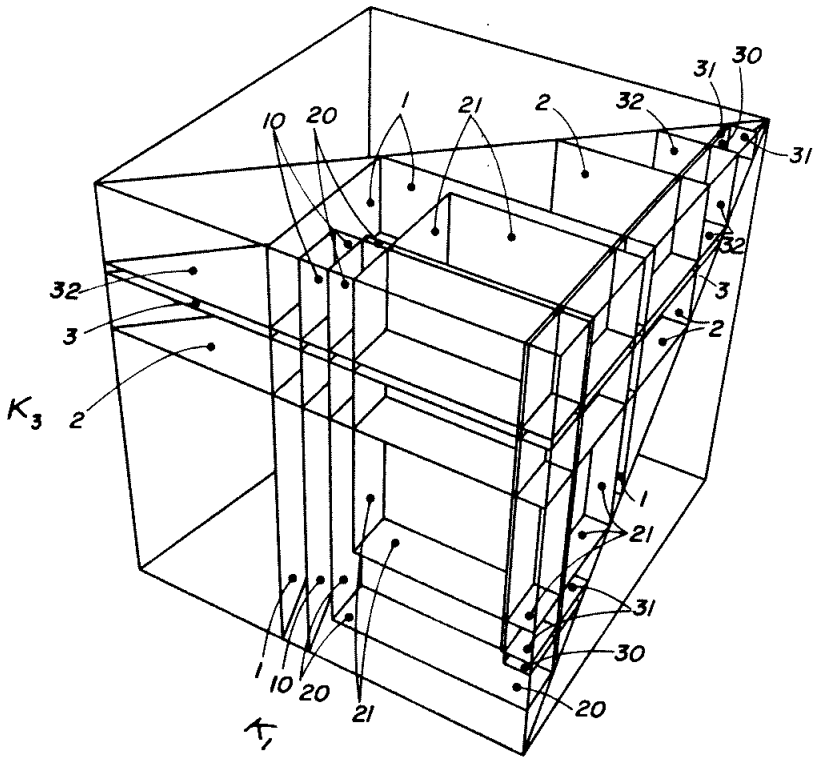

Figure 2.17: The bifurcation planes of period 2 orbits in the trimodal map in the topological parameter space $(\kappa_1, \kappa_2, \kappa_3)$.

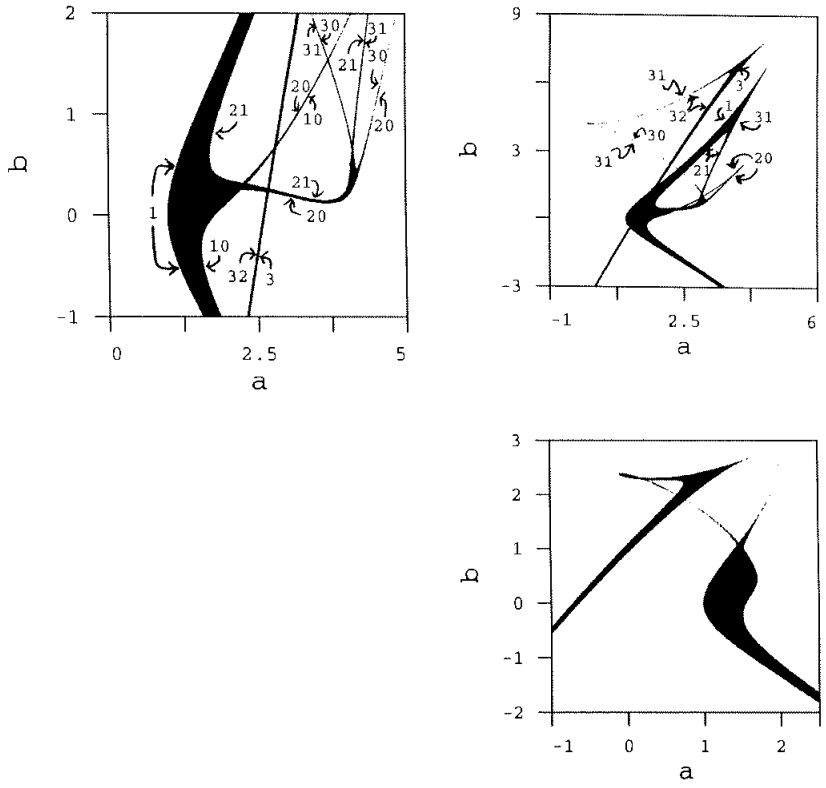

Figure 2.18: The area in parameter space (a, b) for the trimodal map where period 2 orbits are stable. a) $c = 0.2$, b) $c = 0.25$ c) $c = 0.5$.

structure is the same, only the scale is slightly changed since we here use base 3 to calculate κ_1 and κ_2.

In figure 2.17 we find another swallowtail for $\kappa_2 = 0$ which includes the orbits $\overline{\{2,3\}\{0,1\}}$. The two swallowtail crosses are directly connected to each other by having the tail $\overline{2\{0,1\}}$ in common. The scan of the parameter plane (a, b) with $c = 0.2$ in figure 2.18 a) shows these two swallowtail crosses and the common tail. In figure 2.18 the label 1 indicates the plane where the fixed point $\overline{1}$ goes through a period doubling. The labels 20 and 31 indicate the tangent bifurcations which create the two period 2 orbits, and labels 10, 21 and 30 indicate planes where the respective period 2 orbits become unstable.

Figure 2.18 b) shows that at slightly larger value of c the swallowtails crosses get closer together. The figure also shows other cusp points that can be found in the topological parameter space in figure 2.17, and we see how the different tails are connected. Notice also that in the region of figure 2.14 where the fixed point changes

symbolic description from $\overline{1}$ to $\overline{3}$ there is no period 2 orbit that change symbol. When a fixed point becomes unstable close to an inflection point, the bifurcation can not be a period doubling bifurcation, but is an inverse bifurcation where the fixed point becomes unstable by removing an unstable period 2 orbit. In this case the removed orbit is $\overline{31}$. Figure 2.19 shows such bifurcations at different one-parameter scans of the parameter space. In figure 2.19 a) the fixed point changes symbol without going through any bifurcations. In figure 2.19 b) the fixed point becomes stable in a bifurcation which creates the unstable period 2 orbit $\overline{31}$ and the fixed point changes symbols when it is stable but not superstable. At a parameter scan closer to the $\{1,3\}$ cusp in figure 2.14 a) we get figure 2.19 c) where the fixed point has a bifurcation with a stable period 2 orbit, which in turn was created in a tnagent bifurcation together with the unstable period 2 orbit. Finely, in figure 2.19 d) below the $\{1,3\}$ cusp all orbits change symbolic description only at superstable points. One may also find paths in parameter space where the bifurcations are not symmetric, one has a finite number of bifurcations, etc. The important structure of the cusp and the change of symbols are however described by these four figures.

The only period 2 orbit existing in figure 2.19 a) is the orbit $\overline{30}$. This orbit do not change symbol here but at one of the two cusp bifurcations; either to $\overline{10}$ at the cusp $\overline{\{1,2,3\}0}$ middle–right at figure 2.18 b), or to $\overline{32}$ at the cusp $\overline{3\{0,1,2\}}$ to the left in figure 2.18 b). Consequently a loop around the cusp the fixed point changes the description from $\overline{1}$ to $\overline{3}$ but there is no change of any period 2 orbit.

2.2.3 Period 3 orbits

Period 3 orbits form a rather complicated structure in the trimodal map parameter space, and without the topological parameter space bifurcation diagrams would it be difficult to have an overview of the bifurcations. In figure 2.20 all bifurcation planes corresponding to the values of $\tau_i^{\max}$ listed in table 2.1 are drawn. To simplify the reading, the diagram is also drawn in figure 2.20 with the labels restricted to the swallowtail crossings on the planes $\kappa_1 = 1$, $\kappa_2 = 0$ and $\kappa_3 = 1$.

A general observation is that there are many orbits restricted by bifurcation planes to the interior of the trimodal region. Out of 20 orbits there are 6 orbits that only have two τ_i values giving only two sides of the box, and there are 2 orbits which have three values of τ_i but with one corner outside the trimodal region. 4 orbits have the corner of the box in parameter space on the edge of the trimodal region . Hence in all 12 period 3 orbits cannot change the symbolic dynamics description without getting superstable. In contrast for the period 2 orbits only 2 out of 6 orbits cannot change symbols, and all the fixed points may change symbols.

a)

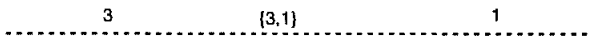

b)

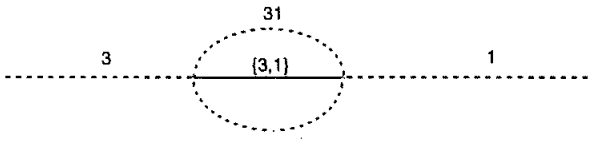

c)

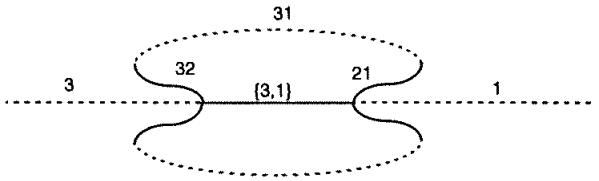

d)

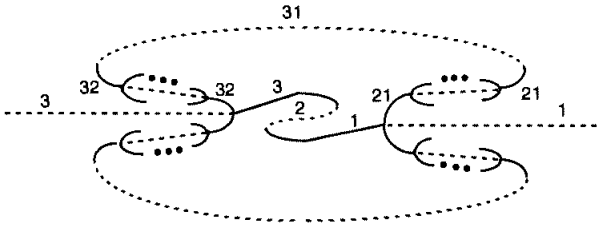

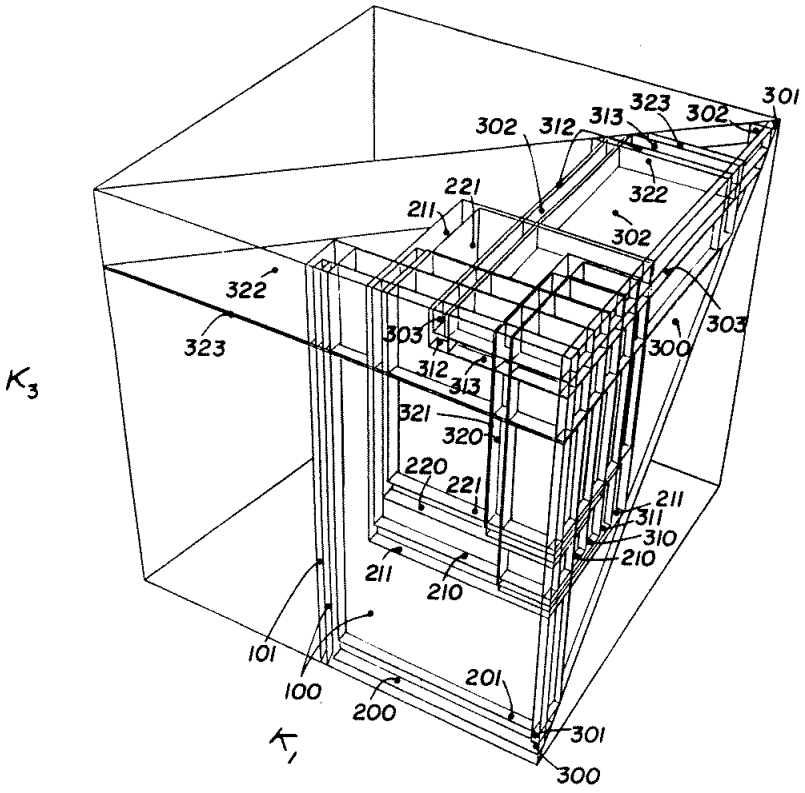

Figure 2.20: The bifurcation planes of period 3 orbits in the trimodal map in the topological parameter space $(\kappa_1, \kappa_2, \kappa_3)$, each plane labeled by the symbols for the period 3 orbit created at this parameter value.

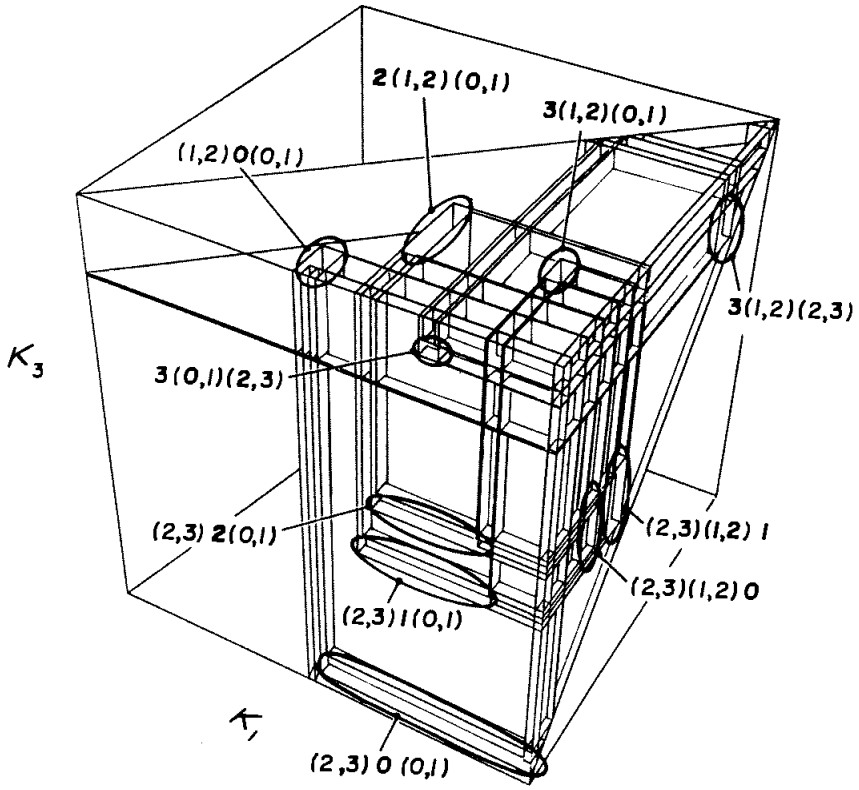

Figure 2.21: The same as figure 2.20, but labeled with the swallowtail crossings rather than the individual period 3 orbits.

For long orbits only a small fraction of the orbits can change symbols. For long symbol strings there are few orbits that do not have any symbols $(i-1)$ or (i) such that τ_i does not exist, or that $\tau_2^{\min}$ is larger than either $\tau_1^{\max}$ or $\tau_3^{\max}$. This is good news because there is relatively few long orbits that we have to worry about whether we use the right symbolic description or not, but some very long orbits will also have the possibility of changing symbolic dynamics without becoming stable.

The plots in figure 2.22 show some scans of the parameter plane (a,b) where the period 3 orbits are stable. The swallowtail crosses are labeled as (and should be compared to) the topological swallowtail crosses in figure 2.21. In figure 2.21 there is a structure consisting of the six crosses $\overline{2\{1,2\}\{0,1\}}$, $\overline{3\{1,2\}\{0,1\}}$, $\overline{\{2,3\}2\{0,1\}}$, $\overline{\{2,3\}1\{0,1\}}$, $\overline{\{2,3\}\{1,2\}0}$ and $\overline{\{2,3\}\{1,2\}1}$ that are connected by tails to each other but not to any other crosses, and they all bifurcates inside the bifurcation box of $\overline{112}$, inside the trimodal region. All these orbits disappear before the map becomes unimodal and they do not change any symbols by moving around a cusp structure without getting superstable. Figures 2.22 a)–f) show that increasing the parameter c makes the (a,b) plane to a surface deeper and deeper in the topological parameter space. In figure 2.22 f) the surface cuts below the box $\overline{112}$, and no structure from the six crosses remains. Each of the boxes in the structure is connected to a swallowtail cross in the three corners of the box. If a box moves above the (a,b) surface, these three crosses have to merge to one cross. If the pruning box of the orbit $\overline{320}$ in figure 2.21 moves above the (a,b) parameter plane, then the three crosses $\overline{3\{1,2\}\{0,1\}}$, $\overline{\{2,3\}2\{0,1\}}$ and $\overline{\{2,3\}\{1,2\}0}$ which have $\overline{320}$ as the only common orbit must merge together. This is exactly the bifurcation taking place in figure 2.22 as the value of c increases. There are other possible ways for the crossings to merge, but a 2-dimensional parameter plane cannot have other mergings of the bifurcation structure than those that can be obtained by moving a surface in the $(\kappa_1,\kappa_2,\kappa_3)$ space.

2.3 Higher n-modal maps

For four-modal and higher n-modal maps it is difficult to draw the n-dimensional topological parameter space bifurcation diagrams, but we can still use symbols to understand possible bifurcation structures.

A swallowtail crossing for a period m orbit in a n–modal map has the form

$$\overline{\{s_1,s_1'\}s_2\cdots s_{j-1}\{s_j,s_j'\}s_{j+1}\cdots s_m} \tag{2.15}$$

where $s_i, s_i' \in \{0,1,\ldots,n\}$ and $|s_i - s_i'| = 1$ (neighbor symbols). A tail from this

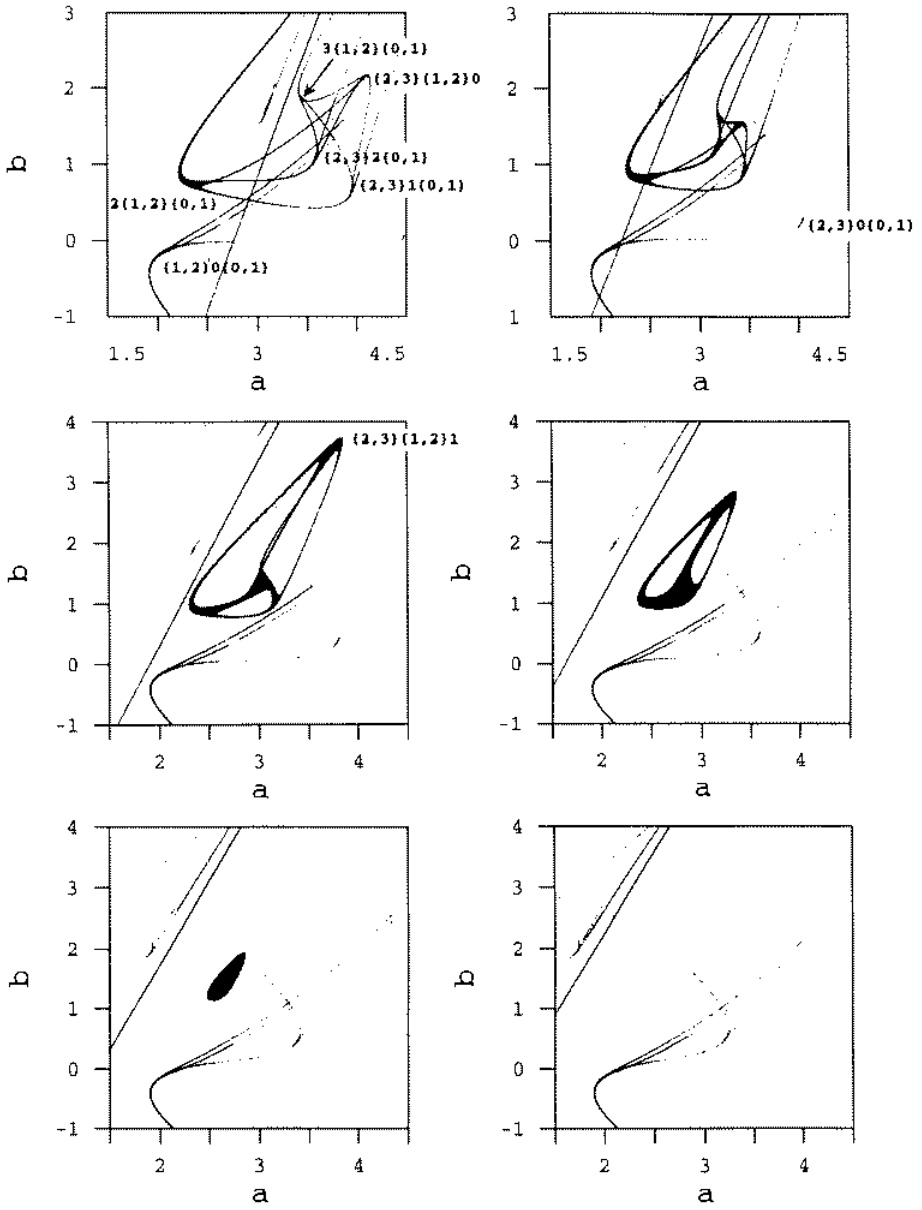

Figure 2.22: The area in parameter space (a, b) for the trimodal map where period 3 orbits are stable. a) $c = 0.195$, b) $c = 0.21$ c) $c = 0.22$ d) $c = 0.23$ e) $c = 0.24$ f) $c = 0.25$.

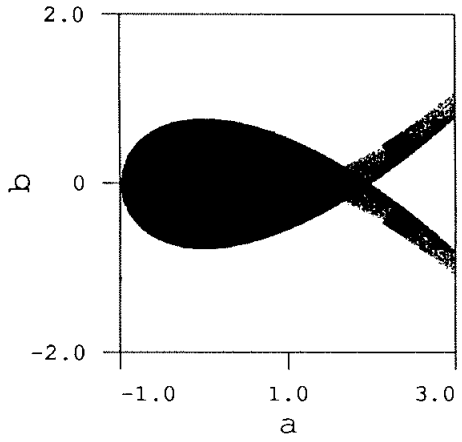

Figure 2.23: The area in parameter plane of map (2.18) with stable fixed point.

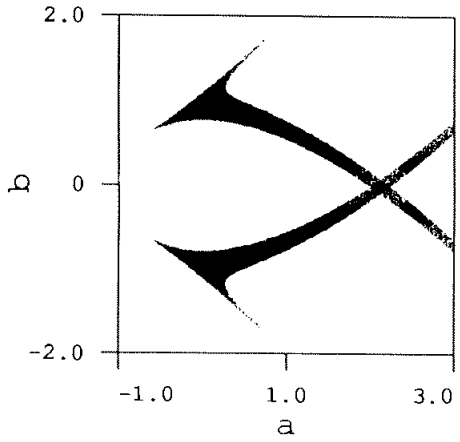

Figure 2.24: The area in parameter plane of map (2.18) with stable period 2 orbits.

crossing is

$$\overline{\{s_1, s_1'\} s_2 \cdots s_{j-1} s_j s_{j+1} \cdots s_m} \tag{2.16}$$

and this tail connects the crossing to another swallowtail crossing

$$\overline{\{s_1, s_1'\} s_2 \cdots s_{k-1} \{s_k, s_k'\} s_{k+1} \cdots s_m} \tag{2.17}$$

where $k \neq j$ if both crossings exist. By using such rules it is easy to find all connected swallow tails, and the possible merging and disappearances of the crossings.

2.4 The − + − bimodal map

To complete the discussion of bimodal maps we can also find the bifurcation diagrams for the bimodal map with $f'(x) < 0$ for $x < x_{c1}$ and $x > x_{c2}$ and with $f'(x) > 0$ for $x_{c1} < x < x_{c2}$, denoted $- + -$. We denote the bimodal map (2.1) according to the sign of $f'(x)$: $+ - +$. We will here just present the bifurcation diagrams and the numerical results from the map

$$f(x) = -x^3 + ax - b \tag{2.18}$$

as the results are very similar to the $+ - +$ bimodal map. The kneading values κ_1 and κ_2 yield a symbolic parameter plane, and bifurcations lines for periodic orbits of length 1, 2, 3 and 4 are drawn in figures 2.25, 2.27 and 2.29. The parameter regions (a, b) with stable periodic orbits for the map (2.18) are drawn in figures 2.23, 2.24, 2.26 and 2.28. The line $\kappa_2 = 1 - \kappa_1$ corresponds to the line $b = 0$ in map (2.18)

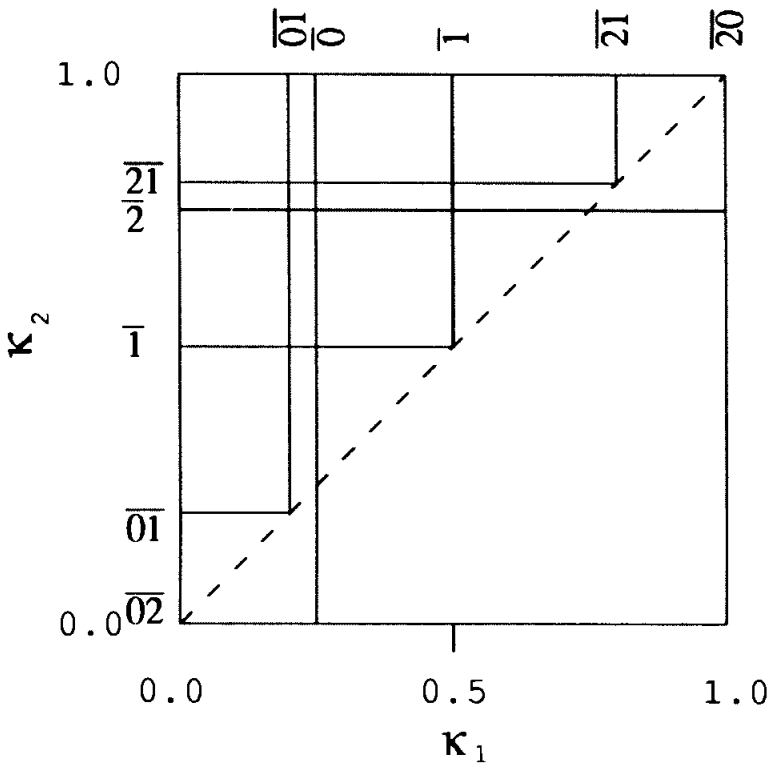

Figure 2.25: The bifurcation lines of the fixed points and period 2 orbit in the symbolic parameter plane of the $-+-$ bimodal map

and at the point $\kappa_1 = 0$, $\kappa_2 = 1$ is the point corresponding to the complete binary repellor. The line $\kappa_2 = \kappa_1$ is the bifurcation line where the two extremum points merge together.

The period 3 and period 4 bifurcation diagrams are different but of the same structure as for the $+-+$ bimodal map. The period 3 orbits yield two swallowtails and the period 4 orbits yield five swallowtails.

The bifurcations of the fixed points and the period 2 orbits yield a slightly different bifurcation structure than for the $+-+$ bimodal map. In the $+-+$ map the stable fixed point $\overline{1}$ and all the period 2 orbits existed only in the bimodal regime; $\kappa_2 < \kappa_1$. For the $-+-$ map the two stable fixed points $\overline{0}$ and $\overline{2}$ and the period two orbit $\overline{20}$ exist also outside the bimodal regime $\kappa_2 > \kappa_1$. This gives a different cusp structures similar to those examined in the trimodal map.

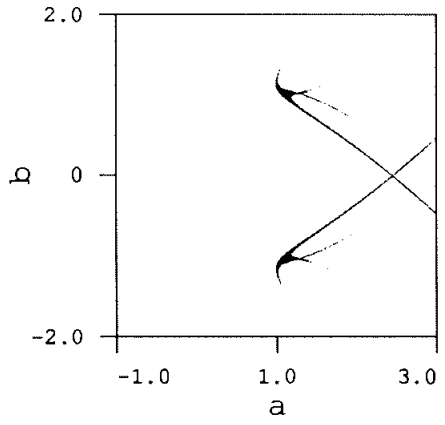

Figure 2.26: The area in parameter plane of map (2.18) with stable period 3 orbits

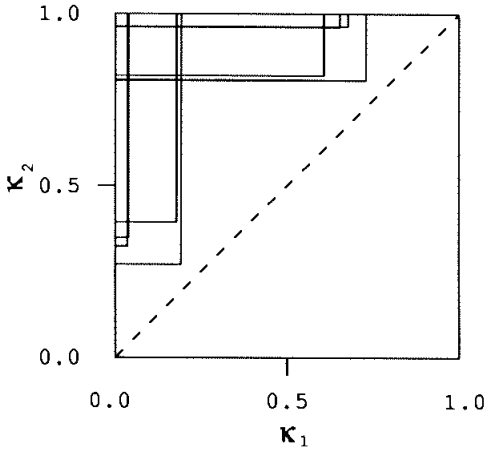

Figure 2.27: Bifurcation lines of the period 3 orbit in the − + − bimodal map

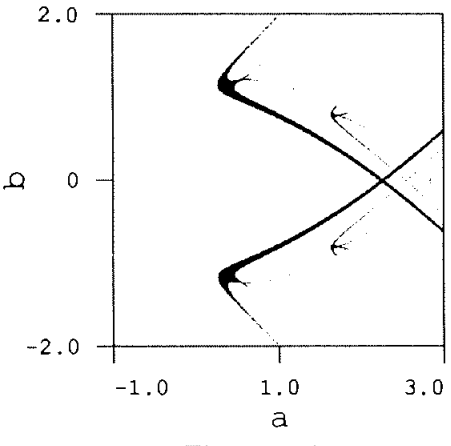

Figure 2.28: The area in parameter plane of map (2.18) with stable period 4 orbits

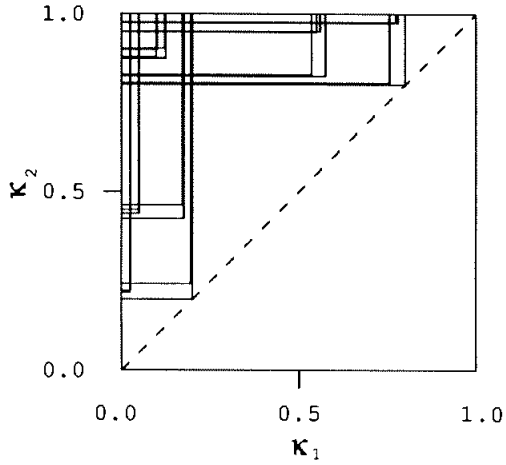

Figure 2.29: Bifurcation lines of the period 4 orbit in the − + − bimodal map

Part II

Two dimensional maps

Chapter 3

Two dimensional folding maps

The symbolic dynamics for the one dimensional maps has a solid mathematical basis [147, 152, 153, 175], and most statements can be proven. Part I introduced a new way to present bifurcations in a symbolic parameter space and gave some examples of calculation of statistical averages by using this symbolic description. When we want to study the symbolic dynamics and the bifurcations of two dimensional pruned maps, our basis is no longer mathematically proven theorems, but conjectures and intuition. The intention with this work on the pruned horseshoe maps is not to give rigorous proofs of the theory, but to show that the theory works and gives several interesting results, e.g. a systematic bifurcation diagram of the Hénon map which has not been obtained before.

To study the symbolic description of a pruned horseshoe like the Hénon map we have to combine the symbolic description of the complete Smale horseshoe [184] and the methods we used discussing the one dimensional n–modal maps. Using this we can obtain bifurcation diagrams for not complete horseshoe maps and a description of the non-wandering set. One way to understand the pruned horseshoe map is to describe its pruning front as done by Cvitanović, Gunaratne and Procaccia [53]. An equivalent description consists of finding a systematic approximation of the horseshoe by one dimensional maps. The later approach is more convenient if we want to find bifurcation diagrams but we discuss the close relation between the two points of view. We will also use the pruning front technique to describe Hamiltonian billiard systems. We will first discuss the horseshoe systems and the results obtained by Smale [184] and discuss the ordering of symbols in different horseshoe maps.

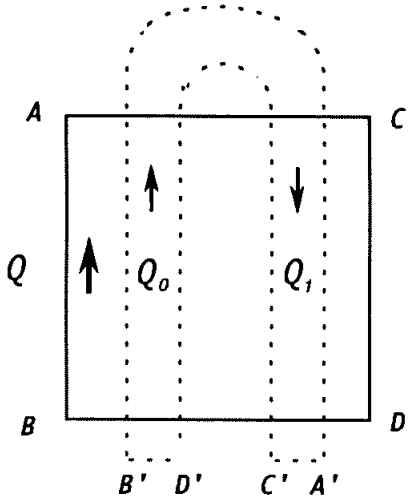

Figure 3.1: The Smale horseshoe map. The function g maps the square Q into the horseshoe.

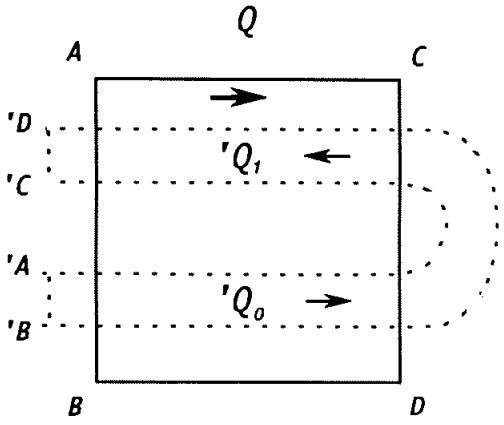

Figure 3.2: The inverse mapping g^{-1} of the Smale horseshoe.

3.1 The Smale horseshoe

The simplest example of a structurally stable chaotic diffeomorphism is the horseshoe map defined by Smale in 1961 [183]. Figure 3.1 shows the construction of this set as defined in ref. [184]. Q is a square in $\mathbb{R}^2$ drawn with solid lines in figure 3.1, mapped by the map g to the area bounded by the dashed lines. The map g is a diffeomorphism on Q and maps the corners $A \to A'$, $B \to B'$, $C \to C'$ and $D \to D'$, and g is a linear map on each component of $g^{-1}(g(Q) \cap Q)$. We denote the intersections $g(Q) \cap Q$ as Q_k with $k \in \{0, 1\}$. The index k is chosen such that when $x \in Q$ moves from the bottom to the top then $g(x)$ run through Q_k with increasing k. Figure 3.2 shows the action of g^{-1} on the square Q. The map g^{-1} maps the corners $A \to 'A$, $B \to 'B$, $C \to 'C$ and $D \to 'D$. We let $'Q_k$ be the two intersections $g^{-1}(Q) \cap Q$ such that $g('Q_k) \subset Q_k$.

We are interested in the subset Ω of Q where Ω is the non-wandering set of Q. A point $x \in Q$ is a wandering point if there is a neighborhood U of x such that $\bigcup_{|m|>0} g^{(m)}(U) \cap U = \emptyset$, and a point is called non-wandering if it is not a wandering point. Ω is the union of all the non-wandering points. Define Λ to be the intersection of all images and preimages of Q.

The following propositions are proved by Smale [184]

PROPOSITION I. *The subset Λ of Q is compact, invariant under g, indecomposable and on Ω, g is topologically conjugate to the shift automorphism $\sigma : X_S \to X_S$,*

with the cardinality of $S = 2$.

PROPOSITION II. *For a perturbation* g' *of* g, Λ' *defined similarly is also compact and invariant under* g'. *Then* $g' : \Lambda' \to \Lambda'$ *is also topologically conjugate to the shift* $\sigma : X_S \to X_S$.

From this follows that the non-wandering set of the Smale horseshoe can be described by a binary symbolic dynamics. A point $x \in \Lambda$ is mapped into a bi-infinite symbol string

$$\ldots s_{-2}s_{-1}s_0 \cdot s_1 s_2 \ldots \qquad s_i \in \{0, 1\} \tag{3.1}$$

by choosing

$$s_i = k \quad \text{if} \quad g^{(i)}(x) \in Q_k \tag{3.2}$$

with $k \in \{0, 1\}$ and $i \in Z$. For horseshoe maps with n folding we generalize to $k \in \{0, 1, \ldots, n\}$. The iteration $x_t \to x_{t+1} = g(x_t)$ is in the symbolic description the shift

$$\sigma(\ldots s_{-2}s_{-1}s_0 \cdot s_1 s_2 \ldots) = \ldots s_{-2}s_{-1}s_0 s_1 \cdot s_2 \ldots \tag{3.3}$$

This is similar to the shift in the unimodal one dimensional map, but in the one dimension the past symbols are thrown away. Since the horseshoe is a diffeomorphism we need to know both the future and the past.

In figure 3.1 we see that the interaction Q_0 is oriented the same way as Q, while Q_1 is turned around and oriented opposite to Q. This gives the same ordering of the future symbols as for the unimodal map with a maximum point, because the change of orientation of Q_1 corresponds to the negative slope $f'(x) < 0$ for $x > x_c$ in the unimodal map. The well ordered future symbols w_i and the future symbolic value γ are obtained from (1.18)

$$\begin{aligned} w_1 &= s_1 \\ w_{t+1} &= \begin{cases} w_t & \text{if } s_{t+1} = 0 \\ 1 - w_t & \text{if } s_{t+1} = 1 \end{cases} \\ \gamma &= 0.w_1 w_2 w_3 \ldots = \sum_{t=1}^{\infty} \frac{w_t}{2^t} \end{aligned} \tag{3.4}$$

This symbolic value γ corresponds to the position of the coordinate x_t in the vertical direction in figure 3.1. The points $x_t \in \Lambda$ closest to the line BD have $\gamma = 0.0$ and the points closest to the line AC have $\gamma = 1.0$.

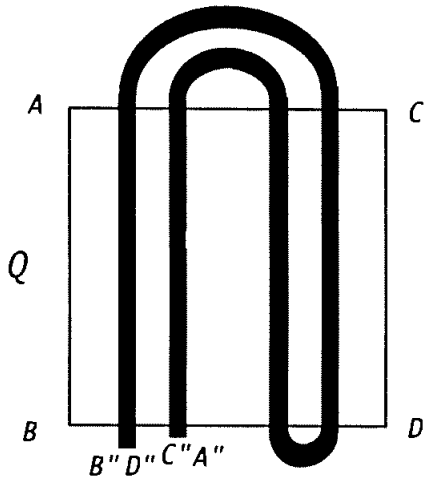

Figure 3.3: The image $g^{(2)}(Q)$ obtained by applying the Smale horseshoe map twice.

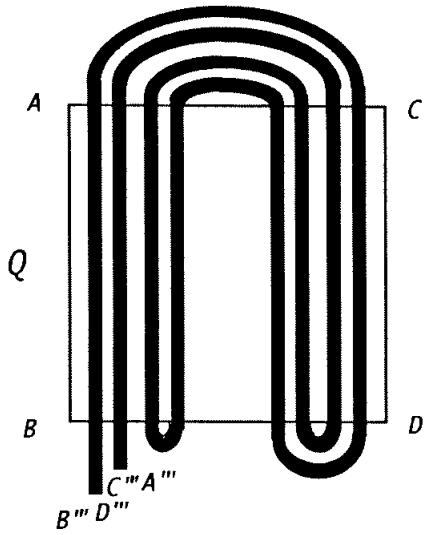

Figure 3.4: The image $g^{(3)}(Q)$ obtained by applying the Smale horseshoe map three times.

Figures 3.3 and 3.4 are the images obtained by applying the horseshoe map two times and three times on Q. The intersections $g^{(2)}(Q) \cap Q$ are 4 rectangles and $g^{(3)}(Q) \cap Q$ are 8 rectangles.

In figure 3.5 the square Q is drawn together with the 2^2 squares of $\Lambda_1 = g^{(-1)}(Q) \cap g^{(1)}(Q)$ and the 2^4 squares of $\Lambda_2 = g^{(-2)}(Q) \cap g^{(2)}(Q)$. The y–axis in figure 3.5 is labeled by $\cdot s_1 s_2$ and the x–axis by $s_{-1}s_0\cdot$ and they give a unique labeling of the 2^4 squares of Λ_2. The n-th generation of the construction of the non-wandering Cantor set gives 2^{2n} squares of the set $\Lambda_n = g^{(-n)}(Q) \cap g^{(n)}(Q)$. From proposition II we know that this is also valid for a perturbation g' and the 2^{2n} parts of the perturbed intersections Λ'_n are called rectangles.

The picture of the inverse map in figure 3.2 shows that $'Q_0$ has the same orientation as Q while $'Q_1$ has opposite orientation. Well ordered symbols for the past are then obtained as for the unimodal map with a maximum point ($f'(x) < 0$ for $x < x_c$ and $f'(x) > 0$ for $x > x_c$) and the symbolic value δ for the past is obtained by the algorithm

$$\begin{aligned} w_0 &= s_0 \\ w_{t-1} &= \begin{cases} w_t & \text{if } s_{t-1} = 0 \\ 1 - w_t & \text{if } s_{t-1} = 1 \end{cases} \\ \delta &= 0.w_0 w_{-1} w_{-2} \ldots = \textstyle\sum_{t=1}^{\infty} \frac{w_{1-t}}{2^t} \end{aligned} \quad . \tag{3.5}$$

The value δ increases along the horizontal position of x_t in figure 3.1. The points

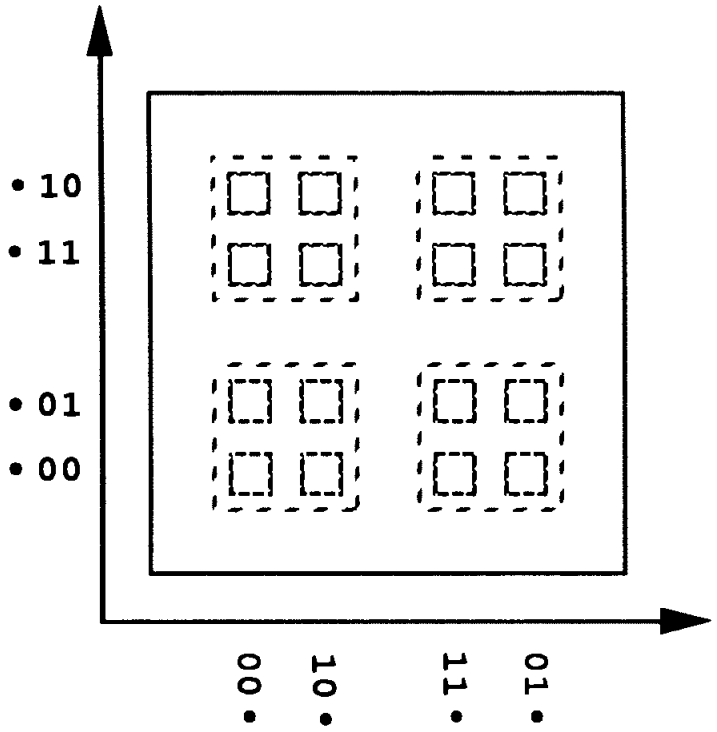

Figure 3.5: The square Q and the sets Λ_1 and Λ_2 of the Smale horseshoe and the labels $\cdot s_1 s_2$ and $s_{-1} s_0 \cdot$.

$x_t \in \Lambda$ closest to the line AB have $\delta = 0.0$ and the points closest to the line CD have $\delta = 1.0$. The symbolic coordinate (δ, γ) gives a position in the Cantor set of figure 3.5 with the gaps removed. We call this coordinate the point in the symbol plane for the phase space point x.

3.1.1 Smale horseshoe with reflection

By adding a reflection around the vertical axis before applying the horseshoe map g we get the map $\tilde{g}$ showed in figure 3.6 and the inverse map $\tilde{g}^{-1}$ drawn in figure 3.7.

From the figures we find that $\tilde{Q}_0$ and $\tilde{Q}_1$ are oriented as Q_0 and Q_1 and the definition of the future symbolic value γ is identical to the not reflected horseshoe. The inverse intersections $'\tilde{Q}_0$ and $'\tilde{Q}_1$ are oriented such that $'\tilde{Q}_0$ is opposite to Q while $'\tilde{Q}_1$ has the same orientation as Q. This give an algorithm for the past symbolic value δ identical to the algorithm for a unimodal map with a minimum point such that the well ordered symbols changes with $s_t = 0$;

$$\begin{aligned} w_0 &= s_0 \\ w_{t-1} &= \begin{cases} 1 - w_t & \text{if } s_{t-1} = 0 \\ w_t & \text{if } s_{t-1} = 1 \end{cases} \quad . \\ \delta &= 0.w_0 w_{-1} w_{-2} \ldots = \sum_{t=1}^{\infty} \frac{w_{1-t}}{2^t} \end{aligned} \tag{3.6}$$

Figure 3.10 shows the set Λ_2 and the labels on the squares.

Two and three applications of $\tilde{g}$ give the folding in figures 3.8 and 3.9.

The Smale horseshoe with and without reflection is closely related and both may be realized by the Hénon map.

The shift operation σ on the symbols s_t in eq. (3.3) becomes more complicated when acting on well ordered symbols w_t. This type of shift operations are discussed for one example by Troll in ref. [193]. A shift operation shift the symbol string to the left but will also change $w_t \to 1 - w_t$ if a symbol that changes the ordering are moved from the future to the past symbolic description.

3.2 Variations of the Smale horseshoe

3.2.1 Once-folding maps

Smale showed that variations of the horseshoe map like figures 3.11, 3.13, 3.15 and 3.21 also yield non-wandering sets. The horseshoe in figure 3.11 is binary but the orientation is different than in figure 3.1. Both Q_0 and Q_1 are oriented the same way as Q and the construction of well ordered symbols is therefore simpler. The

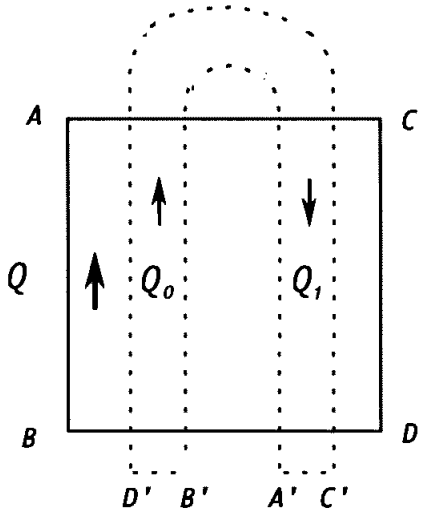

Figure 3.6: The Smale horseshoe map with reflection. The function $\tilde{g}$ maps the square Q into the horseshoe.

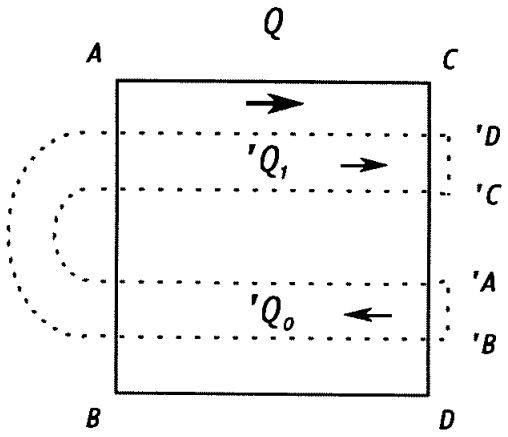

Figure 3.7: The inverse mapping $\tilde{g}^{-1}$ of the Smale horseshoe with reflection.

symbols w_t is constructed as for a one dimensional map with two branches, both having $f'(x) > 0$ like the Bernoulli shift $x_{t+1} = 2x_t \bmod (1)$. This gives simply

$$w_t = s_t \tag{3.7}$$

Figure 3.12 shows that the inverse map also has $'Q_0$ and $'Q_1$ oriented the same way as Q, and the well ordered symbols for the past are therefore given by the same algorithm.

The same map but with a reflection around the vertical axis gives $\tilde{Q}_0$ and $\tilde{Q}_1$ oriented as Q while both $'\tilde{Q}_0$ and $'\tilde{Q}_1$ is oriented opposite to Q and the algorithm becomes

$$\begin{aligned} &\text{if} \quad t > 0 \quad \text{then} \quad w_t = s_t \\ &\text{if} \quad t \leq 0 \quad \text{then} \quad w_t = \begin{cases} s_t & \text{if} \quad t \quad \text{even} \\ 1 - s_t & \text{if} \quad t \quad \text{odd} \end{cases} \end{aligned} \tag{3.8}$$

Figures 3.13 and 3.14 show a horseshoe map and its inverse map where both intersections change the orientation in future and in past. The well ordered symbols and the symbolic values are obtained by

$$\begin{aligned} &\text{if} \quad t > 0 \quad \text{then} \quad w_t = \begin{cases} s_t & \text{if} \quad t \quad \text{odd} \\ 1 - s_t & \text{if} \quad t \quad \text{even} \end{cases} \\ &\text{if} \quad t \leq 0 \quad \text{then} \quad w_t = \begin{cases} s_t & \text{if} \quad t \quad \text{even} \\ 1 - s_t & \text{if} \quad t \quad \text{odd} \end{cases} \end{aligned} \tag{3.9}$$

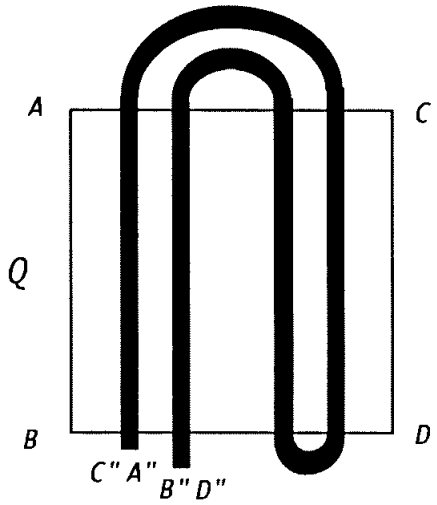

Figure 3.8: The image $\tilde{g}^{(2)}(Q)$ when applying the Smale horseshoe map with reflection twice.

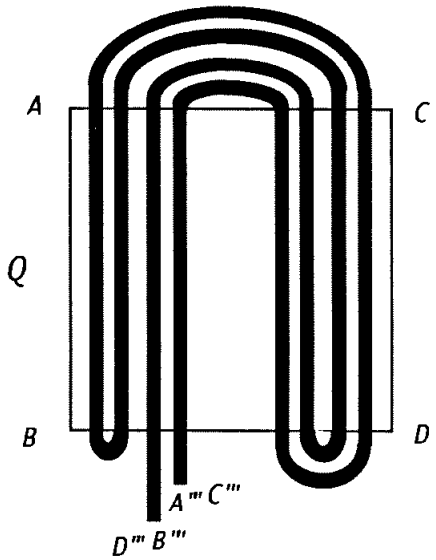

Figure 3.9: The image $\tilde{g}^{(3)}(Q)$ when applying the Smale horseshoe map with reflection three times.

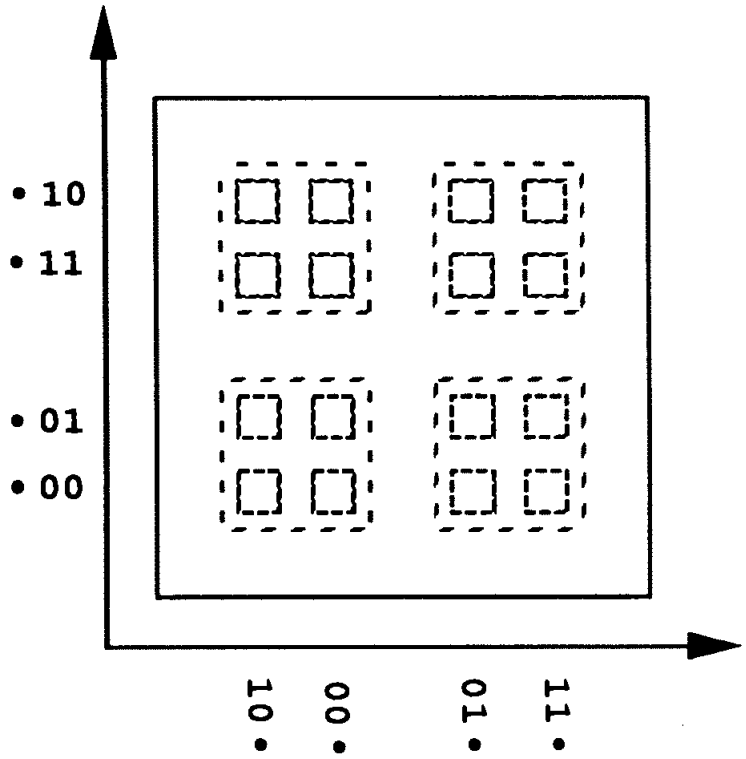

Figure 3.10: The square Q and the sets Λ_1 and Λ_2 of the Smale horseshoe with reflection. and the labels $\cdot s_1 s_2$ and $s_{-1} s_0 \cdot$.

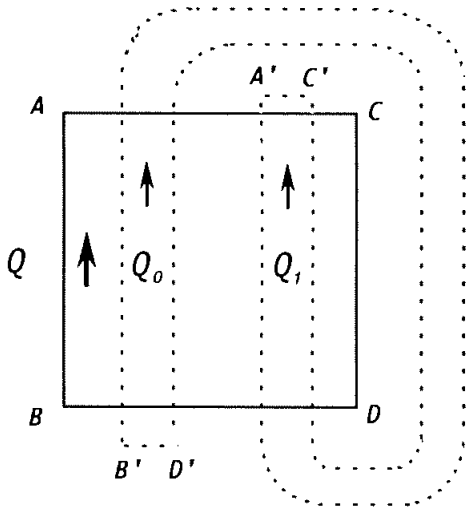

Figure 3.11: The once folding Smale horseshoe map with different folding.

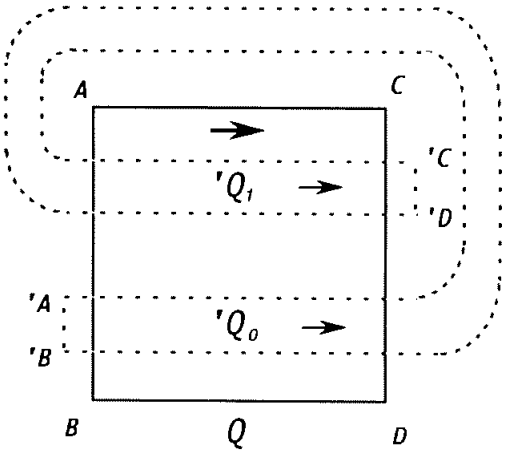

Figure 3.12: The inverse mapping of the Smale horseshoe in figure 3.11.

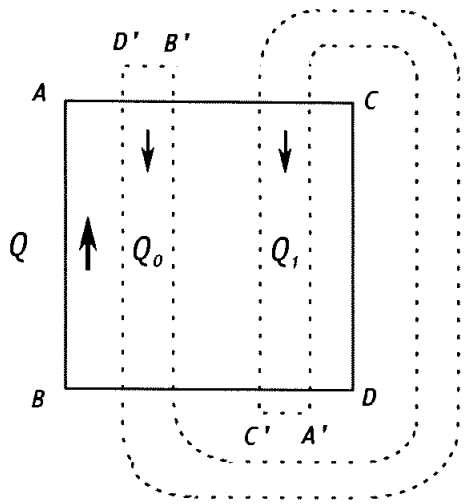

Figure 3.13: A once folding Smale horseshoe map with all symbols reversing the ordering.

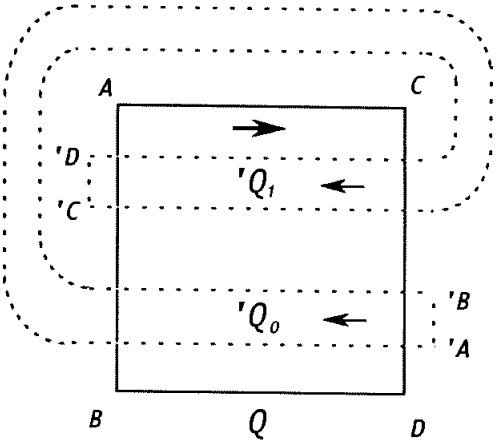

Figure 3.14: The inverse mapping of the Smale horseshoe in figure 3.13.

3.2.2 Twice-folding maps

Figure 3.15 shows a twice-folding horseshoe map with three intersections $g(Q) \cap Q$. The intersections are enumerated in such a way that when $x \in Q$ moves from the bottom to the top, then $g(x)$ visits the intersections in the order: $Q_0 \to Q_1 \to Q_2$. The intersections Q_0 and Q_2 have the same orientation as Q, while Q_1 is oriented opposite to Q. The inverse map is drawn in figure 3.16 and the three intersections $'Q_0$, $'Q_1$, and $'Q_2$ have respectively the same, the opposite, and the same orientation as Q.

The well defined future symbolic dynamics has the same ordering as a bimodal, one-dimensional map with $f'(x) > 0$ for $x < x_{c1}$, and $x > x_{c2}$ and with $f'(x) < 0$ for $x_{c1} < x < x_{c2}$. From the symbols s_t defined as in (3.2) with $k \in \{0, 1, 2\}$ we get

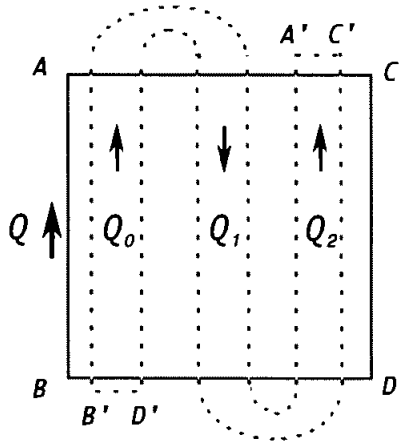

Figure 3.15: The twice folding Smale horseshoe map with simple folding.

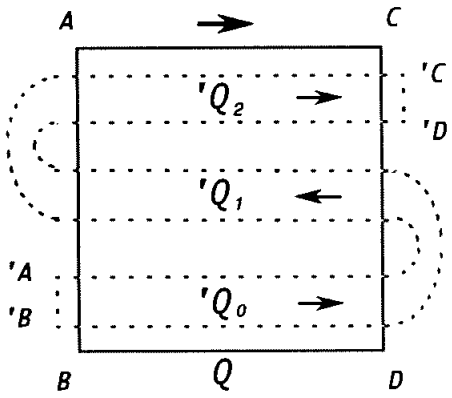

Figure 3.16: The inverse mapping of the Smale horseshoe in figure 3.15.

well ordered symbols w_t from algorithm (2.4) with $n = 2$

$$
\begin{aligned}
w_1 &= s_1 \\
p_1 &= \begin{cases} 1 & \text{if} \quad s_1 = 0 \quad \text{or} \quad s_1 = 2 \\ -1 & \text{if} \quad s_1 = 1 \end{cases} \\
w_t &= \begin{cases} s_t & \text{if} \quad p_{t-1} = 1 \\ 2 - s_t & \text{if} \quad p_{t-1} = -1 \end{cases} \\
p_t &= \begin{cases} p_{t-1} & \text{if} \quad s_t = 0 \quad \text{or} \quad s_t = 2 \\ -p_{t-1} & \text{if} \quad s_t = 1 \end{cases} \\
\gamma &= 0.w_1 w_2 w_3 \ldots = \sum_{t=1}^{\infty} \frac{w_t}{3^t}
\end{aligned}
\tag{3.10}
$$

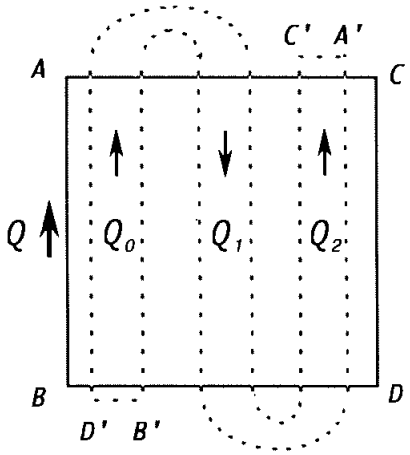

Figure 3.17: The twice folding Smale horseshoe map with reflection.

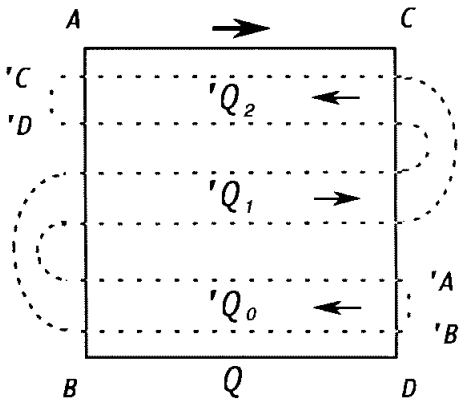

Figure 3.18: The inverse mapping of the Smale horseshoe in figure 3.17.

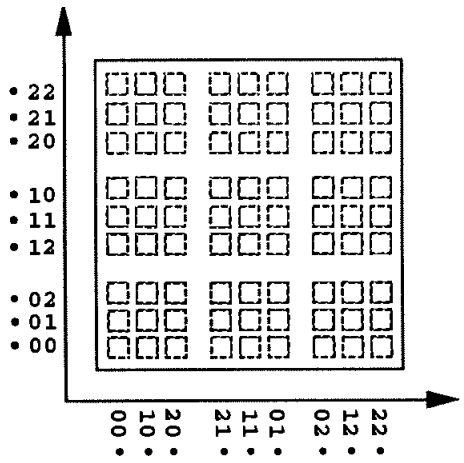

Figure 3.19: The set Λ_2 for the horseshoe in figure 3.15 with symbols $\cdot s_1 s_2$ and $s_{-1} s_0 \cdot$.

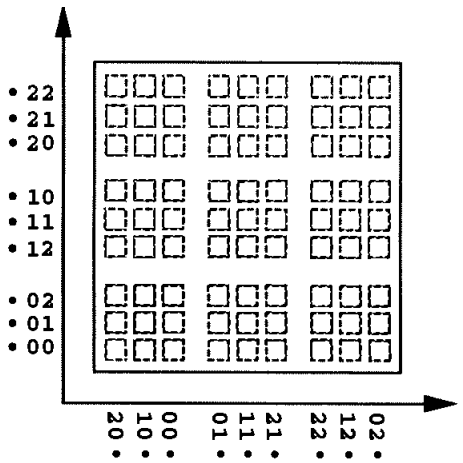

Figure 3.20: The set Λ_2 for the horseshoe in figure 3.17 with symbols $\cdot s_1 s_2$ and $s_{-1} s_0 \cdot$.

The past well ordered symbols are obtained by a similar algorithm:

$$\begin{aligned} w_0 &= s_0 \\ p_0 &= \begin{cases} 1 & \text{if } s_0 = 0 \text{ or } s_0 = 2 \\ -1 & \text{if } s_0 = 1 \end{cases} \end{aligned}$$

$$\begin{aligned} w_t &= \begin{cases} s_t & \text{if } p_{t+1} = 1 \\ 2 - s_t & \text{if } p_{t+1} = -1 \end{cases} \\ p_t &= \begin{cases} p_{t+1} & \text{if } s_t = 0 \text{ or } s_t = 2 \\ -p_{t+1} & \text{if } s_t = 1 \end{cases} \end{aligned} \tag{3.11}$$

$$\delta = 0.w_0 w_{-1} w_{-2} \ldots = \sum_{t=0}^{\infty} \frac{w_{-t}}{3^{(t+1)}}$$

We can also add to this two fold map a reflection. Applying a reflection around the vertical axis before stretching and folding gives the figure 3.17, and the inverse mapping in figure 3.18. The well ordered future symbols are the same for the vertically reflected map as for the not reflected map. The well ordered past symbols are obtained by the algorithm

$$\begin{aligned} w_0 &= s_0 \\ p_0 &= \begin{cases} 1 & \text{if } s_0 = 0 \text{ or } s_0 = 2 \\ -1 & \text{if } s_0 = 1 \end{cases} \end{aligned}$$

$$\begin{aligned} w_t &= \begin{cases} s_t & \text{if } p_{t+1} = 1 \\ 2 - s_t & \text{if } p_{t+1} = -1 \end{cases} \\ p_t &= \begin{cases} -p_{t+1} & \text{if } s_t = 0 \text{ or } s_t = 2 \\ p_{t+1} & \text{if } s_t = 1 \end{cases} \end{aligned} \tag{3.12}$$

$$\delta = 0.w_0 w_{-1} w_{-2} \ldots = \sum_{t=0}^{\infty} \frac{w_{-t}}{3^{(t+1)}}$$

The sets $\Lambda_2 = g^{(-2)}(Q) \cap g^{(2)}(Q)$ for the two twice-folding maps are drawn in figure 3.19 and figure 3.20 together with the symbols $s_{-1}s_0\cdot$ and $\cdot s_1 s_2$ labeling the 3^4 rectangles.

A more complicated twice folding map is shown in figure 3.21 and its inverse map in figure 3.22. The labeling Q_k is done as before, so that when x moves from the bottom to the top, $g(x)$ visits Q_k in the order $Q_0 \to Q_1 \to Q_2$.

The future intersections Q_k are oriented as in the map above; Q_0 and Q_2 oriented as Q, while Q_1 is oriented opposite to Q. The well ordered future symbols

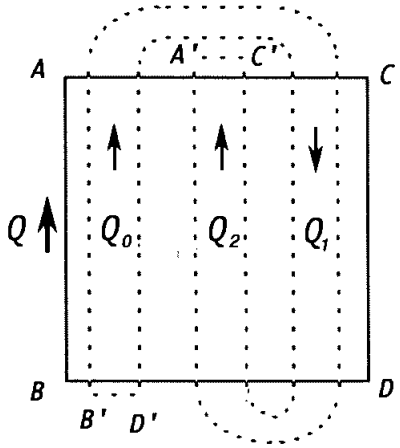

Figure 3.21: The twice folding Smale horseshoe map with more complicated folding.

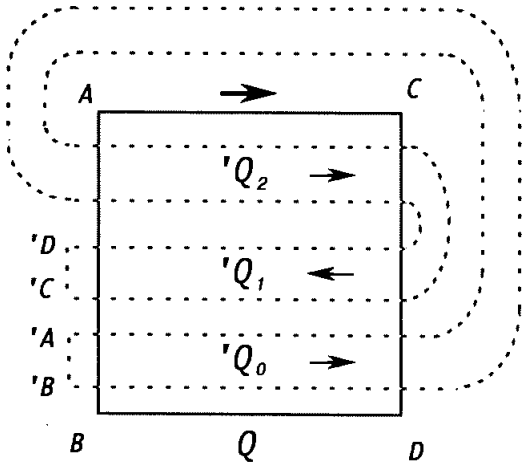

Figure 3.22: The inverse mapping of the Smale horseshoe in figure 3.21.

are therefore obtained by the algorithm (3.10). The intersections $g^{-1}(Q) \cap Q$ are oriented with $'Q_0$ and $'Q_1$ as Q while $'Q_2$ are oriented opposite to Q. This gives the following algorithm for well ordered past symbols:

$$
\begin{aligned}
w_0 &= \begin{cases} 0 & \text{if} \quad s_0 = 0 \\ 1 & \text{if} \quad s_0 = 2 \\ 2 & \text{if} \quad s_0 = 1 \end{cases} \\
p_0 &= \begin{cases} 1 & \text{if} \quad s_0 = 0 \quad \text{or} \quad s_0 = 2 \\ -1 & \text{if} \quad s_0 = 1 \end{cases} \\
& \\
w'_t &= \begin{cases} 0 & \text{if} \quad s_t = 0 \\ 1 & \text{if} \quad s_t = 2 \\ 2 & \text{if} \quad s_t = 1 \end{cases} \\
w_t &= \begin{cases} w'_t & \text{if} \quad p_{t+1} = 1 \\ 2 - w'_t & \text{if} \quad p_{t+1} = -1 \end{cases} \\
p_t &= \begin{cases} p_{t+1} & \text{if} \quad s_t = 0 \quad \text{or} \quad s_t = 2 \\ -p_{t+1} & \text{if} \quad s_t = 1 \end{cases} \\
& \\
\delta &= 0.w_0 w_{-1} w_{-2} \ldots = \sum_{t=0}^{\infty} \frac{w_t}{3^{(t+1)}}
\end{aligned}
\tag{3.13}
$$

The well ordered symbols can be worked out for any horseshoe map like these by observing weather the intersections are oriented as or opposite to Q and flipping the symbols if the symbols correspond to oppositely oriented rectangle.

One example we will use later is an n-folding map with all future intersections $Q_0, Q_1, \ldots, Q_n$ oriented opposite to Q. This is the generalized folding of the once-folding map in figure 3.13. The algorithm giving the well ordered symbols is

$$\begin{array}{l} \text{if} \quad t > 0 \quad \text{then} \quad w_t = \begin{cases} s_t & \text{if} \quad t \quad \text{odd} \\ n - s_t & \text{if} \quad t \quad \text{even} \end{cases} \\ \\ \text{if} \quad t \leq 0 \quad \text{then} \quad w_t = \begin{cases} s_t & \text{if} \quad t \quad \text{even} \\ n - s_t & \text{if} \quad t \quad \text{odd} \end{cases} \end{array} \tag{3.14}$$

Chapter 4

Pruned horseshoes

We will here discuss pruned horseshoe maps in two dimensions and we are going to discuss the ordering of bifurcations in these systems. We are not going to give a precise definition of this class of maps, but we believe this class includes many systems of interest in physics. Our motivation is the Hénon map, discussed in an enormous number of articles [3, 4, 22, 26, 27, 41, 45, 53, 92, 93, 107, 112, 150, 153, 180]. In particular we develop further the approach initiated by the work of Cvitanović, Gunaratne and Procaccia [53]. The complicated bifurcation structure in the parameter space (a, b) of the Hénon map has been noticed in several works [153, 150] and the most complete investigations on the bifurcation has been done by Mira and coworkers [75, 76, 77, 153]. The book by Mira, ref. [153], gives an impressing amount of numerical results but the discussion in the book is difficult to follow and Mira does not use the same notation as most other authors use. We claim that the methods we use apply to all maps "similar" to the Hénon map, and we give some examples of a perturbation of the Hénon map and of other maps for which the method works.

By an n-folding map we understand a map similar to a n-folding Smale horseshoe map which may be perturbed in such a way that its non-wandering set is not a full hyperbolic $n \times n$-Cantor set in the phase space. Under one iteration the perturbed horseshoe map should not fold any region of the phase space more than n times. The simplest folding maps are the once-folding maps, of which the Hénon map is the most well known. We may regard an n-folding map as the two-dimensional analogue of the 1-dimensional n-modal map. The bifurcation that leads to loss of orbits has to be similar to the bifurcations we find in the Hénon map. This excludes the 3-disk system and other billiards that we discuss later, because in billiard systems the bifurcations are not naturally organized in the same hierarchical structure.

We will construct here the bifurcation diagrams for the once-folding maps, and

we will also describe how we can extend this description of the once-folding map to the n-folding maps, and give an example for the 3-folding map. This is an analogue to our discussion of generalizing the unimodal method to n-modal 1-dimensional maps.

To be able to discuss a pruned horseshoe map in symbolic dynamics language we have to assume the following:

Conjecture: *An incomplete horseshoe can be described by a subset of the symbolic dynamics of the corresponding complete Smale horseshoe map.*

This conjecture works for all the examples we discuss, and we do not know any examples of once-folding systems that contradict it. An orbit may change symbols when a parameter changes but this is a consequence of bifurcations and does not contradict the conjecture. We will state below a conjecture on how to obtain a unique symbolic dynamics given the pruned horseshoe map.

The horseshoes in figures 3.1 and 3.7 can be realized by the Hénon map

$$\begin{aligned} x_{t+1} &= 1 - ax_t^2 + y_t \\ y_{t+1} &= bx_t \end{aligned} \tag{4.1}$$

or equivalent

$$x_{t+1} = 1 - ax_t^2 + bx_{t-1} \tag{4.2}$$

A non-smooth tent map version of this is the Lozi map:

$$\begin{aligned} x_{t+1} &= \begin{cases} 1 + ax_t + y_t & \text{if } x < 0 \\ 1 - ax_t + y_t & \text{if } x \geq 0 \end{cases} \\ y_{t+1} &= bx_t \end{aligned} \tag{4.3}$$

Grassberger and Kantz [92] have conjectured that the Hénon map may be described by binary symbols constructed by finding the primary homoclinic tangencies and use these to separate the nonwandering set into two regions denoted by the two symbols. Cvitanović, Gunaratne and Procaccia [53] have used such binary symbols to construct a "pruning front".

A different approach has been done by Biham and Wenzel, who constructed an algorithm that should always find a periodic orbit given a symbol string [26, 27]. This method starts with a guess for n values $\tilde{x}_0, \tilde{x}_1, \ldots, \tilde{x}_{n-1}$ of a given period n orbit. If this was a solution we would have $\Delta_t = \tilde{x}_{t+1} - (1 - a\tilde{x}_t^2 + b\tilde{x}_{t-1}) = 0$, with $0 \leq t \leq n-1$ and $\tilde{x}_0 = \tilde{x}_n, \tilde{x}_{-1} = \tilde{x}_{n-1}$. The nonvanishing errors $\Delta_t \neq 0$ in the general case can be used to change the numbers $\tilde{x}_t$ by the artificial dynamics

$$\frac{d\tilde{x}_t}{d\tau} = s_t \Delta_t \tag{4.4}$$

where $s_t \in \{-1, 1\}$ is the symbolic description of an orbit. This method converges to a period n orbit for most parameter values and symbol strings. We will discuss in section 4.5 why the method cannot always converge. At the moment we just accept the numerical fact that this method often converges, and gives one possible symbolic description of most periodic orbits.

We believe Grassberger-Kantz's point of view that it is possible to find primary homoclinic tangencies and to use these tangencies as the separation points between different symbols in the same way as we used critical points to define symbols in the 1-dimensional maps. Grassberger and Kantz found that it was not one unique way to choose the primary tangencies and different choices gave different possible separations with the same topological entropy. We avoid this ambiguity by a conjecture stated in section 5.2.1 on how to always have a unique set of primary tangencies which are connected by a continuous partition line.

4.1 Bifurcations

4.1.1 Stable and unstable manifolds at bifurcation points

To describe the bifurcations we have to investigate the manifolds of the map. When discussing bifurcations in 2-dimensional maps, pictures of the type in figure 4.1 are usually drawn. These pictures illustrate a homoclinic tangency bifurcation and are used when proving the results of Gavrilov and Silikov [84] and of Newhouse [160], see ref. [100]. In figure 4.1 b) the unstable and the stable manifolds are tangent at a point a finite distance from the hyperbolic point measured along the manifolds. This is a bifurcation analogue to the 1-dimensional map bifurcation where the critical point maps into the fixed point or into an unstable periodic orbit. In 1-dimensional maps this may be a band merging bifurcation, a crisis bifurcation or a chaotic attractor. This bifurcation where the unstable and the stable manifolds are tangent to each other is not the analogous case of the 1-dimensional tangent bifurcation creating a periodic orbit, but there is a bifurcation creating a periodic orbit arbitrarily close to the bifurcation in figure 4.1 b). The picture to draw studying this bifurcation is the drawing in figure 4.2.

In figure 4.2 a) the unstable manifold becomes folded and the turning point converges to a point in a periodic orbit. The stable manifold of a hyperbolic point does not get arbitrarily close to the periodic orbit at a finite distance from the hyperbolic point measured along the manifold. We are therefore not especially interested in the stable manifold when studying the bifurcation creating a stable periodic orbit. A useful drawing is figure 4.2 b) where we have plotted the unstable

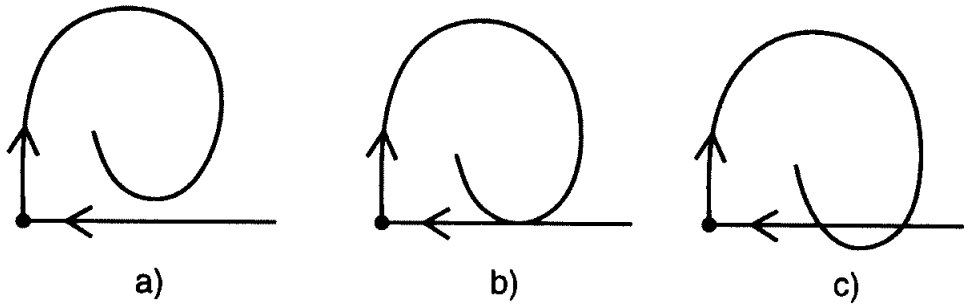

Figure 4.1: A bifurcation where the stable and unstable manifold create a homoclinic point.

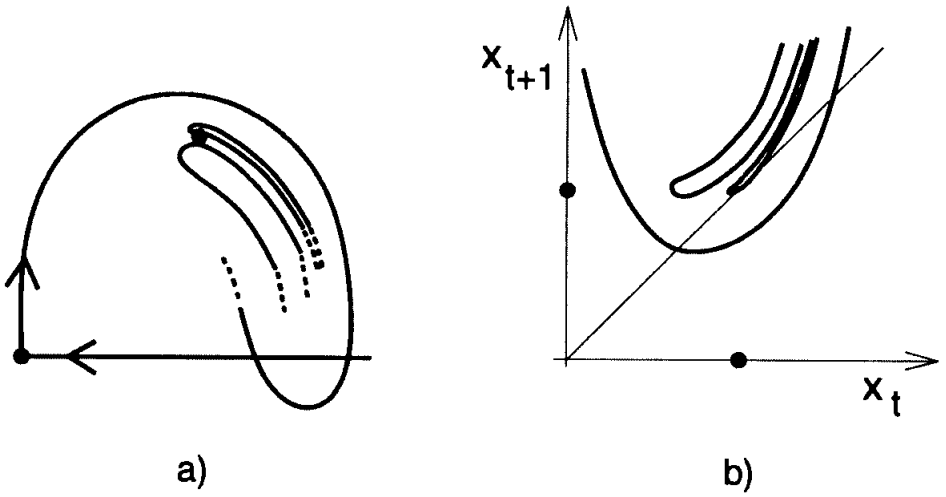

Figure 4.2: a) The two manifolds close to a bifurcation creating a period n orbit. b) The n-th return map of the unstable manifold close to a bifurcation creating a period n orbit.

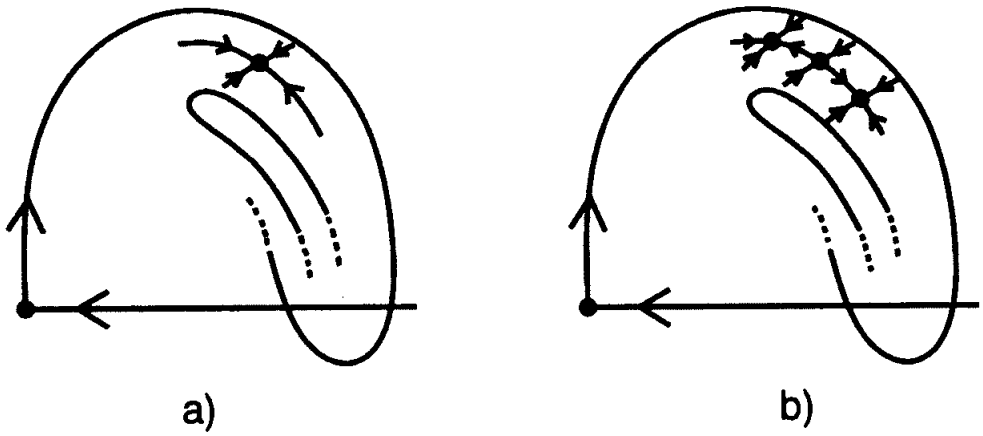

Figure 4.3: The period doubling bifurcation of a periodic orbit.

manifold in the space (x_t, x_{t+n}) where n is the length of the periodic orbit created at the bifurcation. In this space the unstable manifold converges to a curve which is tangent to the diagonal $x_{t+n} = x_t$. The bifurcation is therefore well described by a 1-dimensional map of the unstable manifold.

The period doubling bifurcation is illustrated in figure 4.3. This is a local bifurcation of the periodic orbit and no information of this bifurcation can be obtained by the stable manifold of the hyperbolic point. This stable manifold is never close to the periodic orbit bifurcating inside the basin of attraction. The periodic doubling bifurcation can also be studied by a 1-dimensional map of the unstable manifold.

To be able to apply the symbolic description we use the union of the unstable and stable manifolds for all points in the non-wandering set. We include the manifolds of all hyperbolic orbits, also of an orbit just having a period doubling bifurcation as in figure 4.3 b).

The homoclinic tangency in figure 4.1 b) is the point when the unstable manifold "turns back". We define a *turning point* or a *turnback* to be a point on the unstable manifold where the closest fold of the stable manifold is parallel to the unstable manifold. By this definition we have a turning point in all the three figures 4.1 a) 4.1 b) 4.1 c), but only in figures 4.1 b) do we know that we have a homoclinic tangency. If there is a homoclinic tangency in the other figures this point is identical to the turning point. A turning point may be inside the basin of attraction of a stable periodic orbit. We also use the term turnback for the non-smooth map like the Lozi-map for a point on the unstable manifold where the unstable manifold has a kink.

The turnbacks in the horseshoe maps play the same role as the critical points

in a 1-dimensional map when we study the bifurcations of the map.

There is always at least one turnback close to a stable orbit. The folds of the unstable manifold have a Cantor set structure and each fold has a turnback which can give a stable periodic orbit. This imply that the parameter space is infinite and we can obtain a map with any number of stable orbits existing simultaneously [160]. The bifurcations take place in an infinite dimensional parameter space which seems to be a hopeless system to describe. There are however two observations that simplify the bifurcation description. First; if a turning point gives a stable periodic orbit then the basin of attraction covers all the turnbacks in a neighborhood reducing other possible bifurcations close to this. Second; for the horseshoes there is a natural ordering or hierarchical organization of the folds allowing a systematic approximation scheme of the infinite dimensional parameter space. This is not true for all systems, e.g. billiard systems can not be described in this way.

4.1.2 One-dimensional approximation

The first approximation we make is to consider the horseshoe with n folds to be an n-modal 1-dimensional map $x_t = f(x_{t+1})$ with n parameters. The topological structure of the bifurcations can be described by the kneading sequences of the critical points (turning points) and we can draw a symbolic parameter space. The bifurcation diagrams are given in chapter 1. This unimodal description of the system is a necessary starting point, but not a remarkable result. In a realization of the pruned once-folding horseshoe e.g. the Hénon map, the unimodal bifurcations are not enough to explain the main features of the bifurcation curves in a parameter plane, (a, b), scan. One way to illustrate this approximation is to regard the image obtained by the Smale horseshoe map $g(Q)$ as a line instead of a band. The line is then a 1-dimensional function with a slope depending on the orientation of Q_k. This is equivalent to squeezing all the folds in the unstable manifold together to one curve. This is realized in the Hénon map in the limit $b \to 0$.

The second approximation is obtained by finding the second iterated of the horseshoe map, $g^2(Q)$, and make a 1-dimensional map where the intersections $g^2(Q) \cap Q$ correspond to monotone sections in a 1-dimensional map. If we look at the once-folding map in figures 3.3 and 3.8 we see that if we approximate the band $g^2(Q)$ with a curve this gives a trimodal map with two maximum and one minimum point. The minimum point is however the image of the bending point of $g(Q)$ and is not an independent critical point. This gives a two parameter map with two maximum points as the critical points of interest. The natural choice of the 1-dimensional map is a combination of two unimodal map with two critical points

x_c^0 and x_c^1 where both are maximum points. The kneading sequences from these two critical points give the two dimensional symbolic parameter space. The minimum point has as its only function that if it is as high as one of the maximum points the number of critical points decreases in the way we have discussed for trimodal maps in section 2.2. This kind of bifurcation makes it possible for an orbit in the two dimensional map to change symbolic description without getting stable by moving around a cusp as illustrated in the trimodal 1-dimensional map. The height of the minimum point described in symbols is found by a shift in the kneading sequence of x_c^0 or x_c^1. We then get two values for the minimum point and we have to be careful when discussing this minimum point.

The third approximation is obtained by simplifying $g^{(3)}(Q)$ by choosing a line for each intersection $g^{(3)}(Q) \cap Q$. For the once-folding map in figures 3.4 and 3.9 we get a 7 modal map with 4 independent critical points and we can describe this by four unimodal maps. Again only the kneading sequence of the maximum points are critical points of interest in the once-folding horseshoe. The minimum points are images of the maximum points in the first and second approximation. The parameter space is four dimensional, and we construct the topological parameter space from the kneading sequences of the four critical points x_c^{00}, x_c^{01}, x_c^{10} and x_c^{11}.

The n-th approximation of the once-folding map is now obtained by considering $g^{(n)}(Q)$ to be a 1-dimensional map consisting of 2^{n-1} unimodal maps. The 2^{n-1} maximum points $x_c^{0\ldots00}$, $x_c^{0\ldots01}$, $x_c^{0\ldots10}$, $\ldots$, $x_c^{1\ldots11}$ are the critical points of interest and the kneading sequence of these points give the topological parameter space. The maximum points correspond to the primary turnbacks, while the minimum points correspond to turnbacks that are not primary.

The two-folding map in figure 3.15 is approximated the same way. The first approximation gives a bimodal map with a maximum point x_{c1} and a minimum point x_{c2} and the bifurcation diagrams discussed in section 1.1. The second approximation gives two bimodal maps with the six critical points x_{c1}^0, x_{c1}^1, x_{c1}^2, x_{c2}^0 x_{c2}^1 and x_{c2}^2. The other extremum points are images of the extremum points in the first approximation and corresponds to turnbacks that are not primary. The n-th approximation gives $\cdot 3^{n-1}$ bimodal maps with $2 \cdot 3^{n-1}$ independent critical points, and a $2 \cdot 3^{n-1}$ dimensional parameter space.

A m-folding map have in the n-th approximation $m \cdot (m+1)^{n-1}$ independent critical points, and a $m \cdot (m+1)^{n-1}$ dimensional parameter space.

4.2 Unimodal approximation

The first approximation gives exactly the MSS ordering of periodic orbits as we have discussed in chapter 1 for the once-folding map. This is the ordering we find for the Hénon map and the Lozi map in the limit $b \to 0$.

4.3 Bimodal approximation

The second approximation gives a bimodal map with a two dimensional parameter plane. The topological parameter plane is different from the bimodal three-symbol plane discussed in section 2.1, and we can describe this topological bifurcation plane by using the restrictions we find on the binary symbols.

The two unimodal maps $f_0(x_t)$ and $f_1(x_t)$ corresponds to the two folds in $g^{(2)}(Q)$ and each fold is the image of one of the two parts of $g(Q) \cap Q$; Q_0 and Q_1. From the figures 3.1 and 3.3 we find that for the Smale horseshoe without any reflection Q_0 maps into the outer fold and Q_1 maps into the inner fold. The drawings of the Smale horseshoe with reflections, figures 3.6 and 3.8, show that in this case Q_0 maps into the inner fold and Q_1 maps into the outer fold. The inner fold has a maximum point that are smaller than the maximum point of the outer fold which imply; for not reflected maps $x_c^1 < x_c^0$, and for reflected maps $x_c^0 < x_c^1$. The function of the 1-dimensional map applied to a point x_t is $f_0(x_t)$ if x_{t-1} is in Q_0 which is equivalent to that $s_{t-1} = 0$. The function applied to the point x_t is $f_1(x_t)$ if x_{t-1} is in Q_1 that is if $s_{t-1} = 1$.

The bimodal map is

$$x_{t+1} = f_{s_{t-1}}(x_t) \tag{4.5}$$

We can now find all periodic orbits of a given length and find the topological values $\tau_s(\overline{S})$ of all cyclic permutations of the orbits.

4.3.1 Kneading values of short orbits

The fixed point $\overline{0}$ has $s_{-1} = 0$ and the only kneading value is $\tau_0(\overline{0}) = 0$. This orbit exists when

$$\kappa_0 > \tau_0^{\max}(\overline{0}) \;\; = \;\; 0 \tag{4.6}$$

The fixed point $\overline{1}$ has $s_{-1} = 1$ and kneading value is $\tau_1(\overline{1}) = 0.\overline{10} = 2/3$ and it exists for symbolic parameter values

$$\kappa_1 > \tau_1^{\max}(\overline{1}) \;\; = \;\; 0.\overline{10} = 2/3 \tag{4.7}$$

The period 2 orbit $\overline{10}$ has two cyclic permutations. The point x_{10} with symbolic description $\overline{s_1 s_2} = \overline{10}$ has $s_0 = s_2 = 0$ and $s_{-1} = s_1 = 1$ giving the kneading value $\tau_1(\overline{10}) = 0.\overline{1100} = 4/5$. The second point in the period 2 orbit, x_{01}, is on map 0 since $s_{-1} = 0$ and the kneading value is $\tau_0(\overline{01}) = 0.\overline{0110} = 2/5$. This orbit exists for the symbolic parameter values

$$\kappa_0 > \tau_0^{\max}(\overline{10}) = 0.\overline{0110} = 2/5 \tag{4.8}$$
$$\kappa_1 > \tau_1^{\max}(\overline{10}) = 0.\overline{1100} = 4/5 \tag{4.9}$$

There are two period 3 orbits with the symbolic strings $\overline{s_1 s_2 s_3}$: $\overline{100}$ and $\overline{101}$. Here we have that $s_{-1} = s_2$ describes which map the point is on. The orbit $\overline{100}$ has the following symbolic values: $\tau_0(\overline{100}) = 0.\overline{111000} = 8/9$, $\tau_1(\overline{010}) = 0.\overline{011100} = 4/9$, $\tau_0(\overline{001}) = 0.\overline{001110} = 2/9$. The two values of interest are $\tau_0^{\max}(\overline{100}) = 8/9$ and $\tau_1^{\max}(\overline{100}) = 4/9$. The symbolic parameters where $= \overline{100}$ exists is

$$\kappa_0 > \tau_0^{\max}(\overline{100}) = 0.\overline{111000} = 8/9 \tag{4.10}$$
$$\kappa_1 > \tau_1^{\max}(\overline{100}) = 0.\overline{011100} = 4/9 \tag{4.11}$$

The second orbit has the three symbolic values: $\tau_0(\overline{101}) = 0.\overline{110} = 6/7$, $\tau_1(\overline{110}) = 0.\overline{100} = 4/7$, $\tau_1(\overline{011}) = 0.\overline{010} = 2/7$, and the orbit exists for symbolic parameter values

$$\kappa_0 > \tau_0^{\max}(\overline{101}) = 0.\overline{110} = 6/7 \tag{4.12}$$
$$\kappa_1 > \tau_1^{\max}(\overline{101}) = 0.\overline{100} = 4/7 \tag{4.13}$$

There are three period 4 orbits $\overline{1000}$, $\overline{1001}$ and $\overline{1011}$. The maximum kneading values and the symbolic parameter values where these orbits exist are

$$\kappa_0 > \tau_0^{\max}(\overline{1000}) = 0.\overline{11110000} = 16/17 \tag{4.14}$$
$$\kappa_1 > \tau_1^{\max}(\overline{1000}) = 0.\overline{00111100} = 4/17 \tag{4.15}$$
$$\kappa_0 > \tau_0^{\max}(\overline{1001}) = 0.\overline{1110} = 14/15 \tag{4.16}$$
$$\kappa_1 > \tau_1^{\max}(\overline{1001}) = 0.\overline{0100} = 4/15 \tag{4.17}$$
$$\kappa_0 > \tau_0^{\max}(\overline{1011}) = 0.\overline{10010110} = 10/17 \tag{4.18}$$
$$\kappa_1 > \tau_1^{\max}(\overline{1011}) = 0.\overline{11010010} = 14/17. \tag{4.19}$$

All these orbits of length 1, 2, 3 and 4 are drawn in figure 4.4. Here we see which of the two maps the points in the orbit lies on.

The curves for these bifurcations in the topological parameter plane is drawn in figure 4.5. This figure gives the description of a parameter space assuming that only the bimodal approximation is important and that the map has two maximum points.

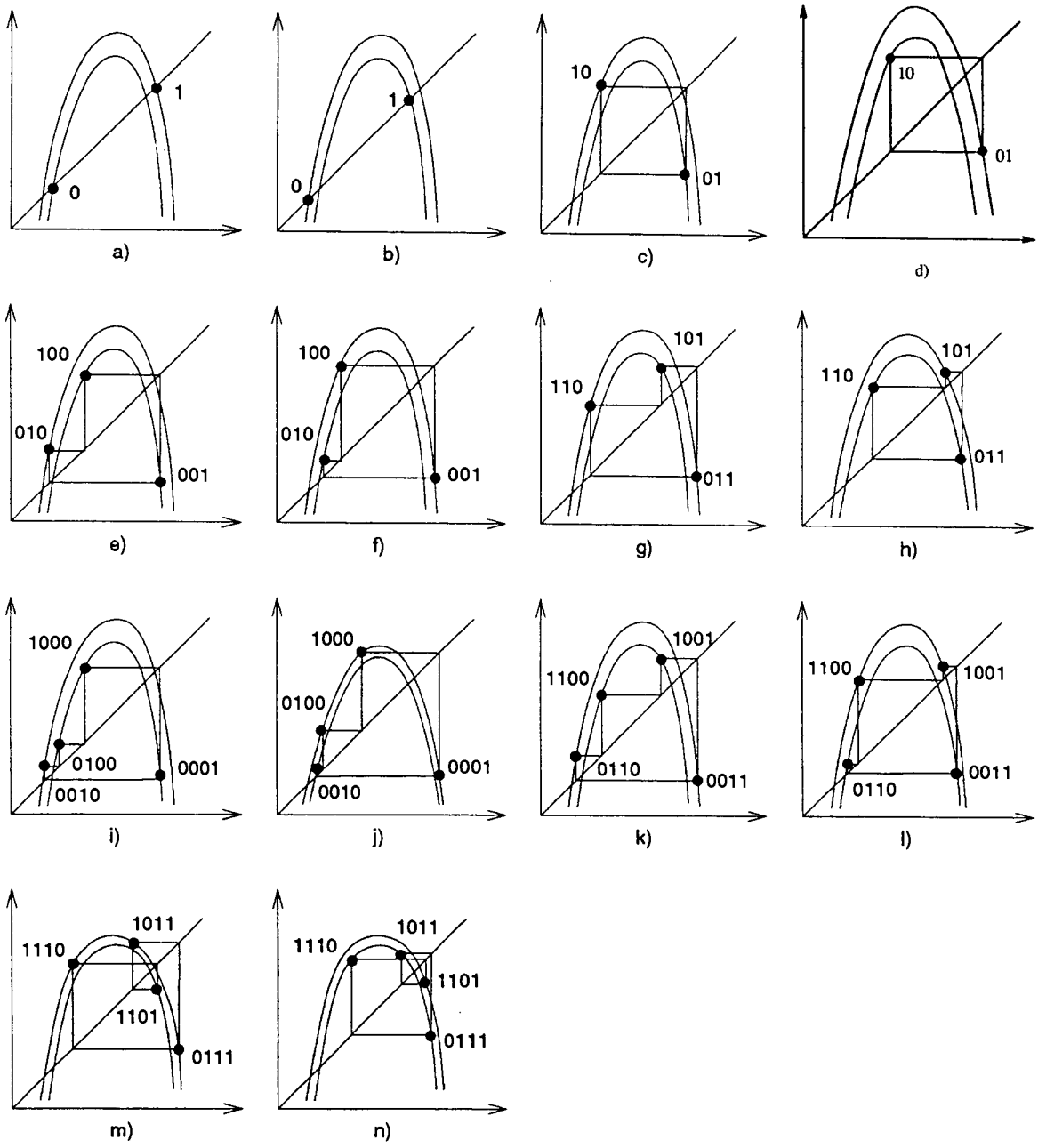

Figure 4.4: The the periodic orbits of length 1, 2, 3 and 4 in the bimodal approximation for the once-folding map. a), c), e), g), i), k) and m) shows once-folding maps with reflection ($b > 0$), the others without reflection ($b < 0$).

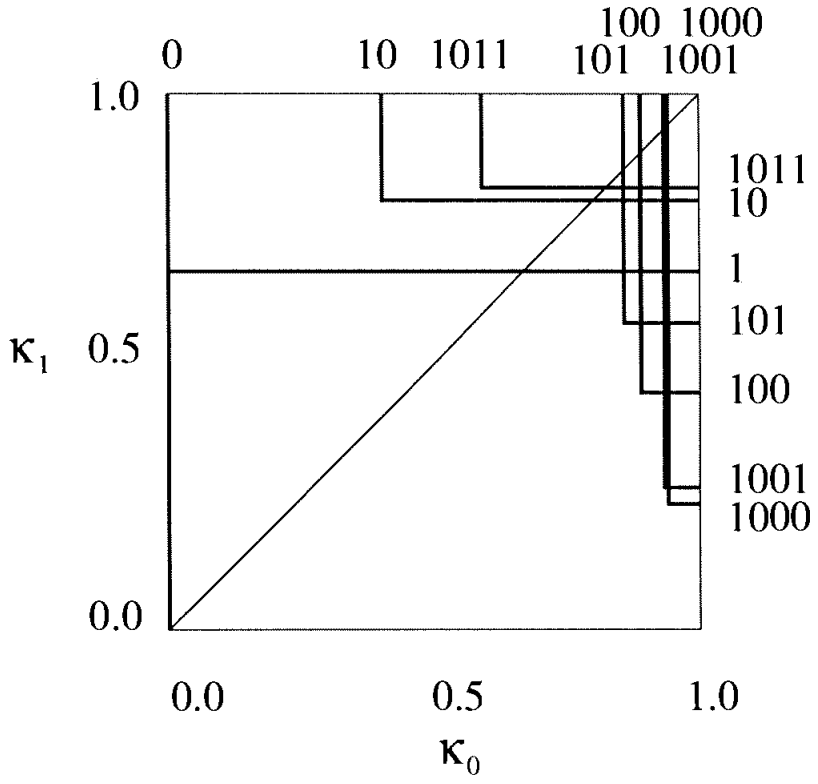

Figure 4.5: The bifurcations of the periodic orbits of length 1, 2, 3 and 4 in the topological parameter space of the bimodal approximation for the once-folding map.

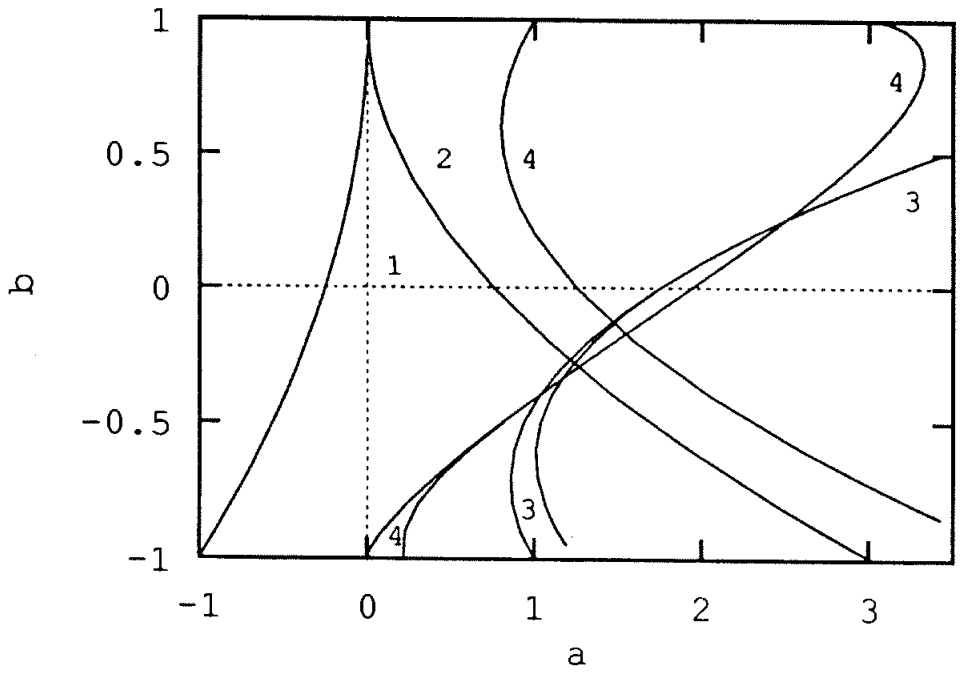

Figure 4.6: The bifurcation curves of the stable periodic orbits with period 1, 2, 3 and 4 in the parameter space of the Hénon map.

This figure can be compared with a two parameter scan of different once-folding maps. The relation between the topological parameter space (κ_0, κ_1) and a real parameter space (a, b) is as for the 1-dimensional maps: The structure of bifurcation curves is the same for the two spaces, but metric properties like smoothness and scaling are different. Figure 4.6 shows the areas in the (a, b) plane for the Hénon map where the periodic orbits of period 1, 2, 3 and 4 are stable. When comparing the drawings we should remember that the diagonal $\kappa_0 = \kappa_1$ corresponds to $b = 0$ in the Hénon map, a positive parameter value b to the triangle $\kappa_0 < \kappa_1$ which is the horseshoe with reflection, and a negative parameter value b corresponds the triangle $\kappa_0 > \kappa_1$ which is the horseshoe map without a reflection. The corner $\kappa_0 = \kappa_1 = 1.0$ in the topological parameter plane corresponds to the complete Smale horseshoe which is realized by the Hénon map for $b = 0$ with $a \geq 2$ and and for $b \neq 0$ with a sufficiently large [153].

The structure in the two figures is similar. For $b < 0$ figure 4.6 shows that the bifurcation curves for the period 3 orbits crosses the period 2 orbit bifurcation curves. The bifurcation curves for the period 4 orbits $\overline{1000}$ and $\overline{1001}$ crosses both the bifurcation lines for the period 2 and the period 3 orbits. For $b > 0$ the bifurcation curves are similar but for the Hénon map the period 4 orbits $\overline{1000}$ and $\overline{1001}$ crosses

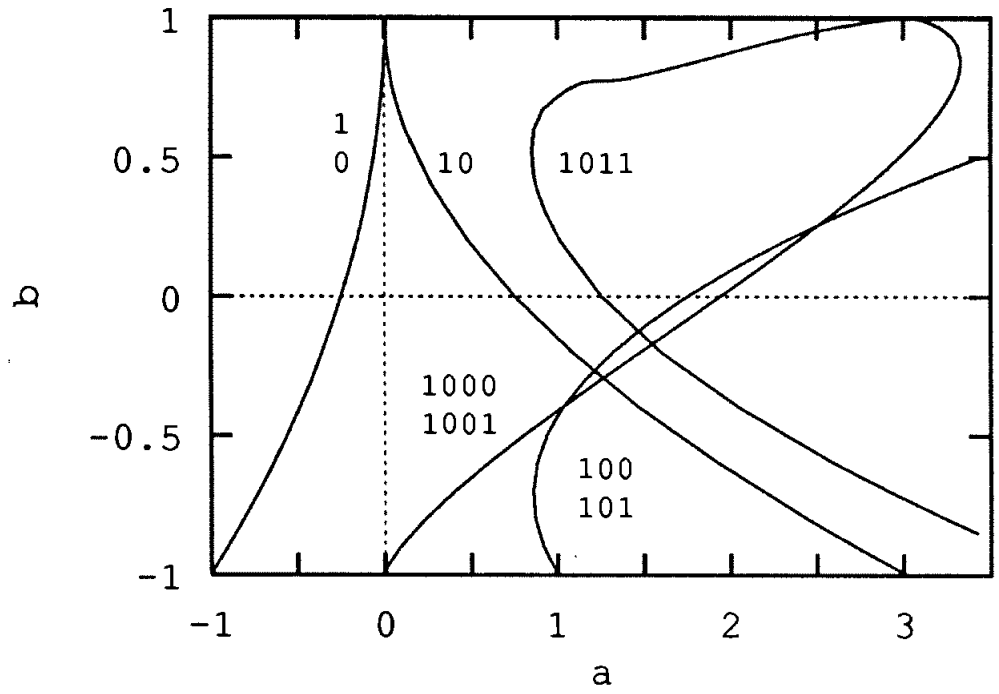

Figure 4.7: The bifurcation curves of the periodic orbits with period 1, 2, 3 and 4 in the parameter space of the Hénon map calculated by using the complex Biham-Wenzel method.

the period 3 curves for a larger value of a. This is not the case in figure 4.5. We show later that there is another bifurcation of the period 4 orbit that will be explained in the next order of approximation.

This is actually better than one could expect, because in drawing figure 4.5 we ignored the possibility that a maximum point of the 1-dimensional approximation could disappear in a bifurcation together with the minimum point. This bifurcation of critical points actually makes it impossible that the period 2 orbit $\overline{10}$ and the period 4 orbit $\overline{1011}$ bifurcate by decreasing κ_0 and that the orbits $\overline{100}$, $\overline{101}$, $\overline{1000}$ and $\overline{1001}$ bifurcate by decreasing κ_1.

The bifurcation of the critical points has taken place if the iteration of the maximum point gives a point larger than the minimum point. A periodic orbit can therefore not be pruned on map 0 (1) if the kneading value $\tau_0^{\max}$ ($\tau_1^{\max}$) is smaller than the kneading value of the once shifted symbol sequence. The value of the shifted sequence $\sigma(S)$ is larger than the value of the original sequence S if the value $\tau(S)$ is $\tau(\overline{0}) < \tau(S) < \tau(\overline{1})$:

$$0 < \tau_i^{\max}(S) <= 0.\overline{10} = 2/3 \tag{4.20}$$

From the kneading values of the period 2 orbit in eq. (4.8) and (4.9) we find that the orbit $\overline{10}$ only can be pruned by κ_1.

The period 3 orbits have kneading values given by eq. (4.10) – (4.13) and can only be pruned by κ_0 and not by κ_1.

The period 4 orbits $\overline{1000}$ and $\overline{1001}$ can as for the period 3 orbits only be pruned by κ_0, while the orbit $\overline{1011}$ is pruned by κ_1 but not by κ_0 as the orbit $\overline{10}$.

The exact description of the change from two to one maximum point in the 1-dimensional approximation is more complicated than the argument above. The following problem is a result of our approximation and is not present in the real horseshoe map: The two fold approximation have one minimum point which is the image of the maximum point of the one fold approximation. The problem in this statement is that we mix two different orders of approximation when we describe the minimum point. The symbolic description of the minimum point of the two fold approximation is then obtained by a shift operation on the maximum point of the one fold approximation. What we have used as the rule in eq. (4.20) is to use the shifted lower maximum point in the two fold approximation as the minimum point. This is a restrictive chose such that the topological description may forbid structures that exists in the horseshoe. This may explain qualitatively that the Hénon bifurcation plane in figure 4.6 shows similar structures as the topological parameter plane in figure 4.5 also for $\kappa_0 < 2/3$ and $\kappa_1 < 2/3$.

By using the method of Biham and Wenzel we can also find bifurcation lines for the orbits given their symbolic description. This diagram is given in figure 4.7. By comparing figure 4.7 and figure 4.6 we find that they are almost identical except that the bifurcation curve for $\overline{1011}$ in figure 4.7 close to $b = 1$ change direction and hit the bifurcation curves for $\overline{1000}$ and $\overline{1001}$ at $a = 3$, $b = 1$.

The bifurcations in the once-folding tent map (the Lozi map) (4.3) is drawn in figure 4.8. The bifurcation lines are a bit different than for the Hénon map, but the overall structure is as the topological parameter plane predicts. In the same way as the bifurcation curves for the Hénon map calculated by the Biham-Wenzel method, the period 4 orbits $\overline{1000}$ and $\overline{1001}$ for large positive b values get above the bifurcation lines of the period 3 orbits $\overline{100}$ and $\overline{101}$ and collide with the period 4 orbit $\overline{1011}$ line at $b = 1$. This we show later is a result of a trimodal bifurcation and is explained at the next level of approximation. A typical bifurcation in the Lozi map is that all period doublings take place at one parameter value as for the 1-dimensional tent map. One exception we find here is that for $b > 0$ the bifurcation lines for the orbits $\overline{10}$ and $\overline{1011}$ split, and therefore the period 2 orbit is stable in a triangle in the parameter plane in figure 4.8.

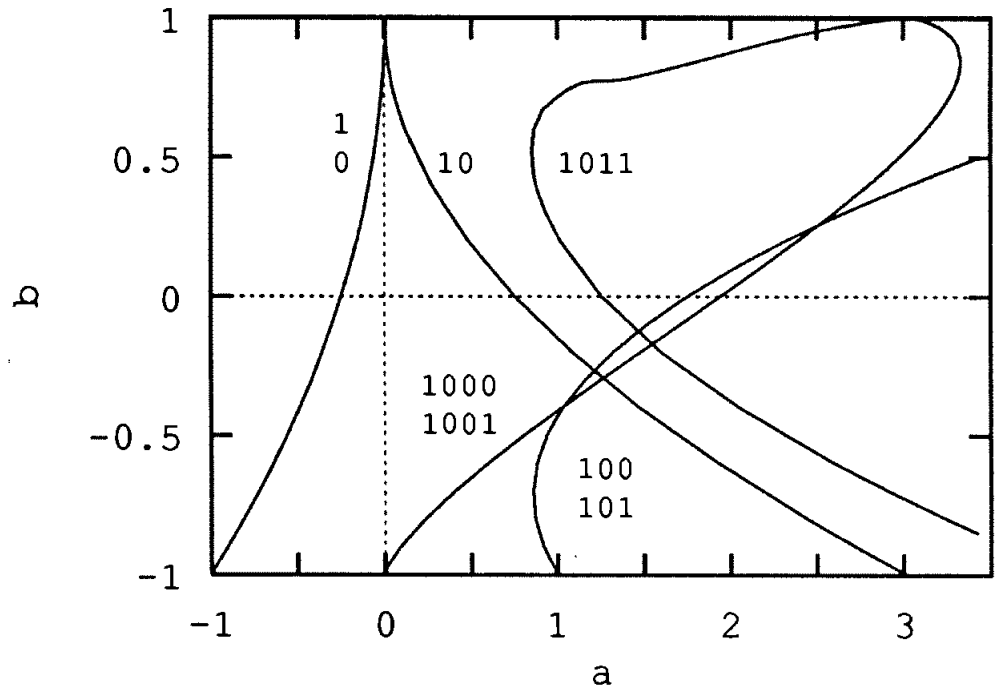

Figure 4.8: The bifurcations of the periodic orbits 1, 2, 3 and 4 in the parameter space of the Lozi map.

4.3.2 Period 5 orbits

The period 5 orbit gives the simplest example of the swallowtail cross in the bimodal approximation of the once-folding map. The six different period 5 orbits exist for the following topological parameter values:

$$\kappa_0 > \tau_0^{\max}(\overline{10000}) = 0.\overline{1111100000} \quad (4.21)$$
$$\kappa_1 > \tau_1^{\max}(\overline{10000}) = 0.\overline{0001111100} \quad (4.22)$$
$$\kappa_0 > \tau_0^{\max}(\overline{10001}) = 0.\overline{11110} \quad (4.23)$$
$$\kappa_1 > \tau_1^{\max}(\overline{10001}) = 0.\overline{00100} \quad (4.24)$$
$$\kappa_0 > \tau_0^{\max}(\overline{10011}) = 0.\overline{1011101000} \quad (4.25)$$
$$\kappa_1 > \tau_1^{\max}(\overline{10011}) = 0.\overline{1110100010} \quad (4.26)$$
$$\kappa_0 > \tau_0^{\max}(\overline{10010}) = 0.\overline{11000} \quad (4.27)$$
$$\kappa_1 > \tau_1^{\max}(\overline{10010}) = 0.\overline{11100} \quad (4.28)$$
$$\kappa_0 > \tau_0^{\max}(\overline{10110}) = 0.\overline{1100100110} \quad (4.29)$$
$$\kappa_1 > \tau_1^{\max}(\overline{10110}) = 0.\overline{1101100100} \quad (4.30)$$
$$\kappa_0 > \tau_0^{\max}(\overline{10111}) = 0.\overline{10110} \quad (4.31)$$
$$\kappa_1 > \tau_1^{\max}(\overline{10111}) = 0.\overline{11010}. \quad (4.32)$$

The bifurcation diagram is drawn in figures 4.9 and 4.10.

The first two orbits can not be pruned by κ_1 from the inequalities (4.22) and (4.24) because the critical point on map 1 disappear before one obtain the pruning value in the bimodal approximation. As for the period 3 orbits, a shift of the symbols gives a larger symbolic value.

The other four period 5 orbits can be pruned by both κ_0 and κ_1.

By choosing $\epsilon_i \in \{0, 1\}$ for $i = 1$ and $i = 2$ the string $\overline{10\epsilon_1 1\epsilon_2}$ gives the symbolic description of these four orbits which will have a bifurcation in a swallowtail cross. This is a bifurcation we know from the simple bimodal maps in section 2.1. Figure 4.10 shows the cross in the symbol plane where the gray area is the symbolic values that can not be obtained from kneading sequences of the critical points. This topological swallowtail cross can be compared with our numerical examples of the pruned horseshoe.

Figures 4.11 and 4.12 show the bifurcation lines of the Hénon map and the Lozi map. The area with stable period 5 orbits in figure 4.11 a) is the typical swallowtail with the same geometrical structure as in figures 2.4, 2.6 and 2.8. We expect the scaling of the period doubling of the crosses to be the same as for a bimodal one-dimensional map. MacKay and van Zeijts [142] showed that the swallowtail crossing

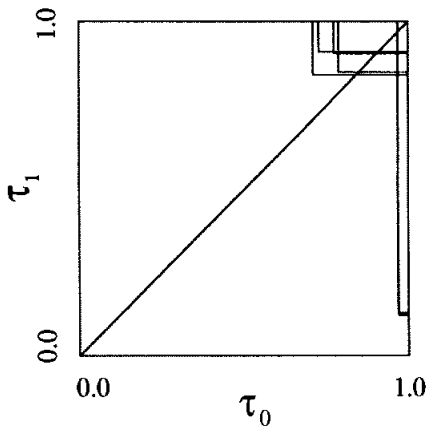

Figure 4.9: The bifurcation lines of all period 5 orbits in the symbol plane (κ_0, κ_1).

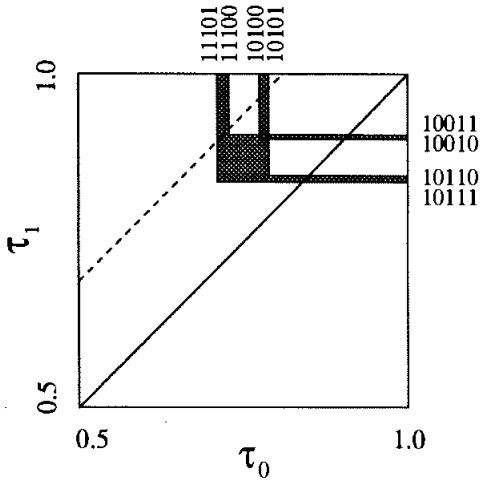

Figure 4.10: The bifurcation lines of the period 5 orbits giving a binary swallow tail in the symbol plane (κ_0, κ_1).

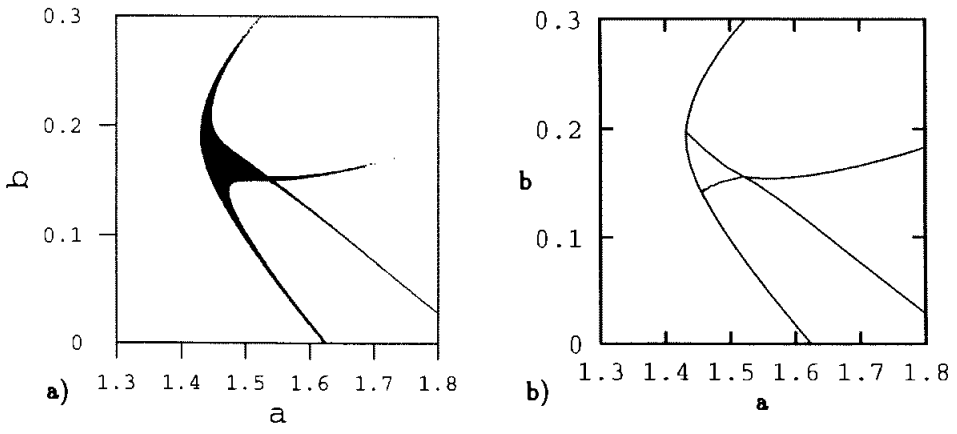

Figure 4.11: The swallowtail of period 5 orbits in the parameter plane (a, b) for the Hénon map. a) Areas with stable period 5 orbit. b) Bifurcation lines calculated with the complex Biham-Wenzel method.

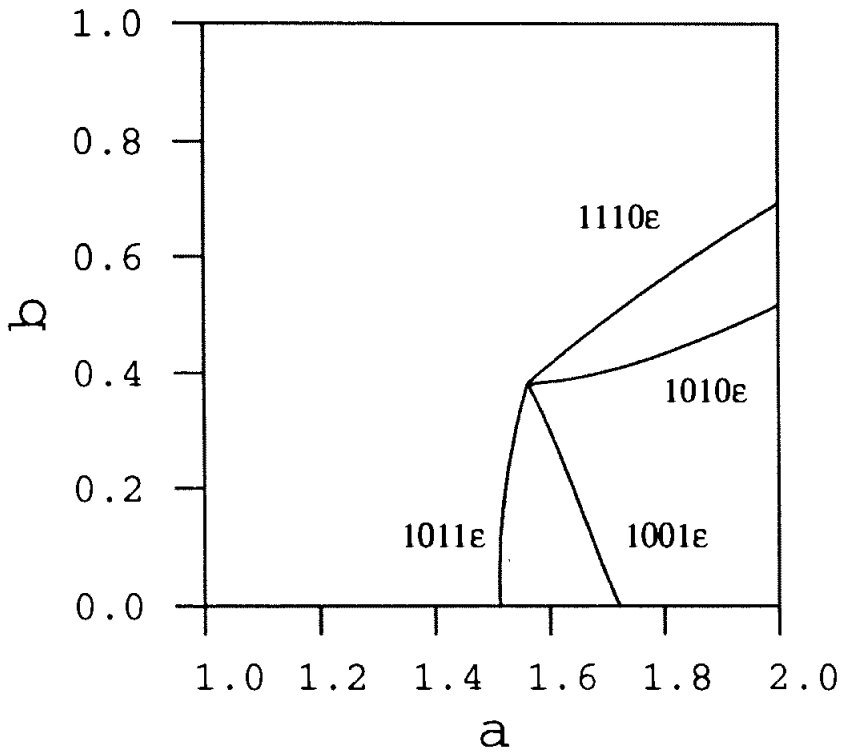

Figure 4.12: The swallowtail of period 5 orbits in the parameter plane (a, b) for the Lozi map.

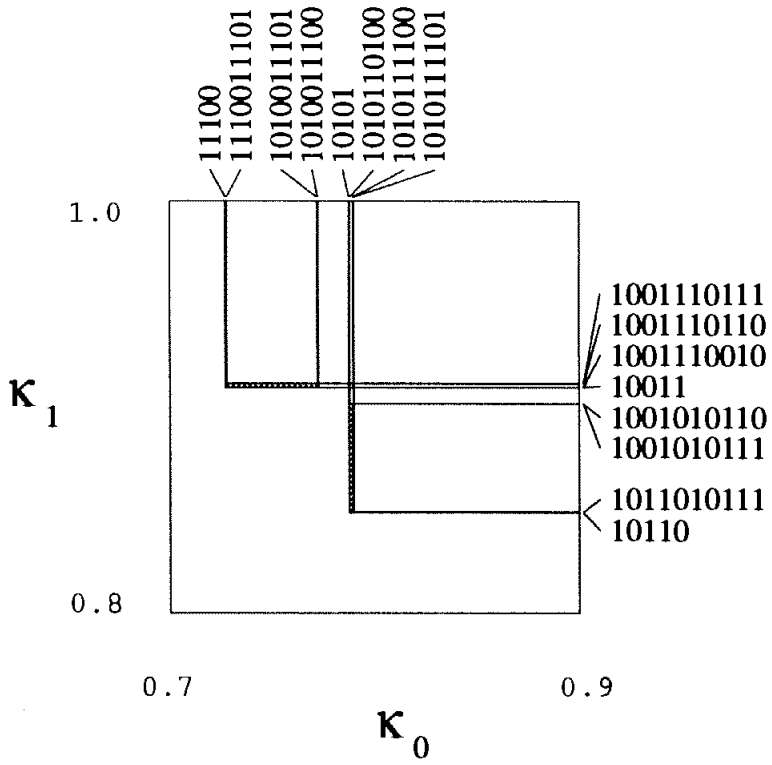

Figure 4.13: The bifurcation lines of period 10 orbits bifurcating from the period 5 swallowtail in the symbol plane (κ_0, κ_1).

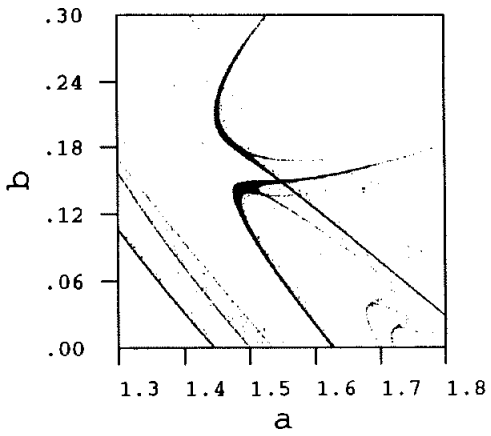

Figure 4.14: The period 10 orbits from the period doubling bifurcation of the period 5 orbits in the parameter plane (a, b) for the Hénon map.

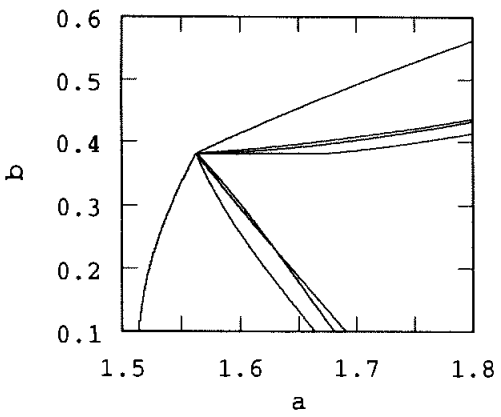

Figure 4.15: The period 10 orbits from the period doubling bifurcation of the period 5 orbits in the parameter plane (a, b) for the Lozi map.

scales with a spectrum of exponents, where the exponent changes with the path one follows in the renormalization of the parameter plane. Figure 4.14 shows the period 10 swallowtails from the period doubling of the period 5 swallowtail of the Hénon map.

The period 10 swallowtails are drawn in the symbolic parameter plane in figure 4.13. This is, using MSS terminology [147], the harmonics of the period 5 swallowtail orbits. The symbolic description is obtained by repeating twice the given cyclic permutation of the 5 symbols and change the last symbol. The scaling of crossings is different in this plane from the normal parameter plane.

Figure 4.11 b) shows the period 5 swallowtail crossing obtained by using the complex Biham Wenzel method. This method gives the tails and the crossing of the swallowtail. In the tails the method converges for both the stable and the unstable orbit up to practically the same bifurcation value. Inside the crossing however does the BW method not converge to the stable orbit. This is the region where a stable orbit in a one-dimensional map changes symbolic description in a rather complicated way sketched in figure 2.11 for the bimodal map. The BW method does not converge in this region while it converges without problems to the stable orbit in the tails where the symbols for an orbit in the one-dimensional map is more simple. The BW method finds here all the unstable orbits that exist.

The period 5 swallowtail crossing for the Lozi map in figure 4.12 is a crossing of bifurcation lines instead of a window structure in the (a, b) plane. Apart from this, the structure is the same as for the Hénon map. The crossing and all the period

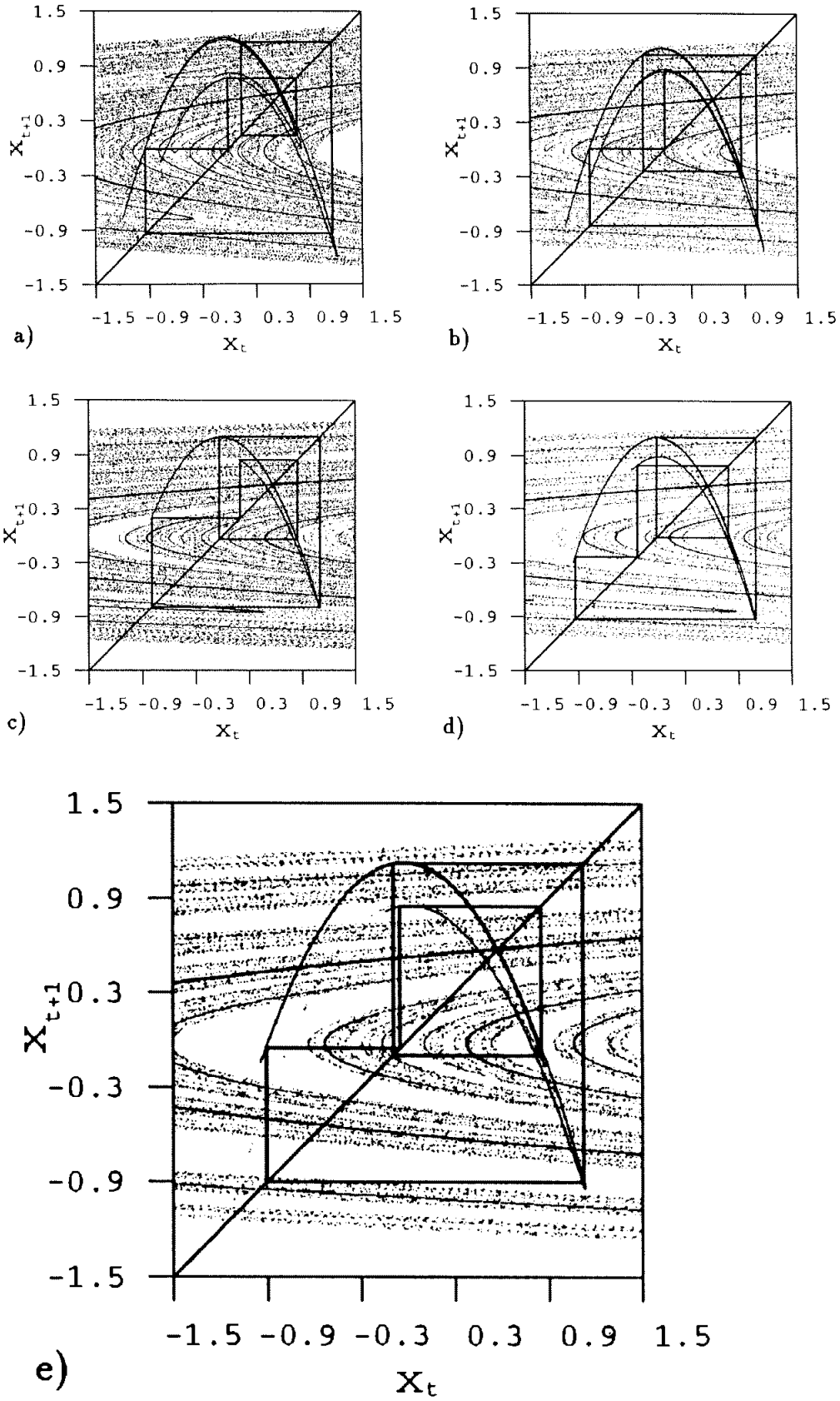

Figure 4.16: The stable period 5 orbit and the stable and unstable manifolds for the Hénon map.
a) $a = 1.465$, $b = 0.25$,

doubled swallow tail crossings of the Lozi map bifurcates at one singular parameter point $a = 1.563\ldots$, $b = 0.380\ldots$, and there is no scaling. Figure 4.15 shows the period 10 orbits from the period doubling of the crossing.

For values of b less than the parameter of the period 5 swallow tail crossing the bifurcation takes place close to the critical point of the fold $f_1(x)$. For larger values of b the critical point on the fold $f_0(x)$ is responsible for the bifurcations. This is the description in the one dimensional bimodal approximation and that the description is valid in the Hénon map is illustrated in the figures 4.16 a), b), c), d) and e). These figures show the stable period 5 orbit, the unstable manifold and parts of the stable manifold at parameter values in the different tails and in the middle of the crossing. The figures 4.16 c) and d) are below the cross and have one point in the stable orbit close to a turning point on the outer fold. In figure a) and b) the orbits have a point close to a turning point on the inner fold of the unstable manifold. When identifying the outer folds with $f_1(x)$ and the inner folds with $f_0(x)$ this is consistent with the one-dimensional approximation. In figure 4.16 e) the orbit is close to both the two turning points.

To further illustrate that the bifurcation is well described by a bimodal one dimensional map, we can plot the unstable manifold in the space (x_t, x_{t+5}). This way to investigate the orbits are discussed in section 4.3.8.

4.3.3 Period 6 orbits

The bifurcation diagram of the period 6 orbits is similar to the period 5 orbit bifurcation diagram but has 3 more orbits. One period 6 orbit is $\overline{100101}$ which is the period doubling of the period 3 orbit. Two orbits; $\overline{101111}$ and $\overline{101110}$ are stable windows in the two chaotic bands. The other 6 orbits have a structure very similar to the period 5 orbits. The two orbits $\overline{100000}$ and $\overline{100001}$ give bifurcations similar to the orbits $\overline{10^k\epsilon}$, $k < 4$. The four orbits $\overline{100\epsilon_1 1\epsilon_2}$ give a swallowtail structure similar to the period 5 swallowtail $\overline{10\epsilon_1 1\epsilon_2}$ and this swallowtail in the symbol plane is drawn in figure 4.17.

4.3.4 Longer periodic orbits

We can also plot the bifurcation plane for longer periodic orbits. To make the pictures readable only the orbits giving swallowtails are drawn. Figure 4.18 give the period 7 swallowtails; $\overline{1000\epsilon_1 1\epsilon_2}$ and $\overline{10\epsilon_1 111\epsilon_2}$. Figure 4.19 shows the period 8 swallowtails; $\overline{10000\epsilon_1 1\epsilon_2}$, $\overline{100\epsilon_1 101\epsilon_2}$, $\overline{100\epsilon_1 111\epsilon_2}$, $\overline{10\epsilon_1 1011\epsilon_2}$ and $\overline{1001\epsilon_1 10\epsilon_2}$, where the last swallowtail is below the diagonal and exists for maps with positive

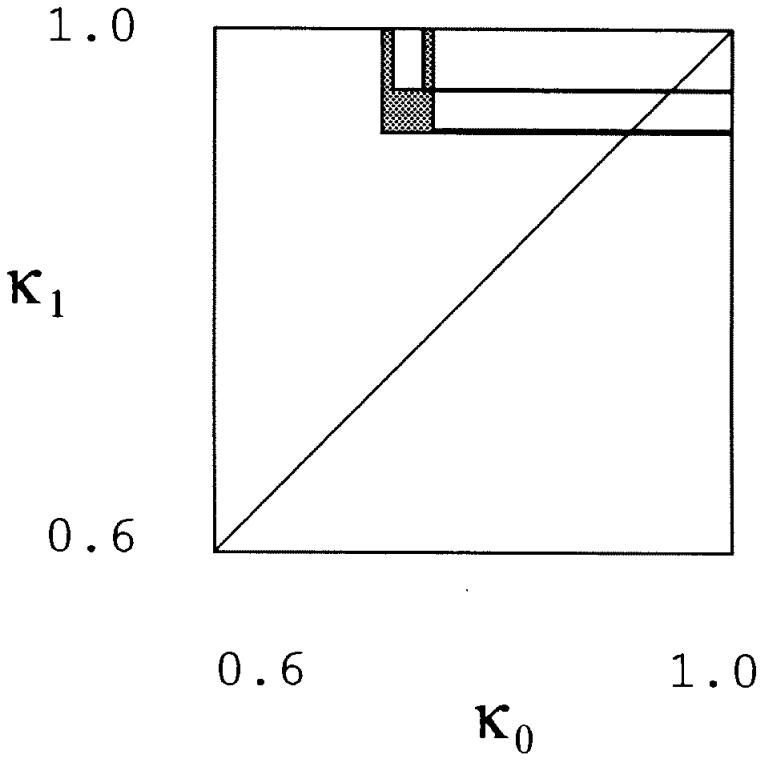

Figure 4.17: The bifurcation lines of the period 6 orbits giving a binary swallow tail in the symbol plane (κ_0, κ_1).

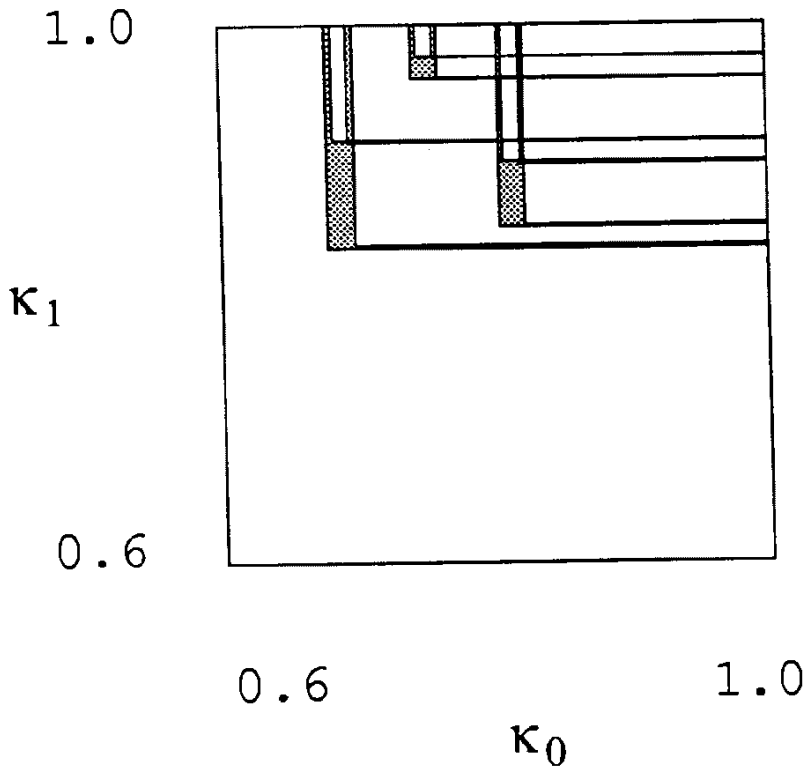

Figure 4.18: The bifurcation lines of the period 7 orbits giving binary swallow tails in the symbol plane (κ_0, κ_1).

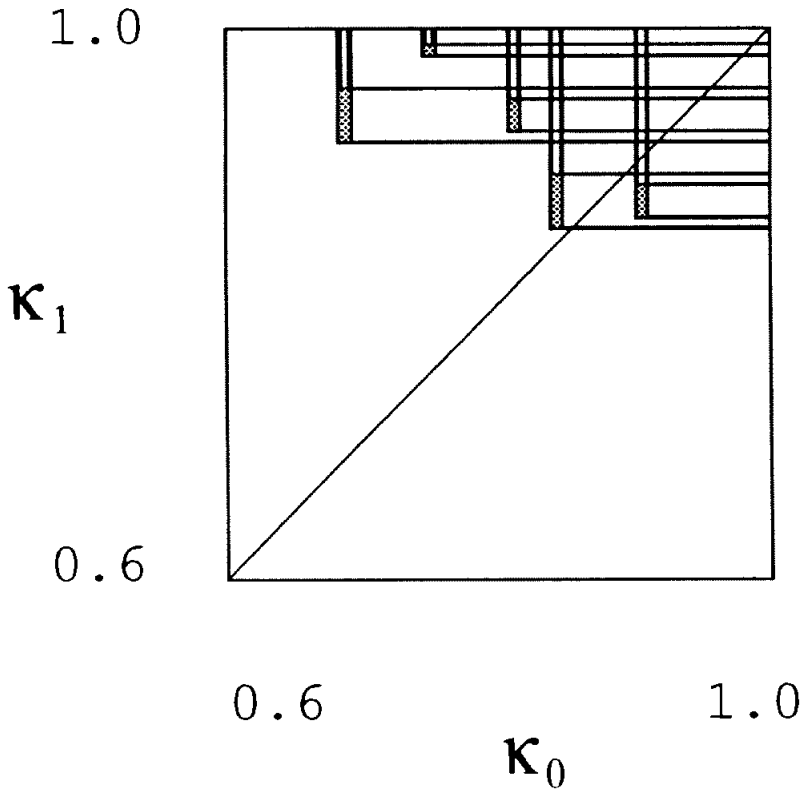

Figure 4.19: The bifurcation lines of the period 8 orbits giving binary swallow tails in the symbol plane (κ_0, κ_1).

$|\mathbb{J}|$ ($b < 0$ for the Hénon and Lozi maps). Figure 4.20 shows the period 9 swallowtails; $\overline{100000\epsilon_1 1\epsilon_2}$, $\overline{1000\epsilon_1 101\epsilon_2}$, $\overline{100\epsilon_1 1001\epsilon_2}$, $\overline{100\epsilon_1 1011\epsilon_2}$, $\overline{10\epsilon_1 11101\epsilon_2}$, $\overline{10\epsilon_1 10111\epsilon_2}$, $\overline{10\epsilon_1 10101\epsilon_2}$, $\overline{10\epsilon_1 11111\epsilon_2}$, $\overline{10011\epsilon_1 10\epsilon_2}$ and $\overline{10001\epsilon_1 10\epsilon_2}$ where the two last exist for positive $|\mathbb{J}|$.

4.3.5 Generic bimodal swallowtails

The most characteristic structure in the bifurcation diagrams in figure 4.9, 4.17, 4.18, 4.19 and 4.20 is the swallowtail crosses. A cross in the bimodal approximation always has two tails crossing the diagonal $\kappa_0 = \kappa_1$ which corresponds to $b = 0$ in the Hénon map. Two windows in the logistic map are then connected at some point for $b \neq 0$ and we can give the generic symbolic description of which two windows in a unimodal map that are connected in the bimodal approximation.

From the one dimensional theory we know that a window in the logistic map has a stable period n orbit with symbolic description $\overline{S} = \overline{s_1 s_2 \cdots s_n}$ where this string is the cyclic permutation giving the largest symbolic value $\tau_i^{\max}(\overline{S}) = \tau(\overline{s_1 s_2 \cdots s_n})$.

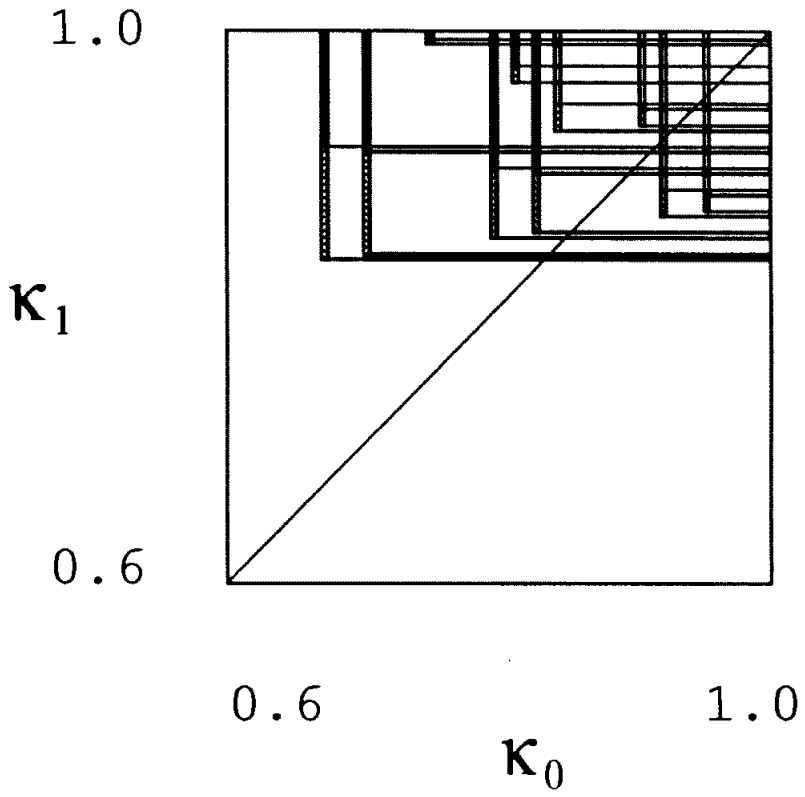

Figure 4.20: The bifurcation lines of the period 9 orbits giving binary swallow tails in the symbol plane (κ_0, κ_1).

The value of s_n changes when the orbit goes through the super-stable point. From the creation of the orbit until the super-stable point, the value of s_n is such that the number of symbol 1's in the string is even. Above the super-stable point s_n changes such that the number of 1's in the string is odd. This because the slope is $+1$ when an orbit is created and -1 when it becomes unstable. At the parameter value where the orbit is created either an orbit of length $n/2$ becomes unstable in a period doubling or an unstable period n orbit is created in a tangent bifurcation. This unstable orbit has the same symbolic description as the stable orbit before the super-stable orbit, that is an even number or 1's. These two orbits can then be described by the string $\overline{s_1 s_2 \cdots s_{n-1}\epsilon_1}$ with $\epsilon_1 \in \{0,1\}$.

The following result states which windows in the unimodal map are connected by a swallowtail cross in the bimodal approximation.

Proposition 1 *Let* $\overline{S} = \overline{s_1 s_2 \cdots s_{n-1}\epsilon}$ *and* $\overline{S'} = \overline{s'_1 s'_2 \cdots s'_{n-1}\epsilon}$, $\epsilon \in \{0,1\}$ *be the symbolic description of the orbits in two windows of the unimodal map. These two windows are the tails from the same bimodal swallowtail cross in a once-folding map if and only if*

$$\begin{aligned}
&s_j = s'_j \quad for \quad j \in \{1,2,\ldots,k-1,k+1,\ldots,n-1\}\\
&s_k = 1 - s'_k\\
&s_{k-1} = 1 - s_{n-1}\\
&\tau^{\max}_{s_{n-1}}(\overline{S}) = \tau(\overline{s_1 s_2 \cdots s_{n-1}\epsilon})\\
&\tau^{\max}_{s_{n-1}}(\overline{S'}) = \tau(\overline{s'_1 s'_2 \cdots s'_{n-1}\epsilon})\\
&\tau^{\max}_{1-s_{n-1}}(\overline{S}) = \tau(\overline{s_{k+1} s_{k+2} \ldots s_{n-1}\epsilon s_1 s_2 \cdots s_k})\\
&\tau^{\max}_{1-s_{n-1}}(\overline{S'}) = \tau(\overline{s'_{k+1} s'_{k+2} \ldots s'_{n-1}\epsilon s'_1 s'_2 \cdots s'_k})
\end{aligned} \tag{4.33}$$

A slightly different way to state this is

Proposition 2 *A bimodal swallowtail of the once-folding map has the symbolic description*

$$\overline{S} = \overline{s_1 s_2 \cdots s_m 0 \epsilon_1 s_{m+3} s_{m+4} \ldots s_{n-2} 1 \epsilon_2} \tag{4.34}$$

with

$$\begin{aligned}
&\tau^{\max}_1(\overline{S}) = \tau(\overline{s_1 s_2 \cdots s_m 0 \epsilon_1 s_{m+3} s_{m+4} \ldots s_{n-2} 1 \epsilon_2})\\
&\tau^{\max}_0(\overline{S}) = \tau(\overline{s_{m+3} s_{m+4} \ldots s_{n-2} 1 \epsilon_2 s_1 s_2 \cdots s_m 0 \epsilon_1})
\end{aligned} \tag{4.35}$$

The crossing is in the map with reflection ($b > 0$ for Hénon) if $\tau^{\max}(\overline{S}) = \tau^{\max}_1(\overline{S})$ *and the crossing is in the map without reflection ($b < 0$ for Hénon) if* $\tau^{\max}(\overline{S}) = \tau^{\max}_0(\overline{S})$

As a short notation we write $\overline{A 0 \epsilon_1 B 1 \epsilon_2} = \overline{s_1 s_2 \cdots s_m 0 \epsilon_1 s_{m+3} s_{m+4} \ldots s_{n-2} 1 \epsilon_2}$

4.3.6 Symbols of period doublings of swallowtails

Each period n swallowtail crossing $\overline{A0\epsilon_0 B1\epsilon_1}$ has a period doubling structure. The two stable orbits have a period doubling and become the outer bounds of two new swallowtail crossings with period $2n$ orbits. In figure 4.13 the two period 10 swallowtail crossings and the stable period 5 orbits bifurcation lines are drawn in the symbol plane. The period n swallowtail bifurcates into 2^k swallowtails of length $2^k n$ giving a family of swallowtails.

The symbolic description of an orbit in the unimodal period doubling bifurcation is obtained by repeating the shorter symbol sequence twice and change the last symbol (a harmonics). This symbol corresponds to the point close to the critical point.

For the swallowtail crossings we take the symbolic string of the stable orbit and write this string twice

$$\overline{A0\epsilon_0 B1\epsilon_1 A0\epsilon_0' B1\epsilon_1'} \tag{4.36}$$

with $\epsilon_0' = \epsilon_0$ and $\epsilon_1' = \epsilon_1$. We now have two points close to critical points. By changing ϵ_1' from ϵ_1 to $(1-\epsilon_1)$ we make a point in an orbit crossing the critical point on map 1; x_c^1. This gives the symbolic description of one new stable orbit. When we change ϵ_0' from ϵ_0 to $(1-\epsilon_0)$ this corresponds to moving a point in an orbit across the point x_c^0 and we get the symbolic description of the other stable orbit. Changing both ϵ_1' and ϵ_0' gives the unstable orbit in the middle of the swallow tail.

With the two choices of ϵ_1 and ϵ_0 that give the two stable period n orbits, this is the symbolic description of the 6 new orbits in the two period $2n$ swallowtail crosses.

4.3.7 Bimodal MSS ordering

The ordering of orbits along the parameter of the unimodal map follows the Metropolis-Stein-Stein (MSS) ordering. In ref. [147] MSS gave a table (table I) with the ordering of the periodic orbits of length 7 and shorter. We can now rewrite this table and include the ordering of both folds in our bimodal approximation of the once-folding map. In table 4.1 we give this table and we use here both the MSS notation and the notation we use.

MSS uses the symbols R and L for a point to the right or left of the critical point. This is identical to 1 and 0 in our notation, but they only write the first $n-1$ symbols for a period n orbit given in the column P_i in table 4.1. They discuss unimodal maps and the last symbol only distinguishes between the stable and the unstable

i	k_i	P_i	S_i	$\tau_{1,i}^{\max}$	S_i	$\tau_{0,i}^{\max}$
$21'$			$\overline{0000010}$	$.\overline{00000111111100}$		
$20'$			$\overline{000010}$	$.\overline{000011111100}$		
$18'$			$\overline{00010}$	$.\overline{0001111100}$		
$14'$			$\overline{0010}$	$.\overline{00111100}$		
$1'$					$\overline{01}$	$.\overline{0110}$
$7'$			$\overline{010}$	$.\overline{011100}$		
$13'$			$\overline{0100110}$	$.\overline{01110111000100}$		
$15'$			$\overline{1100010}$	$.\overline{10000110111100}$		
$8'$			$\overline{110010}$	$.\overline{100011011100}$		
$2'$					$\overline{1101}$	$.\overline{10010110}$
$12'$					$\overline{110100}$	$.\overline{100111011000}$
$3'$					$\overline{111101}$	$.\overline{101001010110}$
$11'$					$\overline{1111100}$	$.\overline{10101110101000}$
$4'$					$\overline{1110101}$	$.\overline{10110010100110}$
$10'$					$\overline{11100}$	$.\overline{1011101000}$
$16'$					$\overline{111000}$	$.\overline{101111010000}$
$19'$					$\overline{1110000}$	$.\overline{10111110100000}$
$17'$					$\overline{1010001}$	$.\overline{11000010011110}$
$5'$					$\overline{10101}$	$.\overline{1100100110}$
1	2	R	$\overline{10}$	$.\overline{1100}$		
$9'$					$\overline{1010100}$	$.\overline{11001110011000}$
$6'$					$\overline{1011101}$	$.\overline{11010010010110}$
2	4	RLR	$\overline{1011}$	$.\overline{11010010}$		
3	6	RLR^3	$\overline{101111}$	$.\overline{110101001010}$		
4	7	RLR^4	$\overline{1011110}$	$.\overline{11010110010100}$		
5	5	RLR^2	$\overline{10110}$	$.\overline{1101100100}$		
6	7	RLR^2LR	$\overline{1011011}$	$.\overline{11011010010010}$		
7	3	RL			$\overline{100}$	$.\overline{111000}$
8	6	RL^2RL			$\overline{100101}$	$.\overline{111001000110}$
9	7	RL^2RLR	$\overline{1001010}$	$.\overline{11100110001100}$		
10	5	RL^2R	$\overline{10011}$	$.\overline{1110100010}$		
11	7	RL^2R^3	$\overline{1001111}$	$.\overline{11101010001010}$		
12	6	RL^2R^2	$\overline{100110}$	$.\overline{111011000100}$		
13	7	RL^2R^2L			$\overline{1001100}$	$.\overline{11101110001000}$
14	4	RL^2			$\overline{1000}$	$.\overline{11110000}$
15	7	RL^3RL			$\overline{1000101}$	$.\overline{11110010000110}$
16	6	RL^3R	$\overline{100011}$	$.\overline{111101000010}$		
17	7	RL^3R^2	$\overline{1000110}$	$.\overline{11110110000100}$		
18	5	RL^3			$\overline{10000}$	$.\overline{1111100000}$
19	7	RL^4R	$\overline{1000011}$	$.\overline{11111010000010}$		
20	6	RL^4			$\overline{100000}$	$.\overline{111111000000}$
21	7	RL^5			$\overline{1000000}$	$.\overline{11111110000000}$

Table 4.1: The Metropolis-Stein-Stein ordering extended to a two fold description of the once-folding map.

orbit born at the same parameter value. As we also discuss bifurcations where orbits bifurcates together with other partners we have to include all n symbols. In table 4.1 we have chosen to let the last symbol be the symbol 0 or 1 such that the symbol string has an odd number of 1's and this is the description of the orbit that is stable for some parameter values in a smooth map.

A number i is used by MSS to identify the different orbits and we have in table 4.1 introduced a notation i' which is the same orbit as i but with the cyclic rotation giving the bifurcation on the other fold. The length of the orbit is denoted k_i by MSS.

The way the MSS table for the unimodal map is used is that the ordering in the table is the same as the ordering at the parameter axis in a unimodal map. The extended MSS table has two columns with respectivally $\tau_{1,i}^{\max}$ and $\tau_{0,i}^{\max}$ and this give two different orderings. The ordering in column $\tau_{1,i}^{\max}$ gives the ordering of the orbits bifurcating at map 1 when map 0 has $\kappa_0 = 1$. The other column $\tau_{0,i}^{\max}$ gives the ordering of the orbits bifurcating at map 0 when map 1 has $\kappa_1 = 1$. This is a table description of the bifurcations along the two lines $\kappa_0 = 1$ and $\kappa_1 = 1$ in the symbolic parameter plane. A swallowtail bifurcation in the symbolic parameter plane imply that the ordering is different in the two columns in table 4.1. We find that the two orbits in the period 5 swallowtail crossing is $i = 5$ and $i = 10$ which according to $\tau_{1,i}^{\max}$ is ordered with $i = 5$ before $i = 10$ but according to the $\tau_{0,i}^{\max}$ value $i = 10'$ comes before $i = 5'$ and the orbits has to cross each other at some point in the parameter space.

This table may be helpfull for people aquanted with the MSS theory, but the drawings of bifurcation lines in the symbolic parameter space gives more information and we prefer to use this.

4.3.8 The n-th return plot

To study the bifurcation of a period n orbit in a one dimensional map we often plot the n-th iterate of the map f. In the space $(x, f^{(n)})$ the period n orbit is a fixed point and by finding when $f^{(n)}$ crosses the diagonal we find the bifurcations of the map. In a once-folding two dimensional map we can try to apply the same technique, but in this case we do not have one function $f(x_t)$ but a fractal manifold which gives x_{t+1} as a function $f(x_t)$ that also depends on x_{t-1}.

The chaotic attractor for $a = 1.6$, $b = 0.14$ is drawn in the two planes (x_t, x_{t+1}) and (x_t, x_{t+5}) in figure 4.21 a) and b). These parameter values are between the tails of the period 5 swallowtail in figure 4.11 where all the four orbits in the family $\overline{10\epsilon_1 1\epsilon_2}$ exist. We then know that 20 of the points where one of the lines in the

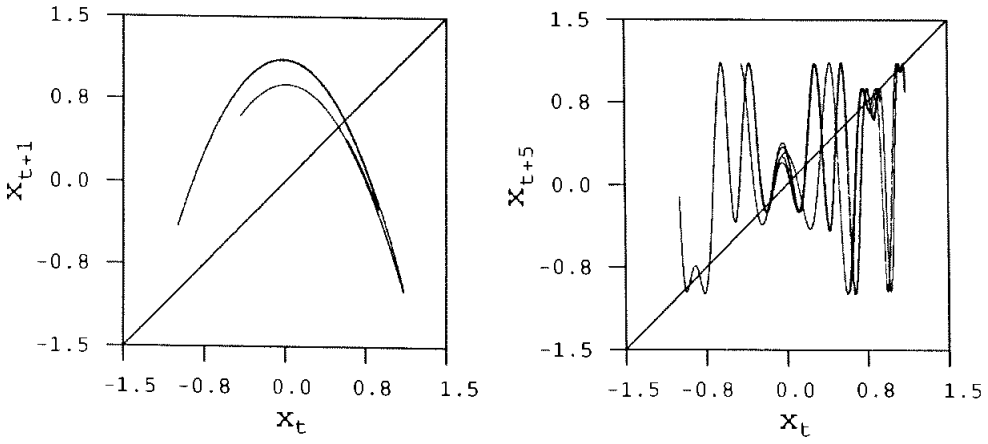

Figure 4.21: The chaotic attractor plotted in (x_t, x_{t+1}) and (x_t, x_{t+5}) with parameters $a = 1.6$ $b = 0.14$.

fractal in figure 4.21 a) crosses the diagonal, are points in period 5 orbits. A period 5 orbit is 5 fixed points in this plot. The 20 fixed points are on different folds and most of the crossings do not correspond to real fixed point. The fixed point are the points where the lines of the fractal crosses the diagonal $x = y = z$ in a three dimensional plot (x_t, x_{t+5}, x_{t+10}) and the picture in (x_t, x_{t+5}) is only a projection of this space. We can not show the exact bifurcations in this two dimensional plot but the picture is useful as a qualitative description of the bifurcation.

Instead of trying to find the exact curves of the chaotic attractor, we draw a small segment of the unstable manifold of the fixed point $\overline{1}$ which gives one single curve in the (x_t, x_{t+5}) plot. This gives an acceptable *qualitative* description of the bifurcation. In figures 4.22 a), b) and c) this curve is drawn together with the fixed points corresponding to period 5 orbits in the Hénon map. We have drawn one of the five points for each orbit with markers of different shapes. The markers for the different orbits are $\circ$ for $\overline{10111}$, $+$ for $\overline{10110}$, $\times$ for $\overline{10010}$ and $\triangle$ for $\overline{10011}$. Figure 4.22 b) has parameter values $a = 1.6$ $b = .14$ which are between the inner tails of the swallowtail crossing in figure 4.11 and all four period 5 orbits exist. Letting b increase or decrease one crosses tails from the swallowtail crossing and two orbits get pruned. Figures 4.22 a) and c) show that the pruning of the two orbits follows from the different possible changes of the $f^{(n)}$ curve. The two minimum points in figure 4.22 have the same height and are controlled by one parameter while the second parameter controls the height of the maximum point.

These figures shows how we can obtain qualitative information of bifurcations by a simple return map and for the Hénon map we find that this information is

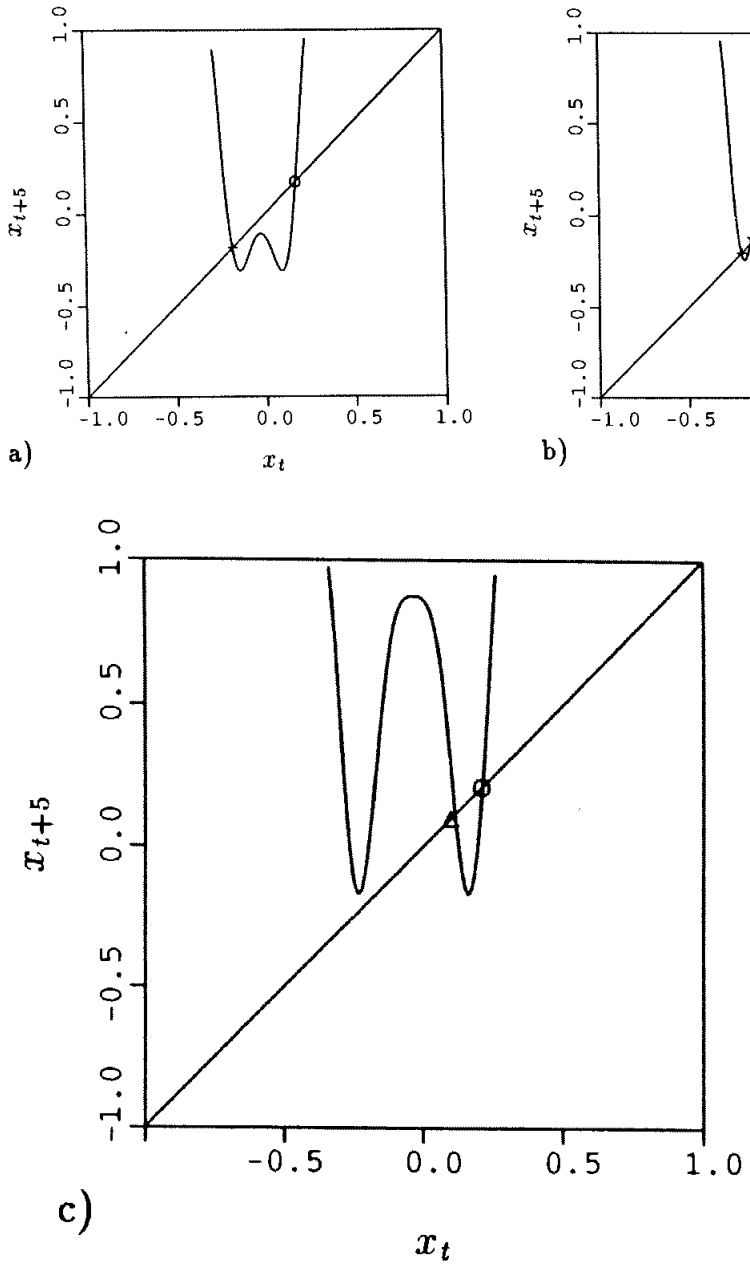

Figure 4.22: The fifth return map of a segment of the unstable manifold and points in the period 5 orbit; $a = 1.6$, a) $b = 0.115$; b) $b = 0.14$ and c) $b = 0.17$.

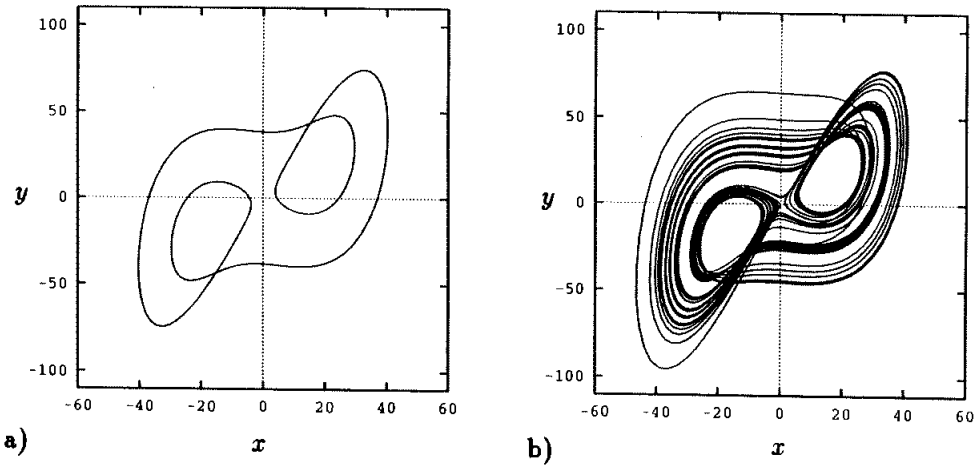

Figure 4.23: The attractor of the Lorenz model projected at the (x, y) plane, $\sigma = 10$, $b = 8/3$, a) $r = 163.5$; b) $r = 135.0$.

consistent with the detailed analysis based on the symbolic dynamics.

4.3.9 The n-th map of the Lorenz model

To illustrate the n-th iterated map on a more complicated system, we have calculated return maps also for the Lorenz system [65, 136, 186]. The Lorenz system is given by the first-order differential equations

$$\begin{aligned} \dot{x} &= -\sigma x + \sigma y \\ \dot{y} &= -xz + rx - y \\ \dot{z} &= xy - bz \end{aligned} \tag{4.37}$$

The bifurcations of this map have often been studied keeping the parameters σ and b fixed to the values $\sigma = 10$ and $b = 8/3$, and changing the parameter r [81, 186]. This gives parameter windows with a stable periodic orbit, and a simple return plot yields qualitative information on what kind of bifurcation structure these windows belongs to in a higher dimensional parameter space.

In the largest window on the r axis is the orbit drawn in figure 4.23 a) stable. The figure is the projection of the orbit to the (x, y) space. When the parameter r increases from this value, $r = 163.5$, the orbit will disappear, while for smaller values of r the orbit becomes unstable. Figure 4.23 b) shows a segment of the chaotic attractor for $r = 135.0$. These plots of the orbit in the (x, y) plane do not give much information of which kind of approximate one dimensional map the orbit locally experiences. To find this we take as a Poincaré map the x_t values where the orbit crosses the x-axis from a positive to a negative value of y. In this Poincaré

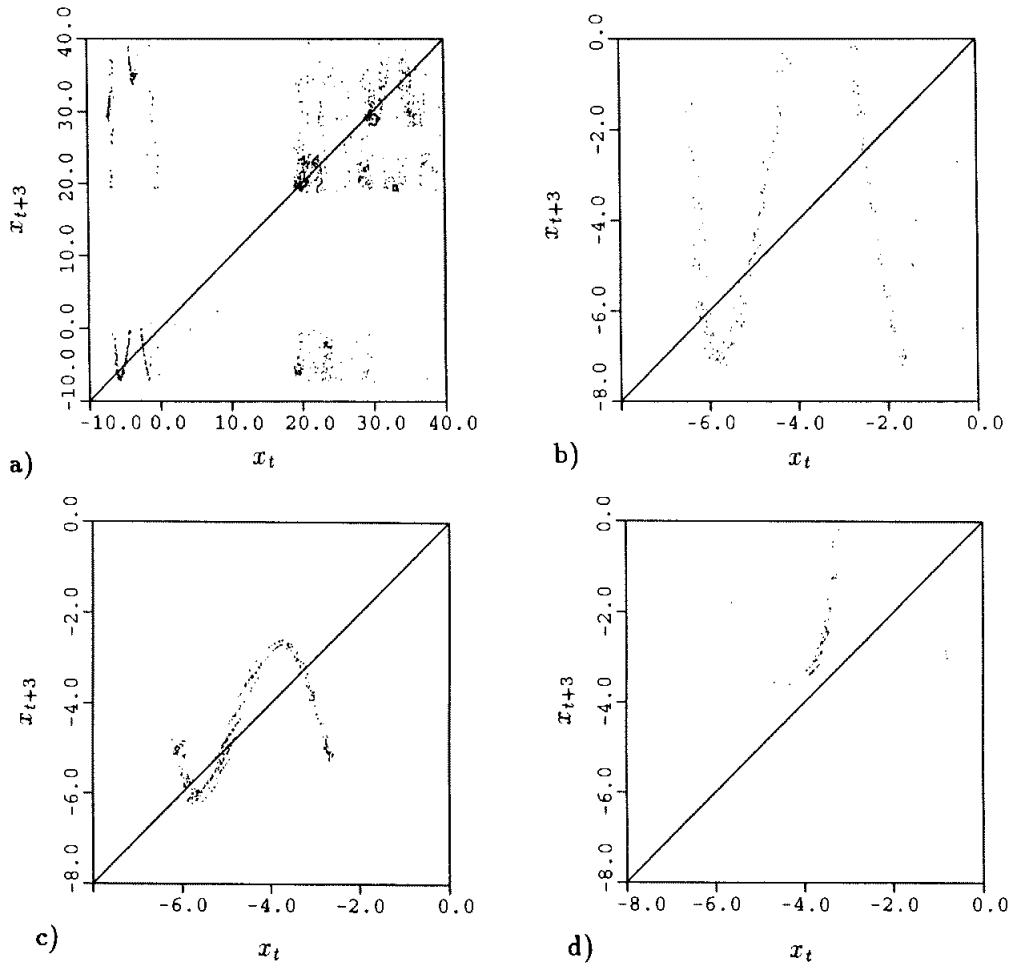

Figure 4.24: The third return map (x_t, x_{t+3}) of the Lorenz model, $\sigma = 10$, $b = 10/3$, a) $r = 135.0$ and the whole Poincaré plane; b) a magnification of a) with the same parameter values; c) $r = 145.0$; d) $r = 163.5$.

map the orbit in figure 4.23 a) is a period 3 orbit and we choose to plot the orbits in the plane (x_t, x_{t+3}) where the period 3 orbit is a fixed point. The time index t is here the integer counting intersections with the Poincaré plane and not the time in the differential equations (4.37).

Points of a chaotic orbit in the Lorenz system are plotted in (x_t, x_{t+3}) in figure 4.24. In figure 4.24 a) all points are plotted for parameter $r = 135.0$, and the structure down and left in this plot is magnified in figure 4.24 b). We find here pictures which are similar to the bimodal bifurcation pictures for the period 5 orbit in the Hénon map, figure 4.21. The points in figure 4.24 b) strongly suggest a bimodal map were there is two independent critical points. The two minimum points seems to be of the same height which excludes a three modal map bifurcation from being

important. By increasing r to 145.0, figure 4.24 c), we find a typical bimodal map which here is restricted to a band (analog to the chaotic band before the period 3 crisis bifurcation in the logistic map). Increasing the parameter further, we obtain figure 4.24 d) for $r = 168.0$, where the orbit does not exist and the structure is very similar a tangent bifurcation in a one dimensional map. There seems to have been a transition to a locally unimodal map here.

From these figures it is not difficult to predict that any two dimensional scan of the parameter space has to give a bimodal swallowtail as the bifurcation of this orbit, and that the line with $\sigma = 10$ and $b = 8/3$ is close to but not exactly in the middle of the swallow tail crossing since the "function" figure 4.24 c) is slightly asymmetric around the fixed point. We expect that with further investigations of this kind and better understanding of the symbols of the system one can construct the bifurcations in a topological parameter space also for the Lorenz system. A simple comparison of the symbolic description of stable windows in the Lorenz map and a cubic map has been done by Hao Bai-lin [106].

We belive that such a numerical procedure can be useful for understanding the bifurcation structure for many low dimensional chaotic systems and may be useful in finding a symbolic description. Further investigations is necessary to test how useful this method is in describing bifurcations and for the understanding of the structure of the non-wandering set of the systems.

4.4 Four unimodal maps approximation

The two-fold description cannot explain all swallowtails observed in the Hénon map [153]. To explain other structures we have to approximate the Hénon map with 4 unimodal maps which we refer to as a second order approximation. The four maps approximation reproduces all the swallowtails we found by the bimodal map approximation as a special case, but it also yields more complicated structures. We know from section 2.2 that a general trimodal one dimensional map already yields rather complicated diagrams like figure 2.20, and we can hardly expect to be able to draw the complete bifurcation diagram for this special four-modal map. We can however trace out some subspaces of the 4 dimensional topological parameter space and use these to explain the bifurcations found in numerical experiments. The four-modal map has co-dimension 4 and all the possible bifurcation structures in the four dimensional parameter space cannot be realized in the Hénon map that has only 2 parameters. It should in principle be possible to construct a Hénon like map with 4 parameters that realized all possible bifurcations. We show below that when we add one new parameter c with a x^4 term to the Hénon function, we obtain bifurcations not existing in the Hénon. These are other possible realizations of the bifurcations in the four-dimensional symbolic parameter space.

This variant of the Hénon map is the map

$$x_{t+1} = 1 - ax_t^2 - cx_t^4 - bx_{t-1} \tag{4.38}$$

For $c > 0$ this is a once-folding map. If $c < 0$ the map is three-folding but for $-1 << c < 0$ most of the bifurcations are described by the bifurcation diagrams of the once-folding map.

An additional term with a fourth parameter yields further bifurcation structure (not investigated here). A good choice of four parameters should reproduce all bifurcations predicted by the four-dimensional topological parameter space and also other smaller bifurcation structures in addition to this. A fifth independent parameter in the map cannot yield further bifurcations described by the four dimensional symbolic parameter space, but any new bifurcations obtained here belongs to a higher order in the one dimensional map approximations. The bifurcations we find in the Hénon map parameter plane should be topological equivalent to a 2 dimensional cut through the 4 dimensional symbolic parameter space.

Let us denote the four unimodal maps by 10, 00, 01 and 11. Point x_t in the non-wandering set with symbolic description $\ldots s_{t-3}s_{t-2}s_{t-1}s_ts_{t+1}s_{t+2}s_{t+3}\ldots$ lies on the map $s_{t-2}s_{t-1}$ and the ordering of the 4 maps in the phase space follows from the folding of the horseshoe. Each map has a critical point with an associated

topological parameter $\kappa_{s's}$ obtained by the kneading sequence of the critical point. The ordering of the maps and the values $\kappa_{s's}$ is found by applying the horseshoe map three times on a rectangle in the (x_t, x_{t+1}) space, as shown in figures 3.4 and 3.9 and we find that the ordering for $b > 0$ is

$$\kappa_{10} < \kappa_{00} < \kappa_{01} < \kappa_{11} \tag{4.39}$$

and for $b < 0$

$$\kappa_{01} < \kappa_{11} < \kappa_{10} < \kappa_{00} \tag{4.40}$$

From our experience with the trimodal maps we expect to find many swallowtail crossings that sometimes combine together into a large complicated crossing, and cusp bifurcations with two tails such that an orbit can change symbolic dynamics without becoming stable.

4.4.1 Period 6 swallowtails

An example of a cusp bifurcation where the modality of the approximation changes from 4 to 2 is given in figure 4.25 (cf. figure 6.32 in Mira [153]). The ordinary swallowtail cross in figure 4.25 a) is the bimodal cross from the symbolic parameter plane in figure 4.17. The tail $\overline{11100\epsilon}$ from this cross bifurcates into a cusp similar to one of the cusp in figure 2.14. In the isolated window to the left in figure 4.25 a) the symbolic dynamics of the stable orbit changes without any visible trace in the (a, b) plane. This implies, as pointed out in ref. [107] that an unstable orbit can change symbolic dynamics moving adiabatically along a loop in the parameter plane.

The bimodal swallowtail is described by figure 4.17, and we can also describe other structures in the symbolic space $(\kappa_{00}, \kappa_{01}, \kappa_{10}, \kappa_{11})$. From figure 4.25 a) we find that the two tails from the bimodal swallowtail that do not cross the $b = 0$ axis, $\overline{11100\epsilon}$ and $\overline{10100\epsilon}$, bifurcate along the κ_{00} axis since $s_{-2}s_{-1} = s_4 s_5 = 00$. The second tail from the simple swallow and the uppermost part of the isolated window bifurcate along the κ_{10} axis. In figure 4.27 the bifurcation lines of these orbits are drawn. The unstable orbit $\overline{111001}$ is common for two tails, with the usual associated cusp structure. At this cusp point we have drawn a dashed line to indicate that this cusp is at a point where the four modal map changes into a two modal map. To understand that this is a topological feature we have to consider in detail the maximum and minimum points in the four modal map.

The Biham-Wenzel method gives the bifurcation lines for the different symbol strings drawn in figure 4.26. We find by comparing the figures that the symbolic description of the two tails from the simple cusp in figure 4.25 b) has symbolic

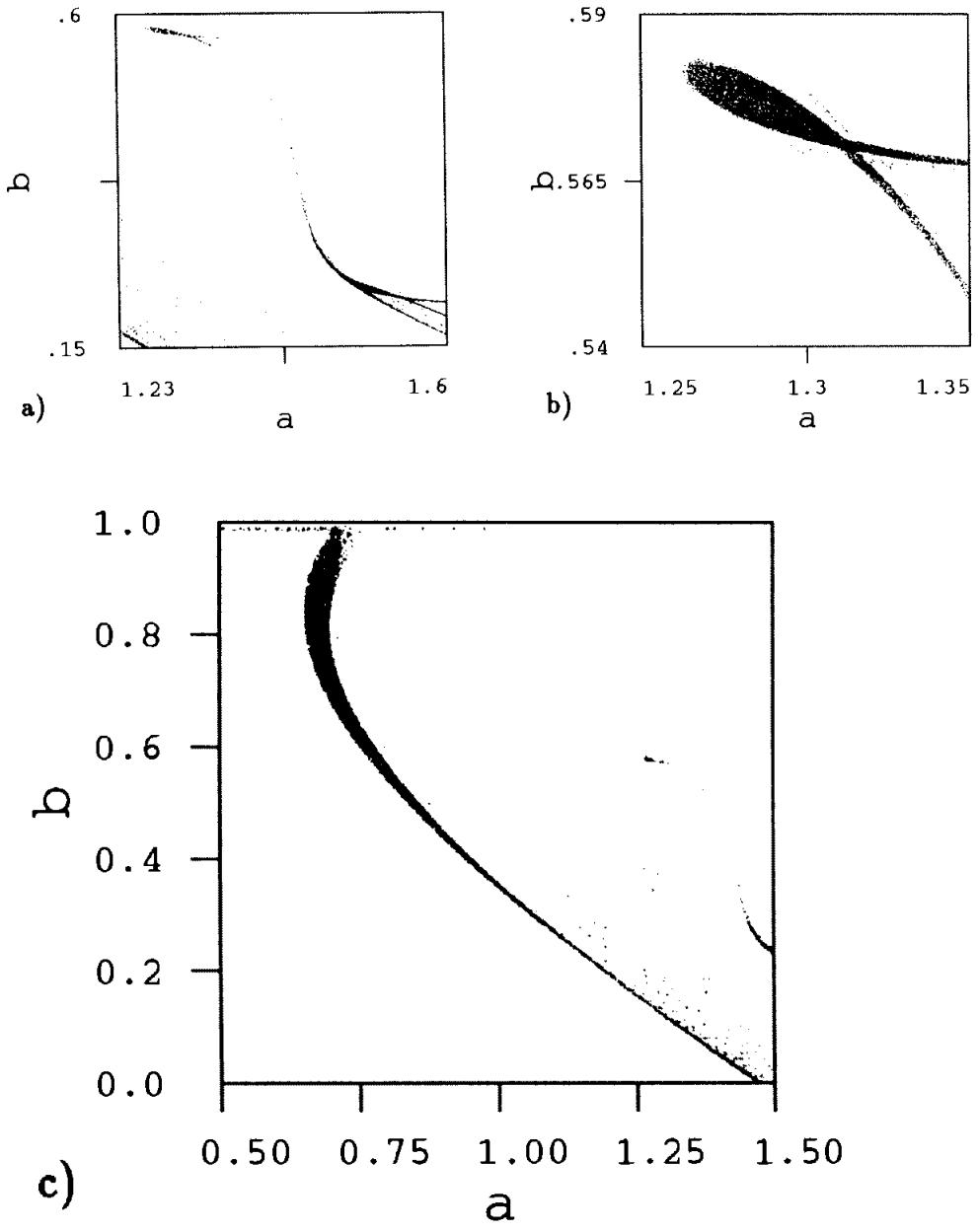

Figure 4.25: The bifurcation of the period 6 orbits in the Hénon map in the parameter space (a, b). a) The stable windows. b) The simple cusp magnified. c) The simple stable window starting as $\overline{10111\epsilon}$ when $b = 0$.

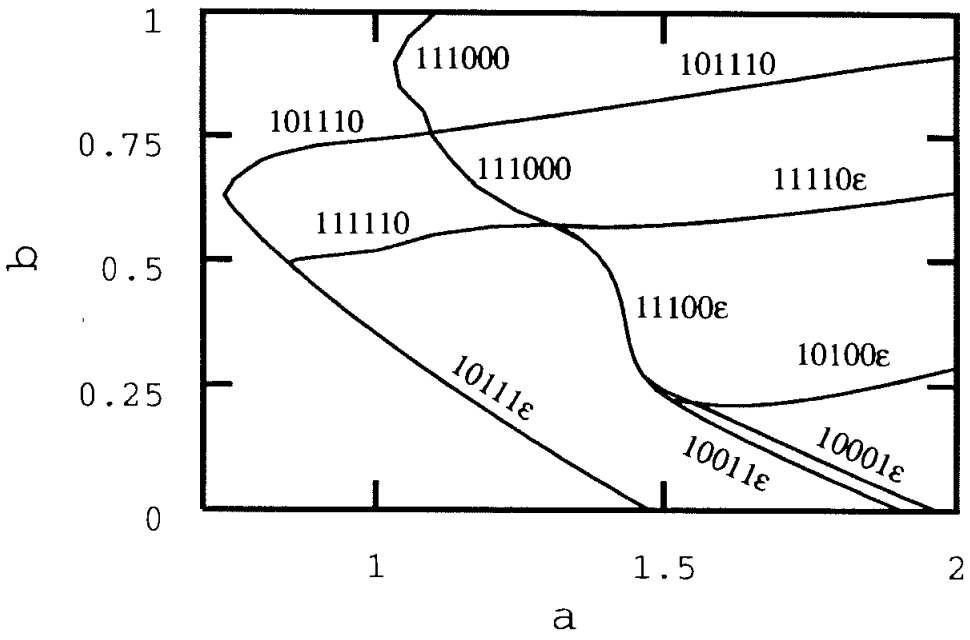

Figure 4.26: The bifurcation of the period 6 orbits in the Hénon map calculated with the complex Biham-Wenzel method.

description $\overline{11100\epsilon}$ and $\overline{11110\epsilon}$. Along the $\overline{11110\epsilon}$ tail the two orbits are close to the maximum point of the map 10, the lowest map in the 4 modal approximation (4.39). The iterate of this maximum point is the minimum point connecting the maps 00 and 01. The symbolic description of this minimum point is the shifted symbol string of the symbolic description of the maximum point on map 10:

$$\sigma(\overline{11110\epsilon}) = \overline{1110\epsilon 1} \tag{4.41}$$

The tail $\overline{11100\epsilon}$ has the two orbits close to the maximum point of the map 00. At the point where the two tails meet we find that the unstable orbit $\sigma(\overline{111100}) = \overline{111001}$ is common for the two tails and we have a cusp bifurcation. Note that the symbolic description of the point on this unstable orbit close to the minimum point is $\overline{111001}$, and at the same time the symbolic description of the maximum point is also $\overline{111001}$. This means that this cusp point is a bifurcation point where the maximum point of the map 00 merges with the minimum point on the same map and the critical point of map 00 disappears. Also the minimum point disappear and since this is an image of the maximum point on map 10 then also the independent critical point on map 10 disappears.

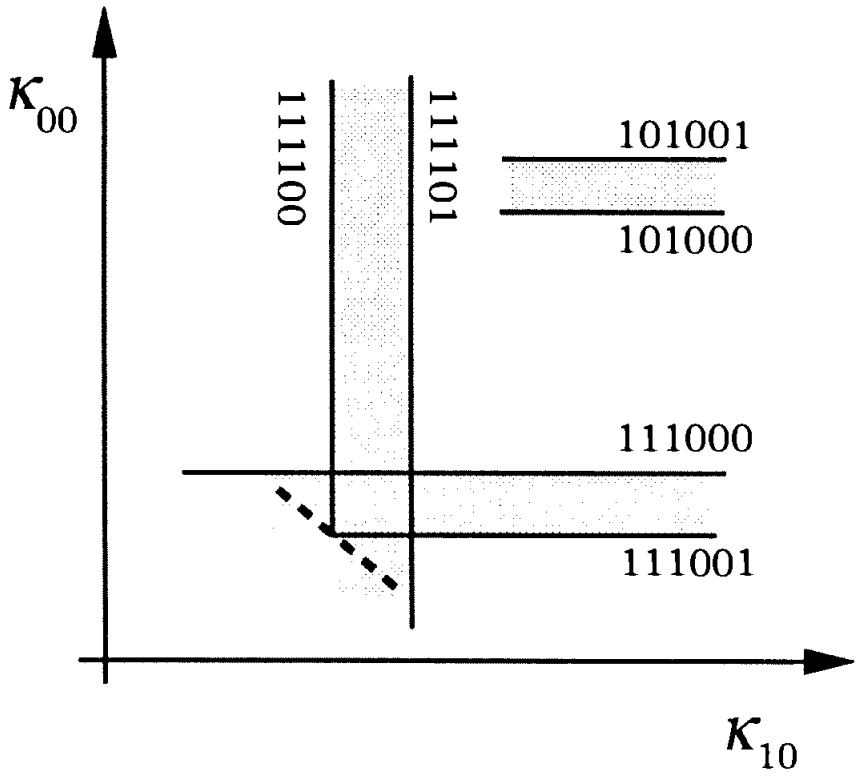

Figure 4.27: The bifurcation lines of some period 6 orbits in the sub-plane $(\kappa_{10}, \kappa_{00})$ of the topological parameter plane.

Proposition 3 *At the parameter values ($b > 0$) where the kneading sequences from the two maps 00 and 10 satisfy*

$$K_{00} = \sigma(K_{10}) \tag{4.42}$$

there is a bifurcation from a four-modal to a two-modal map.

We divide the isolated cusp bifurcations into two types; type 1 where the stable orbit exists around the singular point and type 2 where the parameter values with a stable orbit is a cusp ending in the singular point. With this definition we have the following proposition:

Proposition 4 *If K_{10} is a periodic string, and $K_{00} = \sigma(K_{10})$ then there is a cusp bifurcation of an periodic orbit in the parameter space. If the number of symbols 1 in the repeating string is even then it is a cusp of type 1, and if the number of symbol 1 in the repeating string is odd then it is a cusp of type 2.*

For the period 6 example considered here we have

$$K_{10} = 111100111100111100\ldots \tag{4.43}$$
$$K_{00} = 111001111001111001\ldots = \sigma(K_{10}) \tag{4.44}$$

when we have the topological parameter values

$$\kappa_{10} = 0.\overline{101000} \tag{4.45}$$
$$\kappa_{00} = 0.\overline{101110} \tag{4.46}$$

The number of 1's in this periodic orbit is even and we have a cusp of type 1, with a stable orbit surrounding the cusp point in the parameter space (a, b). The two types are illustrated by the fixed point bifurcation in the trimodal map in section 2.2.

The bifurcation of the period 6 orbits in the Lozi map is drawn in figure 4.28. In this map there are no cusp bifurcation and one crossing is on the $b = 1$ line.

For $b < 0$ ($\det \mathbb{J} > 0$) we have the same propositions with the strings $K_{11} = \sigma(K_{01})$.

The bifurcation lines for the Lozi map is drawn in figure 4.28. Because the manifolds are piecewise linear this map has not any cusp bifurcations. We find in this figure that the Lozi map does not have the bimodal swallowtail but a four-modal swallowtail crossing $\overline{10\epsilon_1 11\epsilon_2}$ in the $(\kappa_{10}, \kappa_{11})$ plane.

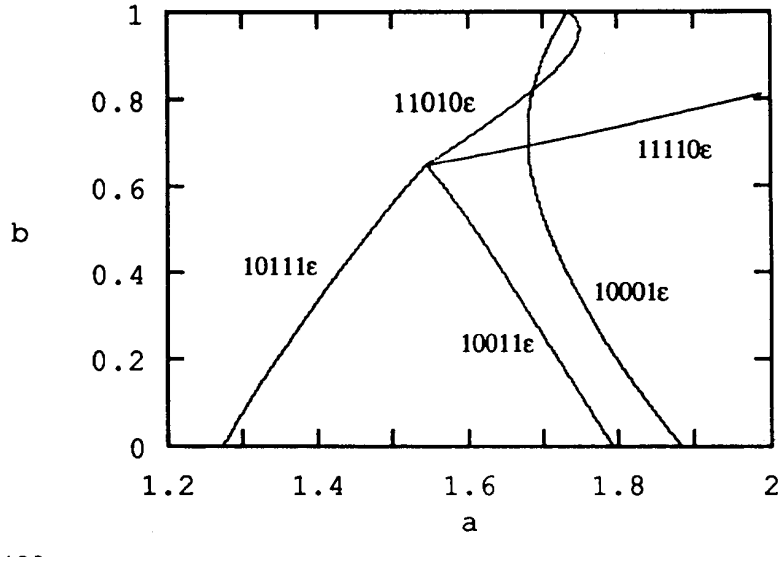

Figure 4.28: The bifurcation lines for period 6 orbits in the Lozi map.

4.4.2 Period 4 orbit cusp bifurcation

The period 4 orbits $\overline{1000}$, $\overline{1001}$ and $\overline{1011}$ have a type 1 cusp bifurcation in the symbolic parameter space $(\kappa_{10}, \kappa_{00})$ in figure 4.29. The unstable orbit $\overline{1001}$ is the common orbit in the two tails. This cusp is exactly on the line $b = 1$. It was showed by Mira [153] that this is because there is a symmetry in the symbol string $\overline{1001}$ ("self-adjoint cycle"). In the n-modal map approximation is it not obvious why this cusp is on the area preserving line, but this symmetry is visible in the symbol plane (γ, δ) and we return to this question in section 5.4. The bifurcation lines for the Lozi map is given in figure 4.30 and figure 4.31 shows the bifurcation lines in the Hénon map. The Biham-Wenzel method in figure 4.31 b) converges the same way for this cusp as for the cusps in the dissipative region. For $b > 1$ the tail consists of an orbit unstable in two directions and by iterating backward the orbit is an attractor. The bifurcation diagram is sketched in figure 4.31 a). There is also additional structures close to this cusp, cf. Mira [153].

4.4.3 Bifurcation of period 8 orbits

Another example of bifurcations in the Hénon map that is explained by the four-modal approximation is the bifurcation structure in figure 4.32. This structure has a complexity comparable to the period 3 orbits in the trimodal map in figure 2.22. Instead of trying to draw a complete four dimensional topological parameter space, we find the symbolic description of the structures and show that this is possible

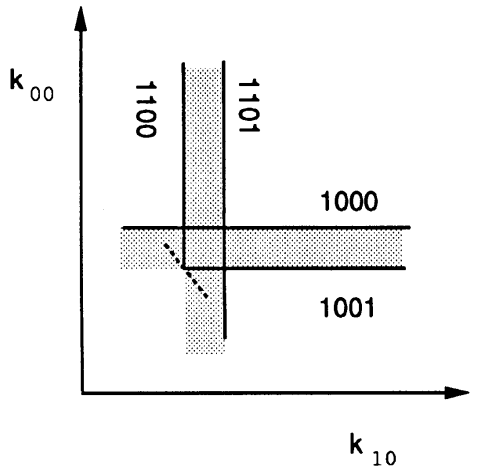

Figure 4.29: The bifurcation of the orbits $\overline{1000}$, $\overline{1001}$ and $\overline{1011}$ in the symbolic parameter plane $(\kappa_{10}, \kappa_{11})$.

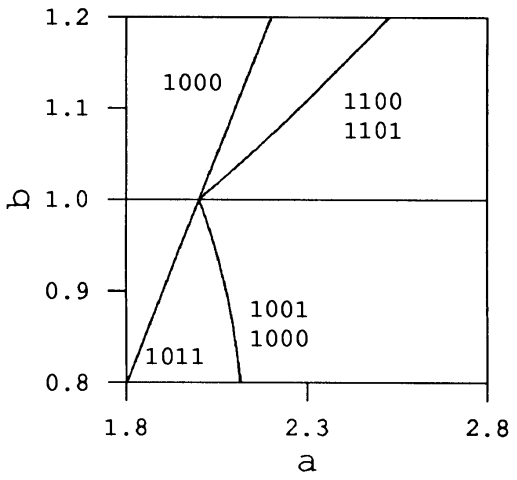

Figure 4.30: The bifurcation curves of period 4 orbits in the Lozi map.

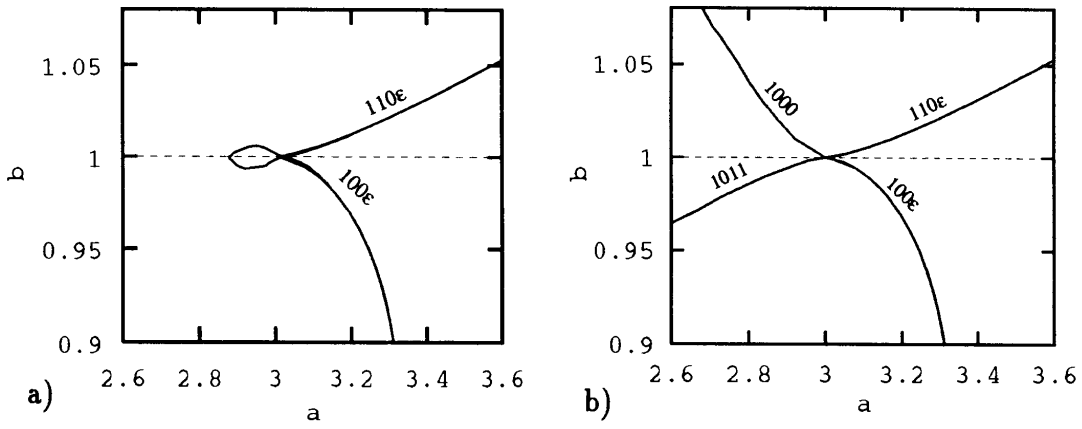

Figure 4.31: The bifurcation curves of the period 4 orbits in the Hénon map. b) Bifurcation curves from the BW-method.

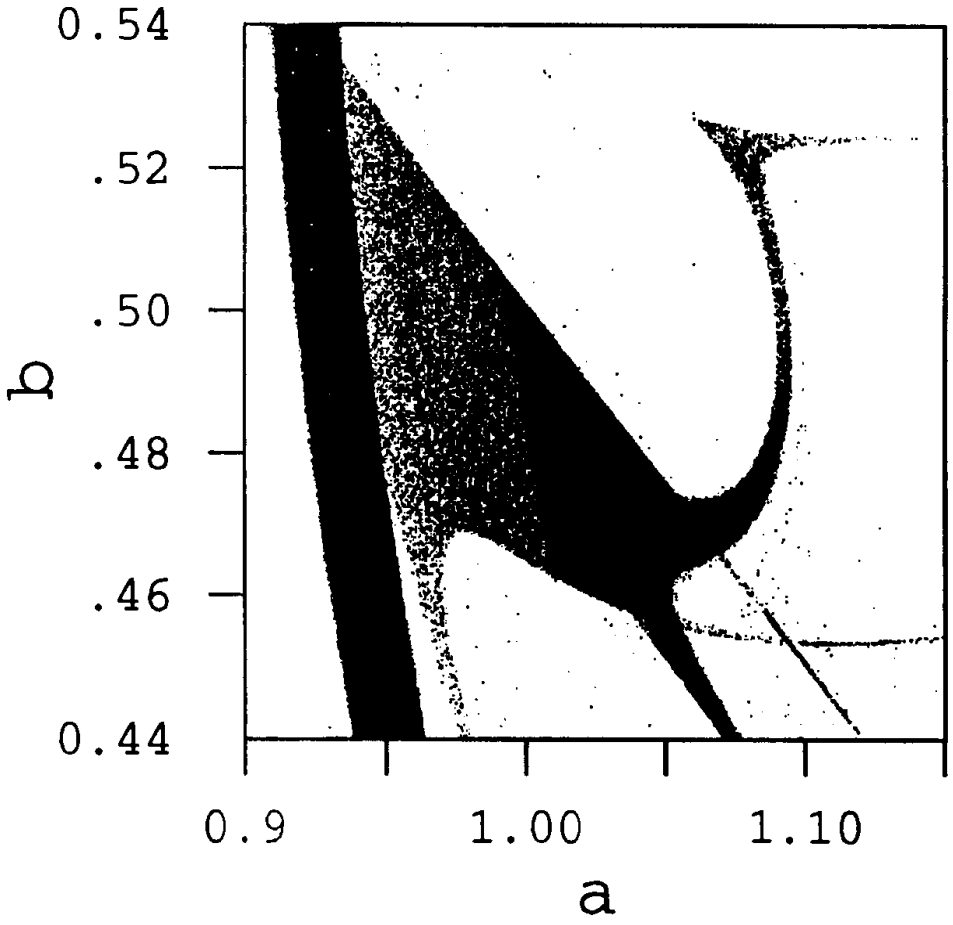

Figure 4.32: The parameter values with stable period 8 orbits in the Hénon map in the parameter space (a, b).

bifurcations in a two dimensional subspaces of the symbolic symbol space. We then perturb the Hénon map with a cx^4 term, and show the transitions to other possible bifurcations in the parameter plane as c varies.

In figure 4.32 there is one window which is a simple almost vertical strip in the left side of the plot. This is the period 8 orbit $\overline{10111010}$ originating from the period doubling family of the fixed point. This orbit is bifurcating along the κ_{01} axis in the symbolic parameter space and is not connected with the other structure in the figure and we will not discuss this any more.

In figure 4.33 the bifurcation lines found by the complex Biham-Wenzel method is drawn in the (a, b) parameter plane. We assume that when these bifurcation lines coincide with the tails of stable orbits in figure 4.32 this is the correct symbolic

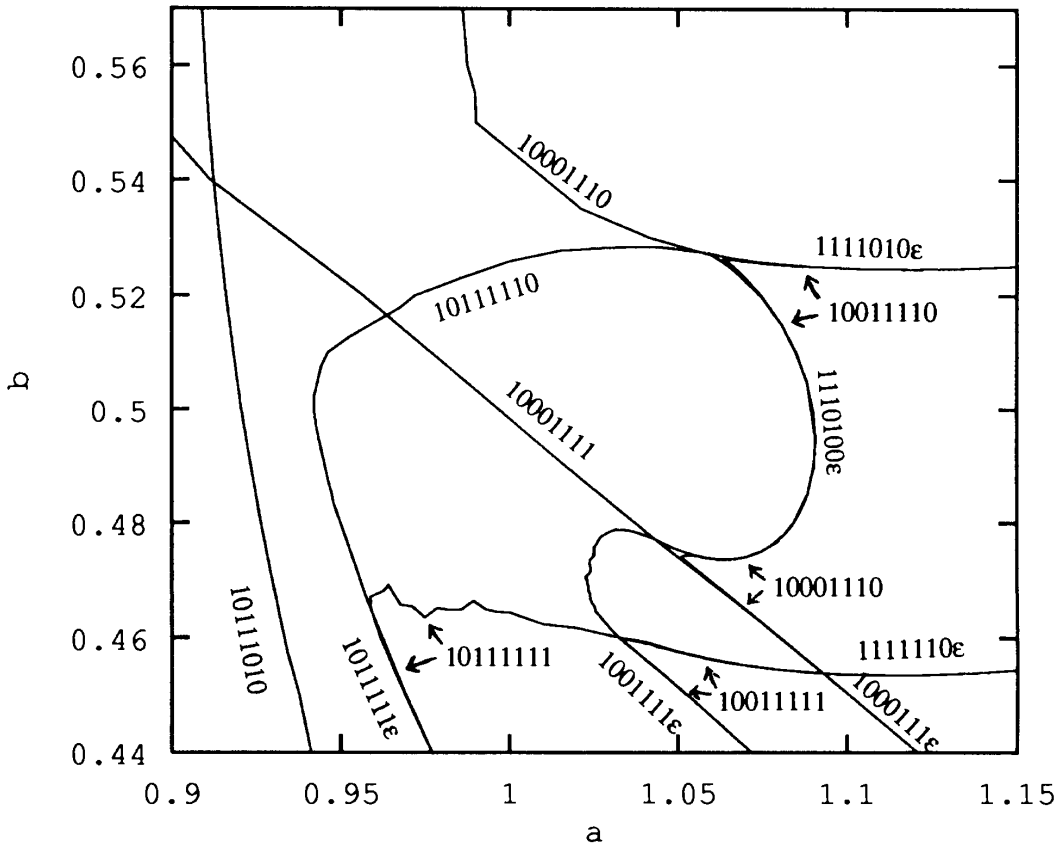

Figure 4.33: The bifurcation of the period 8 orbits in the Hénon map in the parameter space (a, b) calculated with the complex Biham-Wenzel method.

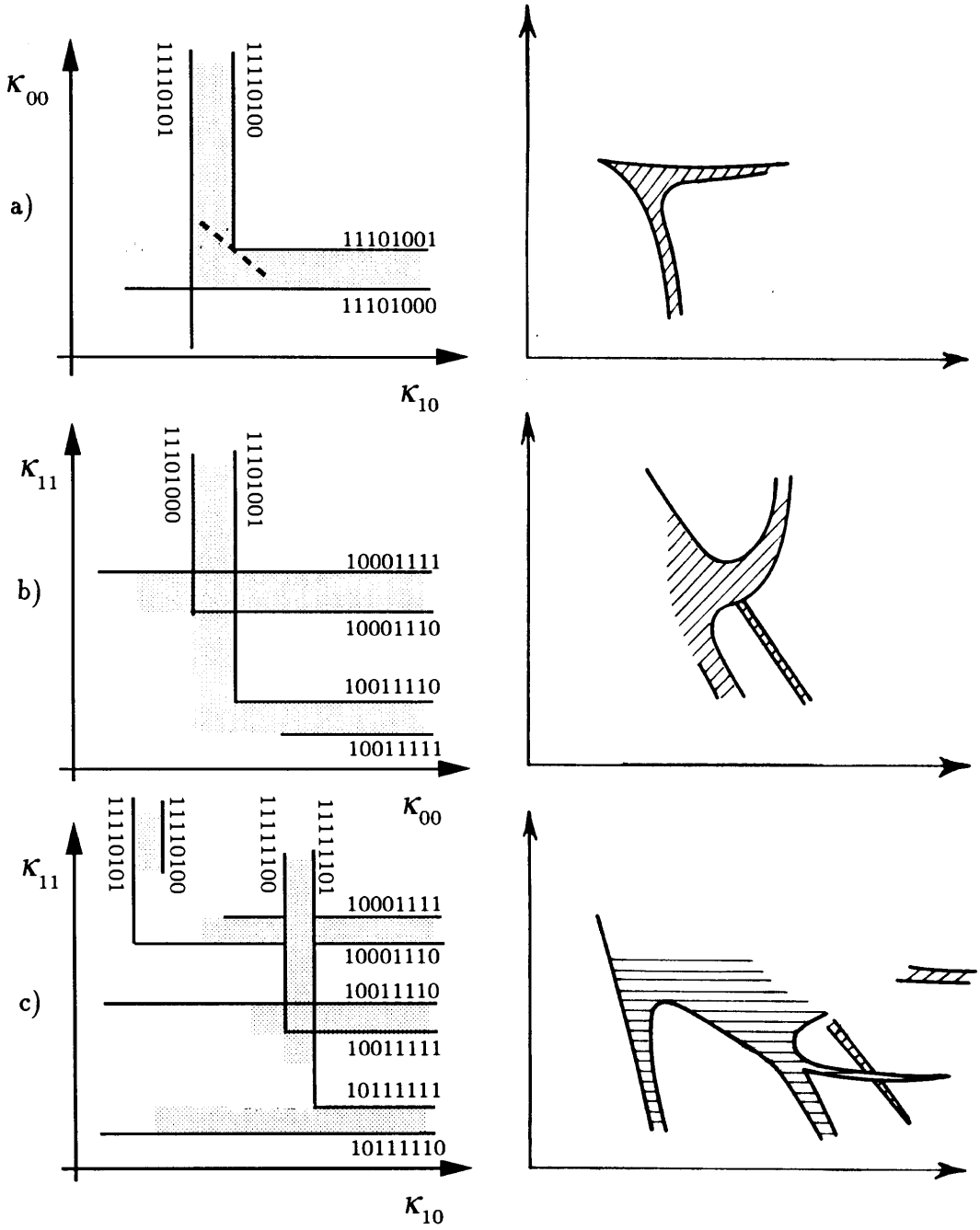

Figure 4.34: The bifurcation lines of some period 8 orbits in the sub-planes of the topological parameter plane and the corresponding structure in the real parameter space. a) $(\kappa_{10}, \kappa_{00})$ b) $(\kappa_{00}, \kappa_{11})$ c) $(\kappa_{10}, \kappa_{11})$

description of the orbit. In figure 4.33 the bifurcation curves are labeled and the double curves that corresponds to a tail are labeled $s_1s_2s_3s_4s_5s_6s_7\epsilon$. This is the cyclic permutation where the two orbits have one different symbol in the end of the string and the two orbits in the tail are pruned on map s_6s_7. All the swallowtail crossings are bifurcations in a two dimensional symbolic parameter plane and in figure 4.34 three pictures show these crosses in three different symbolic parameter planes. Notice that the symbol strings given in the figure have the cyclic rotation giving the largest value $\tau_{s_6s_7}$. If there was a cyclic permutation of an orbit giving a larger $\tau_{s_6s_7}$ then this cyclic permutation would give the correct bifurcation structure.

Figure 4.34 a) shows that the simple cusp of type 2 is a bifurcation in the plane $(\kappa_{10}, \kappa_{00})$ of the three orbits $\overline{11101001}$, $\overline{11101000}$ and $\overline{11110101}$. In agreement with proposition 4 one shift of the symbol string on map 10 with an odd number of 1's give the symbol string on map 00

$$\overline{11101001} = \sigma(\overline{11110100}). \tag{4.47}$$

The figure 4.34 b) shows that the three orbits $\overline{10001111}$, $\overline{10001110}$ and $\overline{11101001}$ bifurcates in a swallowtail crossing in the plane $(\kappa_{00}, \kappa_{11})$. We find that the orbits do not bifurcate along κ_{01} and the bifurcation can therefore not be a cusp where the modality of the map changes.

In figure 4.34 c) we find that the third cross is the bifurcation of the orbits $\overline{10011110}$, $\overline{10011111}$ and $\overline{11111101}$ in the $(\kappa_{10}, \kappa_{11})$ plane. There is no bifurcations giving a cusp and reducing the number of critical point in this plane. From this figure we find that the three tails $\overline{1011111\epsilon}$, $\overline{1001111\epsilon}$ and $\overline{1000111\epsilon}$ bifurcates along the κ_{11} axis and these tails will not cross each other. Figure 4.34 c) also shows that the two tails $\overline{1111010\epsilon}$ and $\overline{1111110\epsilon}$ both bifurcates along κ_{10} and the tails never cross each other.

We find in the (a, b) plane in figure 4.33 the tail $\overline{1111110\epsilon}$ below the tail $\overline{1110100\epsilon}$. In the symbolic parameter plane we do not find that this is necessary as the first tail bifurcates along κ_{10} and the second along κ_{11}.

To further test the symbolic parameter description we numerically investigate the perturbed Hénon map (4.38). The figures 4.35 a) – f) show how the bifurcation structure for the period 8 orbits changes when c changes from $+0.08$ to -0.06. We describe the two extremum cases and some important transitions in the structures.

Figure 4.35 a) for $c = 0.08$ shows that the tail $\overline{1011111\epsilon}$ has become disconnected from the other structure, the cusp of type 2 has not changed while the remaining structure has turned into a bimodal swallowtail crossing and a cusp of type 1. These structures are drawn in the symbolic parameter plane in figure 4.36. In 4.36 a) the two simple cusps are drawn. Both bifurcates in the plane $(\kappa_{10}, \kappa_{00})$ as proposition 4

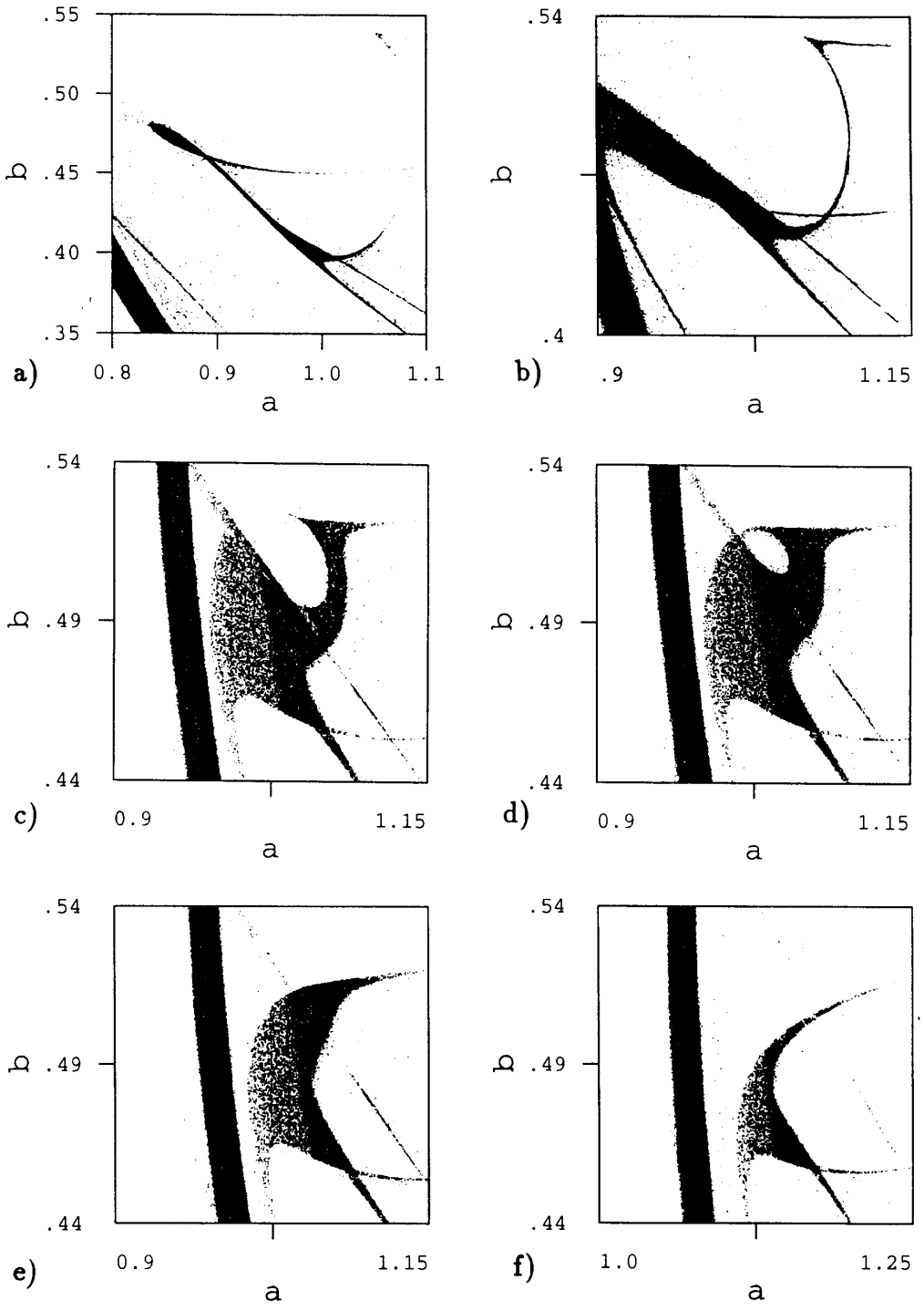

Figure 4.35: The parameter values giving stable period 8 orbits in the perturbed Hénon map (4.38) in the parameter space (a, b) with different values of c. a) $c = 0.08$, b) $c = 0.02$, c) $c = -0.01$ d) $c = -0.013$, e) $c = -0.02$, f) $c = -0.06$.

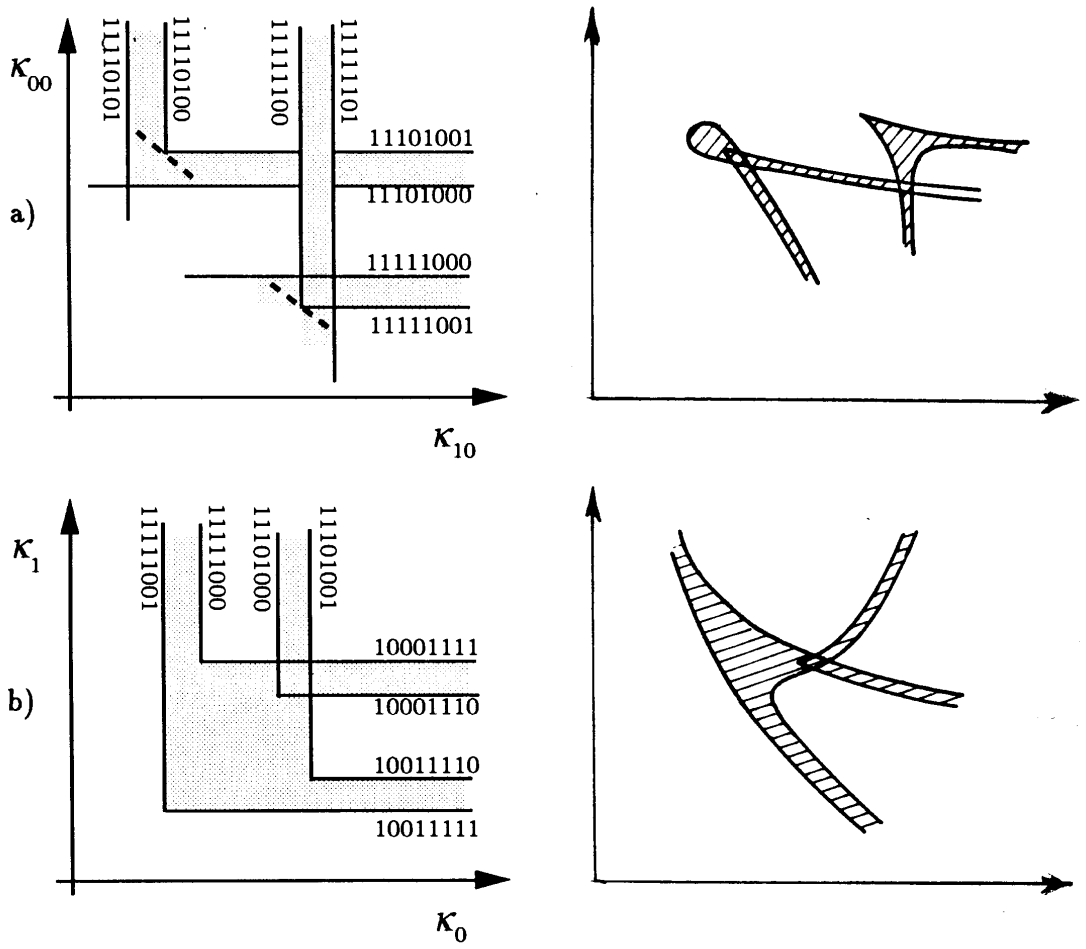

Figure 4.36: Bifurcation lines of some period 8 orbits in the sub-planes of the topological parameter plane and the corresponding structure in the real parameter space for the perturbed Hénon map with $c = 0.08$. a) $(\kappa_{10}, \kappa_{00})$ b) (κ_0, κ_1)

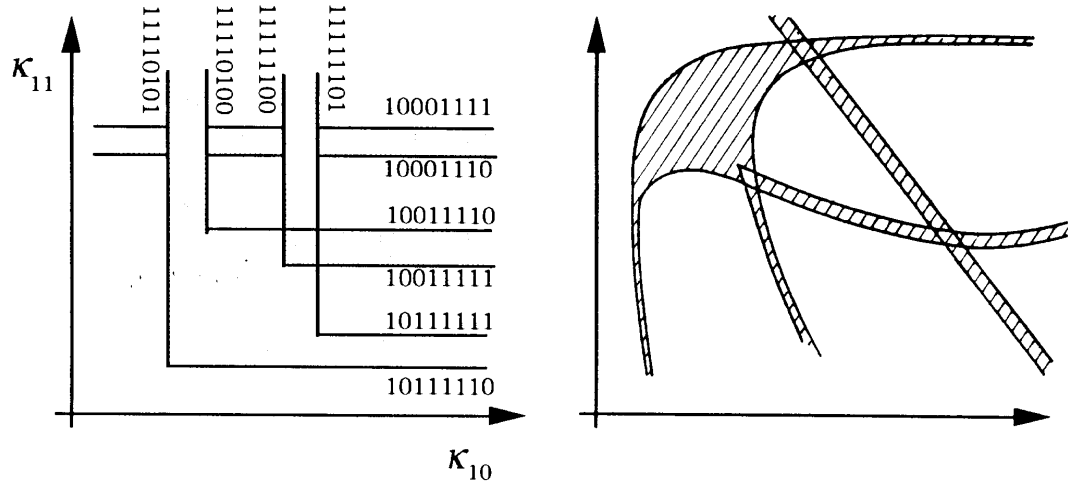

Figure 4.37: Bifurcation lines of some period 8 orbits in the sub-plane $(\kappa_{10}, \kappa_{11})$ of the topological parameter plane and the corresponding structure in the real parameter space for the perturbed Hénon map with $c = -0.06$.

predict. The swallowtail in figure 4.36 b) is one of the bimodal swallowtails in figure 4.19 bifurcating in the bimodal parameter plane (κ_0, κ_1). This example shows that not all the bimodal bifurcation structure can be found in the Hénon map, but when adding new parameters to the map we can find the swallowtails predicted by the bimodal approximation.

We have a different bifurcations structure in figure 4.35 f). For $c = -0.06$ the structure has changed into one simple band and one ordinary swallow tail. This structure is drawn in the topological parameter plane $(\kappa_{11}, \kappa_{10})$ in figure 4.37. The simple band is the tail $\overline{1000111\epsilon}$. The swallowtail looks like the bimodal swallowtails we found in the bimodal approximation but this is not a bimodal structure because the tail $\overline{1111010\epsilon}$ is the cyclic permutation giving $\tau_{10}^{\max}$ but not the cyclic permutation giving $\tau_0^{\max}$. In figure 4.39 we find that the map for $c = -0.06$ indeed is three-folding, but that the period 8 orbit we study here is in the once-folding part of the manifolds.

There is an interesting transition of the bifurcations from figure 4.35 d) ($c = -0.13$) to figure 4.35 e) ($c = -0.2$). In the Hénon map ($c = 0$) there is a tail $\overline{1110100\epsilon}$ connecting two cusp bifurcations. When c decreases this tail merge into a loop and finally disappear. From figure 4.32 it is not easy to guess that this is a possible transition. However from the BW calculations in figure 4.33 we have some bifurcation structures indicating this possibility. A bifurcation line of the orbit $\overline{10111110}$ is going in an arc from the tail $\overline{1011111\epsilon}$ to the tail $\overline{1111010\epsilon}$ exactly as the

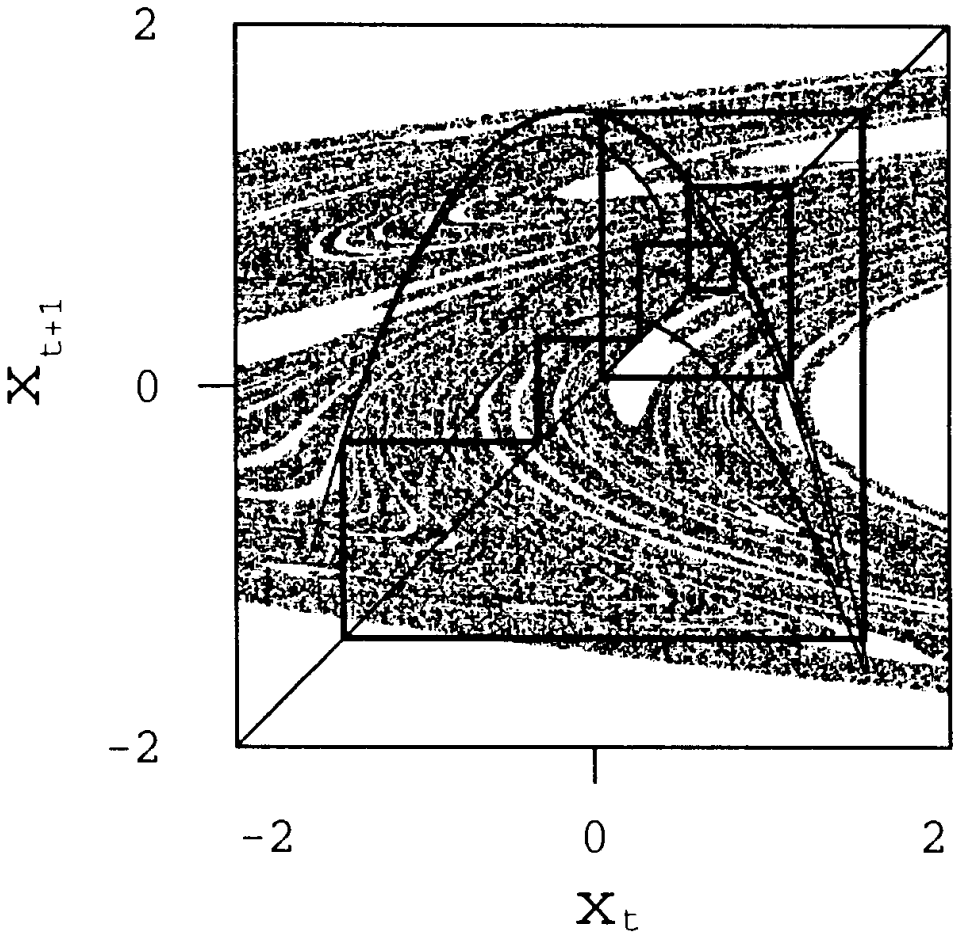

Figure 4.38: The stable period 8 orbit and the manifolds in the cusp in figure 4.35 a) with parameters $a = 0.8683$, $b = 0.4677$, $c = 0.08$.

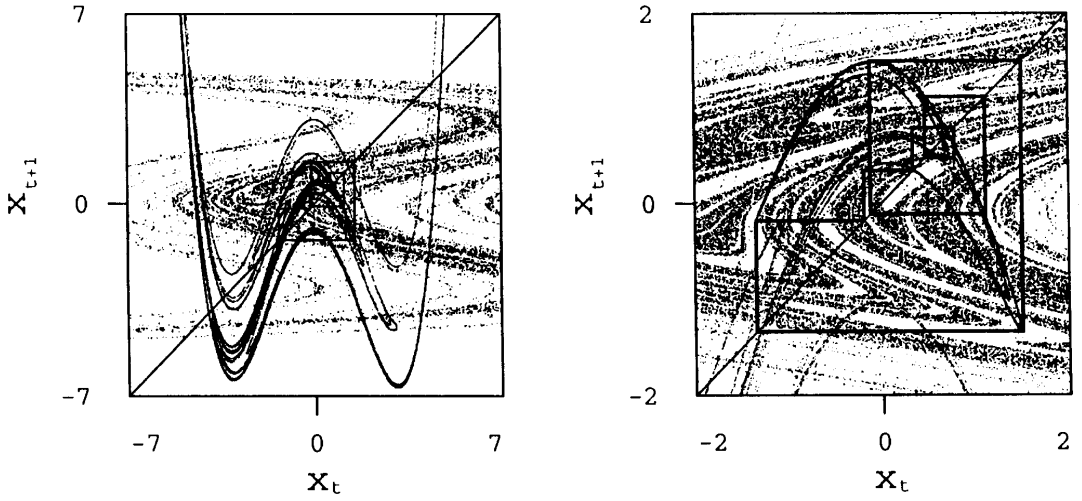

Figure 4.39: The stable period 8 orbit and the manifolds in the swallowtail cross in figure 4.35 f) with parameters $a = 1.15$, $b = 0.465$, $c = -0.06$.

bifurcation line at the back of the swallowtail in figure 4.35 f). In figure 4.32 there is a loop consisting of the tail $\overline{1110100\epsilon}$ and the curves $\overline{10001111}$ and $\overline{10111110}$. If we ignore this loop then we find the following: the four tails $\overline{10\epsilon_1 1111\epsilon_2}$ goes into the bifurcation structure, from down right comes the tail $\overline{1000111\epsilon}$ and to the top left leaves the two curves $\overline{10001110}$ and $\overline{10001111}$. The only difference is that the two orbits $\overline{1000111\epsilon}$ have split up in the left top corner. At the bifurcation point where the loop disappears all three tail $\overline{1000111\epsilon}$, $\overline{1110100\epsilon}$ and $\overline{1111010\epsilon}$ go together at one point and then the stable point is close to the turning-point of the three maps 10, 00 and 11.

4.5 Biham-Wenzel method

After using the method suggested by Biham and Wenzel (BW) to make bifurcations diagrams it is of interest to look closer at this method and its convergence properties.

In earlier investigations [26, 27, 93] this method has been used numerically as a tool to find periodic orbits in the Hénon map. It has been showed by Grassberger et. al [93] that this method fails in certain cases while Biham and Wenzel [27] have replied that that these cases can be solved by introducing some numerical tricks as changing the method slightly or choosing starting points in a special way etc. After the better understanding of symbolic dynamics given here and the study of the convergence of the BW method as a function of the (a, b) plane is it useful to discuss the method again. The motivation of Biham and Wenzel was a Hamiltonian

formalism, but we find this irrelevant and we will not discuss this argument.

Biham and Wenzel have suggested one method finding only real solutions and a more complicated method which also finds complex solutions for a (possibly) complex Hénon map. Biham and Wenzel uses the convention of the Hénon map

$$x_{t+1} = a - x_t^2 + bx_{t-1} \tag{4.48}$$

which is turned into the map we use by changing $x \to x/a$ while the parameters a and b are the same.

The real BW method to find a period n orbit works as follows [26]: Choose x_i for $i \in \{1, 2, \ldots, n\}$ to be random numbers and let $x_0 = x_n$ and $x_{n+1} = x_0$. Let then the values x_i evolve with time according to the differential equation

$$\dot{x}_i = s_i F_i, \qquad i = 1, \ldots, n \tag{4.49}$$

with

$$s_i \in \{-1, 1\}$$

and

$$F_i = -x_{i+1} + a - x_i^2 + bx_{i-1} \tag{4.50}$$

The "force" F_i is just a rewriting of the Hénon map (4.48) which is equal 0 if the values x_i are the points in a period n orbit of the Hénon map. The periodic orbits we are interested in are one possible solution of eq. (4.49) and it is not very surprising that this kind of method may work. What is interesting is that the choice of values s_i gives a symbolic dynamics and that this symbolic dynamics with $s = -1 \to s = 0$ in most cases is the same symbolic dynamics as the Smale horseshoe type of symbols.

Biham and Wenzel also have extended this method to a complex version which can include complex parameters and gives the complex periodic orbits when the real orbits do not exist [27]. By using real parameters this method gives the real and the imaginary solutions of periodic orbit if the method converges. The advantage with this method is that we can check whether we did not get the real periodic orbit because the orbit was imaginary or because the method failed to converge.

Let all the variables in the equations above become complex numbers with $z_i = x_i + iy_i$ where $z_0 = z_n$ and $z_{n+1} = z_0$, and $F_i = f_i + i\phi_i$, $A = a + i\alpha$ and $B = b + i\beta$. The differential equation we choose as before to be

$$\dot{z}_i = c_i F_i, \qquad i = 1, \ldots, n \tag{4.51}$$

with

$$F_i = -z_{i+1} + A - z_i^2 + Bz_{i-1} \tag{4.52}$$

but here we choose

$$c_i = s_i + i\,\mathrm{sgn}(y_i)$$

with $s_i \in \{-1, 1\}$ the symbols as in the real case. The introduction of the $i\,\mathrm{sgn}(y_i)$ terms seems to be just ad hoc but numerical experiments show that this term is necessary to get a convergence to the complex solutions.

Writing the differential equations as two real equations give

$$\begin{aligned} \dot{x_i} &= s_i\left(-x_{i+1} + a - x_i^2 + y_i^2 + bx_{i-1} - \beta y_{i-1}\right) \\ &\quad +\mathrm{sgn}(y_i)\left(-y_{i+1} + \alpha - 2x_i y_i + \beta x_{i-1} + by_{i-1}\right) \end{aligned} \tag{4.53}$$

and

$$\begin{aligned} \dot{y_i} &= s_i\left(-y_{i+1} + \alpha - 2x_i y_i + \beta x_{i-1} + by_{i-1}\right) \\ &\quad +\mathrm{sgn}(y_i)\left(-x_{i+1} + a - x_i^2 + y_i^2 + bx_{i-1} - \beta y_{i-1}\right) \end{aligned} \tag{4.54}$$

These equations with $\alpha = \beta = 0$ have we used to find the bifurcation lines in the parameter space integrated with a fourth-order Runge-Kutta method.

Figure 4.7 shows that for the short orbits of length 1, 2 and 3 the bifurcation lines the BW method gives is the same lines as the bifurcation lines where these orbits start to exist.

In the swallowtail in figure 4.11 the BW does not converge to the stable orbit in the center of the cross. In this region the stable orbit in a one dimensional bimodal map changes symbolic dynamics in a complicated way. The BW method solves this problem of choosing the right symbolic description by not converging at all.

More interesting is the bifurcation curves close to the simple cusp as in figure 4.26. On the back of the cusp the BW does not converge to the unstable orbit. It is natural to relate this to the change of modality on the back side of the cusp. As one adiabatically changes the parameters and follows the unstable orbit one observe that the orbit start with one symbolic description and then has to change to an other symbolic description. In the area where there is a smaller modality of the map there is no obvious reason why one or the other of the symbol string should make the BW converge. Assume that the BW artificial dynamics makes the points move in one direction away from the turning point and the direction is determined by the symbol, then it is a reasonable guess that it does not converge when the turning point vanishes.

The numeric indicate that that the BW method in this case converges for parts of the parameter space where the map has lost its turning point. In figure 4.40 the curves where BW losses convergence for the period 6 and 8 orbits are drawn together with the dashed curve where the fold ...101111 looses its turning point.

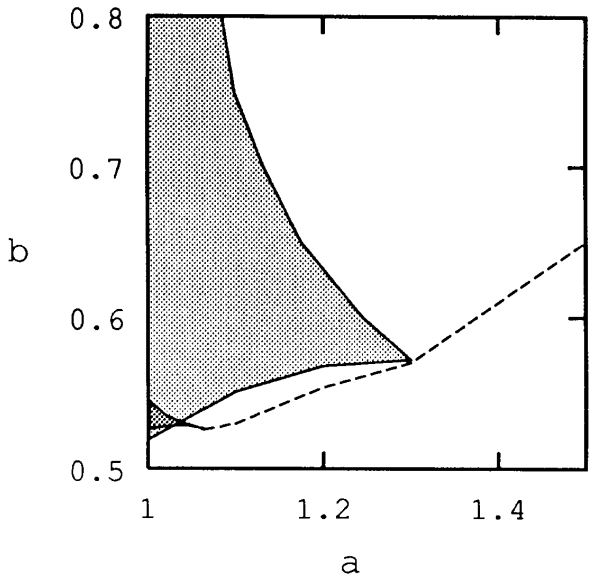

Figure 4.40: Border curves where the complex Biham-Wenzel method fails to converge for period 6 and 8 orbits. The dashed curve is the bifurcation line where the fold ...101111 looses its turning point.

This dashed curve is obtained simply by looking at pictures of the stable and the unstable manifold and judge by eye if the fold has a primary turning point or not. When the parameters get closer to the lines where the BW method fails, then the convergence of the BW method gets slower and slower. In the area where it fails to converge it also fails if we starts close to the correct solution. The periodic orbit can be found by a Newton algorithm and followed adiabatically through the parameter plane where it exists as done in ref. [107].

In ref [27] Biham and Wenzel discuss the convergence of the period 8 orbit $\overline{10001110}$ for parameters $a = 1.0$ and $b = 0.54$. They find that the method converges to a limit circle and not to a periodic orbit but that when one multiply the left side of eq. (4.54) with a number larger than 1.43 such that the x and y values do not converge with the same speed then the method converges to the right solution. They use this example as an argument that the method will converge with small adjustments.

We have in figure 4.33 plotted the curve where the method does not converge any more for the orbit $\overline{10001110}$. For the parameter $b = 0.54$ we find the bifurcation line at $a = 1.0105$ which imply that the method does not converge to the orbit for $a = 1.0$ but this parameter is very close to the convergence region. These parameters are above a cusp in figure 4.32. We correctly find that by increasing the relative size

of eq. (4.54) compared to eq. (4.53) we obtain a converging method for $a = 1.0$. The value of a where the method stops converging decreases but it reach a minimum value at approximately $a = 0.985$ when we choose (4.54) to be around 8 times as large as (4.53) and then a increases again for larger ratios. This numerical trick seems to be able to move the bifurcation line slightly, but not enough to prevent that in a large area the method fails to converge.

The dashed line in figure 4.40 represents the most important of the bifurcations reducing the modality of the map. There are similar lines arbitraryly close to the $b = 0$ line and therefore we conjecture that for any parameter value of the pruned Hénon map, the BW method will fail to find all periodic orbits existing. The orbits it fails to find are those which are above a cusp bifurcation and therefore do not have a unique symbolic description even in a one dimensional map.

4.6 Twice-folding maps

The twice-folding horseshoe map has parameter space of higher dimension than the once-folding map and a bifurcation structure that is more difficult to draw in a symbolic parameter space. We will only discuss a few examples of bifurcations and show that that these are consistent with the symbolic parameter space description.

The map we choose for illustrating the twice-folding bifurcations is

$$x_{t+1} = x_t^3 - ax_t + b + Bx_{t-1} \tag{4.55}$$

Instead of adding a cubic term to the Hénon map we choose to use the cubic map in section 2.1 and add a term Bx_{t-1} to this. As for the Hénon map this map reduces to a one dimensional map for $B \to 0$ and the bifurcations of the map $B = 0$ is discussed in section 2.1. The bifurcations we find in section 2.1 can be considered a first order approximation valid for small values of B and some of these bifurcations are shown in figures 2.4, 2.6 and 2.8. This is bifurcations in a two dimensional parameter space.

The second approximation gives three bimodal maps with the topological parameters given by the 6 kneading values of the 6 independent extremum points in the approximation. The ordering of the kneading values depends only on the sign of B. As for the Hénon map we find that for $B > 0$ the horseshoe is orientation reversing and

$$\kappa^1_{\text{map }0} < \kappa^1_{\text{map }1} < \kappa^1_{\text{map }2} \tag{4.56}$$

$$\kappa^2_{\text{map }0} < \kappa^2_{\text{map }1} < \kappa^2_{\text{map }2} \tag{4.57}$$

For the orientation preserving case $B < 0$ we have

$$\kappa^1_{\text{map } 2} < \kappa^1_{\text{map } 1} < \kappa^1_{\text{map } 0} \tag{4.58}$$

$$\kappa^2_{\text{map } 2} < \kappa^2_{\text{map } 1} < \kappa^2_{\text{map } 0} \tag{4.59}$$

One interesting new bifurcation structure is the bifurcations of the period 3 orbits. In the parameter space (a, B) for $b = 0$ we find that the two tails $\overline{22\{0,1\}}$ and $\overline{21\{0,1\}}$ cross each other when B increases and that the tail $\overline{21\{0,1\}}$ has a cusp bifurcation of type 2 (see page 127) shown in figure 4.41. The stable orbit in the cusp is drawn in figure 4.42 together with the stable and the unstable manifolds, and the stable orbit in the other tail in figure 4.41 is drawn in figure 4.43 together with the unstable manifold.

The cusp has the two tails $\overline{21\{0,1\}}$ and $\overline{02\{1,2\}}$, where the stable orbit $\overline{210}$ is the common orbit. This kind of structure is familiar from the Hénon map parameter spaces. We can find the bifurcation diagram in a universal two dimensional symbolic symbol plane drawn in figure 4.44 a). This is the bifurcation plane with the two symbolic parameters $\kappa^1_{\text{map } 1}$ and $\kappa^2_{\text{map } 2}$. The symbolic parameter subspace $(\kappa^1_{\text{map } 1}, \kappa^2_{\text{map } 2})$ has the structure in figure 4.44 when all other values of κ is constant and when $\kappa^1_{\text{map } 2}$ is sufficiently large; $1 \geq \kappa^1_{\text{map } 2} >> \kappa^1_{\text{map } 1}$ As for the once-folding map, the common orbit is in this case related in the two tails by a single shift of symbols. A generalization of proposition 4 to the twice-folded map is straight forward.

The first order approximation predicts that these two orbits bifurcate in an ordinary swallowtail bifurcation. This bifurcation is showed in the ordinary parameter space and the topological parameter space in figures 2.6 and 2.7. We can numerically study the transition from this swallowtail to the isolated cusp in figure 4.44 by following the bifurcations in the (a, b) plane as B increases.

At $B = 0.12$ figure 4.45 shows that the two tails $\overline{21\{0,1\}}$ and $\overline{22\{0,1\}}$ are closer in the parameter space, but topologically there is still a connected swallowtail with the tails ordered as for $B = 0$. At $B = 0.2$, figure 4.46, the two tails have changed order, such that $\overline{22\{0,1\}}$ is to the left of $\overline{21\{0,1\}}$ and the crossing is broken up into one cusp and one tail. This tail is thicker close to the cusp because there the unstable manifold bends less sharp here.

The sketch of bifurcation lines in figure 4.44 b) is drawn as expected from a Biham-Wenzel type algorithm. In the area above the cusp the unstable period 3 orbit has to change its symbolic description and it does not have a definite description in a 3 letter alphabet. We expect that if we could construct an algorithm of this type it would fail to converge in this area.

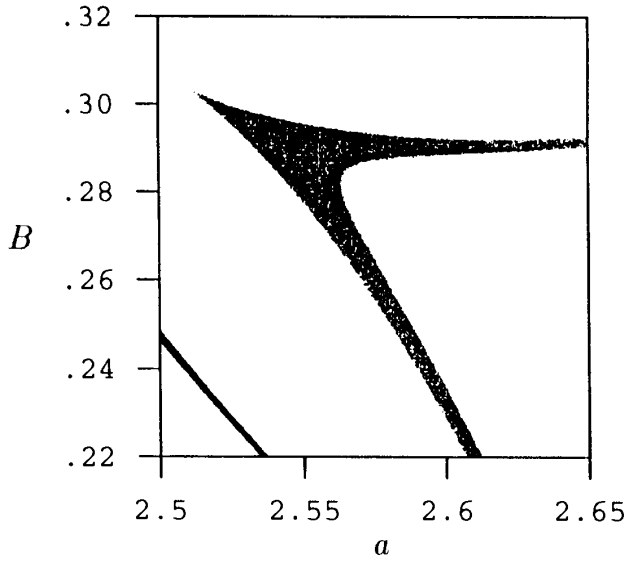

Figure 4.41: The area in parameter space (a, B) of the twice-folding map $b = 0$ where period 3 orbits are stable.

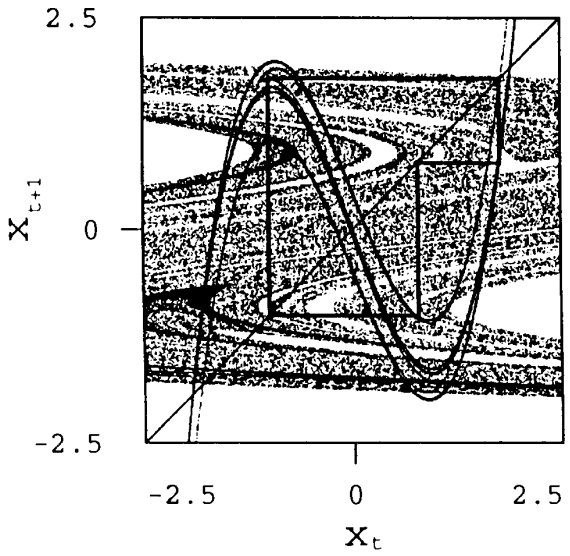

Figure 4.42: The stable and the unstable manifolds and the stable period 3 orbit $\overline{210}$ in the cusp bifurcation $a = 2.55$, $b = 0$, $B = 0.29$.

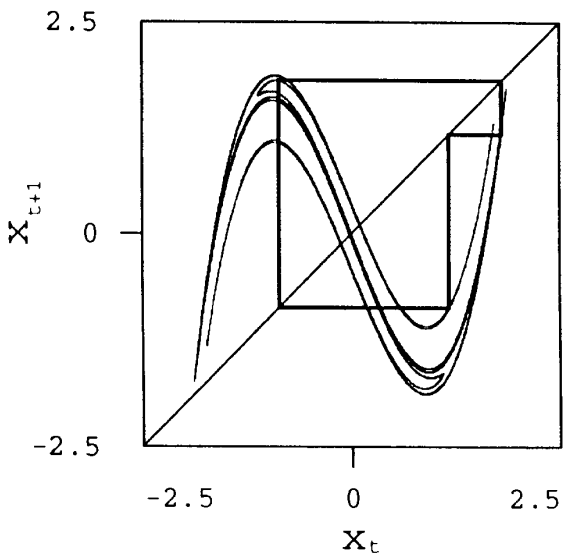

Figure 4.43: The unstable manifold and the stable period 3 orbit $\overline{221}$ $a = 2.5$, $b = 0$, $B = 0.2485$.

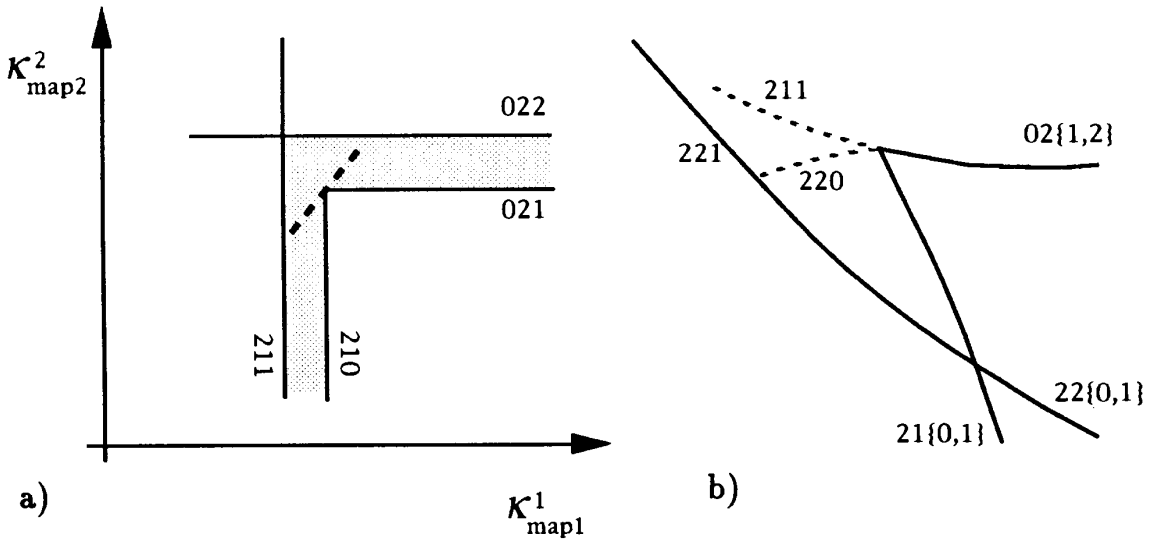

Figure 4.44: a) Bifurcation lines for period 3 orbits in a two dimensional subspace $(\kappa^1_{\text{map }1}, \kappa^2_{\text{map }2})$ of the symbolic parameter space of the twice-folding map. b) A sketch of bifurcation lines in the parameter space (a, B).

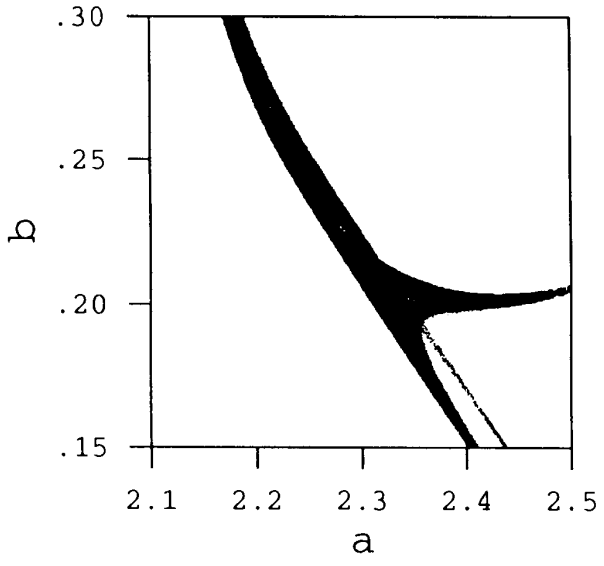

Figure 4.45: The area in parameter space (a, b) of the twice-folding map $B = 0.12$ where period 3 orbits are stable.

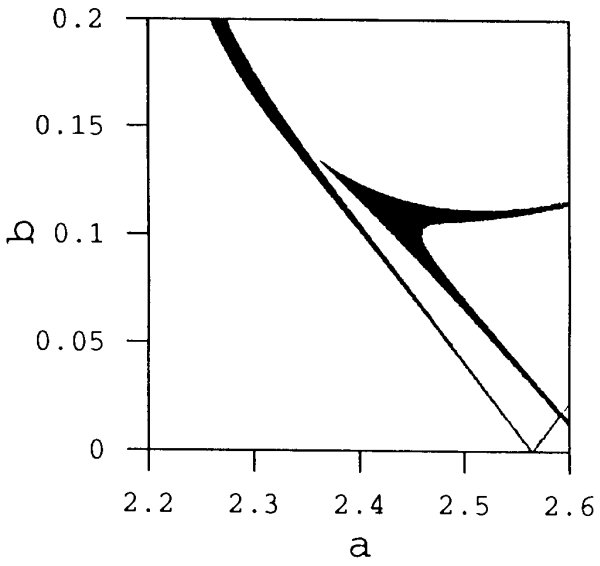

Figure 4.46: The area in parameter space (a, b) of the twice-folding map $B = 0.2$ where period 3 orbits are stable.

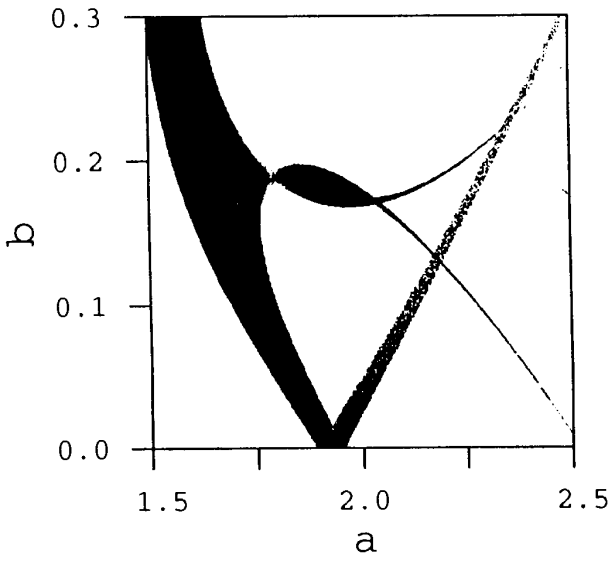

Figure 4.47: The area in parameter space (a, b) of the twice-folding map $B = 0.2$ where period 4 orbits are stable.

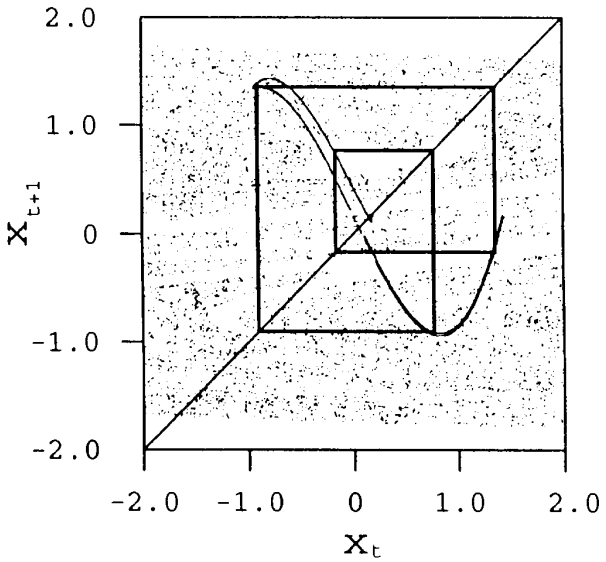

Figure 4.48: The unstable manifold and the stable period 4 orbit in the cusp of figure 4.47 $a = 1.95$, $b = 0.175$, $B = 0.2$.

A different example of the breakup of the swallowtail is given by the period 4 orbit swallowtail cross $\overline{21\{1,2\},\{0,1\}}$. In the $B = 0$ limit this is an ordinary swallow tail shown in figure 2.8. When B increases, this tail splits up, but in a different way than in the period 3 example above. In this case the inner part of the crossing becomes disconnected, and we get a cusp bifurcation of the type where the unstable orbit is the common orbit in the two tails. This does not require crossing of tails; figure 4.47 shows the bifurcation structure in the plane (a, b) for $B = 0.2$. The manifolds and the stable orbit in the isolated cusp are drawn in figure 4.48. The cusp is isolated if the symbolic value $\kappa^1_{\text{map }2}$ is sufficiently larger than $\kappa^1_{\text{map }1}$ which in ordinary parameters means that B is sufficiently large. The symbolic parameter plane $(\kappa^1_{\text{map }1}, \kappa^2_{\text{map1}})$ gives this cusp bifurcation with the two tails $\overline{211\{0,1\}}$ and $\overline{021\{1,2\}}$.

The structures we find numerically for this model all fits into the description with a symbolic parameter space organized hierarchically with approximations with 2 parameters, 6 parameters, 18 parameters, etc. We conjecture that the symbolic parameter space describes all bifurcations in this map.

Chapter 5

Pruning front for the Hénon map

Our starting point, the pruning front picture of the once-folding map as defined by Cvitanović, Gunaratne and Procaccia [53] is in many ways equivalent to the multi-modal map picture. Assuming the pruning front description is correct, then this picture gives all admissible orbits of the map. Discrete approximations to the pruning front may be given as n-modal one-dimensional maps, and we show how one can describe the different n-modal bifurcations using the approximate pruning front. We will argue that the procedure we propose for defining a partition yields a unique partition for a pruned horseshoe map. The question of one unique partition is difficult and the discussion here should be regarded as the first step towards a rigorous treatment of this problem.

5.1 Symbol plane

The pruning front conjectured in ref. [53] is defined in a two dimensional symbol plane $(\delta, \gamma) \in ([0,1],[0,1])$. While ref. [53] uses coordinates (x_t, y_t) and (γ, δ), we prefer to use coordinates (x_t, x_{t+1}) and (δ, γ) because they simplify the comparison with the n-modal discussion. The coordinate γ is defined in (3.4); and coordinate δ is defined in (3.5) for a Smale horseshoe without reflection ($b < 0$ in the Hénon map), and in (3.6) for the Smale horseshoe with reflection ($b > 0$ in the Hénon map).

For the full Smale horseshoe the Cantor set in (x_t, x_{t+1}) is mapped uniquely by the rules above into the the symbol plane, preserving the phase-space topological ordering. We will now use this symbol plane to also describe the pruned horseshoe map.

5.2 Primary turning points

The main problem in the definition of the pruned horseshoe symbol plane is the choice of the symbol s_t corresponding to a phase space point (x_t, x_{t+1}) for the given parameters.

In the n-th one-dimensional approximation of the once-folding map we chose the symbols $s_t = 0$ if x_t lies to the left of the critical point and $s_t = 1$ if x_t lies to the right. The critical point is the the point where $dx_{t+1}/dx_t = 0$ and an important question is how many critical points we have for a given approximation and how this number changes. The complete horseshoe map has 2^n critical points but it may be less critical points in the pruned horseshoe.

We found that in the three-modal one-dimensional map in section 2.2 we had a bifurcation changing the modality from three to one. In the three-dimensional symbolic parameter space this bifurcation happens at two planes drawn in the figures 2.13, 2.17 and 2.20. In figure 2.16 a) and c) the function has three critical points and orbits are described by a four letter alphabet while in figure 2.16 b) the map is unimodal and a two letter alphabet describes all orbits. The typical bifurcation of periodic orbits are the cusp bifurcations discussed in section 2.2. The bifurcation changing modality creates difficulties when we want a complete description of all the bifurcations in one-dimensional map given by a polynomial of degree n.

For the four-modal approximation of the Hénon map discussed in section 4.4 we found a bifurcation from a four-modal map to a bimodal map for kneading sequences given in proposition 3. The border of the four-modal symbolic parameter space is a three-dimensional space which in a two-dimensional parameter space like (a, b) for the Hénon map, is a curve sketched in figure 4.40. This give the cusp bifurcations we found numerically for the Hénon map. Any higher modal approximation to the once-folding map has bifurcations decreasing the modality of the map.

To understand this changing of modality seems to be essential when we want to describe the pruned once-folding map by symbolic dynamics in an exact description.

In the Hénon map there can be no critical points in the strict one-dimensional map sense since $\det \mathbb{J} = b$ is constant, and no derivative vanishes for $b \neq 0$. Here the points that play a role similar to the critical points of one-dimensional maps are the *turning points* of the unstable manifold W^U, defined as points where the stable manifold W^S and the unstable manifolds W^U are parallel. If the attractor is chaotic then the turning points are identical to the homoclinic tangencies of W^S and W^U. If there are stable periodic orbit some turning points are in the basin of attraction. If the map is a repellor then some turning points are in the basin of

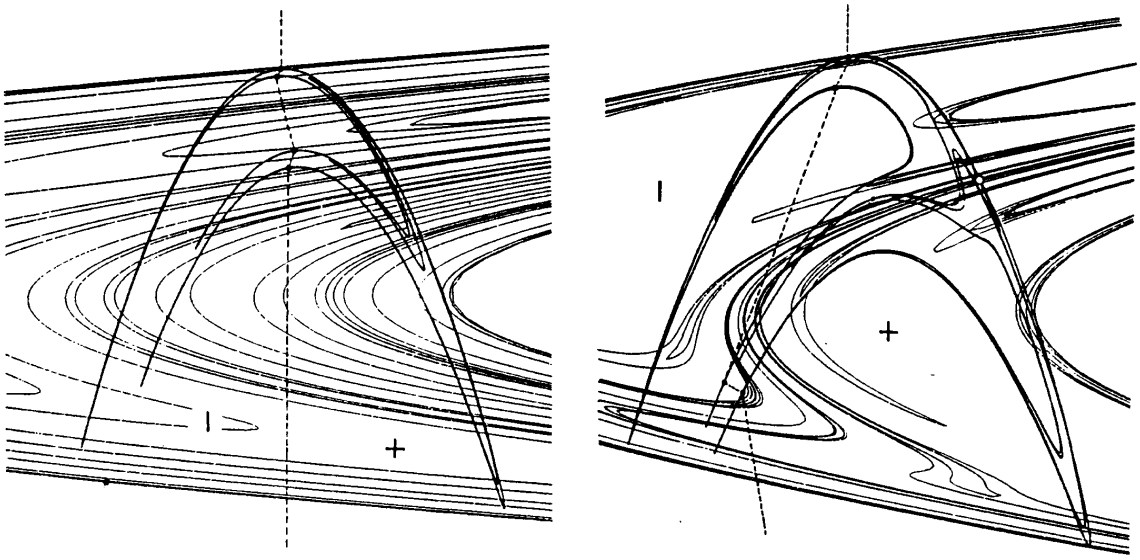

Figure 5.1: The Grassberger-Kantz partition line for the Hénon map for parameters a) $a = 1.4$, $b = 0.3$; b) $a = 1.0$, $b = 0.54$. From ref. [92].

attraction of infinity.

Grassberger and Kantz [92] have proposed that the "primary" homoclinic tangencies (turning points) generate a partition of the Hénon map. One of the images or preimages of a turning point has to be chosen as the primary turning point; according to Grassberger, Kantz and Moening [93] this choice is "...of course arbitrary, as all (pre-)images are equally good candidates".

We shall introduce here a prescription for determining which (pre-)images of the turning points that should be taken as primary and we believe this prescription is unambiguous.

In figure 5.1 the Grassberger-Kantz partition of the Hénon map is plotted for Hénon parameters $a = 1.4$, $b = 0.3$, and for the parameters $a = 1.0$, $b = 0.54$. In ref. [93] Grassberger, Kantz and Moening compare their partition to the partition obtained by the symbols of periodic orbits found using the real version of the Biham-Wenzel (BW) method (4.49). They find that their choice and the BW method give the same partition for $= 1.4$, $b = 0.3$, while for $a = 1.0$, $b = 0.54$ they get a different partition drawn in figure 5.2. The two partitions give the same entropy and the different symbols can be translated into each other by a finite set of substitution rules up to the given accuracy. However, we shall now argue that a partition different from both these two are preferable for reasons given below. This partition is indicated in figure 5.3.

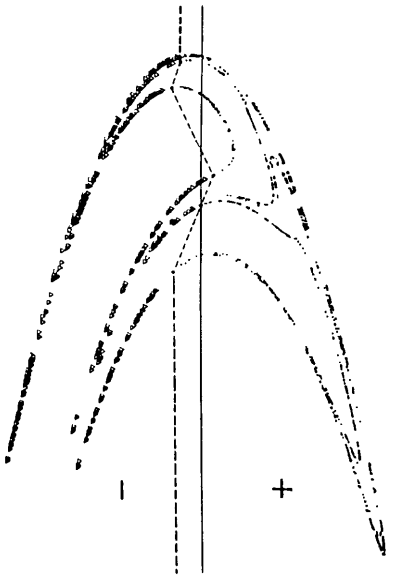

Figure 5.2: The partition line for the Hénon map for parameters $a = 1.0$, $b = 0.54$ calculated by the BW-method. From ref. [93].

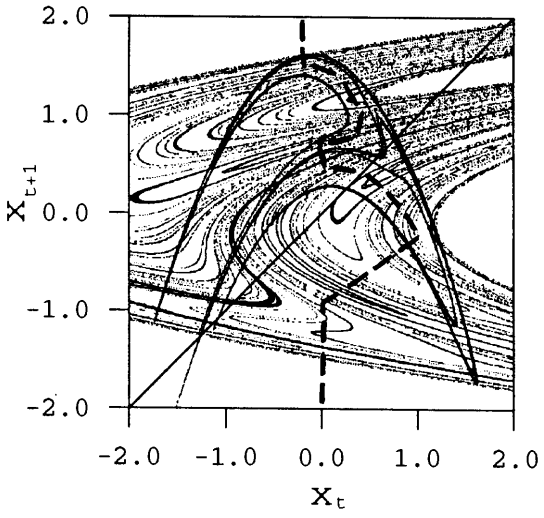

Figure 5.3: The partition line for the Hénon map for parameters $a = 1.0$, $b = 0.54$, constructed by the algorithm proposed here.

5.2.1 Bifurcations of turning points

We define a primary turning point (PTP) for the complete smooth Smale horseshoe map to be a point on one fold of W^U (the unstable manifold) at the point where this fold of W^U is parallel to the closest fold of W^S (the stable manifold) and the point has to be in the primary bent region of the horseshoe; in $g(Q)$ close to to middle of $g(Q)$ above Q in figure 3.1. For non-smooth maps like the Lozi map a PTP is at the point on W^U where the fold turns. In the Lozi map this is the line $x_t = 0$.

Each fold in the complete Smale horseshoe has one PTP, and each PTP has an infinite number of images and preimages that are turning points (TP) which are not primary. All the images of a PTP are below Q in figure 3.1, while the preimages of a PTP are in Q.

We choose some physical realization of the complete Smale horseshoe, e.g. the Hénon map, and then change smoothly the parameters. The number of TPs and folds in the Hénon map may be less than in the complete horseshoe. The folds changes smoothly with the parameters and we can study the bifurcation removing a TP. The bifurcation creating (or removing) a tangency between two given folds of W^U and W^S is much studied in mathematical literature and is very important

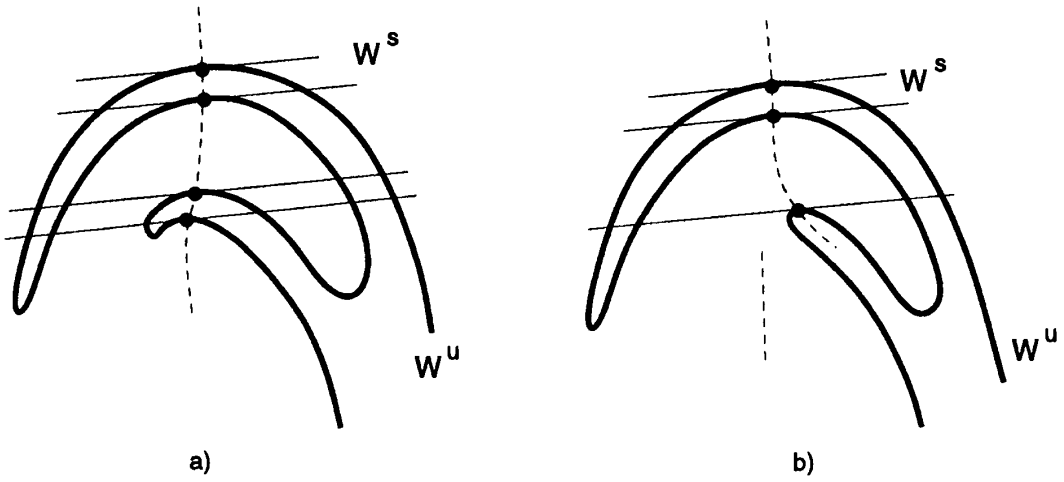

Figure 5.4: A partition of the once-folding map under a bifurcation of TPs that gives a discontinuous partition line.

in proving the Newhouse phenomena [160, 100] and in proving that a subset of the non-wandering set is given by a complete horseshoe. In these discussions the turning point exists both before and after the bifurcation and the bifurcation creating a TP is a different and much less studied bifurcation [115, 116]. We want to use PTPs as the partition giving symbolic dynamics. To understand how the symbolic dynamics change when we smoothly change the parameters we have to examine the bifurcation of TPs.

A simple way to describe the bifurcations appears to be to claim that when one PTP vanish this does not affect any other PTP. This is illustrated with the bifurcation sketched in figure 5.4: the thin lines are folds of W^S, the thick lines are folds of W^U and the dashed line is the partition line. The partition line we have in figure 5.4 b) through the three remaining PTPs are not continuous through the whole W^U. The partition line goes into one fold and has to continue outside this fold. In the limit $b \to 0$ for the Hénon map this partition does not approach a simple line through the critical point of the parabola. This is also not consistent with choosing $x = 0$ as the partition line for the Lozi map.

We find it necessary to choose a different and more complicated way to describe the partition line under a bifurcation of a PTP.

Assume that the fold A of W^U in figure 5.5 a) has three TPs labeled 1, 2 and 3 where TP no 2 is a PTP and that after n iterations of these folds of W^U and W^S we have the folds in B where TP 1 and TP 3 are PTPs. The partition line is drawn through TP 2 in A and TP 1 and TP 3 in B. As we change parameters

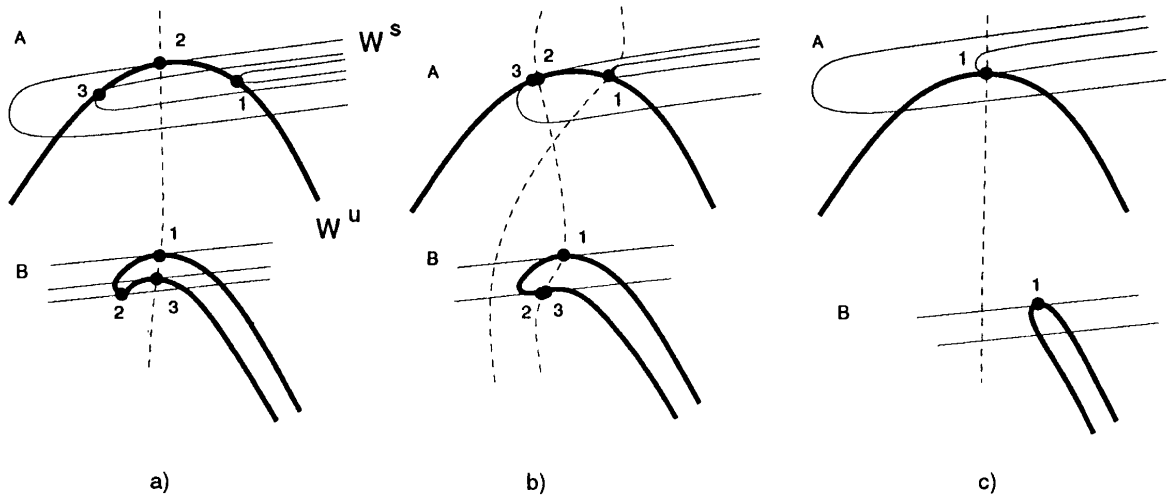

Figure 5.5: Bifurcation of the primary turning points of the once-folding map.

the two TPs 2 and 3 move closer and in figure 5.5 b) the two points disappears in of flip bifurcation. When only TP 1 is left in figure 5.5 c), we choose to draw the partition line through TP 1 at fold A of W^U and not through TP 1 at fold B. *At the bifurcation point we change which image of turning point 1 we consider primary from the point on fold B to the point on fold A which is its n-th preimage.* We claim that this is a general picture of the bifurcations of TPs and state the following conjecture.

Conjecture 1 *If there is a bifurcation where a TP disappears then there is always two TPs merging together and one can always find a (pre-)image A where one of the TPs is primary. One can also find a (pre-)image B where the second of the two TPs is primary and where the fold of W^S has a third TP which is primary in B. After the bifurcation the third TP is primary in A and not in B. This gives a continuous partition line and the partition is uniquely changing moving through the parameter space for all TPs that exist all along this path.*

That the partition line will be continuous follows because each folded part of W^U have either two PTPs or no PTPs and the folds of W^U is not dense in the phase space so two PTPs on neighbor folds of W^U can be connected by a curve. We have not managed to proof that the partition is unique when moving along different paths in the infinite dimensional parameter space but the example below suggests that this is the case. At the inflection point there may be created more than two TPs but it will be an even number of points and we can let two and two of the TPs bifurcate together.

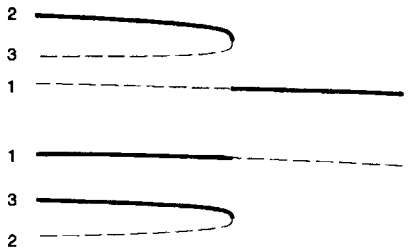

Figure 5.6: The bifurcation of primary (solid lines) and not primary (dashed lines) turning points as a function of a parameter.

The bifurcation in figure 5.5 is sketched as a function of a parameter in figure 5.6 with the same labeling of the turning points.

In figure 5.7 we show one numerical example for the Hénon map of this type of bifurcation. In this example fold B of W^U is above fold A in the phase space and fold B is the 3rd iterated of A such that the folding of B is modest. In figure 5.7 a) the down-most fold has the three TPs as in figure 5.5 a) fold A. In figure 5.7 b) a part of the uppermost foliation of figure 5.7 a) is magnified and we find the fold B which also has three turning points. The figures 5.7 c) and 5.7 d) show the manifolds at parameter values close to the bifurcation and in figures 5.7 e) and 5.7 f) there is only one PTP on the folds we are looking at. The partition line has jumped where it crosses fold A. Fold B is here on the right side of the partition line.

The most important bifurcation of this type is the one illustrated in figure 5.8 a) which give the bifurcation of the folds $\ldots 100s$ and $\ldots 101s$. This is the bifurcation giving the cusp structure in the examples of chapter 4. We follow the same principle in this case: the bent fold B moves to the left of the partition line and the partition line on fold $\ldots 10s$ jumps. This gives a partition which is not the one chosen by Grassberger and Kantz or the one the BW-method gives for parameters $a = 1.0$, $b = 0.54$. Instead it gives the one we indicated in figure 5.3.

Figure 5.8 b) illustrates a variation of the same bifurcation. In figure 5.5 we assumed that W^U is dense in the phase space such that the bifurcation is happening when the two turning points 1 and 2 are close in the phase space. This bifurcation may take place inside a basin of attraction. We are only interested in describing the non-wandering set and therefore is the bifurcation drawn in figure 5.8 b) of more interest than the point where the folding vanishes. In figure 5.8 b) the bifurcation is where the fold of W^U is tangent to the fold of W^S on the border of the basin of attraction. In figure 5.8 b) the turning points 1 and 3 is in the basin of attraction of ∞ and the of interest bifurcation takes place when also the turning point 2 moves out in the basin of attraction of ∞.

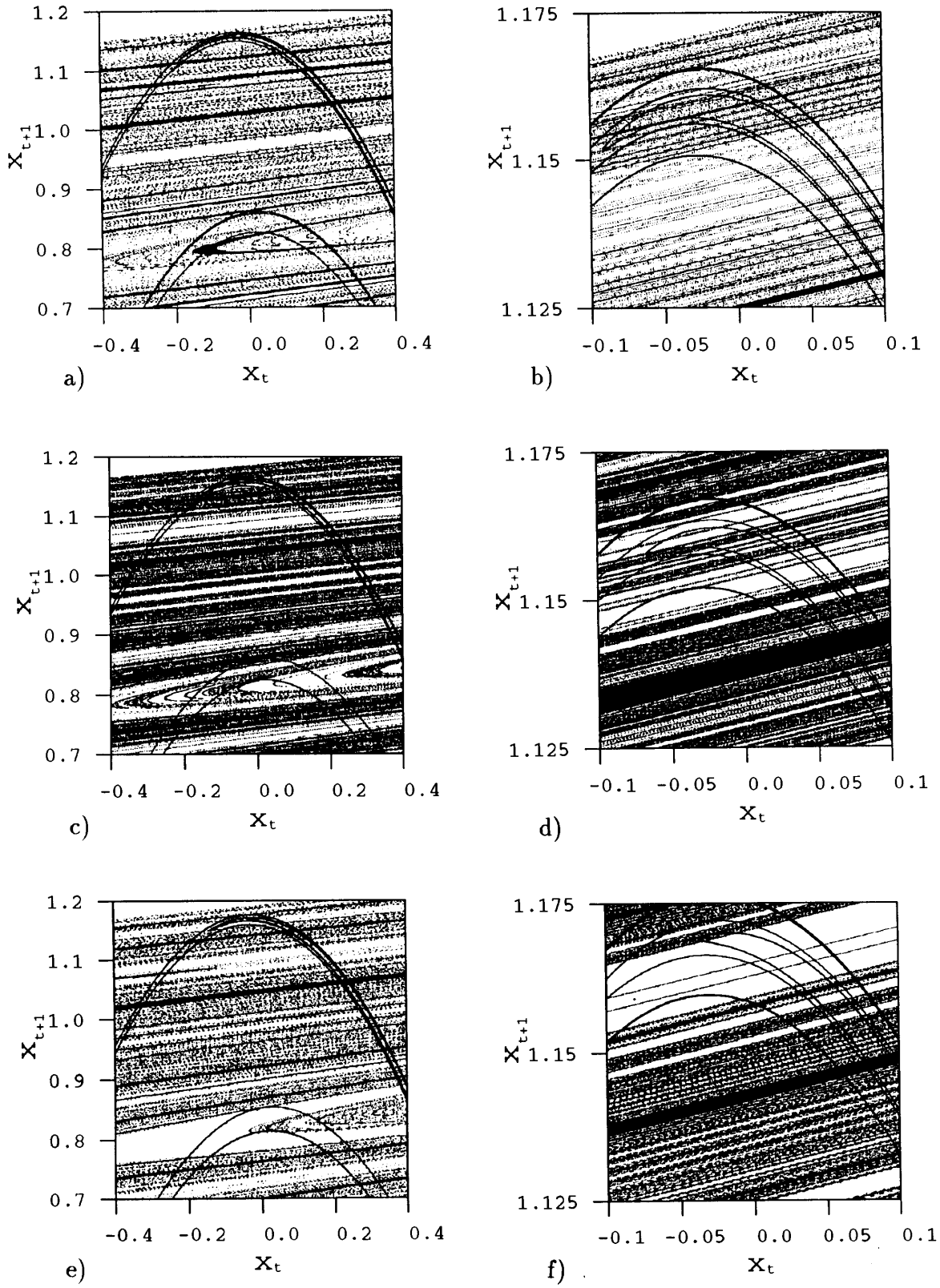

Figure 5.7: Bifurcation of the primary turning points of the Hénon map map. a) and b) $a = 1.6$, $b = 0.2$; c) and d) $a = 1.571$, $b = 0.2$; e) and f) $a = 1.562$, $b = 0.21$. b), d) and f) are magnifications.

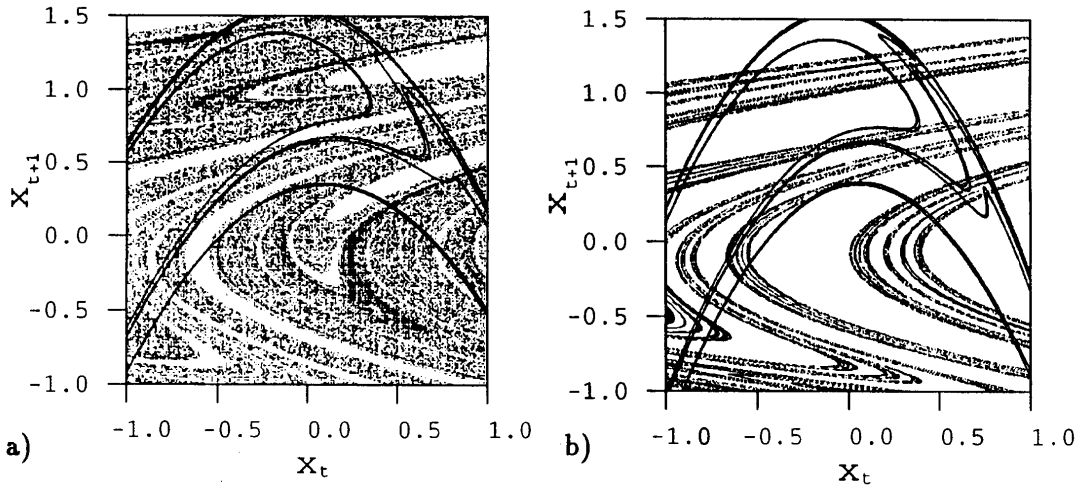

Figure 5.8: Bifurcation of a primary turning points of the Hénon map map. a) $a = 1.1$, $b = 0.522$; b) $a = 1.5$, $b = 0.58333$.

We examine some possible bifurcations in figure 5.9 to show how the mechanism of changing PTPs works in more complicated cases, and to investigate the uniqueness of the partition. Figure 5.9 a) and b) shows the same bifurcation as figure 5.5. The only differences is that we have drawn W^U as a straight line in A and we have added a new iteration C of the manifolds. In C none of the TPs are primary. In figure 5.9 c) there are 5 TPs and by pruning TP 4 and TP 5 from figure 5.9 c) we get figure 5.9 b). Notice that before the bifurcation TP 1 and TP 4 are primary in image C and TP 5 is primary in image B. The bifurcation changes TP 1 from being primary in C in figure 5.9 c) to be primary in B in figure 5.9 b). In figure 5.9 d) there are 7 TPs. The two TPs 6 and 7 can bifurcate together and we then after the bifurcation have the picture in figure 5.9 c). We have here a rather complicated foliation but in the bifurcation from figure 5.9 d) to figure 5.9 c) we are only interested in the fold with TP 3, TP 6 and TP 7. In figure 5.9 d) TP 6 is primary in B and TP 3 and TP 7 are primary in C. At the bifurcation TP 3 has to change from being primary in C to be primary in B which is the case in figure 5.9 c). These pictures describe a parameter path taking us from figure 5.9 d) to figure 5.9 a) through three bifurcations of turning points.

The figures 5.9 e) and f) show steps along another possible path in the parameter space changing figure 5.9 d) into figure 5.9 a). Instead of removing TP 6 and TP 7 from figure 5.9 d) we can remove TP 2 and TP 4 in a bifurcation. This give figure 5.9 e) and change TP 7 from being primary in C to be primary in A. From figure 5.9) we can have a bifurcation removing TP 6 and TP 7 giving figure 5.9 f)

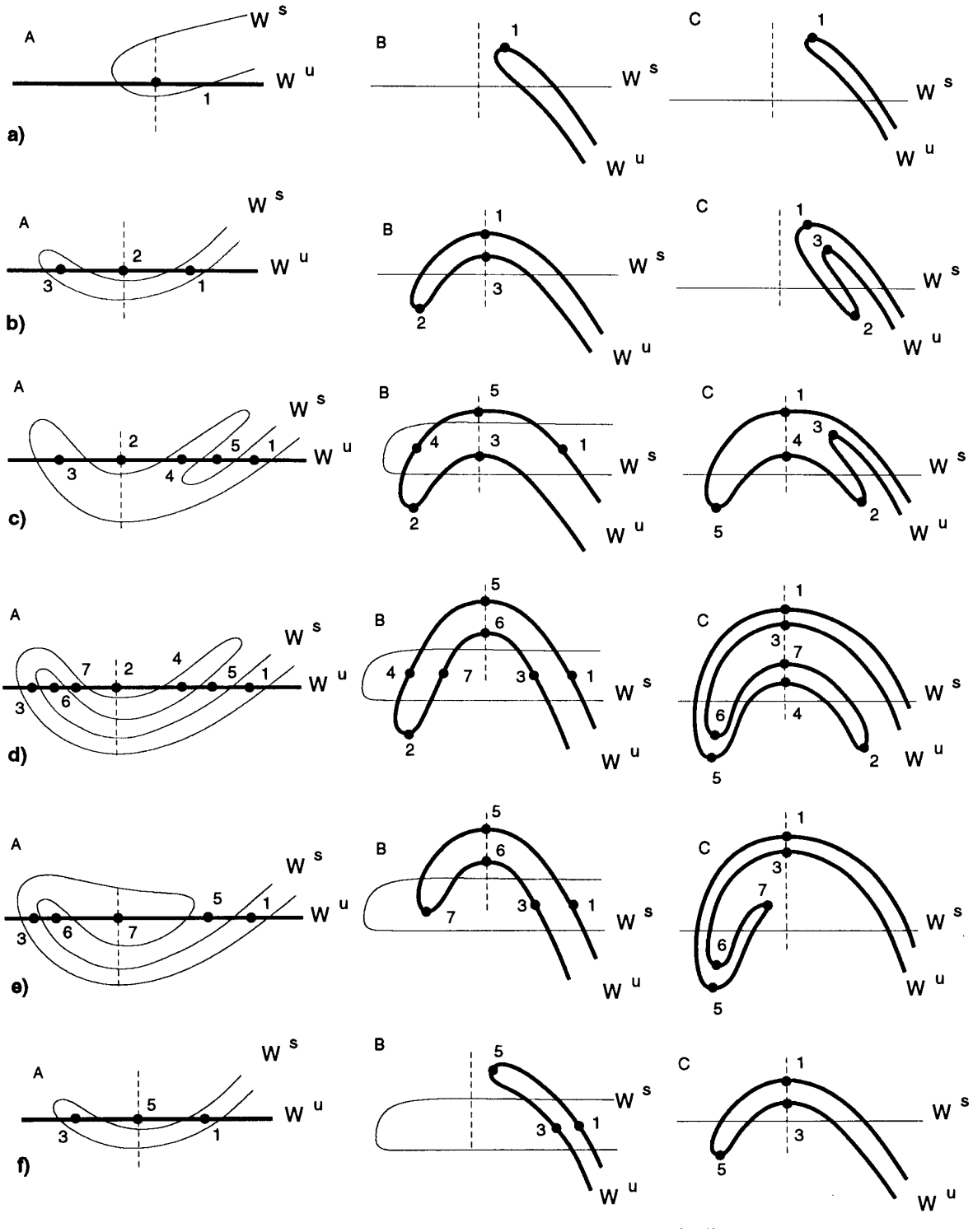

Figure 5.9: Different bifurcations of TPs in the once-folding map.

and we find that this change TP 5 from being primary in B to be primary in A. The figure 5.9 f) can be compared with figure 5.9 b) since both have three TPs but they are different since one TPs is different and the TPs are primary on different folds. By letting TP 3 and TP 5 in figure 5.9 f) bifurcate together we obtain figure 5.9 a) again and TP 1 will again be primary in A.

The path d)→c)→b)→a) changed TP 1 from being primary in C to be primary in A. The path d)→e)→f)→a) also changed TP to be primary in A. If the last path had given A primary in B or C this would have contradicted the uniqueness of the conjecture.

One bifurcation which can make the discussion more complicated is if one fold outside a second fold looses its PTP. This is unlikely to happen but if this happens we have to include more iterations of the innermost fold such that the PTPs on this folds jumps. In our example this would be the case if 4 and 5 bifurcated in figure 5.9 d).

Independent investigation has been done by Giovannini and Politi [85]. They have used a numerical method to investigate bifurcations of the PTP in the Hénon map and they use the point where the curvature is largest to define a PTP. They find that the PTP can jump when changing parameters in the way discussed here. They also discuss the case where the period 6 orbit changes symbolic description presented in ref. [107] and they conclude that the definition of which turning points that are primary is ambiguous and propose a pragmatic trial-and-error procedure. We suggest here that the definition of the primary turning points in the Smale horseshoe and the procedure to change the primary point each time there is a bifurcation gives a rigorous and unambiguous definition of all primary turning points. This procedure may however not be so useful in numerical studies but the principle may be combined with a numerical method like the one of Giovannini and Politi.

A consequence of our definition is that not only Does a PTP have a possibility to jump but it will jump each time the fold of W^U moves through a fold of WS. Because the turning points are bent sharply after some iterations for $|b|$ not too close to 1, most of these jumps are very small and not numerically detectable. This makes a discussion of an adiabatically change of a PTP more difficult.

5.3 Pruning front

Running a long orbit and plotting the (δ, γ) points for each iteration gives the figure 5.10 using the partition of Grassberger and Kantz $a = 1.4$, $b = 0.3$. The white region in the symbol plane is the symbolic values which no points in the

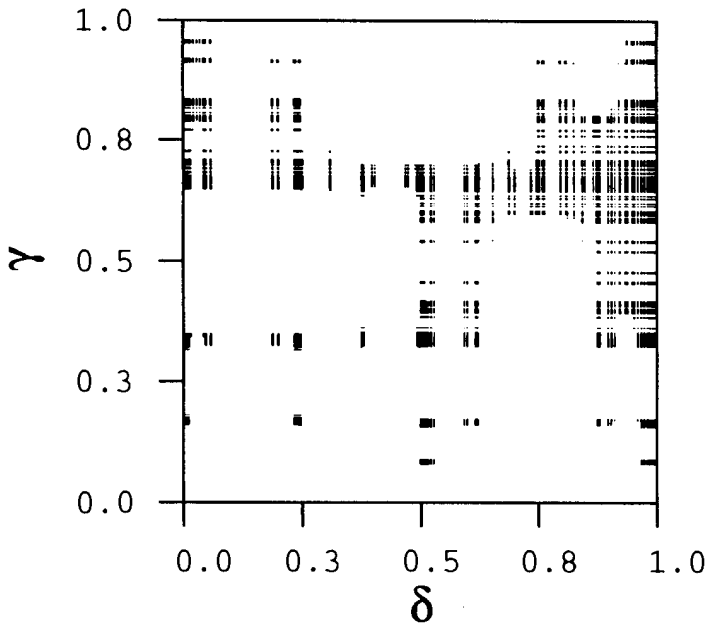

Figure 5.10: The chaotic orbit for $a = 1.4$, $b = 0.3$ plotted in the symbol plane.

chaotic attractor gives and these are the symbolic plane representation of the non existing orbits in the non-wandering set. We call this the forbidden regions of the symbol plane. Cvitanović et al. conjectured that in a plot like this (they plotted the unstable periodic orbits) the primary forbidden region is limited by the symbolic values (δ, γ) for the primary turning points. All forbidden regions are the primary forbidden region or a (pre-)image of this primary region. The border line is called the pruning front by Cvitanović et al. [53], and we also call the primary forbidden region in the symbol plane the primary pruned region.

In general is the pruning front a complicated monotone staircase curve but we can first investigate a simple example where the pruning front is an exact description of the non-wandering set.

5.3.1 Period 5

In figure 5.11 the stable and the unstable manifolds are plotted for the parameter values $a = 1.46$, $b = 0.17$. This are parameters inside the swallowtail crossing in figure 4.11 where the period 5 orbit is stable and in the two unimodal maps approximations the orbit has two points close to the two critical points. In figure 5.11 we find all turning points inside the basin of attraction for the period 5 orbit. This imply that the repellor is a hyperbolic set, a complete Smale horseshoe with a com-

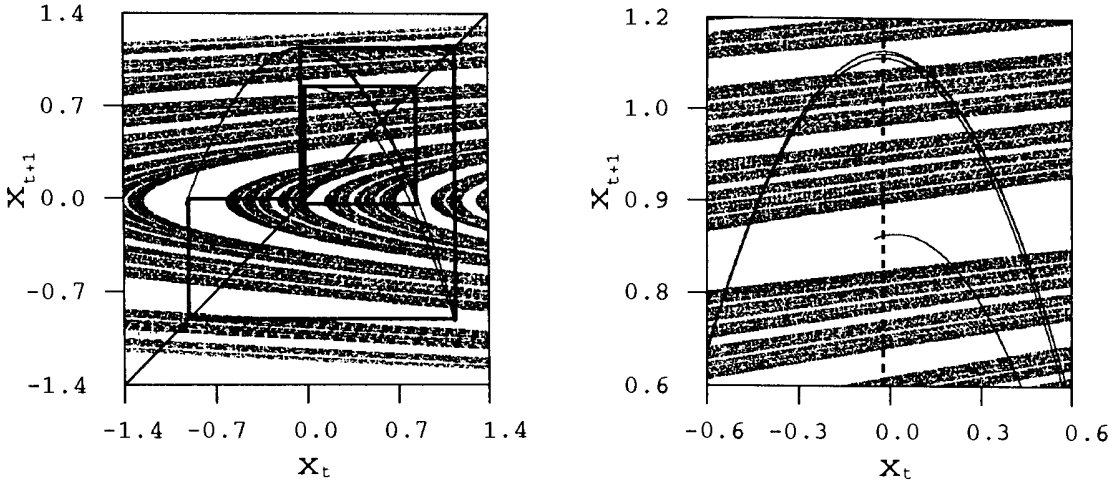

Figure 5.11: The stable and unstable manifolds and the stable period 5 orbit for $a = 1.46$, $b = 0.17$.

plicated folding. The repellor is plotted in the (x_t, x_{t+1}) plane in figure 5.12 and in the symbolic plane (δ, γ) in figure 5.13. We choose symbols according the the partition line indicated in figure 5.12. We want to describe the repellor and any partition curve crossing the unstable manifold in this basin of attraction gives the same symbolic dynamics for the repellor.

The symbolic strings which give the pruning front is the description of the unstable period 5 orbit. In figure 5.13 we have also plotted symbolic values for the four period 5 orbits; $\Box$ for $\overline{10111}$, $+$ for $\overline{10110}$, $\times$ for $\overline{10010}$ and $\triangle$ for $\overline{10011}$. We have plotted (δ, γ) only for the two cyclic permutations giving $\tau_0^{\max}$ and $\tau_1^{\max}$. In figure 5.13 we find that the values of γ $(= \tau)$ for the orbit $\overline{10111}$ gives the two maximum values the points of the repellor has. We have here an exact pruning front which is

$$\begin{aligned} \gamma &= 0.\overline{11010} \quad \text{for} \quad \delta \in (0, 1/4) \cup (3/4, 1) \\ \gamma &= 0.\overline{10110} \quad \text{for} \quad \delta \in (1/4, 3/4) \end{aligned} \tag{5.1}$$

In the symbolic parameter plane for the bimodal approximation this is the point $(\kappa_0, \kappa_1) = (0.\overline{10110}, 0.\overline{11010})$ and the approximation is exact in this case. This is the point in the corner of the swallowtail in the symbolic parameter plane in figure 4.10.

In figure 5.14 we have plotted the forbidden region and some of its images obtained by the shift operation. We find that the pruning front maps into the pruning front under iterations in the future which imply a finite markov partition. This is a consequence of that the pruning front is on periodic orbits.

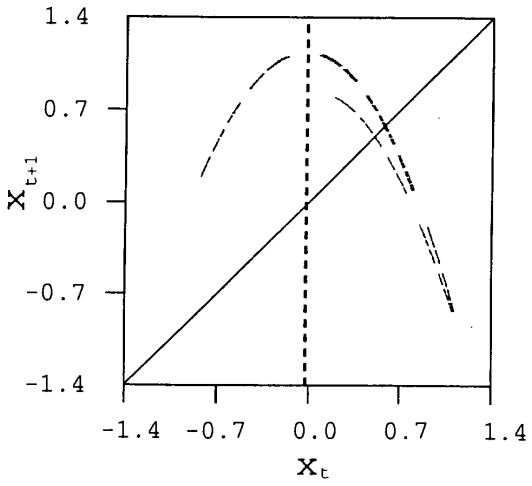

Figure 5.12: The repellor plotted in phase space (x_t, x_{t+1}) with the partition line defining symbols for $a = 1.46$, $b = 0.17$.

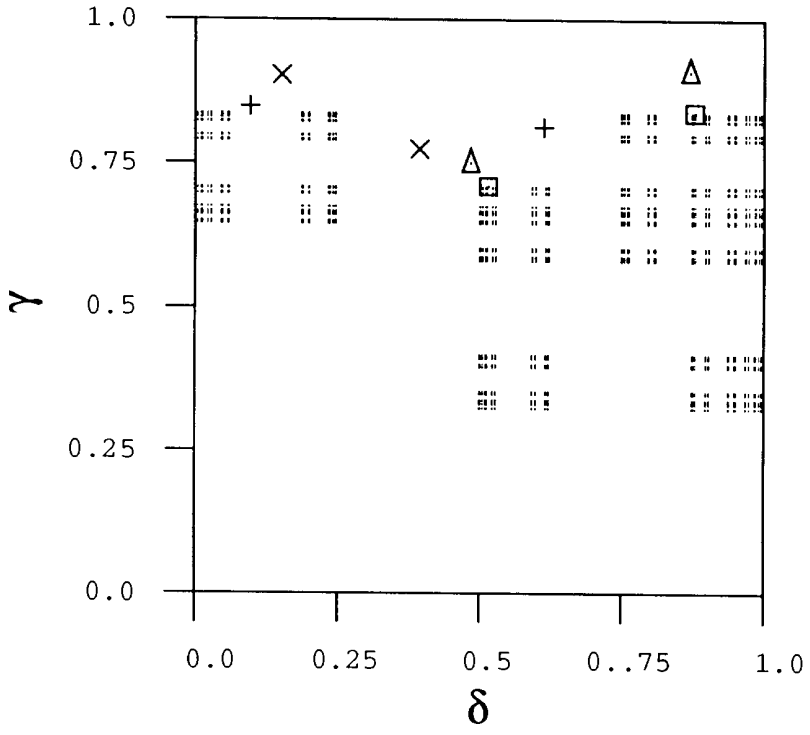

Figure 5.13: The repellor plotted in the symbol plane for parameters in the period 5 swallow tail crossing. The markers are : □ $\overline{10111}$, + $\overline{10110}$, × $\overline{10010}$ and △ $\overline{10011}$.

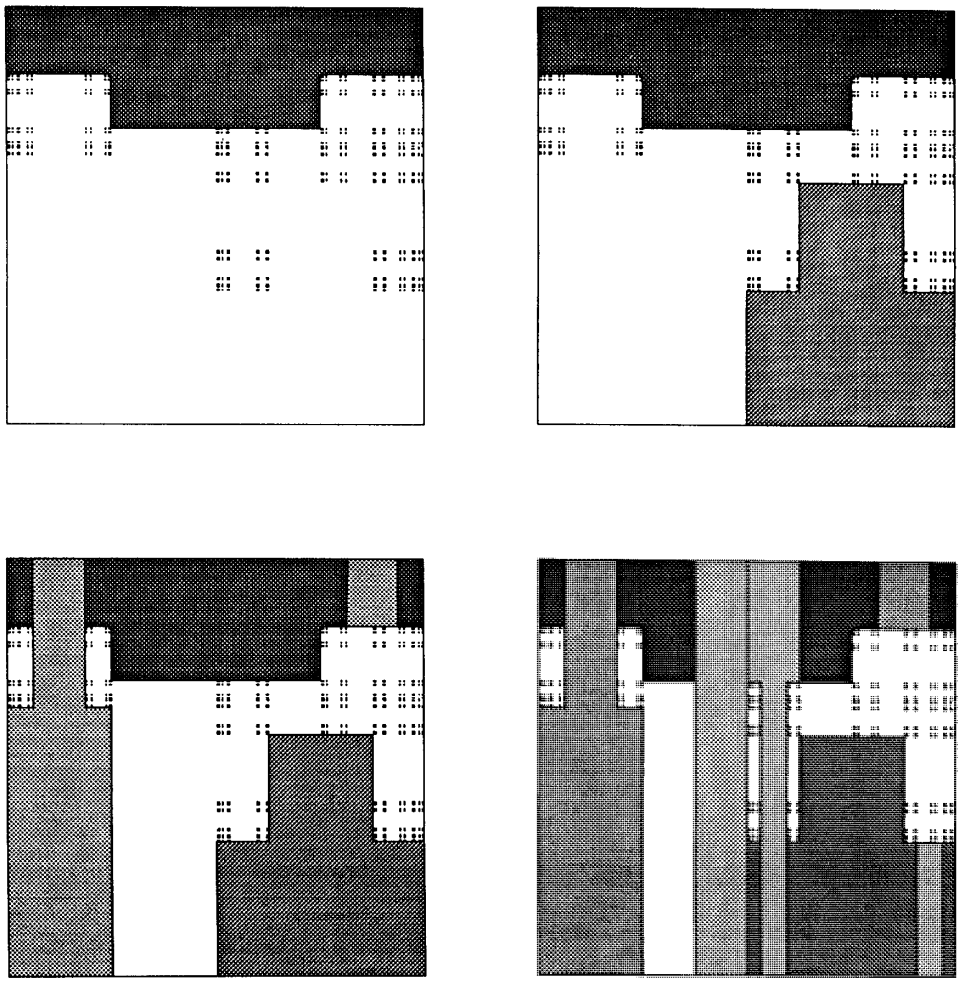

Figure 5.14: The primary forbidden region and its images.

In fact in this special case where we have a swallowtail crossing we only need one pruning front to describe the repellor because the step with the largest value $\gamma = 0.\overline{11010}$ maps onto the smaller value in the region above the non-wandering set as showed in the forth iteration in figure 5.14. The jump of the turning point here only affects the stable orbit which we know has to change symbolic description.

In other cases where a two step pruning front is exact, like the stable period 3 and stable period 5 orbit for parameters $a = 1.8125797$, $b = 0.0228643$ discussed in ref. [53] the front cannot be reduced to a one step front.

We can now use the two step pruning front to describe the bifurcation giving the period 5 swallowtail. The assumption we do is to assume that the pruning front only has two steps for all parameter values. If both steps have the same γ value and we let it decrease from 1.0, the pruning front passes through the markers in figure 5.13 in the order $\overline{10011}$, $\overline{10010}$, $\overline{10110}$ and $\overline{10111}$. These bifurcations give the two windows $\overline{1011\epsilon}$ and $\overline{1011\epsilon}$. Let then γ for the step $\delta \in (0, 1/4) \cup (3/4, 1)$ decrease while γ for $\delta \in (1/4, 3/4)$ is fixed at 1.0. Then the pruning front passes the markers in the symbol plane in the order $\overline{10110}$, $\overline{10010}$, $\overline{10011}$ and $\overline{10111}$ and this is the two windows $\overline{1010\epsilon}$ and $\overline{1110\epsilon}$. When we let both steps in the pruning front decrease we obtain the situation in figure 5.13. This is the same result as we obtained in the discussion with the approximation of a bimodal map. The bimodal approximation is identical to approximation the pruning front with two steps.

5.3.2 4 modal approximation

We can now easily see the connection between the multi-modal map description and the pruning front. The symbolic past of the point x_0 that is used to determine the value δ is the same symbols that we used to determine which map a point was on in the bimodal, four-modal, eight-modal, etc. approximation. In the bimodal approximation a point x_t is on map 1 if $s_{t-1} = 1$ which corresponds to that $\delta \in (0, 1/4) \cup (3/4, 1)$. A point on map 0 has $s_{t-1} = 0$ and therefore $\delta \in (1/4, 3/4)$. The two map approximation then corresponds to a pruning front with only two values; $\gamma = \kappa_1$ in the intervals $\delta \in (0, 1/4) \cup (3/4, 1)$ and $\gamma = \kappa_0$ in the interval $\delta \in (1/4, 3/4)$.

In a similar way a four-modal approximation correspond to approximate the exact pruning front with the values:

$\gamma = \kappa_{11}$ for $\delta \in (0, 1/8) \cup (7/8, 1)$

$\gamma = \kappa_{01}$ for $\delta \in (1/8, 1/4) \cup (3/4, 7/8)$

$\gamma = \kappa_{00}$ for $\delta \in (1/4, 3/8) \cup (5/8, 3/4)$

$\gamma = \kappa_{10}$ for $\delta \in (3/8, 5/8)$

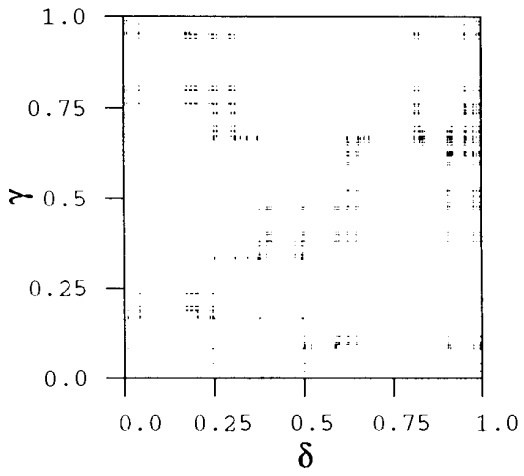

Figure 5.15: A chaotic orbit plotted in symbol space defined by the partition line in figure 5.3 for $a = 1.0$, $b = 0.54$.

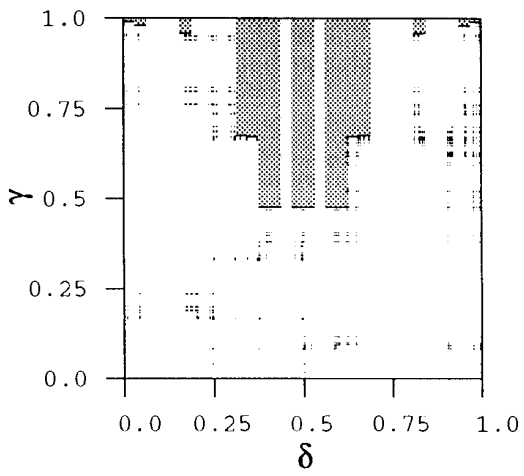

Figure 5.16: The pruning front plotted together with a chaotic orbit in the symbol space for $a = 1.0$, $b = 0.54$

The generalization to any 2^n partition in δ works the same way.

5.3.3 Pruning front for $a = 1.0$, $b = 0.54$

We can construct the pruning front for the chaotic attractor with parameters $a = 1.0$, $b = 0.54$. We use the partition in figure 5.3 which we believe is the unique partition following the role given above. The chaotic orbit gives the points in the symbol plane plotted in figure 5.15.

To construct the pruning front up to a given resolution we have numerically found the primary turning points of the 2^4 or less folds of the unstable manifold that are described by the symbol strings $s_{-4}s_{-3}s_{-2}s_{-1}s_0\cdot$. The symbol s_0 tells whether the point on the fold is to the right or to the left of the primary tangency and it does not distinguish between different folds. The symbol string specify a part of the foliation of the unstable manifold and we choose the primary tangency on the the fold with largest future symbolic value γ.

We find that the following 8 folds have a primary tangency:

$$1110s_0\cdot \quad 0010s_0\cdot \quad 1010s_0\cdot \quad 1000s_0\cdot \quad 0000s_0\cdot \quad 0001s_0\cdot \quad 0111s_0\cdot \quad 1111s_0\cdot \qquad (5.2)$$

while the other 8 folds do not have any primary tangencies. The primary tangency points give respectively the future symbolic values γ; 0.476190, 0.476201, 0.476225, 0.672550, 0.675583, 0.958018, 0.979120, 0.989622. The symbol string $s_{-4}s_{-3}s_{-2}s_{-1}s_0\cdot$ gives 2^5 intervals on the δ axis of length 2^{-5}. For 16 of these intervals which have a primary tangency point we draw the pruning front line and draw

the forbidden region as a gray rectangle above the pruning front line in figure 5.16. The white strips in figure 5.16 is from the 16 intervals on δ which do not have a primary tangency. We do not need a pruning front here because this part of the region is pruned by an image of one of the gray regions. If we want the primary pruned region to be a connected region we can include the white regions above the largest of the two γ values of the neighboring part of the pruning front.

Since the homoclinic tangencies are ordered along the manifolds and the symbol plane has the same ordering as the manifold structure then it follows that the pruning front is monotonously increasing from $\delta = 1/2$ when δ increases or decreases.

5.4 Pruning front for the $|b| = 1$ limit

In the limit of an area preserving map, assuming the symbolic description of orbits is still valid, we have a symmetry between the pruning front and the preimage of the pruning front.

The backward iteration of the Hénon map (4.1) is

$$x_{t-1} = -\frac{1}{b}(1 - ax_t^2 - x_{t+1}) \tag{5.3}$$

If $b = -1$ we have

$$x_{t-1} = 1 - ax_t^2 - x_{t+1} \tag{5.4}$$

This map is the same backward in time as forward in time and interchanging the horizontal and the vertical axis in the phase space plane leaves the non-wandering set unchanged. The non-wandering set and the manifolds are symmetric with respect to the diagonal $x_{t+1} = x_t$. In symbol plane this imply that the points in the non-wandering set are symmetric around the diagonal $\gamma = \delta$. The pruning front is then also symmetric with its preimage. One can think of this preimage as a pruning front of the stable manifold which in this case have to be identical to the pruning front of the unstable manifold.

If $b = 1$ we have

$$x_{t-1} = 1 - ax_t^2 + x_{t+1} \tag{5.5}$$

The sign in front of x_{t+1} has changed and this implies that a point in the non-wandering set is symmetric to a point reflected both around the diagonal and the x_{t+1} axis and this gives $x_{t+1} = -x_t$ as a symmetry line. In the symbol plane the symmetry line is $\gamma = 1 - \delta$. The pruning front is symmetric to its preimage with respect to $\gamma = 1 - \delta$ when $b = 1$. This preimage may be regarded as the pruning front of the stable manifold.

The pruning front is exactly symmetric to its preimage. An approximation of the pruning front with constant γ for intervals of δ of length $2^{-(n+1)}$ is in a general case not symmetric with its preimage because the values of γ will not be equal $m \cdot 2^{-(n+1)}$ with $0 \leq m \leq 2^{(n+1)}$. We can however by using the symmetry identify the cusp bifurcations in a n-approximation which will be at the $b = 1$ or $b = -1$ line.

We can study the isolated cusp bifurcations in the 4-fold approximation of the once-folding map. At the bimodal cusp bifurcation (codimension 2) one period k orbit has two points at the exact pruning front and also two points at the approximated pruning font. We call the cyclic permutations of the symbol string giving κ_{00}: $\overline{S}$, and the permutations giving κ_{10}: $\overline{S'}$. The cusp can be on the $b = -1$ line if

$$\begin{aligned} \gamma(\overline{S}) &= \delta(\sigma^{-1}(\overline{S'})) \\ \delta(\overline{S}) &= \gamma(\sigma^{-1}(\overline{S'})) \\ \gamma(\overline{S'}) &= \delta(\sigma^{-1}(\overline{S})) \\ \delta(\overline{S'}) &= \gamma(\sigma^{-1}(\overline{S})) \end{aligned} \tag{5.6}$$

and on the $b = 1$ line if

$$\begin{aligned} \gamma(\overline{S}) &= 1 - \delta(\sigma^{-1}(\overline{S'})) \\ \delta(\overline{S}) &= 1 - \gamma(\sigma^{-1}(\overline{S'})) \\ \gamma(\overline{S'}) &= 1 - \delta(\sigma^{-1}(\overline{S})) \\ \delta(\overline{S'}) &= 1 - \gamma(\sigma^{-1}(\overline{S})) \end{aligned} \tag{5.7}$$

where σ^{-1} is the inverse shift operation of the symbol string, corresponding to a map once backward in time. This imply that all points in the symbol plane are symmetric to each other with respect to a symmetry line. These symmetric orbits are called the self-adjoint orbits by Mira [153].

The period 4 orbit $\overline{1001}$ gives a cusp for the topological parameter values $\kappa_{00} = \tau(\overline{1001}) = 0.\overline{1110}$ and $\kappa_{10} = \tau(\overline{1100}) = 0.\overline{1000}$. For the two cyclic permutations $\overline{S} = \overline{1001}$ and $\overline{S} = \overline{1100}$ we find

$$\begin{aligned} &\gamma(\overline{1001}) = 0.\overline{1110} = 1 - 0.\overline{0001} = 1 - \delta(\overline{0110}) = 1 - \delta(\sigma^{-1}(\overline{1100})) \\ &\delta(\overline{1001}) = 0.\overline{1011} = 1 - 0.\overline{0100} = 1 - \gamma(\overline{0110}) = 1 - \gamma(\sigma^{-1}(\overline{1100})) \\ &\gamma(\overline{1100}) = 0.\overline{1000} = 1 - 0.\overline{0111} = 1 - \delta(\overline{1100}) = 1 - \delta(\sigma^{-1}(\overline{1001})) \\ &\delta(\overline{1100}) = 0.\overline{0111} = 1 - 0.\overline{1000} = 1 - \gamma(\overline{1100}) = 1 - \gamma(\sigma^{-1}(\overline{1001})) \end{aligned} \tag{5.8}$$

This is the symmetry relation in (5.7) and this cusp is numerically found to be on the $b = 1$ axis, figure 4.31. Several examples of cusps on the $|b| = 1$ lines are given by Mira [153]. Codimension 2 bifurcations in other approximations have a similar symmetry.

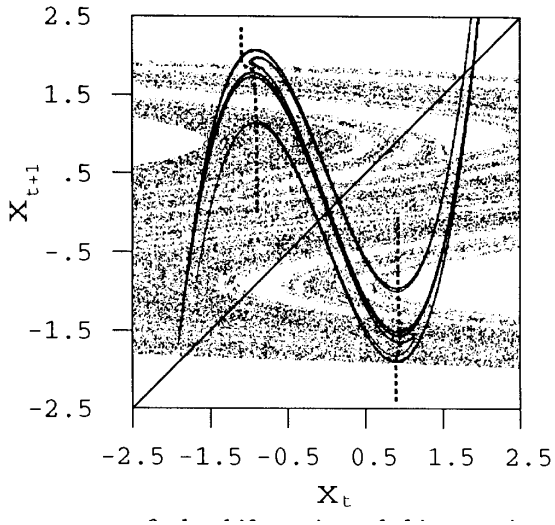

Figure 5.17: The stable and unstable manifolds and the partition lines (dashed lines) for the twice-folding map, $a = 2.55$, $b = 0.1$ and $c = 0.29$.

Codimension 3 and higher bifurcations may also be centered on the $|b| = 1$ line if there are three or more points on the pruning front which have a symmetry around one of the symmetry lines. We do not expect to find a bifurcation of this type in the Hénon map since the Hénon map only has two parameters. As we have seen for the period 8 orbit crossings may a codimension 3 bifurcation structure be revealed in the Hénon map by adding a second parameter.

5.5 Pruning fronts for the twice-folding map

We can also construct the pruning fronts for a n-folding two dimensional map. Each region close to the critical points of the one dimensional map has a partition line through the primary turning points. This give n independent pruning fronts describing the system. We show a numerical example of the pruning front for the twice-folding map (4.55).

The stable and the unstable manifolds are drawn in figure 5.17 for the map (4.55) with $a = 2.55$, $b = 0.1$ and $B = 0.29$. Two partition curves are drawn with dashed lines through the primary turning points in figure 5.17. Also for this twice-folding map we use the rule for changing the partition line defined above for the Hénon map. The difference from the Hénon map to this map is that here the folds A and B in figure 5.5 can go through two different partition lines. The bifurcation of the turning points take place in the same way and the definition of which of the turning points that are primary changes the same way as above. By starting with a complete Smale horseshoe we conjecture that there is a unique partition line.

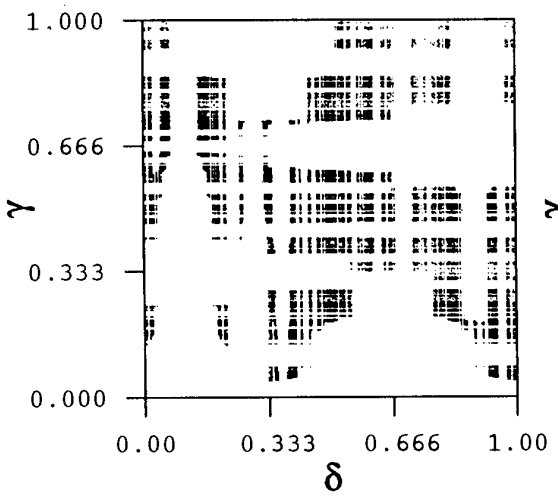

Figure 5.18: The repellor plotted in the symbol plane for $a = 2.55$, $b = 0.1$ and $c = 0.29$.

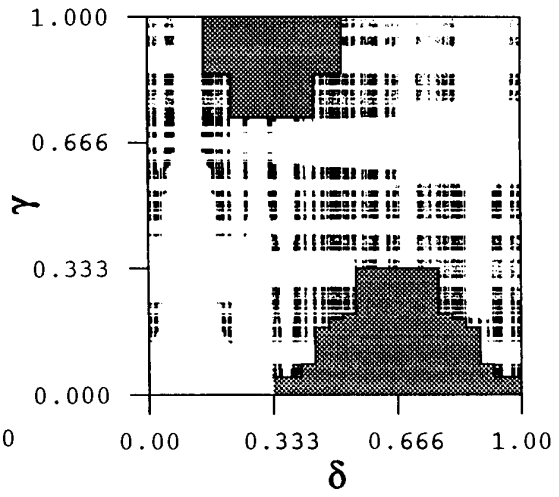

Figure 5.19: The repellor and the two pruning fronts plotted in the symbol plane for $a = 2.55$, $b = 0.1$ and $c = 0.29$.

This map is a pruned version of the flipped twice folded Smale horseshoe in figure 3.15, and the well ordered symbols and the symbolic values (δ, γ) are given in eqs. (3.11) and (3.10). The repellor is drawn in the symbol plane in figure 5.18. We can construct the pruning front by finding the primary turning points, calculate the symbolic description of these and draw the two primary pruned regions. In figure 5.19 the pruning front and the forbidden region is drawn together with the repellor. The two pruning fronts are independent of each other and the two forbidden regions are quite different in this example. We have here chosen to draw the connected primary pruned region.

5.6 Lozi map

The piecewise linear Lozi map (4.3) has a stable manifold W^S and an unstable manifold W^U which also are piecewise linear and are drawn in figure 5.20 for parameter values $a = 1.7$, $b = 0.5$ and for $a = 1.53$ and $b = 0.5$. The analysis of this map is simpler than the Hénon map because W^U has all the primary turning points on the line $x = 0$ and the symbolic description of a point (x_t, x_{t+1}) is given by the sign of x_{t+1}. The pruning front for the Lozi map was also given by Cvitanović, Gunaratne and Procaccia in ref. [53]. The partition and the pruning in the Lozi map has also been studied in detail by D'Alessandro, Isola and Politi [2].

A bifurcation of a primary turning point of the Lozi map is sketched in fig-

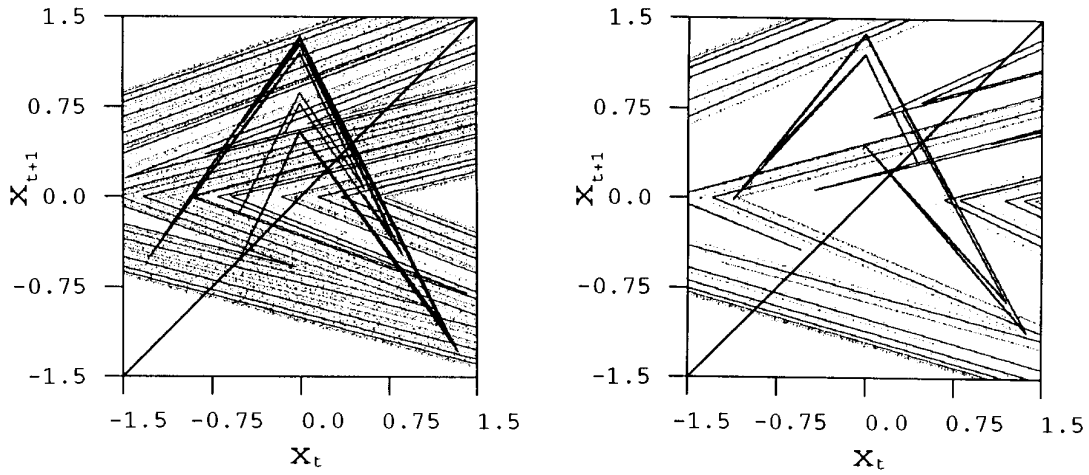

Figure 5.20: The stable and unstable manifolds for the Lozi map, a) $a = 1.7$, $b = 0.5$. b) $a = 1.53$, $b = 0.5$.

ure 5.21. The three points bifurcates together and a jump of the primary turning point is 0. We can not have an isolated cusp in the Lozi map and an orbit does not change symbolic dynamics in a loop in parameter space.

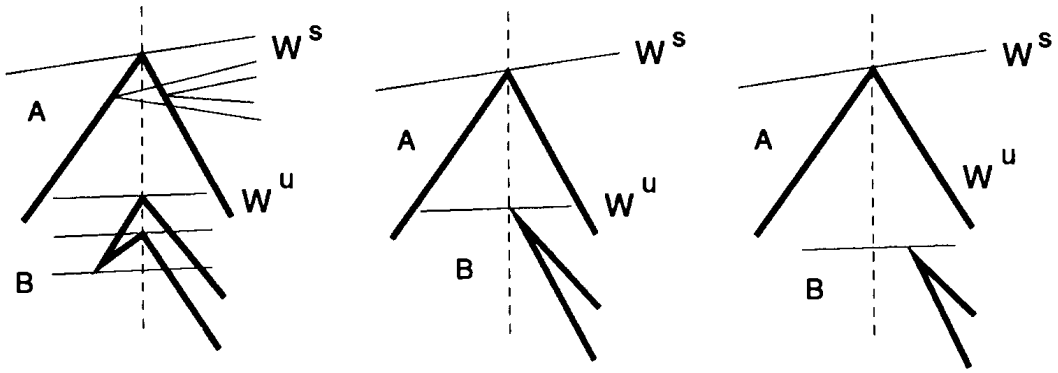

Figure 5.21: The bifurcations of primary turning points in the Lozi map.

Part III

Billiards

A large class of mechanical systems is called billiards in the chaos literature. The billiards considered here are 2-dimensional dynamical systems consisting of a point particle bouncing elastically off the billiard walls. The motion between collisions is either a free motion with constant velocity or an other simple motion for example a fall in a constant gravitational field.

We shall here present a general method to describe these systems with symbolic dynamics. We show on a number of examples that we can construct a well ordered symbol plane and a pruning front in this symbol plane. The method gives systematic approximate Markov partitions and approximate zeta functions that we expect to have better convergence than what can be obtained by expansions obtained by a simple numerical searches for periodic orbits. There are at present no other methods for describing the admissible orbits, except exhaustive numerical search for all periodic orbits up to a given length.

Some billiards, for example the 3-disk system can easily be identified with a Smale horseshoe for some parameter values, and a well-ordered symbol plane can be established. In other cases, like the stadium and the wedge billiard there is no direct correspondence to a simple horseshoe, but the idea of keeping the ordering by finding which symbols preserve or reverse the ordering still applies.

In the billiards we consider here there are no stable orbits. The bifurcations take place with the stable and the unstable manifolds crossing at a finite angle. The limiting orbits are singular orbits, analog to the orbits from the critical point of the tent map. Billiards are important as a test of the pruning front idea of Cvitanović et.al. [53], as the pruning front are here *exact* and not resting on conjectures, as is the case for the Hénon map and the smooth potentials we study in chapter 10.

Chapter 6

Symbolic dynamics of billiards

Our goal is to find a way to describe the orbits in the billiard systems by applying symbolic dynamics. This will be different than the methods applied by Sinai and others which proof for some billiards the existence of a countable Markov partition. As our first step we will define a covering symbolic description of the system, which is exact in one limit of parameters, or symbols which always give a unique description of orbits existing but which also describe orbits not existing in the system. In the case of billiards that give a complete Smale horseshoe non-wandering set, the definition of symbols is straightforward. In other systems finding a good symbolic description may be more difficult, but we outline a general method for approaching this problem.

The second important step, necessary for determining the symbolic strings corresponding to admissible orbits is to determine a symbolic representation of orbits which has an orientation topologically faithful to the orientation of the foliation of stable and unstable manifolds in the phase space. This is necessary because the mechanism giving forbidden orbits reflects this ordering in the phase space. This is the case for all examples given here and we conjecture that this is, if not always true, at least typical for most systems.

There is unfortunately no general theory for construction of symbolic dynamics for an arbitrary dynamical system. For each new system one has to *think* before defining the symbols. However, for simple billiard systems it seems that giving one symbol for each bounce off the different dispersive walls, and two symbols for focusing walls; one for clockwise and one for counterclockwise bounces suffices. Fictitious straight walls introduced to reduce the dynamics to a fundamental domain can also be given one symbol each. If there are other forces in the system, like gravity or rotation, other definitions of the symbols may be required.

A correctly ordered symbol alphabet is obtained from the first alphabet by

investigating how the symbolic description of the orbit changes when we change one of the phase space variables. If the non-wandering set in some limit of parameters is a complete Smale horseshoe then we define the new symbols from one of the alphabets introduced in chapter 3. at each level of the Cantor set such symbols increase as we scan across the vertical strips and the horizontal strips. If there is no limit in which the billiard is a complete horseshoe, we define well ordered symbols by using the same method of ordering the vertical and horizontal strips in phase space. In general the strips are overlapping and not complete, and strips corresponding to some symbol string may not exist. We first assume the strips are complete, then construct the well ordered symbols and finally remove from the symbol plane the parts of the strips that do not exist in phase space. Examples of such systems are the stadium (section 6.5) and the wedge billiard (section 6.4).

6.1 3-disk

The simplest example of a billiard is the 3 disk system. The 3 disk system consists a point particle moving freely on a 2-dimensional plane and bouncing elastically off the walls of 3 disks placed in the plane. We will mostly work with the symmetric system where the 3 disks have the same radius, and the same distance between any two disks. In this system we set the radius to be 1 and choose the parameter r to be the distance between the centers of the disks. This system is studied by Eckhardt and Cvitanović [66, 48], Gaspard and Rice [83, 82] and others.

We choose the bounce of the particle off one disk to be our Poincaré map. The 1-dimensional position along the edge of the disk x, and the angle ϕ, between the normal vector of the wall and the direction of the outgoing velocity are variables sufficient to uniquely specify an orbit. In the symmetric 3 disks system the three disks yield the same Poincaré map. For some configurations of the 3 disks system this two dimensional Poincaré map gives a once folding complete horseshoe with two vertical and two horizontal strips ordered as in figure 3.13. In the symmetric system this configuration is obtained by choosing the distance between the disks sufficiently large.

The two horseshoe strips are constructed as follows: we choose to observe the particle when it bounces off the disk that we denote no. 1. The other disks are enumerated counterclockwise as no. 2 and no. 3. If the particle bounces out from point x then there are two intervals of the angle ϕ which give a new bounce in one of the other two disks. In figure 6.1 we draw the outgoing angles. Doing this for all x-values gives two strips sketched in figure 6.2 a). This is the first generation in

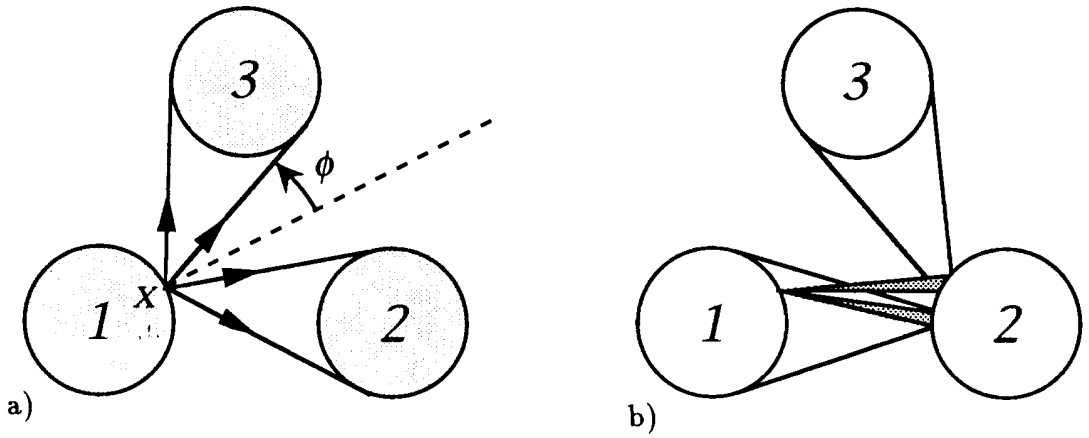

Figure 6.1: a) The 3 disk system and the phase space variables. b) Orbits of different angles bouncing into the next disk.

the construction of the forward Cantor set which corresponds to the vertical strips in the horseshoe map in figure 3.11. We use Smale's horseshoe notation and call these two strips $g(Q) \cap Q$. The strips are limited to the region

$$-\pi/2 \leq x \leq 2\pi/3, \quad -\pi/2 \leq \phi \leq \pi/2 \tag{6.1}$$

An angle $|\phi| > \pi/2$ would correspond to a particle penetrating the disk. If x is less than $-\pi/2$ or larger than $2\pi/3$ one can not reach either of the other disks.

The two strips are given symbolic description by recording the labels of the two disks that the particle has bounced off. This gives the two symbolic strings

$$\{12, 13\}. \tag{6.2}$$

In figure 6.2 a) the lower strip is 12 and the upper strip is 13.

The next generation in this Cantor set of strips, $g^{(2)}(Q) \cap Q$, is obtained by finding all points in (x, ϕ) for which the outgoing particle reaches at least two disks. In figure 6.1 b) we have drawn the orbits from disk 1 that first bounce off disk 2, and then reach either disk 1 or 3. This are two intervals of angles strictly inside the interval giving one bounce off disk 2. In the phase space this gives four strips strictly inside the two first strips, figure 6.2 b), with the symbolic descriptions

$$\{121, 123, 132, 131\} \tag{6.3}$$

ordered from the lowermost strip to the uppermost strip. The third level of the Cantor set, figure 6.2 c), gives eight strips and their symbolic description from the lowermost to the uppermost is

$$\{1212, 1213, 1231, 1232, 1323, 1321, 1312, 1313\} \tag{6.4}$$

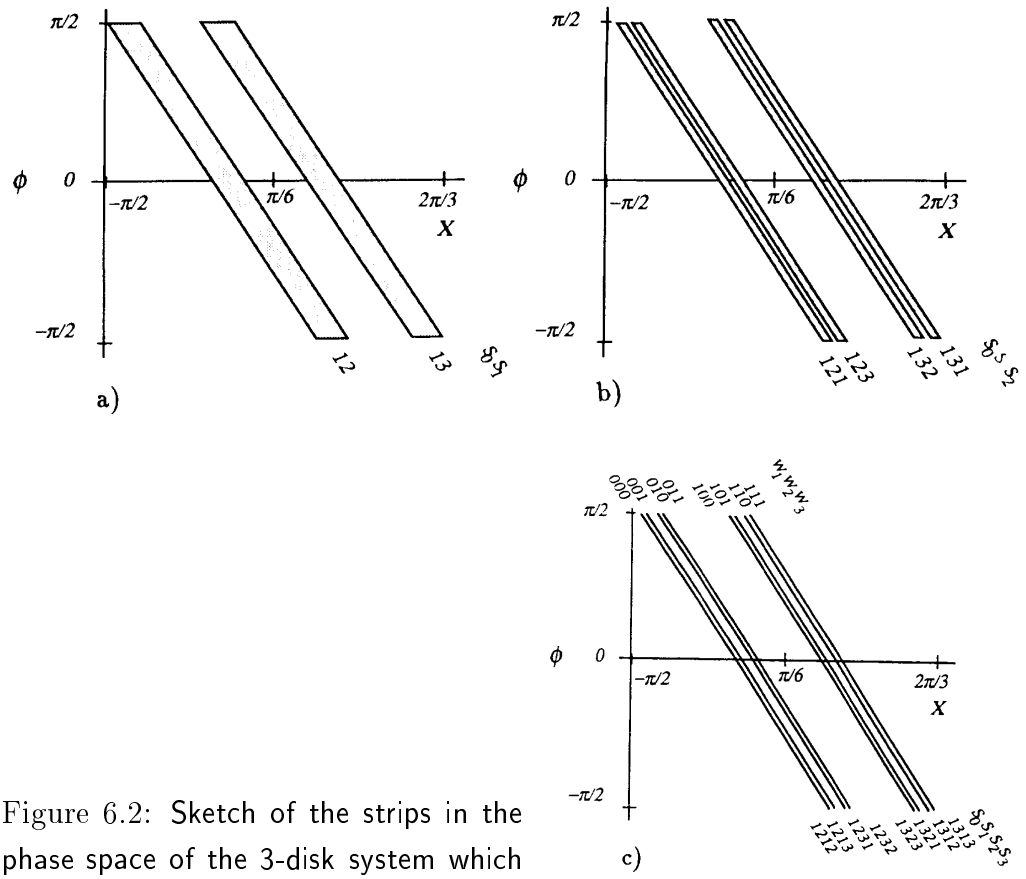

Figure 6.2: Sketch of the strips in the phase space of the 3-disk system which correspond to a point bouncing in the system at least a) once, b) twice, c) three times.

In this way we construct the forward Cantor set of lines as the union of all orbits that continue to bounce between the disks forever. Each line in the Cantor set has a unique label

$$s_0 s_1 s_2 s_3 \ldots \tag{6.5}$$

where $s_i \in \{1, 2, 3\}$. Since this is a binary Cantor set, a three letter alphabet is larger than necessary. A two letter alphabet description can be obtained by choosing the letter $v_i = 0$ if the bounce is counterclockwise, that is if $s_{i-1}s_i = 12$ or 23 or 31, and choosing the letter $v_i = 1$ if the bounce is clockwise $s_{i-1}s_i = 13$ or 21 or 32. We can state this as the algorithm

$$\begin{aligned} &v_i' = s_i - s_{i-1} \\ &\text{if } v_t' < 0 \text{ then } \; v_t = v_t' + 2 \\ &\text{else } \; v_t = v_t' - 1 \end{aligned} \tag{6.6}$$

In the case of a symmetric system one does not need to remember the starting disk. This two letter alphabet $v_i \in \{0,1\}$ is then the alphabet corresponding to the alphabet used in the Smale horseshoe. A time iteration of this orbit corresponds to a simple shift in the symbol sequence.

Because of the dispersive mirror reflection at each disk both strips change the orientation both forward and backward in time as in figures 3.13 and 3.13. We will below discuss the different change in orientation for bounces off dispersing or focusing walls. We then obtain well ordered symbols by the algorithm (3.9)

$$\begin{array}{rcl} w_t & = & \begin{cases} v_t & \text{if } t \text{ odd } > 0 \\ 1-v_t & \text{if } t \text{ even } > 0 \end{cases} \\ w_t & = & \begin{cases} v_t & \text{if } t \text{ even } \leq 0 \\ 1-v_t & \text{if } t \text{ odd } < 0 \end{cases} \end{array} \tag{6.7}$$

The strips in figure 6.2 c) are also labeled by the symbol strings $w_1 w_2 w_3$ and we find that from the lowermost to the uppermost they are ordered as

$$\{000, 001, 010, 011, 100, 101, 110, 111\} \tag{6.8}$$

A symbolic value

$$\gamma = 0.w_1 w_2 w_3 \ldots = \sum_{t=1}^{\infty} \frac{w_t}{2^t} \tag{6.9}$$

then increases along any curve that monotonously crosses the lines in the Cantor set, exactly as a well ordered forward symbolic value should do.

The backward iteration is found by finding the orbits that arrived at the point (x, ϕ). Some of these orbits have been bouncing off one of the other two disks before reaching the point (x, ϕ), and this gives the two strips corresponding to the backward iteration of the Smale horseshoe $g^{(-1)}(Q) \cap Q$. These are the vertical strips in the horseshoe picture. Since we know that the incoming angle is the negative of the outgoing angle (time reversal invariance) we obtain the strips $g^{(-1)}(Q) \cap Q$ by reflecting the strips $g(Q) \cap Q$ around the x-axis. These strips and the four rectangles $g(Q) \cap g^{(-1)}(Q)$ are sketched in figure 6.3 a).

The two backward strips $g^{(-1)}(Q) \cap Q$ have the symbolic description $s_{-1} s_0 \in \{21, 31\}$. In the same way as for the future symbols we define v_i as the symbol giving either a clockwise or an anticlockwise bounce. The well ordered symbol w_i is also given by (3.8) and we define the symbolic value for the past to be

$$\delta = 0.w_0 w_{-1} w_{-2} \ldots = \sum_{t=1}^{\infty} \frac{w_{1-t}}{2^t} \tag{6.10}$$

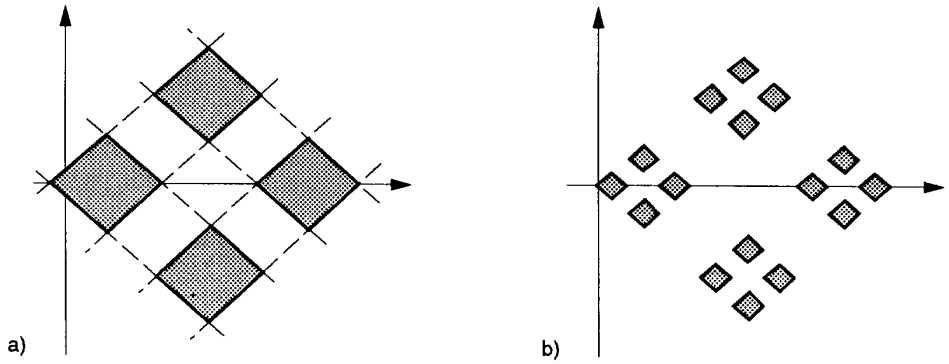

Figure 6.3: Sketch of the points in the phase space of the 3 disk system which correspond to an orbit bouncing both in the future and past at least a) once, b) twice.

Figure 6.4: The fundamental domain of the 3 disk system.

This value δ gives the correct ordering of the backward strips and the symbolic value plane (γ, δ) represents all points in the non-wandering set ordered the same way as in the phase space. In figure 6.3 b) the values for the 16 rectangles of $g^{(2)}(Q) \cap g^{(-2)}(Q)$ are drawn and we find that the γ-axis is a curve going down left in (x, ϕ) and the δ-axis is a curve going up left in (x, ϕ).

If the 3 disk system is symmetric then the (γ, δ) plane is the same for all three disks. Time symmetry implies that (γ, δ) is equal (δ, γ), and the phase space (x, ϕ) symmetry around the line $x = \pi/6$ implies that (δ, γ) is equal $(1 - \gamma, 1 - \delta)$. One may study the dynamics in the fundamental domain, a 6-th of the original system, see figure 6.4.

If the 3 disk system is not symmetric, then the pruning may look different in the symbolic planes of the different orbits, and is not necessarily symmetric.

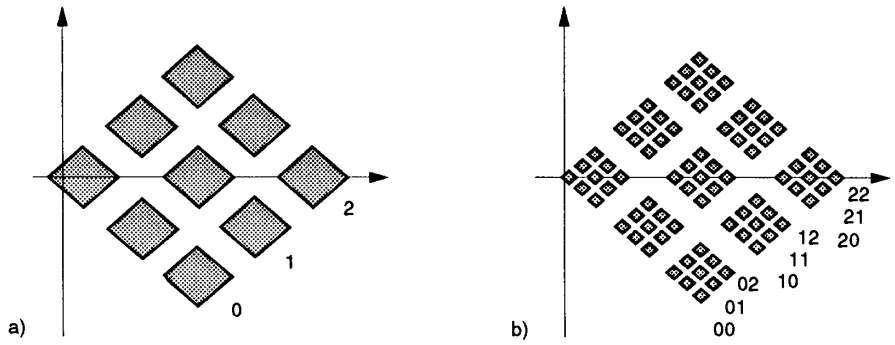

Figure 6.5: Sketch of the points in the phase space of the 4 disk system giving an orbit bouncing in the future and past at lest a) once, b) twice.

6.2 4-disk

The system with a particle bouncing between 4 disks gives a Cantor set in a way very similar to the 3 disk system, but with 3 strips in each generation of the Cantor set, like the three folding Smale horseshoe. If we have a symmetric four disk system with sufficiently separated disks, then the non-wandering set is the the same, as in the complete three folding Smale horseshoe. The orientation changes for all three folds in the horseshoe.

We enumerate the disks anticlockwise, $s_i \in \{1,2,3,4\}$, and obtain the well ordered symbols $w_i \in \{0,1,2\}$ by the algorithm

$$\begin{aligned} v_t &= s_t - s_{t-1} \\ &\text{if } v_t < 1 \text{ then } v_t = v_t + 4 \\ w_t &= \begin{cases} v_t - 1 & \text{if } t \text{ odd} \\ 3 - v_t & \text{if } t \text{ even} \end{cases} \end{aligned} \tag{6.11}$$

The symbolic values for the future and past are base 3 numbers given as

$$\gamma = 0.w_1 w_2 w_3 \ldots = \sum_{t=1}^{\infty} \frac{w_t}{3^t} \tag{6.12}$$

$$\delta = 0.w_0 w_{-1} w_{-2} \ldots = \sum_{t=1}^{\infty} \frac{w_{1-t}}{3^t} \tag{6.13}$$

A sketch of the first generation of the Cantor set in the phase space with the symbols w_i is drawn in figure 6.5. For the symmetric 4-disk system, another convenient choice of a symbolic alphabet are the three discrete group operations C_2, σ_x and σ_y [49]. The relationship between the group operations denoted $g_i \in \{C_2, \sigma_x, \sigma_y\}$ and

the well ordered symbols $w_i \in \{0,1,2\}$ is given by the algorithm

$$\begin{aligned} v_i &= \begin{cases} 0 & \text{if} \quad g_i = \sigma_x \\ 1 & \text{if} \quad g_i = C_2 \\ 2 & \text{if} \quad g_i = \sigma_y \end{cases} \\ r_i &= \begin{cases} r_i + 1 & \text{if} \quad g_i = C_2 \\ r_i & \text{else} \end{cases} \\ w_i &= \begin{cases} v_i & \text{if} \quad r_i \text{ odd} \\ 2 - v_i & \text{if} \quad r_i \text{ even} \end{cases} \end{aligned} \tag{6.14}$$

The symbols g_i can be obtained from w_i by

$$\begin{aligned} g'_i &= \begin{cases} \sigma_x & \text{if} \quad w_i = 0 \\ C_2 & \text{if} \quad w_i = 1 \\ \sigma_y & \text{if} \quad w_i = 2 \end{cases} \\ r_i &= \begin{cases} r_i + 1 & \text{if} \quad w_i = 1 \\ r_i & \text{else} \end{cases} \\ g_i &= \begin{cases} C_2 & \text{if} \quad g'_i = C_2 \\ \sigma_x & \text{if} \quad g'_i = \sigma_x \text{ and } r_t \text{ is even} \\ \sigma_x & \text{if} \quad g'_i = \sigma_y \text{ and } r_t \text{ is odd} \\ \sigma_y & \text{if} \quad g'_i = \sigma_x \text{ and } r_t \text{ is odd} \\ \sigma_y & \text{if} \quad g'_i = \sigma_y \text{ and } r_t \text{ is even} \end{cases} \end{aligned} \tag{6.15}$$

6.3 N-disk systems

Assume the system consists of N disks. If the disks are well separated, the non-wandering set is a Cantor set of the Smale horseshoe type, with one symbol for bouncing into each of the other disks. This symbolic description can be turned into a well ordered alphabet as we have done it for the 3 and 4 disk systems, but the algorithm translating from the alphabet s_t of enumerated disks to the well ordered alphabet w_t can become rather complicated. We show this algorithm for a few N-disk systems with special symmetry.

6.3.1 Symbolic dynamics for N disks on a circle

Let N equal disks have the center of each disk on a large circle, and let r, the distance between centers of neighbor disks on the large circle, be large. Then Λ_1^+ consists of $(N-1)$ strips in the phase space. The well ordered symbols $w_t \in \{0,1,2\ldots,(N-2)\}$

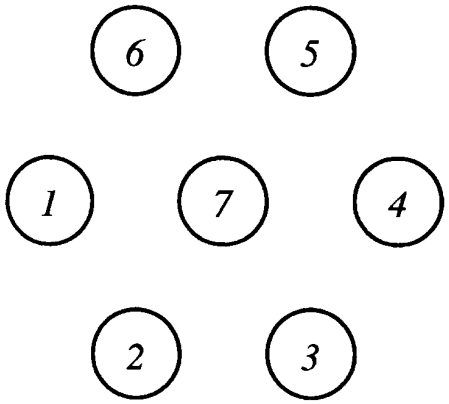

Figure 6.6: The configuration space of the 6+1 disk system.

are constructed from the anticlockwise enumeration of the disks $s_t \in \{1, 2, \ldots, N\}$ using the algorithm

$$\begin{aligned} v &= s_t - s_{t-1} \\ &\text{if} \quad v_t < 1 \quad \text{then} \quad v_t = v_t + N \\ w_t &= \begin{cases} v_t - 1 & \text{if} \quad t \text{ odd} \\ N - v_t - 1 & \text{if} \quad t \text{ even} \end{cases} \end{aligned} \tag{6.16}$$

When $N = 3$ this is the same algorithm as (6.7), and for $N = 4$ this is the algorithm (6.11). From w_t we construct base $(N-1)$ symbolic coordinates $\gamma = 0.w_1 w_2 w_3 \ldots = \sum_{t=1}^{\infty} w_t/(N-1)^t$ and $\delta = 0.w_0 w_{-1} w_{-2} \ldots = \sum_{t=1}^{\infty} w_{1-t}/(N-1)^t$ where $0 \leq \gamma, \delta \leq 1$.

6.3.2 N disks with a center disk

Let the billiard be a configuration of N disks on a large circle as in the billiard above and in addition one disk in the center of this large circle. The radius of each disks is 1, and the distance between two neighbor disks is r. The disks on the circle is enumerated anticlockwise from 1 to N ,and a bounce off the disk in the center is given the symbol $(N + 1)$. Figure 6.6 shows this configuration with $N = 6$. If the number of disks on the large circle is even, then, because of the disk in the center, a point particle can not bounce between two disks opposite to each other on the large circle. From the $(N + 1)$ symbols of the disks, we get $(N - 1)$ well ordered symbols, and Λ_1^+ $(= g(Q) \cap Q)$ consists of $(N - 1)$ strips in the phase space. With N (even) disks on the large circle and the center disk with symbol $(N + 1)$, the

algorithm defining the well ordered symbols $w_t \in \{0, 1, 2 \ldots, (N-2)\}$ is

$$
\begin{array}{lll}
\text{if} & s_t = (N+1) & \text{then} \quad w_t = (N-2)/2 \\
\text{else if} & s_{t-1} \neq (N+1) & \text{then} \\
& v_t = s_t - s_{t-1} & \\
& \text{if} \quad v_t < 1 & \text{then} \quad v_t = v_t + N \\
& w_t \quad = & \begin{cases} v_t - 1 & \text{if} \quad t \text{ odd} \\ N - v_t - 1 & \text{if} \quad t \text{ even} \end{cases} \\
\text{else if} & s_{t-1} = (N+1) & \text{then} \\
& v_t = s_t - s_{t-2} & \\
& \text{if} \quad v_t < -(N-2)/2 & \text{then} \quad v_t = v_t + N \\
& \text{if} \quad v_t > (N-2)/2 & \text{then} \quad v_t = v_t - N \\
& w_t \quad = & \begin{cases} (N-2)/2 + v_t & \text{if} \quad t \text{ odd} \\ (N-2)/2 - v_t & \text{if} \quad t \text{ even} \end{cases}
\end{array}
\tag{6.17}
$$

$$
\gamma \quad = \quad 0.w_1 w_2 w_3 \ldots = \sum_{t=1}^{\infty} \frac{w_t}{(N-1)^t} \tag{6.18}
$$

$$
\delta \quad = \quad 0.w_0 w_{-1} w_{-2} \ldots = \sum_{t=1}^{\infty} \frac{w_{1-t}}{(N-1)^t} \tag{6.19}
$$

The configuration with $N = 6$ can be looked at as a first step toward a description of the Lorentz gas [137, 181], a triangular lattice with a hard disk in each lattice point and a point particle scattering in the lattice.

If the number of disks N on the large circle is odd and the disks are sufficiently separated, a point particle can reach all other disks after bouncing off one disk. The algorithm giving the symbols $w_t \in \{0, 1, 2 \ldots, (N-1)\}$ is

$$
\begin{array}{lll}
\text{if} & s_t = (N+1) & \text{then} \quad w_t = (N-1)/2 \\
\text{else if} & s_{t-1} \neq (N+1) & \text{then} \\
& v_t = s_t - s_{t-1} & \\
& \text{if} \quad v_t < 1 & \text{then} \quad v_t = v_t + N \\
& w_t \quad = & \begin{cases} v_t - 1 & \text{if} \quad t \text{ odd} \\ N - v_t - 1 & \text{if} \quad t \text{ even} \end{cases} \\
& \text{if} \quad w_t > (N-1)/2 & \text{then} \quad w_t = w_t + 1 \\
\text{else if} & s_{t-1} = (N+1) & \text{then} \\
& v_t = s_t - s_{t-2} & \\
& \text{if} \quad v_t < -(N-1)/2 & \text{then} \quad v_t = v_t + N \\
& \text{if} \quad v_t > (N-1)/2 & \text{then} \quad v_t = v_t - N \\
& w_t \quad = & \begin{cases} (N-1)/2 + v_t & \text{if} \quad t \text{ odd} \\ (N-1)/2 - v_t & \text{if} \quad t \text{ even} \end{cases}
\end{array}
\tag{6.20}
$$

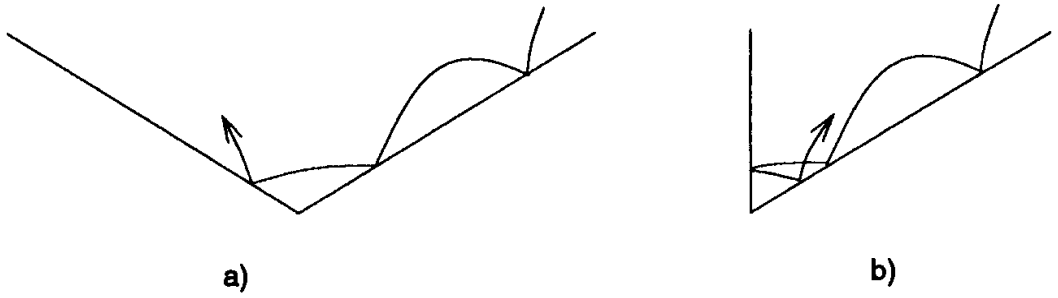

Figure 6.7: The wedge billiard. a) The whole domain. b) The fundamental domain.

6.4 Wedge billiard, or Two Bouncing Balls

The next example is another type of a billiard system, which has two mechanical realizations both described by the same mathematics. We first describe the physics of the two problems and how they are related to each other.

6.4.1 Wedge billiard

One realization is given by a point particle with a mass m moving in a plane with constant gravitation, and bouncing off two symmetrically tilted planes, figure 6.7 a). This system was introduced and studied numerically by Lehtihet and Miller [131]. The system can be reduced to the the fundamental domain billiard in figure 6.7 b) with a vertical wall replacing one of the tilted walls. Two orbits which are symmetric to each other with respect to the y-axis in the full domain are mapped into the same orbit in the fundamental domain, and correspondingly a single orbit in the fundamental domain can correspond to two full space orbits. A periodic orbits in the fundamental domain is mapped into only one orbit in the full domain if this orbit is symmetric with respect to the y-axis in the full domain.

The Hamiltonian for this system is

$$H = \frac{1}{2}\left(p_x^2 + p_y^2\right) + y, \quad x > 0, \;\; y > x\cot\phi. \tag{6.21}$$

At the collision with the tilted wall the perpendicular component of the momentum switches direction.

Lehtihet and Miller[131] have shown that this flow can be turned into a map as follows: Let $\vec{e}_r$ be the unity vector pointing from the tip of the wedge to the position of the ball, and $\vec{e}_\phi$ be the unity tangent vector orthogonal to $\vec{e}_r$. Let $\vec{v}$ be

the velocity of the ball. The map T is given by (x and y are respectively the radial and the tangential components of the velocity vector):

$$\begin{array}{rcl} & \text{if} & (x_t - 2y_t)^2 \cos^2\theta + y_t^2 \sin^2\theta < 1 \\ T_0 \;:\; \left\{ \begin{array}{rcl} x_{t+1} &=& x_t - 2y_t \\ y_{t+1} &=& y_t \end{array} \right. & & \\ & \text{else} & \\ T_1 \;:\; \left\{ \begin{array}{rcl} x_{t+1} &=& y_t - x_t - y_{t+1} \\ y_{t+1} &=& \sqrt{2 + 2\xi(y_t - x_t)^2 - y_t^2} \end{array} \right. & , & \qquad \xi = \frac{1-\tan^2\theta}{(1+\tan^2\theta)^2} \,. \end{array} \tag{6.22}$$

The map T_0 corresponds to two consecutive bounces off the inclined plane, while map T_1 describes the particle bouncing from the inclined plane to the vertical wall and then back again to the inclined plane. The time reversal amounts to reversing the velocity component parallel to the plane of reflection, $x \to -x$:

$$T_i^{-1} = \tau^{-1} T_i \tau \qquad \tau = \begin{bmatrix} -1 & 0 \\ 0 & 1 \end{bmatrix}, \tag{6.23}$$

The phase space is manifestly symmetric under reflection across the y-axis.

6.4.2 Two Bouncing Balls

A second problem that gives rise to the same dynamical system is the system of two balls moving along a vertical line in constant gravitational field. The upper ball, no. 2, has mass m_2 and bounces elastically off the ball below. The ball underneath, no. 1, with mass m_1, bounces off the floor and off the ball above. Figure 6.8 a) shows the the system, and motion in time is sketched in figure 6.8 b).

The Hamiltonian for the motion between the bounces is

$$H = \frac{p_1^2}{2m_1} + \frac{p_2^2}{2m_2} + m_1 q_1 + m_2 q_2 \tag{6.24}$$

When ball no. 1 bounces elastically off the floor we have

$$v_1 \to -v_1 \tag{6.25}$$

and at an elastic bounce between ball no. 1 and ball no. 2

$$\begin{array}{rcl} v_1 &\to& \gamma v_1 + (1-\gamma) v_2 \\ v_2 &\to& (1+\gamma) v_1 - \gamma v_2 \end{array} \tag{6.26}$$

where $\gamma = (m_1 - m_2)/(m_1 + m_2)$.

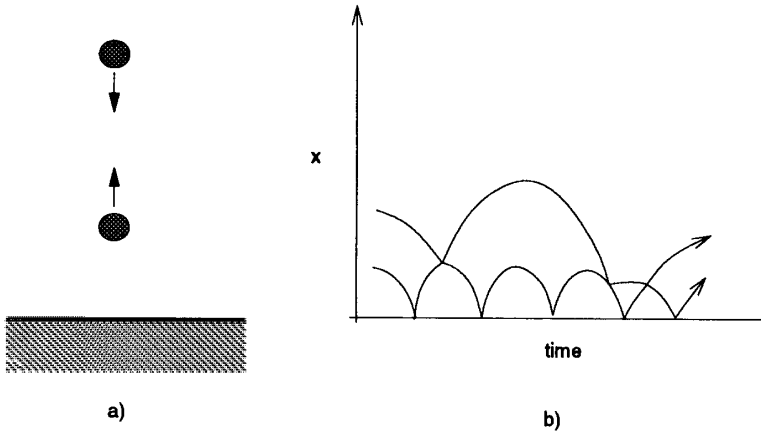

Figure 6.8: a) The two bouncing balls system in one dimension. b) The position of the balls as a function of time.

It was showed by Wojtkowsky [200] that this system has nonzero Lyapunov exponents for almost every starting point. He also showed that the linear change of variables

$$\begin{aligned} x_1 &= \sqrt{m_1 m_2}(q_1 - q_2) \\ x_2 &= m_1 q_1 + m_2 q_2 \\ p_{x_1} &= \sqrt{\frac{m_2}{m_1}} p_1 - \sqrt{\frac{m_1}{m_2}} p_2 \\ p_{x_2} &= p_1 + p_2 \end{aligned}$$

with masses normalized to $m_1 + m_2 = 1$, yields the Hamiltonian

$$H = \frac{1}{2}(p_{x_1} + p_{x_1}) + x_2 \tag{6.27}$$

in the configuration space

$$\begin{aligned} x_1 &\leq 0 \\ x_2 &\geq \frac{x_1}{\tan\theta} = \frac{m_2}{m_1} x_1 \end{aligned}$$

which is identical to the wedge billiard (6.21) in the fundamental domain.

This problem was first studied by Wojtkowski [200], and he also studied a generalizations of this problem to a problem with n bouncing balls in one dimension. Chernov [35] showed how Wojtkowski's proof of the local instability can be turned into a proof that this is an ergodic system for $m_1 > m_2$. A Galilei version of this problem can be done as a simple experimental demonstration of chaotic vs. integrable motion. An air pressure rail which exists in all physics teaching labs may be tilted a few degrees and with two wagons of different mass, stable and chaotic motion may be demonstrated.

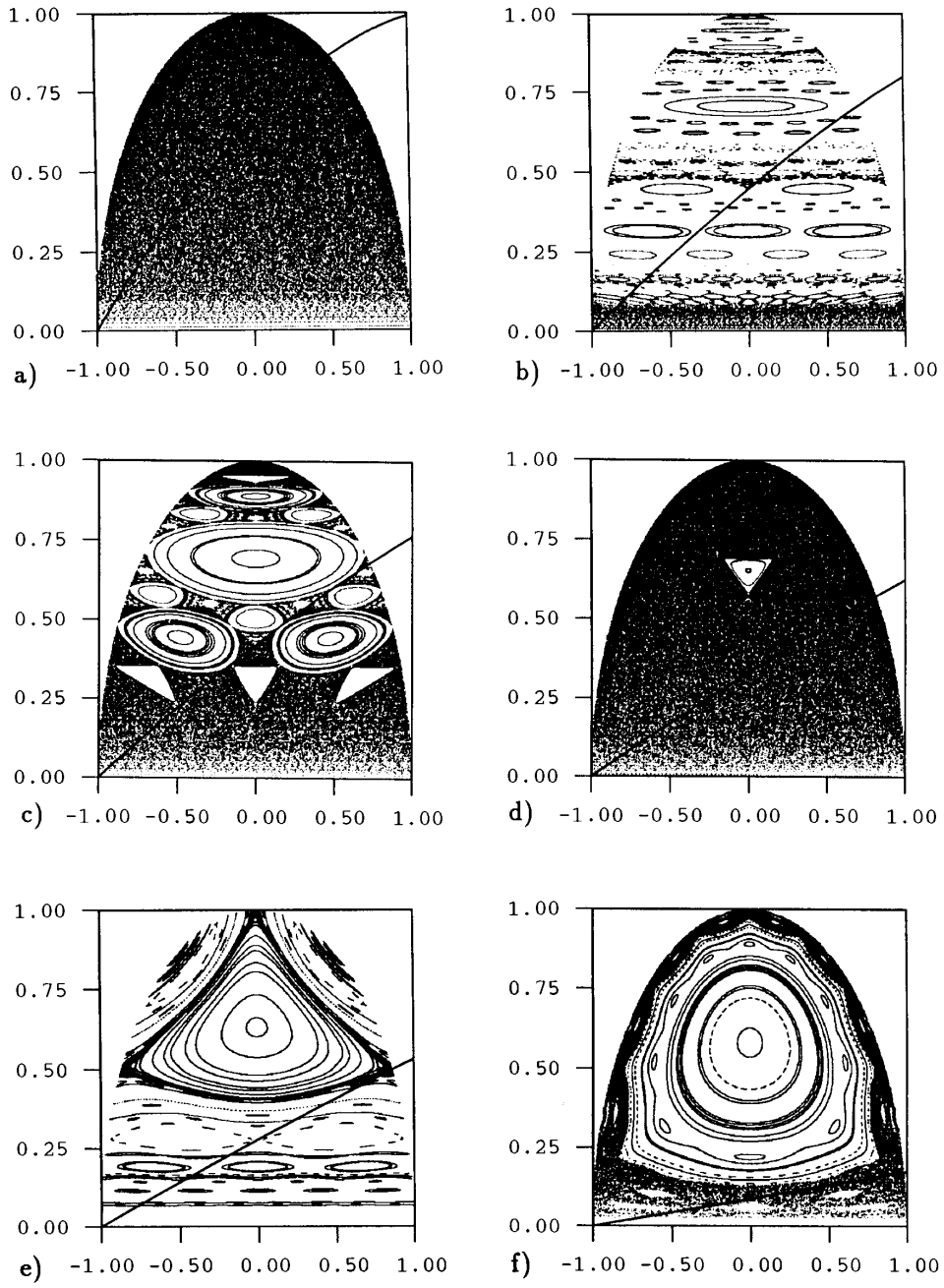

Figure 6.9: Different orbits in the wedge billiard. a) $\theta = 60°$ b) $\theta = 44.8°$ c) $\theta = 43°$ d) $\theta = 35°$ e) $\theta = 30°$ f) $\theta = 10°$

6.4.3 Numerical simulations

Simple numerical explorations revel a first picture of the dynamics of the system. We use the map (6.22) for numerical work. A few numerically obtained trajectories are shown in figure 6.9 for different values of the parameter θ. Lehtihet and Miller [131] have observed that for $\xi > 0$ there exist stable periodic orbits surrounded by KAM torii, and these bifurcate in a complicated way as the parameter changes. In the two ball system $\theta < 45$ corresponds to the upper ball has a larger mass $m_2 > m_1$.

Close to $\theta = 45^\circ$ these stable orbits organize into a Farey-tree like structure visible in figure 6.9 b). We explain below why this happens, and how it is expressed in symbolic dynamics as a tree construction of the admissible symbols.

In the limit of $\theta = 0^\circ$ the fixed point and the KAM tory around it dominates the whole phase space; in the limit of a very narrow wedge there exists a stable orbit of period 2 bouncing back and forth between the two walls. The other orbits are bouncing back and forth between the two walls and rotate around the short periodic orbit in the phase space. In the two ball picture this periodic orbit corresponds to the upper ball bouncing once off the ball below between each time this ball bounces off the floor.

The "wide" wedge billiard has an angle θ between 45° and 90°, which in the two ball system corresponds to the lower ball has a larger mass, $m_1 > m_2$. In figure 6.9 a) the parameter $\theta = 60^\circ$ and there are no stable islands anywhere in the phase space. Changing the parameter results in no visible difference when plotting a chaotic orbit in the phase space. The orbit does change, but the the Poincaré map only shows uniform ergodic distribution of trajectory points. Wojtkowski [200] showed for the two ball system, that for $m_1 > m_2$ almost all points have one positive Liapunov exponent, and Chernov [35] used this to prove the ergodicity of the system for these parameter values. He actually showed this for a more general system with not necessarily constant gravitation $V(q) = gq$ but with a force directed downward $V'(q) > 0$ not increasing with the height, $V''(q) \leq 0$.

The proof ensures that for $m_1 > m_2$ the stable and unstable manifolds are never parallel. A picture of the manifolds is obtained by iterating a short line segment along the unstable eigenvector of the fixed point $\overline{1}$. In figure 6.10 a line of length 0.001 starting at the fixed point is drawn, together with a number of iterations of the line. The same curves reflected across the y–axis trace out the stable manifold of the fixed point. As expected, the unstable and stable manifolds are nowhere parallel. However, in the limit $\theta \to 45^{\circ +}$ the stable and unstable manifolds become horizontal and tangent to each other, as expected, since for $\theta = 45^\circ$ the system is integrable, and all orbits are marginally stable.

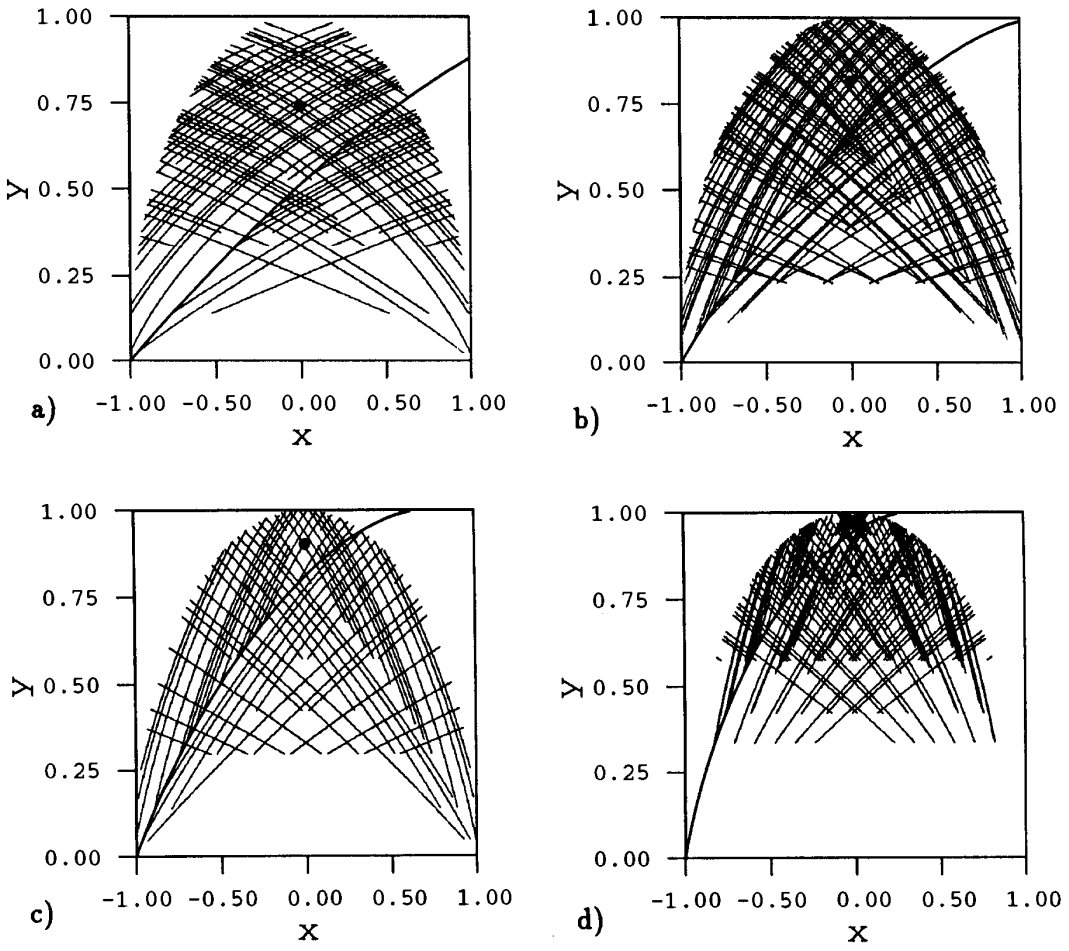

Figure 6.10: The stable and the unstable manifolds of the fixed point in the wedge billiard. a) $\theta = 50^\circ$ b) $\theta = 60^\circ$ c) $\theta = 70^\circ$ d) $\theta = 80^\circ$

6.4.4 Symbolic dynamics

The discontinuity in the map (6.22) suggests a natural way to define symbolic dynamics. Szeredi and Goodings [188, 189] denote a bounce of the ball from the tilted wall directly back to the tilted wall by the symbol T. The bounce from the tilted wall into the vertical wall and then back to the tilted wall they denote by V. We prefer to use 0 for their symbol T, and 1 for their symbol V. Using the map (6.22), we assign symbol 0 when the iteration is obtained by using map T_0, and symbol 1 when the iteration is according to map T_1. Szeredi and Goodings have tested this symbolic dynamics numerically and found that for the completely chaotic wedge billiard $45^\circ < \theta < 90^\circ$ this symbolic alphabet assigns a unique symbol string to each physically realized periodic orbit. They also found a lot of pruning, i.e. that many symbol strings did correspond to admissible orbits.

In the two ball system the same symbolic dynamics is obtained by assigning symbol 0 to be a bounce of ball no. 1 off the floor and then back to the floor without hitting the ball no. 2. The symbol 1 is assigned to the case where ball no. 1 bounces off the floor, bounces into ball no. 2, and then returns back to the floor. As long as $m_2 < m_1$, the two balls cannot collide more than once between two consecutive bounces off the floor.

The well ordered symbols for the map are determined by how the orientation changes under the maps T_0 and T_1. There is no limit of parameter values where the map is a complete horseshoe; instead we study the foliation of its stable and unstable manifolds. The map T_0 corresponds to a simple linear shear, with change in orientation. The map T_1 reverses the orientation in both the stable and the unstable directions. The fixed point $\overline{1}$ has two negative eigenvalues for all parameter values $m_1 > m_2$. The manifolds in figure 6.10 in the part of the phase space on which T_1 acts are reversed after one iteration.

A map with manifolds that have the same orientation under T_0 but where both manifolds are reversed under T_1 gives the same ordering of symbols as the once folding horseshoe without any reflection. The well ordered symbols are then obtained by the algorithms (1.18) and (3.5).

We will show below that there is always pruning in this system, so we cannot draw a complete cantor set for any parameter values.

6.5 Stadium Billiard

One of the best known challenges in nonlinear dynamics is the problem of the description of the Bunimovich stadium billiard [32]. The stadium and a segment

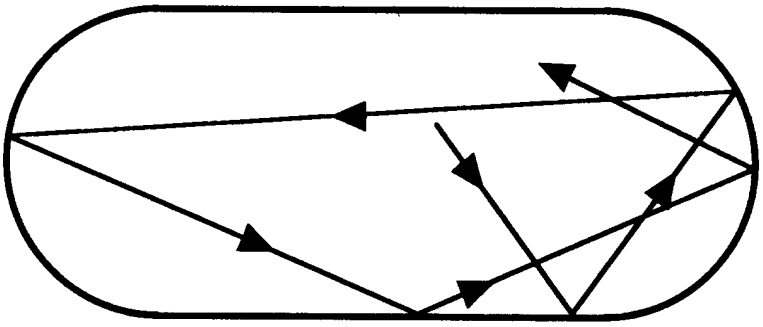

Figure 6.11: The stadium billiard and an orbit in this billiard.

of a typical orbit are drawn in figure 6.11. The system is a point particle moving freely inside and bouncing off the walls that consist of two semi-circles connected by two straight lines. We set the radius of the two semi-circles equal to 1 without any loss of generality. The length of the straight lines is the only parameter in the system, and we set it to $2a$. Bunimovich [32] proved that this system has a positive Liapunov exponent almost everywhere and that it is ergodic. There is a line of marginally stable cycles, orbits bouncing up and down between the two straight lines, while all other orbits are unstable.

The symbolic dynamics of the stadium is more complicated than in the systems studied above. The use of both straight walls and focusing walls as the border gives a more complicated algorithm for the well ordered symbols. Also, as in the wedge billiard, we cannot find a complete Smale horseshoe at any parameter values. But we show here that in the limit of infinity long straight walls there exist a Markov partition with a good choice of symbols.

The most interesting work on the symbolic dynamics of the stadium done so far is the article by Biham and Kvale [25]. They introduce a symbolic dynamics that we shall mostly follow here, and apply this finding numerically periodic orbits. They also discuss pruning of orbits and show how one may find a periodic orbit for each symbol string and check whether it is pruned The new results presented here are: implementation of the parameter independent (or "geometrical" [25]) pruning roles as a transition matrix, the topological entropy determined exactly in the $a \to \infty$ limit, and the description of parameter dependent (or "dynamical" [25]) pruning rules by a pruning front.

6.5.1 Phase space

A natural Poincaré map for the stadium is θ, the position of a bounce off the wall and ϕ, the outgoing angle of the particle. Since the system is ergodic a long chaotic orbit should visit arbitrarily close to all points in the phase space. Even so there are structures in the phase space that cannot be seen in a plot of the Poincaré map of one chaotic orbit. The structure of stable and unstable manifolds can be illustrated by iterating a short line segment along the unstable direction of the period 2 orbit at (θ, ϕ). The structure is similar to the figures for the other billiard systems with pruning; the stable and the unstable manifolds have tent-like turning points instead of homoclinic tangencies, similar to the Lozi map, figure 5.20. We will return to this below in order to describe the pruning. In figure 7.3 we sketch how a line is folded in order to yield the tent like structure in figure 6.12.

6.5.2 Symbolic dynamics

As for the disk billiards, it is necessary to have different symbols for the different parts of the wall. However, as noticed by Biham and Kvale is also necessary to have some distinction between a clockwise and an anticlockwise bounce in the semi-circular part. Otherwise would we not be able to distinguish between two orbits such as the two drawn in figures 6.13 a) and b). The first guess is to give one symbol to each straight line and for a bounce in the semi-circle to distinguish between if it is the right or the left semi-circle and if it is a clockwise or anticlockwise bounce with respect to the center of the semi-circle. This gives a six letter alphabet which we believe is covering such that any admissible orbit in the billiard has a unique symbol string as its symbolic description, and no other orbits are described by the same symbol string but there will be symbol strings which do not correspond to any orbit. We show below that this alphabet has the unpleasant feature that with it there seems to be no way to find a finite Markov graph of the stadium, even in the $a \to \infty$ limit. Figure 6.14 shows the definition of this alphabet $s_t^a \in \{0, 1, 2, 3, 4, 5\}$.:

$s_t^a = 0$ a bounce off the bottom line.

$s_t^a = 2$ a bounce off the upper line.

$s_t^a = 1$ a clockwise bounce off the left semi-circle.

$s_t^a = 4$ an anticlockwise bounce off the left semi-circle.

$s_t^a = 3$ an anticlockwise bounce off the right semi-circle.

$s_t^a = 5$ an clockwise bounce off the right semi-circle.

Orbits that go through the center of the semi-circle have to be treated specially, but for the moment we give these orbits both the symbol for a clockwise and an

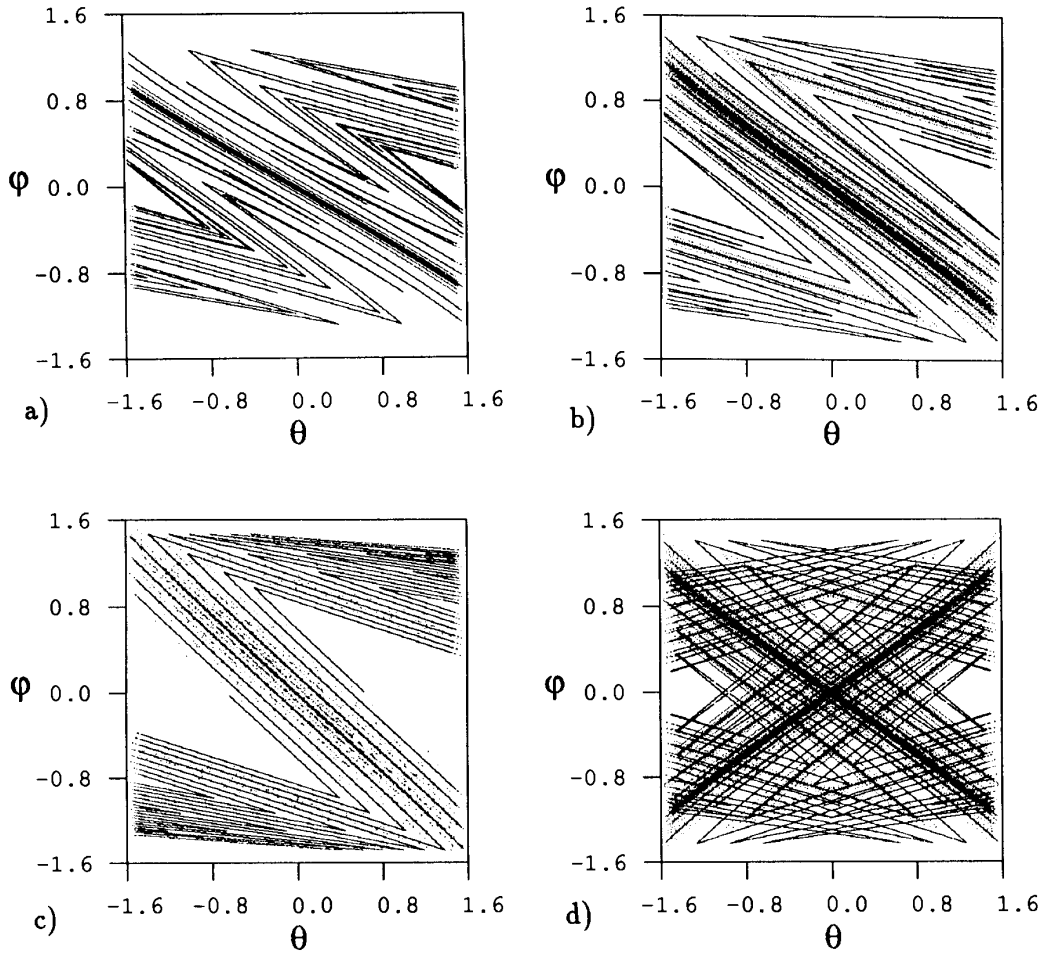

Figure 6.12: The unstable manifold of the periodic orbit at $(\theta, \phi) = (0, 0)$ in the stadium billiard with θ the position on the semi-circle and ϕ the outgoing angle for a) $a = 0.5$ b) $a = 1.0$ c) $a = 5.0$. d) Stable and unstable manifold for $a = 1.0$.

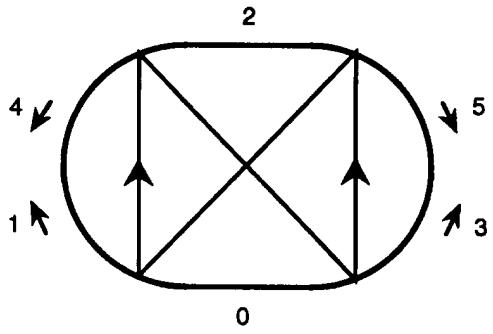

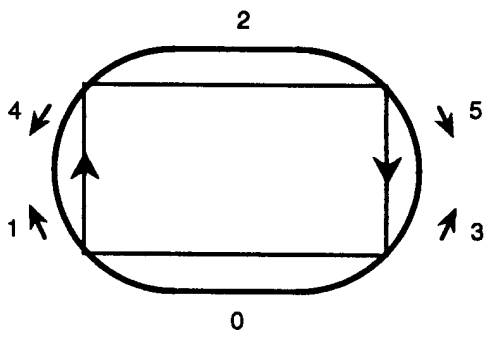

Figure 6.13: Two different period 4 orbits illustrating the necessity of distinguishing clockwise and anticlockwise bounces. a) $\overline{s_1^a s_2^a s_3^a s_4^a} = \overline{1133}$, b) $\overline{s_1^a s_2^a s_3^a s_4^a} = \overline{1155}$.

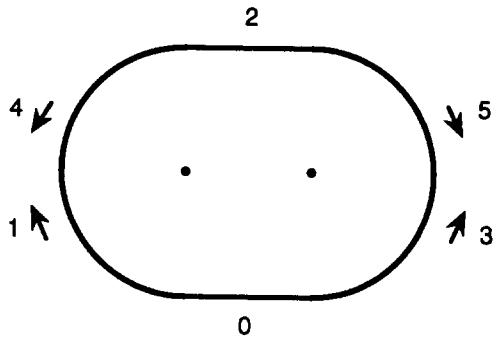

Figure 6.14: The symbols s_t^a in the stadium.

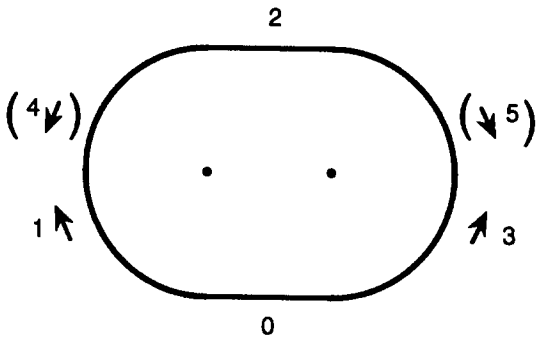

Figure 6.15: The Biham-Kvale symbols s_t^b.

anticlockwise bounce, and keep in mind that such orbits are double counted.

The alphabet introduced by Biham and Kvale [25] is a small modification of this alphabet which remove the degeneracy counting orbits through the center. They use a 6 letter alphabet $s_t^b \in \{0, 1, 2, 3, 4, 5\}$ as above, but if an orbit bounces only once in a semi-circle then they denote it by the same symbol independent of whether it bounced clockwise or anticlockwise. They choose to let a single bounce that had symbol $s_t^a = 1$ still has the symbol $s_t^b = 1$ while a single bounce with $s_t^a = 4$ is renamed to $s_t^b = 1$. A single bounce that had symbol $s_t^a = 3$ still has the symbol $s_t^b = 3$, while a single bounce with $s_t^a = 5$ is renamed to $s_t^b = 3$. Figure 6.15 illustrates the alphabet s_t^b.

Instead of working with symbols denoting each bounce as above we introduce symbols which describe how a bounce changes the path. This reduces the number of symbols to 5. In this alphabet will some orbits with the same length and stability be described by the same symbol string. An important observation is that a single

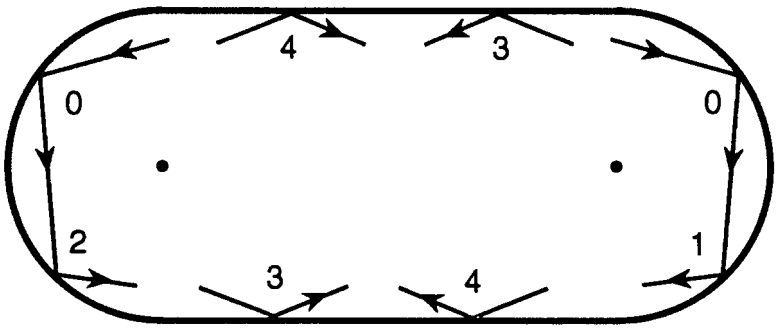

Figure 6.16: The symbols s_t^c in the stadium.

bounce should not distinguish between clockwise and anticlockwise. We define a new alphabet s_t^c as follows:

$s_t^c = 0$ if the bounce is the first bounce in a semi-circle,

$s_t^c = 1$ if the bounce is clockwise in a semi-circle and not the first bounce in the semi-circle,

$s_t^c = 2$ if the bounce is anticlockwise in a semi-circle and not the first bounce in the semi-circle,

$s_t^c = 3$ if the bounce is either in the bottom line in the direction to the right or if it is a bounce in the top line going to the left,

$s_t^c = 4$ if the bounce is either in the bottom line in the direction to the left or if it is a bounce in the top line going to the right.

These symbols are illustrated in figure 6.16.

To determine the well ordered symbols for the stadium we have to observe how the symbols change as we move a point in the phase space. The symbols s_t^a can be changed into well ordered symbols by observing the change in symbols in figure 6.17. The figure shows how the next symbol change under monotone increase of the outgoing angle, starting with one of the 6 symbols. From the figure 6.17 a) we find that starting at the bottom line with symbol $s_t^a = 0$ gives for $\theta \to -\pi/2$ symbol $s_{t+1}^a = 3$ because the next bounce is a clockwise bounce in the right semi-circle. When θ increases then at some point the particle goes through the center of the right semi-circle and the symbol changes to $s_{t+1}^a = 5$. The value where it changes depends on the position and on the parameter. For even larger values of θ the particle hits the top straight line and then the next symbol is $s_{t+1}^a = 2$. For some value $\theta > 0$ the particle starts to hit the left semi-circle bouncing clockwise giving $s_{t+1}^a = 4$. Finally for some larger value of θ the particle moves through the center of the left semi-circle and for angles larger than this up to $\pi/2$ the

$s^a_{t-1}s^a_t$	v^a_t
03	0
05	1
02	2
04	3
01	4

$s^a_{t-1}s^a_t$	v^a_t
10	0
13	1
15	2
12	3
11	4

$s^a_{t-1}s^a_t$	v^a_t
24	0
21	1
20	2
23	3
25	4

$s^a_{t-1}s^a_t$	v^a_t
33	0
32	1
34	2
31	3
30	4

$s^a_{t-1}s^a_t$	v^a_t
44	0
40	1
43	2
45	3
42	4

$s^a_{t-1}s^a_t$	v^a_t
52	0
54	1
51	2
50	3
55	4

Table 6.1: Construction of the well ordered alphabet in the stadium billiard from the symbols s^a_t. The well ordered symbols w^a_t are constructed by choosing $w^a_t = v^a_t$ when the number of 0's and 2's (bouncing in a straight lines) in the symbol string $s^b_0 \dots s^b_{t-1}$ is *odd* and choosing $w^a_t = 4 - v^a_t$ when the number is *even*.

next symbol is $s^a_{t+1} = 1$. The ordering of the two symbols combination with the first symbol 0 is then: $\{03, 05, 02, 04, 01\}$ and we rename these combinations to be respectively $v^a = \{0, 1, 2, 3, 4\}$. The definition of the symbol v^a_t for the other two symbol combinations is given in table 6.1. Symbols v^a_t are analogue to symbols s_t for the Smale horseshoes and the symbols v_t of the disk billiards. These symbols are correctly ordered for one bounce but not globally.

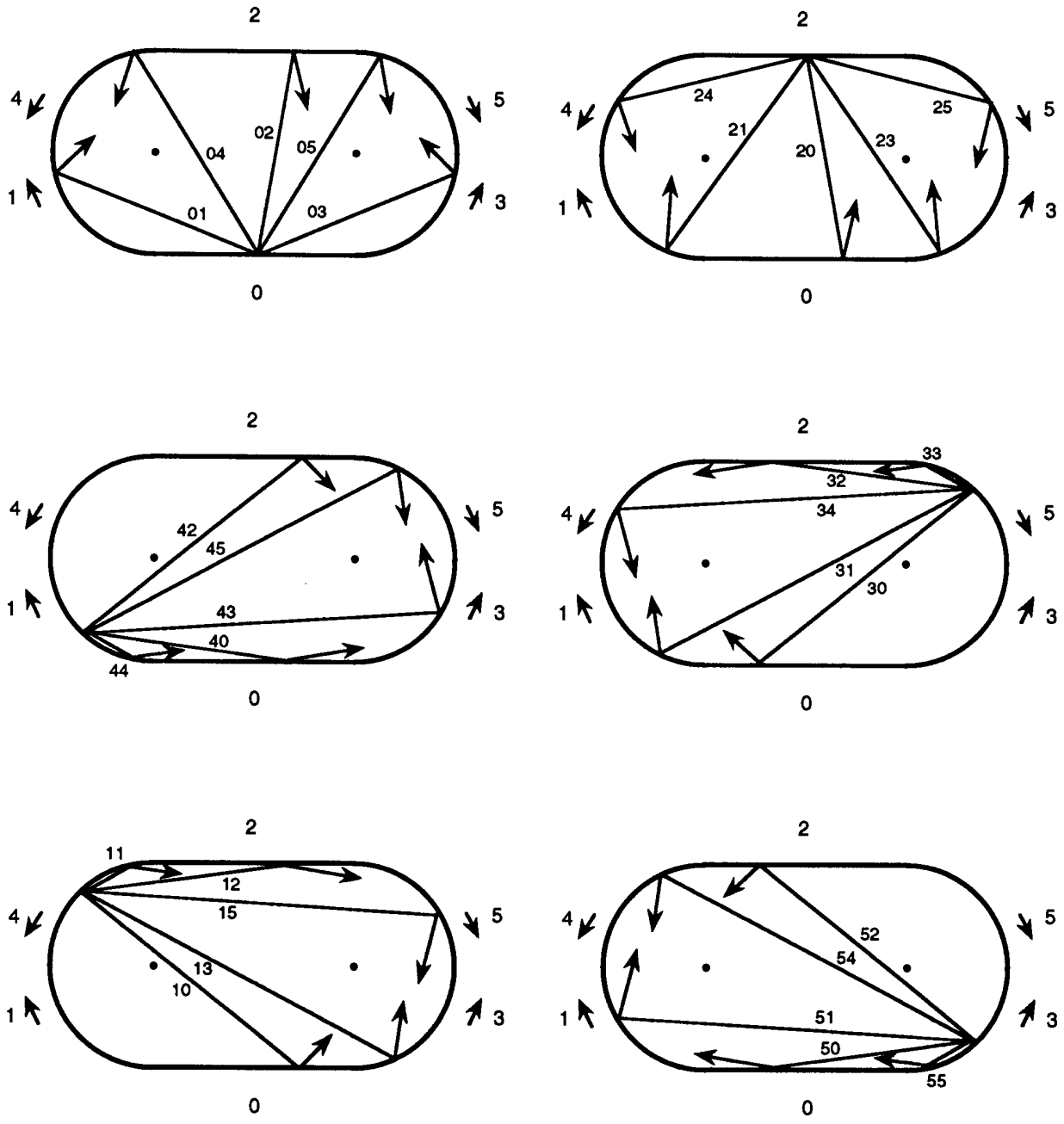

Figure 6.17: Construction of the well ordered symbols from symbols s^a, see table 6.1.

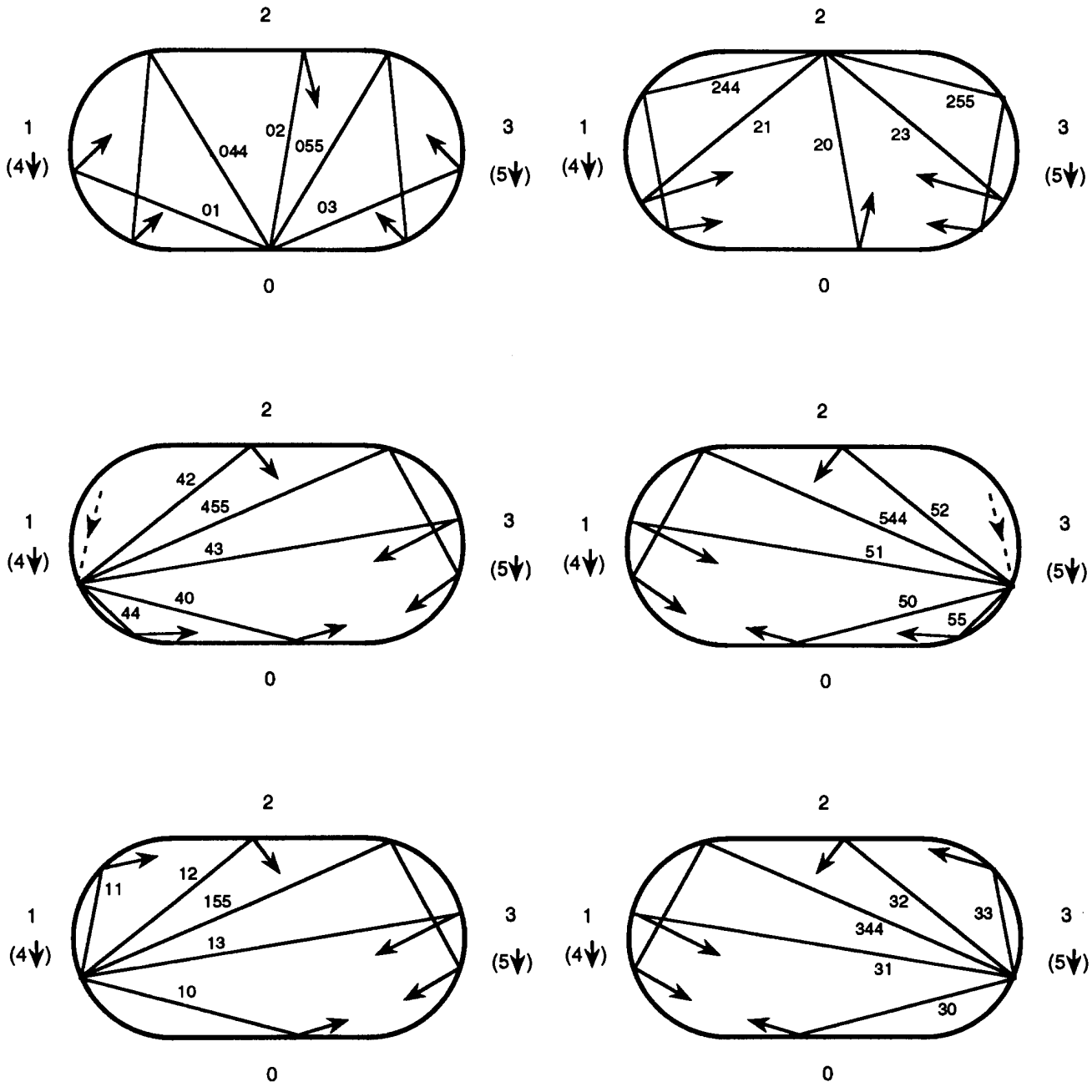

Figure 6.18: Construction of the well ordered symbols from symbols s^b, see table 6.2.

$s_t^b s_{t+1}^b (s_{t+2}^b)$	v_{t+1}^b
03	0
055	1
02	2
044	3
01	4

$s_t^b s_{t+1}^b (s_{t+2}^b)$	v_{t+1}^b
44	0
40	1
43	2
455	3
42	4

$s_t^b s_{t+1}^b (s_{t+2}^b)$	v_{t+1}^b
10	0
13	1
155	2
12	3
11	4

$s_t^b s_{t+1}^b (s_{t+2}^b)$	v_{t+1}^b
244	0
21	1
20	2
23	3
255	4

$s_t^b s_{t+1}^b (s_{t+2}^b)$	v_{t+1}^b
52	0
544	1
51	2
50	3
55	4

$s_t^b s_{t+1}^b (s_{t+2}^b)$	v_{t+1}^b
33	0
32	1
344	2
31	3
30	4

Table 6.2: Construction of the well ordered alphabet in the stadium billiard from symbols s_t^b. The well ordered symbols w_t^b are constructed by choosing $w_t^b = v_t^b$ when the number of 0's and 2's (bounces off straight lines) in the symbol string $s_0^b \ldots s_{t-1}^b$ is odd and choosing $w_t^b = 4 - v_t^b$ when the number is $even$.

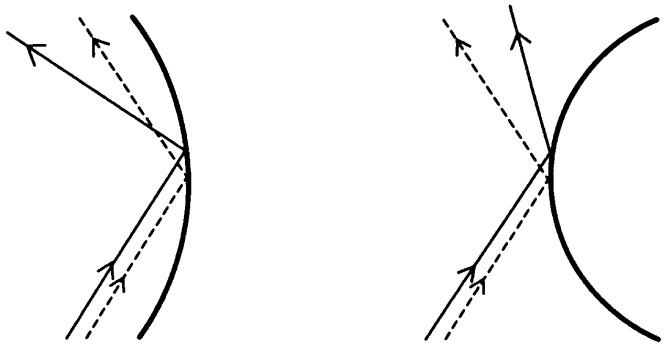

Figure 6.19: Orientation change for a bounce off; a) a convex, b) a concave wall.

In order to construct well ordered symbols we have to know how the manifolds flip at a bounce. A bounce in a focusing (convex) wall does not change orientation; figure 6.19 a) illustrates that two close orbits have the same relative orientation after a bounce as before the bounce. A bounce off a straight line reverses the directions in the same way as a dispersing wall in figure 6.19 b), so we have to count the number of straight wall bounces. If p_t is the number of symbols 0 and 2 in the sequence $s_0^a s_1^a s_2^a \dots s_{t-1}^a$, the well ordered symbols are given by

$$w_t^a = \begin{cases} v_t^a & \text{if } p_t \text{ odd} \\ 4 - v_t^a & \text{if } p_t \text{ even} \end{cases} \tag{6.28}$$

The symbolic value γ^a is now given as a real number in base 5

$$\gamma^a = 0.w_1^a w_2^a w_3^a \dots = \sum_{t=1}^{\infty} \frac{w_t^a}{5^t} \tag{6.29}$$

The simplest way to find the well ordered symbols of the past is to change the symbolic description of the past into a string of future symbols. Reversing the time for an orbit change all clockwise bounces into anticlockwise bounces and all anticlockwise bounces into clockwise bounces. This implies that symbol 1 becomes 4, 4 becomes 1, 3 becomes 5 and 5 becomes 3. Then the symbols $w_t^{a\prime}$ obtained from table 6.1 and algorithm (6.28) gives the well ordered symbols of the past. The symbolic value of the past is then

$$\delta^a = 0.w_1^{a\prime} w_2^{a\prime} w_3^{a\prime} \dots = \sum_{t=1}^{\infty} \frac{w_t^{a\prime}}{5^t} \tag{6.30}$$

The Biham-Kvale symbols v_t^b yield well ordered symbols and symbolic values γ^b and δ^b in the same way.

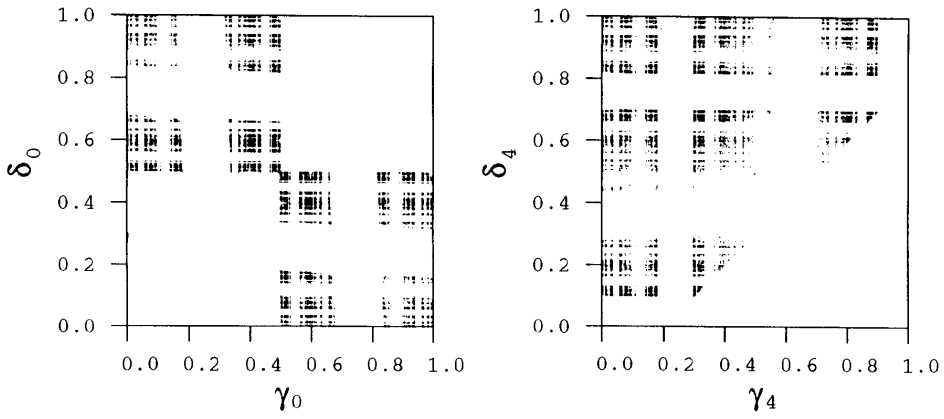

Figure 6.20: A chaotic trajectory in the symbol plane (γ^a, δ^a) for $a = 5.0$. Symbolic values for bouncing off a) the straight line, b) the semi-circle.

6.5.3 Symbolic dynamics in the limit $a \to \infty$

The description of the orbits in the stadium in the limit $a \to \infty$ depends on the choice of symbolic dynamics. We first show how the alphabet s_t^a gives a very complicated description and then how the other alphabets simplify the description.

The pruning depends on the parameter a monotonically, with the number of admissible orbits orbits increasing with increasing a. In the limit $a \to \infty$ we have as many orbits as it is possible to have in the stadium billiard. The topological entropy is largest for $a \to \infty$ and decreases monotonically with a.

By iterating a long chaotic orbit and plotting the symbolic values (γ^a, δ^a) for each bounce we obtain figure 6.20. In figure 6.20 a) the points (γ^a, δ^a) are plotted for the bounces with $s_0^a = 0$; we denote this symbol plane (γ_0^a, δ_0^a). In figure 6.20 b) the points (γ^a, δ^a) are plotted for the bounces with $s_0^a = 1$; we denote this symbol plane (γ_1^a, δ_1^a). The symbol plane for $s_0^a = 2$ is identical to (γ_0^a, δ_0^a), the symbol planes for $s_0^a = 3$ is identical to the plane (γ_1^a, δ_1^a) and the symbol planes (δ_4^a, γ_4^a) and (δ_5^a, γ_5^a) are identical to (γ_1^a, δ_1^a).

White regions in the plot of the symbol plane are forbidden regions corresponding to symbol strings that never appear in the dynamics. When we choose a large value of the parameter like $a = 5$ in figure 6.20, the visible forbidden regions are mostly the parameter independent $(a \to \infty)$ pruned regions.

In figure 6.20 a) we find that the two squares $\gamma_0^a > 1/2, \delta_0^a > 1/2$ and $\gamma_0^a < 1/2, \delta_0^a < 1/2$ are forbidden regions. The first region $\gamma_0^a > 1/2, \delta_0^a > 1/2$ translated back to the symbols s_t^a, contains all strings where a bounce in a straight line (symbol 0 or 2) has as its last symbol before a string of 0 and 2 symbols a bounce in the left

semi-circle (symbol 1 or 4). Also the first semi-circle symbol after this string of 0 and 2 symbols is a bounce in the left semi-circle (symbol 1 or 4). These are the forbidden strings 101, 1021, 10201,..., 104, 1024,.... The second square is the corresponding strings with bounces in the right semi-circle 303, 3023, 30203,..., 305, 3025,.... The limit of the regions are the lines $\gamma = 1/2$ and $\delta = 1/2$, which are orbits of form $1(02)^\infty 1$, etc. Even thought that there is no finite list of forbidden strings covering these forbidden regions, the rules are simple and can be implemented by a Markov graph.

In figure 6.20 b) there is a triangle shaped forbidden region below the line $\delta = \frac{1}{5} + \gamma$. One short string in this region is the string $\ldots 3 \cdot 13 \ldots$. This string is forbidden because the string $\ldots 3 \cdot 1$ imply a bounce off the left semi-circle at a point *below* the center of the left semi-circle. If the particle bounces off this left semi-circle clockwise (symbol 1) and immediately hits the right semi-circle, this has to be at a point *above* the center of the right semi-circle, and since the orbit was above both centers of the two semi-circles this is a bounce 5 and cannot be turned into a symbol 3 by changing starting position and angle. The limit of this region $\delta = \frac{1}{5} + \gamma$ translated back to the s_t^a symbols imply that there is a string

$$\ldots s_{-n} \ldots s_{-2} s_{-1} s_0 s_1 s_2 \ldots s_n \ldots$$

and for all these symbols we have $s_{-n} = 0$ if $s_n = 0$, $s_{-n} = 2$ if $s_n = 2$, $s_{-n} = 4$ if $s_n = 1$, $s_{-n} = 1$ if $s_n = 4$, $s_{-n} = 5$ if $s_n = 3$ and $s_{-n} = 3$ if $s_n = 5$ such that s_{-n} is the time reversed of s_n. This is the string describing an orbit going through the center of the semi-circle at the bounce $t = 0$.

To understand why this is the limit, draw an orbit through the center of a semi-circle as in figure 6.21. For example the orbit is given either by the symbol string $\ldots 1502113442034 \ldots$ or by the string $\ldots 1502115442034 \ldots$since the bounce is normal to the disk, there are two possible ways to write this string in the s_t^a alphabet. Assume now that we change the orbit slightly such that the bounce that used to be normal becomes an anticlockwise bounce. The first symbol string with $s_0^a = 3$ is the correct symbolic description of this orbit. If we perturb the orbit more such that the symbol string $\ldots 1502113$ still describe the first part of the orbit the last part of the symbol string can only change the following way. The symbol $s_1 = 4$ can only change to 2 or 3 and not to 1 or 0. If $s_1 = 4$ then the symbol $s_2 = 4$ cannot change. If $s_1 s_2 = 44$ then $s_3 = 2$ can change to 5, 3, 0 or 4. If $s_1 s_2 s_3 = 442$ then $s_4 = 0$ can change to 3 and 5. If $s_1 s_2 s_3 s_4 = 4420$ then $s_5 = 3$ cannot change to any other symbol. If $s_1 s_2 s_3 s_4 s_5 = 44203$ then $s_6 = 4$ can only change to 2 or 3 and not change to symbol 1 or 0. These rules for all t exactly define the forbidden triangle $\delta < 1/5 + \gamma$.

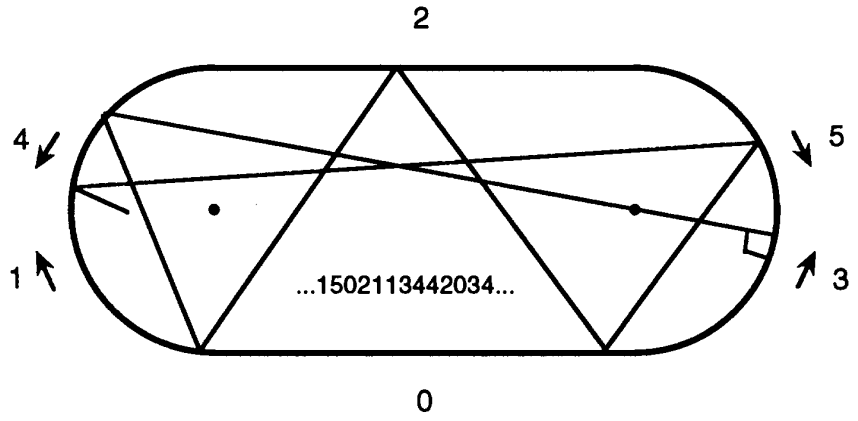

Figure 6.21: An orbit in the stadium going through one center of a semi-circle.

It seems to be extremely difficult to construct a Markov graph from these "triangle" rules. The symbolic string contains an infinite memory in a complicated way, and we have not been able to construct a finite Markov graph.

The simplest way to get rid of the triangle region is by not distinguishing between a right and a left bounce if there is only one simple bounce in the semi-circle as in the Biham and Kvale [25] alphabet s_t^b. This removes both the forbidden orbits of the triangle, and the double counting of the orbits bouncing normal to the semi-circle. We plot a long chaotic orbit in the symbol plane (γ^b, δ^b) for $a = 5$ in figure 6.22. In figure 6.22 a) the orbit is plotted in the symbol plane for bouncing off a straight line, with $s_0 = 0$, and in figure 6.22 b) for bouncing off the semi-circle with $s_0 = 4$. In (γ_0^b, δ_0^b) the same two squares are pruned as in (γ_0^a, δ_0^a). However in the (γ_4^b, δ_4^b) plane there is no triangular forbidden region as in the (γ^a, δ^a) plane. The largest forbidden regions are the rectangles $\gamma_4^b > 9/10$, $\delta_4^b < 1/10$, $2/10 < \gamma_4^b < 3/10$ and $7/10 < \delta_4^b < 8/10$. These are simple shifts of the squares in (γ_0^a, δ_0^a).

Biham and Kvale conjectured the forbidden orbits in the limit $a \to \infty$. Their forbidden orbits agrees with our forbidden square regions and in addition that the fixed points $\overline{1}$, $\overline{3}$, $\overline{4}$ and $\overline{5}$ do not exist. These fixed points are orbits bouncing infinitely many times in one semi-circle and these does not exist, while orbits bouncing any number of times in one semi-circle and then bounces somewhere else exist and are called "whispering gallery" orbits.

By using symbols s_t^b we can now construct a Markov diagram in the s_t^b symbols which gives all legal symbol strings. The only role that cannot be implemented is the forbidden fixed points $\overline{1}$, $\overline{3}$, $\overline{4}$ and $\overline{5}$, because only the fixed points are forbidden while any number of repetitions of the symbols are legal. We will discuss how this are implemented for the zeta-function in chapter 11. This graph is drawn in figure

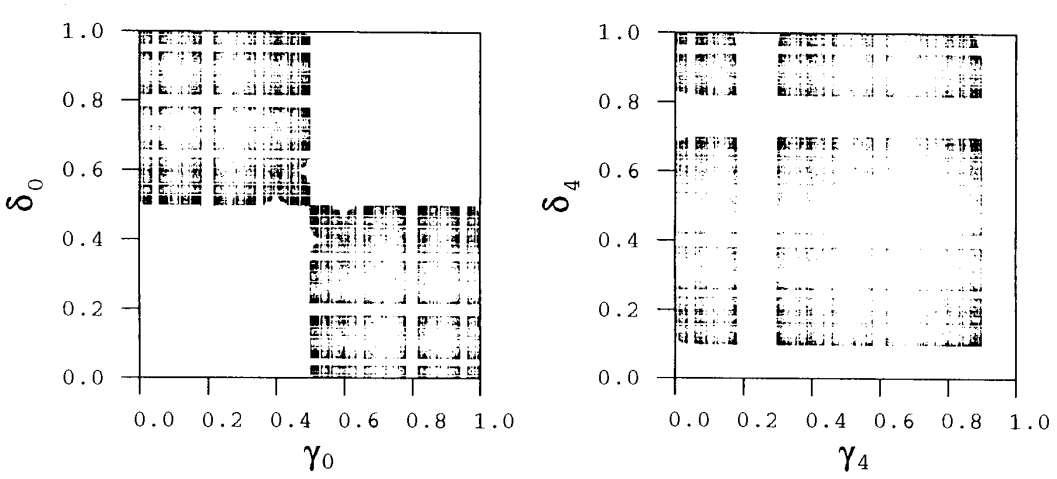

Figure 6.22: The points of a chaotic orbit in the symbol plane (γ^b, δ^b) for $a = 5.0$. Symbolic values for bouncing in a) the straight line $s_0 = 0$ b) the semi-circle with $s_0 = 4$.

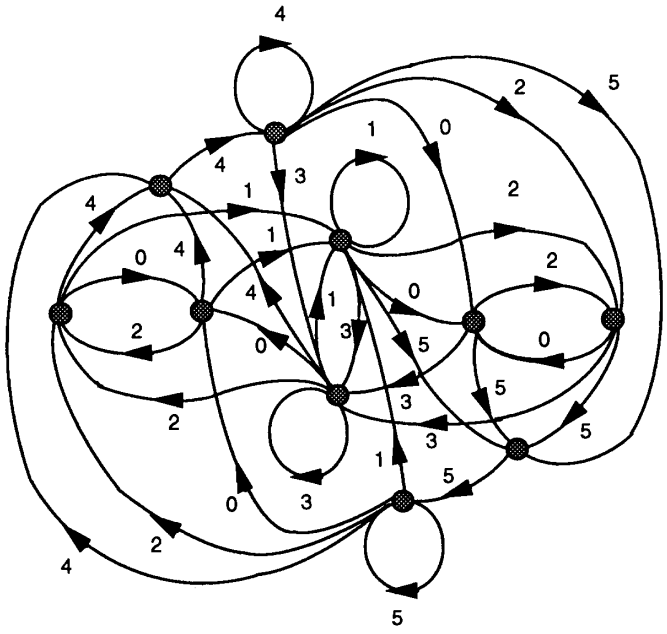

Figure 6.23: The Markov graph for the symbols s_t^b of the stadium.

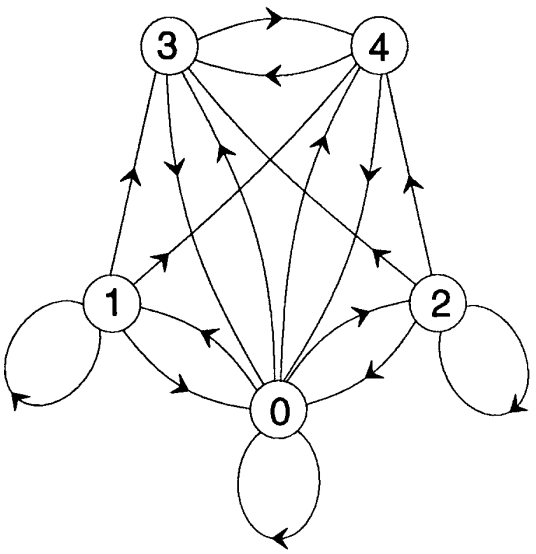

Figure 6.24: The Markov graph for stadium with alphabet s^c.

6.23 and it looks somewhat complicated. By using the method of counting loops and combinations of loops (section 1.3) we find the characteristic polynomial

$$p(z) = (1-z)^2(1+z)^2(1-z+3z^2+z^3)(1-3z-z^2-z^3) \tag{6.31}$$

All factors except the last one have to do with the symmetry of the graph [49] and the leading zero of the last factor gives the topological entropy:

$$z = -\frac{1}{3} - \frac{2^{\frac{8}{3}}}{3\left(13+3\sqrt{33}\right)^{\frac{1}{3}}} + \frac{2^{\frac{1}{3}}\left(13+3\sqrt{33}\right)^{\frac{1}{3}}}{3} = 0.2956\ldots \tag{6.32}$$

$$h = \ln z^{-1} = \ln 3.38298\ldots = 1.21875\ldots \tag{6.33}$$

We will show below that the graph can be simplified to figure 6.24 by using the alphabet s_t^c, and further to the graph in figure 6.25 using the alphabet s_t^d defined in table 6.3. The characteristic polynomial for the simple graph in figure 6.25 is

$$p(z) = 1-3z-z^2-z^3 \tag{6.34}$$

which is the last factor in (6.31) and the factor giving the topological entropy. That we have no other factors show that this alphabet s_t^d is in the fundamental domain and have no symmetries left.

The topological entropy is here not directly of physical interest for the dynamics because the "whispering gallery" orbits converge differently than the other orbits. It

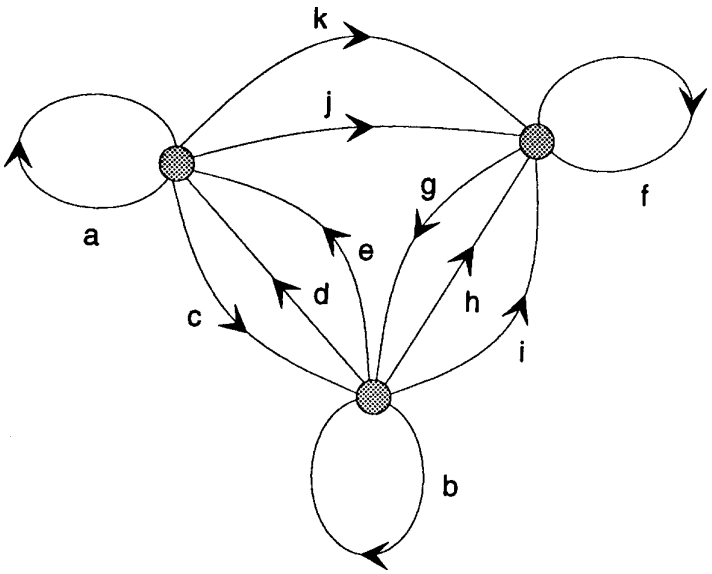

Figure 6.25: The reduced Markov graph for the stadium with alphabet s^d.

is however simple to calculate the topological entropy and it gives some information. In a complete horseshoe map the number of symbols is given as $\exp(h)$. This argument say that we here need 3.38 symbols in average to describe the possible orbits with these kind of orbits. In ref. [25] Biham and Kvale have calculated periodic orbits up to length 11 and they give the orbits which are left after applying geometrical pruning roles and from this table we find $h \approx \ln 3.1$ which is slightly less orbits than we expect from the diagrams. This may be due to the finite length of the orbits in Biham and Kvale's calculations.

The Markov graph, figure 6.24, describing the admissible orbits in the alphabet s_t^c are constructed by observing the following rules; The first bounce off a semi-circle,0, can be followed by a bounce off the other semi-circle, symbol 0, or by a second bounce off the same semi-circle either clockwise, symbol 1, or anticlockwise, symbol 2, or it can be followed by a bounce off one straight line with either symbol 3 or 4. These are the 5 arrows out from node 0 in figure 6.24. A second bounce in one semi-circle can be followed by a further bounce in the same semi-circle (with the same (anti-)clockwise direction) or by a bounce in the other semi-circle, symbol 0, or by a bounce in one of the two straight lines, symbol 3 or 4. This gives the 4 arrows out from the nodes 1 and 2 in figure 6.24. After a bounce in a straight line, symbol 3 or 4, a bounce in the other straight line has the opposite symbol as is clear from the inspection of figure 6.16. The other possible bounce after a straight line bounce is a first bounce in a semi circle, symbol 0. These two possibilities yields

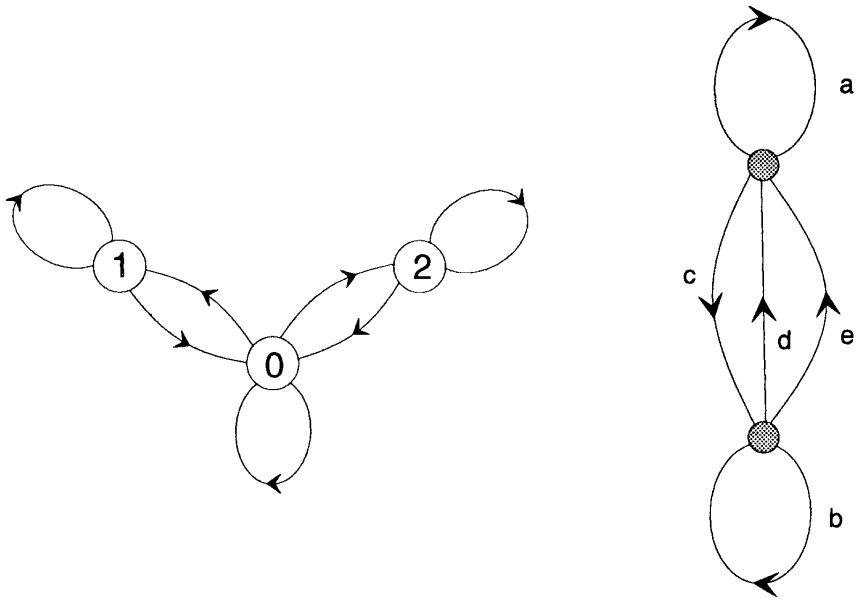

Figure 6.26: The reduced Markov graph for the simplified stadium scatterer. a) symbols s^c, b) symbols s^d.

the 2 arrows out from the nodes 3 and 4 in figure 6.24. Drawing the nodes and arrows gives the transition matrix in figure 6.24 with the characteristic polynomial

$$p(z) = (1-z)(1+z)(1-3z-z^2-z^3) \tag{6.35}$$

There is only half as many factors as in (6.31) since the alphabet s_t^c remove some of the symmetries.

To simplify this further and remove the symmetry in time and between clockwise and anticlockwise bounces we have to figure out which combinations of symbols that give the same segment of an orbit and which combinations of symbols that give essential different segments.

We define a fourth alphabet for the stadium in table 6.3, with symbols $s^d \in \{a, b, \ldots, k\}$. Symbols s^d are defined from two-symbol combinations of symbols s^c which in some cases depend on the symbolic string that preseeds the two-symbol configuration.

To understand why the dependence on the earlier symbols is necessary, look at the two symbol strings; s_t^c: $1(0)^n1$ and $2(0)^n2$. These two strings describe the same kind of segment of an orbit where the first string describes a clockwise orbit, and the second an anticlockwise orbit. A symbolic string $1(0)^n2$ describe a different kind of segment of an orbit which is symmetric to the segment described by the string $2(0)^n1$. Since the symbol 0 does not distinguish between clockwise and anticlockwise

s_t^d	$s_{t-1}^c s_t^c$	$\ldots s_{t-3}^c s_{t-2}^c s_{t-1}^c$
a	22	
	11	
b	00	
c	10	
	20	
d	01	$\ldots 1(0)^n$
	01	$\ldots 4(0)^n$
	02	$\ldots 2(0)^n$
	02	$\ldots 3(0)^n$
e	01	$\ldots 2(0)^n$
	01	$\ldots 3(0)^n$
	02	$\ldots 1(0)^n$
	02	$\ldots 4(0)^n$
f	34	
	43	
g	30	
	40	
h	03	$\ldots 2(0)^n$
	03	$\ldots 3(0)^n$
	04	$\ldots 1(0)^n$
	04	$\ldots 4(0)^n$
i	03	$\ldots 1(0)^n$
	03	$\ldots 4(0)^n$
	04	$\ldots 2(0)^n$
	04	$\ldots 3(0)^n$
j	23	
	14	
k	24	
	13	

Table 6.3: Definition for stadium symbols s^d from the symbols s^c.

bounces it is necessary to know the symbol preseeding the first 0 in a string of repeated 0's.

The Markov diagram in figure 6.25 with the s^d symbol is then constructed from labeling the arrows in the Markov diagram in figure 6.24, turning arrows into nodes and identify nodes with the same future. If we do not include the bounces in the straight lines $s^c = 3$, and $s^c = 4$ we obtain the diagrams in figure 6.26 a) and b). These diagrams are subsets of the full diagrams and describes the symbolic strings in the repellor consisting of only the two semicircles. These simpler diagrams can be constructed from inspecting the legal orbits in this repellor.

A difference between the s^d Markov graph and the preceding graphs is that in the preceding graphs the symbols can be associated either with the nodes or with the arrows between the nodes. In the s^d diagrams the symbols have to be associated with the arrows because there are two different arrows connecting the same two nodes.

The existence of the marginally stable periodic orbit bouncing between the two straight lines; s^a: $\overline{02}$ and the forbidden fixed points: s^a: $\overline{1}$, $\overline{3}$, $\overline{4}$, $\overline{5}$, suggests that we may introduce a new alphabet of the type applied in ref. [10] to study the Gauss map. We prefer however to construct the Markov graphs with includes all these special orbits, and when we find the expansion of the Zeta function from the graphs we sum up infinite families and avoid these orbits. This is further discussed in chapter 11.

Chapter 7

Pruning in billiards

We now give a pruning front description of the admissible orbits in all billiard introduced in chapter6. The pruning fronts are then approximated by converging sequences of approximate fronts which give finite Markov diagram description of the symbol strings of the admissible orbits.

7.1 Singular points

In the smooth two-dimensional folding maps such as the Hénon map, the pruning front is a symbolic representation of the primary turning points of the unstable manifold. Also in the piecewise linear Lozi map the kneading sequences from all primary (non-smooth) turning points mapped into the well ordered symbol plane define the pruning front. The Lozi map manifolds, figure 5.20, gives the most useful image in motivating our approach to determining pruning fronts in the billiard systems. Pictures of the manifolds of orbits in the 3 disk system and the stadium billiard are shown in figures 7.1 and 6.12. The manifolds have a structure similar to the Lozi map manifolds, figure 5.20, except that in a close billiard both manifolds are dense in the phase space. The manifolds are smooth lines changing direction at a singular points which we for the Lozi map called the turning points. The manifolds of the wedge/two ball problem, figure 6.10, and the overlapping disks are slightly different because the manifolds end at a singular point, but then continue somewhere else in the phase space instead of just change direction. To understand why these manifolds are discontinuous, we investigate closer the singularities in the different billiards.

For a dispersive billiard the point corresponding to the turning point of a 2-d map is the orbit touching the wall tangentially. Figure 7.2 shows how a line is folded at a dispersing wall and the point moving tangential to the wall is the turning point

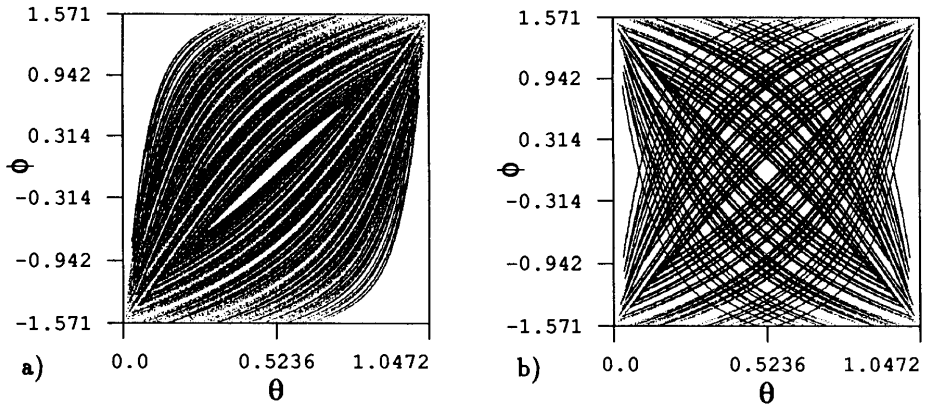

Figure 7.1: A part of the manifold of the orbit s: $\overline{123}$ in the touching 3 disk system, $r = 2$. a) The unstable manifold. b) The stable and unstable manifold.

of the folding. This orbit is usually called the singular orbit [181]. This grazing orbit in the dispersing billiard plays the same role in this system as the critical point in a unimodal map and the pruning front can be constructed by finding the symbol string (kneading sequence) of all orbits grazing the wall of the billiard domain.

The stadium billiard [32] has a singular point where a semi-circle joins a straight line. Figure 7.3 shows how a line of phase space points is folded when reflected in the neighborhood of a singular point. The picture is similar to the dispersive billiard; the curve after the folding is continuous with one sharp turning point. The turning point is the singular orbit bouncing off the singular point on the wall. At this point the wall is continuous and has a continuous first derivative but the second derivative is discontinuous. This gives the sharp folding of the neighborhood of the orbit through the singular point, acting as the turning point. The symbol strings for all orbits that bounce with different angles through this singular point yield a pruning front in a well-ordered symbol plane.

In the wedge billiard, as well as in the overlapping dispersive billiards, the folding of curves is qualitatively different than in the stadium and the non-overlapping dispersive billiards because a curve breaks up into two disconnected parts at the singular orbit. In other billiards the limit orbits from each side of the singular orbit converge to the same orbit, but this is not true in general, see figure 7.4. This is the simplest way a curve can break up, but if the incoming angle or the angles of the walls close to the corner are different, the limiting orbits to the singular point may bounce more than once close to the corner. In the integrable $\theta = 45°$ limit for the wedge billiard, the two limit orbits to the tip point are identical to each other for all incoming angles, and the same is of course true for $\theta = 90°$. Smilansky [185] has

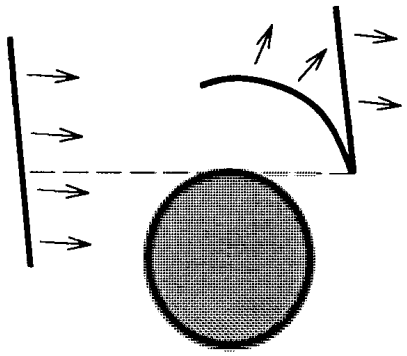

Figure 7.2: Folding of a line in the configuration space when bouncing off a dispersing wall.

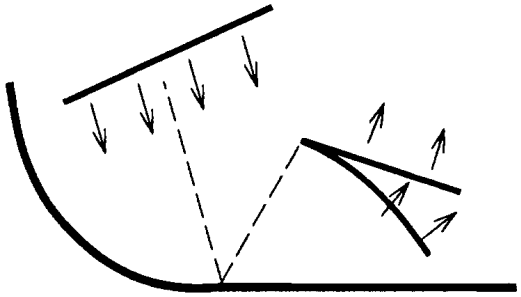

Figure 7.3: Folding of a line in the configuration space when bouncing off the stadium close to the singular point.

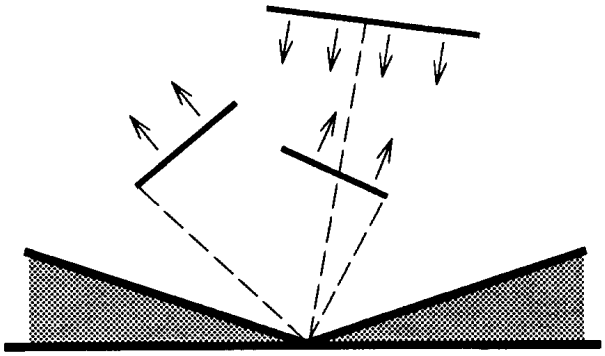

Figure 7.4: The breakup of a line in the configuration space when bouncing off a corner in the wedge billiard, or an overlapping disk system.

observed that for $\theta = 60^\circ$ many orbits return out in the same direction independent of whether they bounce to the right or to the left of the tip point. There may be other exceptions of this kind, but in general the folds are discontinuous as, for example, the manifold in figure 6.10. This makes the problem less like the Lozi map, and more like a two-dimensional version of a Bernoulli shift.

Discontinuity of folding does not lead to any problems in determining the pruning front. The pruning front is given by the symbolic strings of the two limits to the singular orbit, bouncing close to the corner with varying incidence angles. We let the orbits bounce off one of the two walls, and scan all outgoing angles (in the wedge billiard from $-\theta$ to θ); the symbol strings for each angle yields a point on the pruning front. If the folding had been continuous, we would only have scaned the angles between 0 and θ, so the consequence of the discontinuity is less symmetry in

the pruning front.

Similarely, in a dispersing billiard that has a corner with a finite angle, the corner leads to a discontinuity in the manifolds. The turning points are not tent-like bending points, but points where the manifolds end. An example is an overlapping disk billiard, where the distance between the disk centers is less than the sum of the two radii. Scanning through the different outgoing angles starting in the corner gives a second pruning front which we denote as the corner pruning front, to distinguish it from the tangent pruning front obtained from the tangent singularity discussed above. The point corresponding to the orbit bouncing from the corner tangentially to the wall is common to the two pruning fronts. This is the end point for both kinds of fronts, and by using this point we can combine the two fronts into one.

7.2 3-disk

The three-disk system gives a complete horseshoe for some parameter values. In a symmetric system the horseshoe is complete when the distance r between the centers of the disks is sufficiently large. At some critical parameter value the non-wandering set becomes a not complete binary Cantor set, but to determine this critical parameter value is not trivial.

We want a condition on the geometrical construction of the non-wandering set to distinguish between sufficiently separated disks and the case of pruning. We find that the non-overlapping disks are sufficiently separated to realize a complete horseshoe if condition 1 below is true.

Definition: Λ_1^+ consists of M strips in the phase space, with each strip m^+ the union of initial points (x, ϕ) from which a trajectory starting at x with angle ϕ hits a particular disk. As such a trajectory might have to penetrate other disks, the M strips are not necessarily disjoint. Λ_1^- consists of the M strips, with each strip m^- the union of points (x, ϕ) where the trajectory starting at x with angle $-\phi$ hits a particular disk. We call a transverse intersection of a strip m^+ and a strip m^- a *rectangle*. The set $\Lambda_1 = \Lambda_1^+ \cap \Lambda_1^-$ then consists of M^2 rectangles, not necessarily disjoint. The set $\Lambda_T = \Lambda_T^+ \cap \Lambda_T^-$ with $T > 1$ consists of intersections of forward and backward strips corresponding to T consecutive bounces with the outgoing angle at each bounce equal to the incoming angle, but allowing the trajectories to go through discs. Then Λ_T consists of M^{2T} rectangles.

Condition 1 *There exists a finite integer T such that Λ_T consists of M^2 disjoint areas where each area is inside one of the M^2 rectangles of Λ_1.*

The iteration of the M^2 disjoint areas corresponds to one more bounce and gives that each of the M^2 disjoint areas contains M^2 new disjoint areas. The M^4 rectangles of Λ_2 then contains M^4 disjoint areas. By induction we find that $\Lambda_{T+T'}$ gives $M^{2T'}$ disjoint areas inside the $M^{2T'}$ rectangles of $\Lambda_{T'}$. From this it follows that even if the rectangles of $\Lambda_{T'}$ overlap each other, the parts of the non-wandering set belonging to different rectangles do not overlap. A symbol string $(w_{-T'+1}w_{-T'+2}\dots w_{T'-1}w'_T)$, with $w_t \in \{0,1,\dots,(M-1)\}$ corresponds to a unique rectangle, and is a substring of the symbol strings for all trajectories that pass through this rectangle. It then follows that the disks are sufficiently separated and the non-wandering set a complete horseshoe.

If the condition is not satisfied, there might be an infinitesimal change of the parameters that yeilds a finite a $0 < T < \infty$; this is the critical parameter value where pruning starts. If such finite T cannot be realized for any perturbation of parameters, then the rectangles always overlap, and the symbol dynamics is always pruned.

A different and more intuitive way to describe the orbits that disappear first is to find the point in the Cantor set Λ in (x,ϕ) with the largest angle ϕ, and determine the parameter value for which $\phi = \pi/2$, i.e. this point represents an orbit bouncing tangential to a disk. In the symmetric three-disk system this point is the hetroclinic point where the unstable manifold of one period two orbit crosses the stable manifold of the other period two orbit. Numerically this can be found by starting an orbit grazing off the disc at the symmetry line and find the parameter value for which the orbit converges to the period two orbit. Figure 7.5 shows this orbit for the critical parameter value $r_c = 2.04821419\dots$.

There are two different homoclinic orbits that look like the orbit drawn in figure 7.5 for the critical parameter value r_c. For $r > r_c$ one of the orbits bounces off the disc, and the other orbit passes by the disk without bouncing for $r > r_c$. An orbit may then become singular either because a bounce gets an angle $\phi = \pi/2$ or because at a place without any bounce the path is grazing the disk. There orbits will define two pruning fronts for the non-overlapping dispersive billiards.

7.2.1 Pruning front

For $2 \le r < r_c$ the above two pruning mechanisms give two forbidden regions in the symbol plane. We shall call the border of the regions the "tangential pruning front". The two mechanisms are illustrated in figure 7.6. Figure 7.6 a) shows sections of two admissible orbits. One orbit passes by the dispersing wall, and the other one bounces off the wall from the dispersing side. Figure 7.6 c) shows corresponding

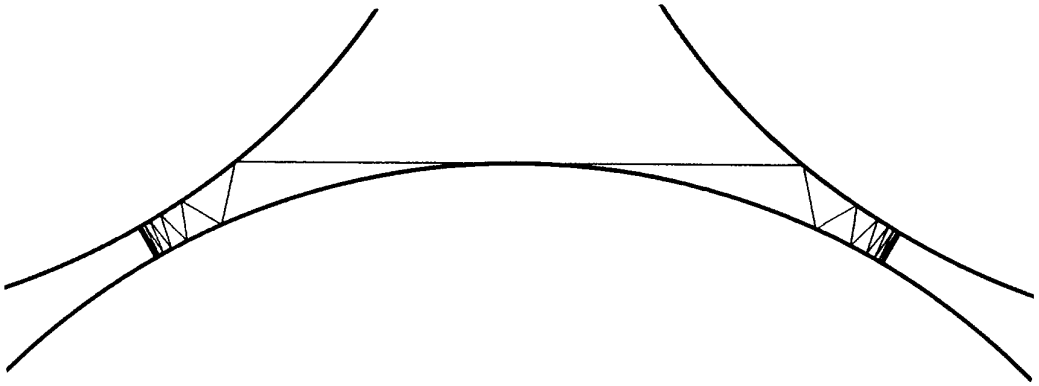

Figure 7.5: The hetroclinic orbit of the 3 disk system at the critical parameter value $r_c = 2.04821419\ldots$ where this orbit bifurcates and becomes the first pruned orbit of the 3 disk system.

sections of two forbidden orbits. In one the trajectory penetrates the disk along a straight line. The other orbit bounces off the wall with the incidence angle θ larger than $\pi/2$, so thetrajectory penetrates into the disc and bounces off the wall from the wrong side. The reason for including these unphysical orbits is that with them every n-ary alphabet symbol string is realized. The inadmissible orbits can be distinguished from the admissible orbits by observing that they include bouncing angles larger than $\pi/2$, or that the orbit goes through a wall. The singular limit orbit between the admissible and inadmissible orbits is the orbits tangentially to the wall, figure 7.6 b).

The pruning front can be calculated numerically by starting a tangential orbit at a point x on the disk, following the orbit through any number of bounces (in our numerical examples 30), and recording the corresponding symbol string. Given this future symbol string and the past symbol string obtained by bouncing tangentially off the disk in the oposite direction, we find for each initial $(x, \pm\pi/2)$ the corresponding symbol plane point (γ, δ). As an orbit starting tangenially at a point x may be considered as the limit either of an orbit bouncing off the wall, or an orbit not touching the disk, we have two choices for the symbol s_0. Either the symbol s_0 is the symbol corresponding to this disk and s_1 is the symbol of the next disk the particle bounces off, or we ignore the symbol of this disk and let s_0 be the symbol for the next bounce. In this way the tangent in phase space corresponds to two different pruning front points (γ, δ) in the symbol plane.

Assume (γ, δ) is the symbolic coordinate for an orbit bouncing tangentially off a disk. Then assume that the symbolic past is constant and change one symbol s_t in the future symbolic description. If the incidence angle for the corresponding orbit

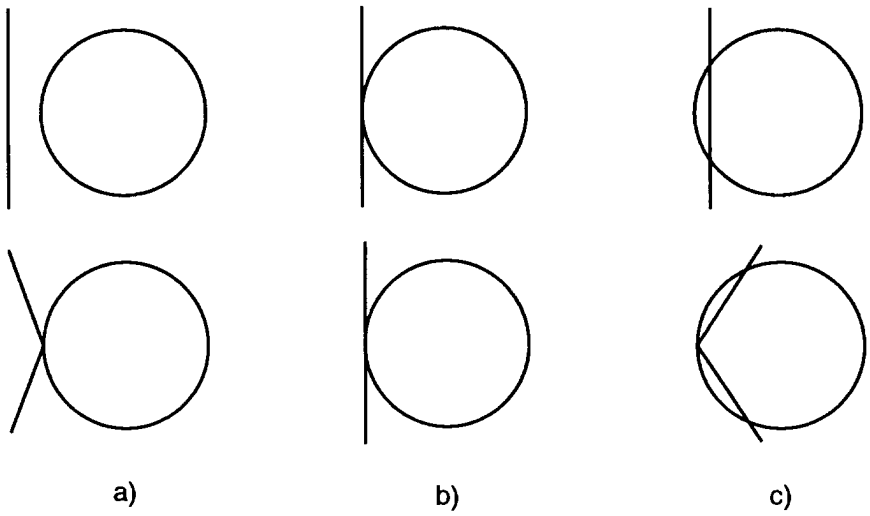

Figure 7.6: Orbit segments which are a) admissible, b) at the pruning point, and c) inadmissible. The two inadmissible orbits in c) are the only two pruning mechanisms for dispersive billiards without corners.

changes to $\phi > \pi/2$, this symbol string is pruned. It may also happen that the angle changes to $\phi < \pi/2$, in case which the orbit is admissible. The well-ordered symbols are constructed in such a way that an increase in the angle ϕ is an increase in the symbolic value, and in the well ordered symbol plane (γ, δ), the symbolic representation of the tangent orbit is the border between the admissible and the pruned orbits i.e. the pruning front. An other important question is whether the front changes monotonously in the symbol plane. When we scan the different tangent orbits we increase monotonically the value of the position coordinate x, keeping the angle $\phi = \pi/2$ constant. As we move in the x-direction in the phase space we cross the foliation of both the stable and the unstable manifolds in only one direction. We then move monotonously in the space defined by the manifolds which is our symbol plane. The pruning front is obtained by the symbol strings from such a scan of x-values and is piecewise *monotone* in the symbol plane. The shifted symbol stings of these orbits are piecewise monotone, and we give examplels of this in the figures below.

The second pruning front is given by the same symbolic string, except that the symbol for the tangential bounce is omitted. This pruning front then also has to be monotone. The second pruning front describes the orbits that do not bounce off the tangency disk and therefore has no representation in the symbol plane for this bounce. As any shift of the symbol strings is equivalent, we choose to draw

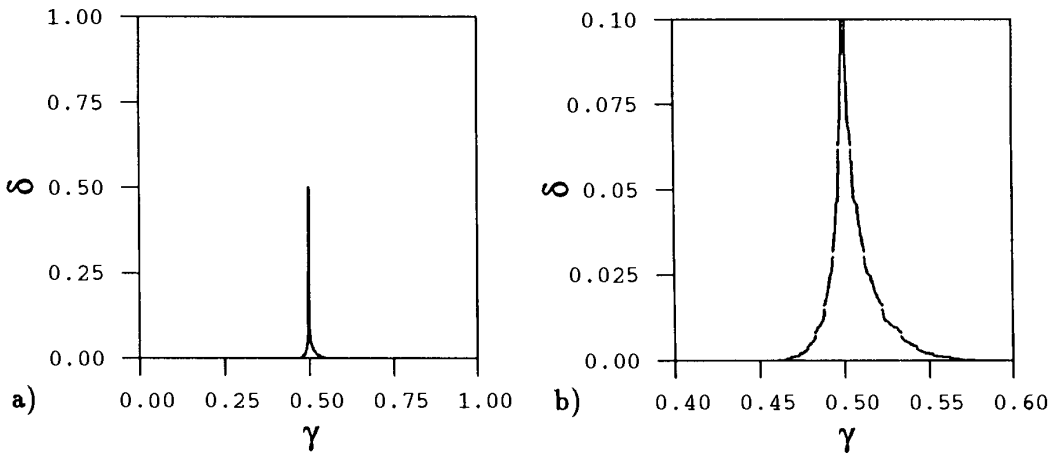

Figure 7.7: a) The tangent pruning front for the 3-disk system for touching disks, $r = 2$. b) Magnification.

both pruning fronts in the symbolic plane corresponding to the bounce immediately before the tangent bounce. These are of course also monotone curves. The region bounded by the two pruning fronts, from the two families of strings with and without the symbol of the tangent disk, and by the border of the unit square, is the *primary pruned region*.

Examples of the pruning fronts for the three-disk system are drawn in figures 7.7, 7.8 and 7.9.

We can numerically test the pruning front by plotting symbolic values (γ, δ) for a long chaotic orbit with random initial point. Such chaotic orbits are plotted in (γ, δ) in figures 7.10, 7.11 and 7.12. Comparing these with the pruning fronts of figures 7.7, 7.8 and 7.9 we see that the pruning front together woth the edges of the symbol plane are the limites of white areas which are never visited by the chaotic orbits. We refere to the white area limited the pruning front as the primary forbidden region.

Beyond the primary forbidden regions, there are also other white areas in the figures. For figures 7.10 and 7.11 it follows from the conjecture of existence of only two pruning mechanisms for non-overlapping disks that all other white regions in the (γ, δ) plane are images or preimages of the primary regions. For example, it is easy to see that in figure 7.10 the largest visible white regions are around the lines $\gamma = 1/2^n$ and $\delta = 1/2^n$. The shift operation is a binary shift, so the large primary regions surrounding the lines $\gamma = 1/2$ and $\delta = 1/2$ are partly mapped into regions surrounding the lines $\gamma = 1/2^n$ and $\delta = 1/2^n$ because the shift operation make $\delta \to \delta/2$ if $\gamma < 1/2$, and similarly backward in time $\gamma \to \gamma/2$ if $\delta < 1/2$. At

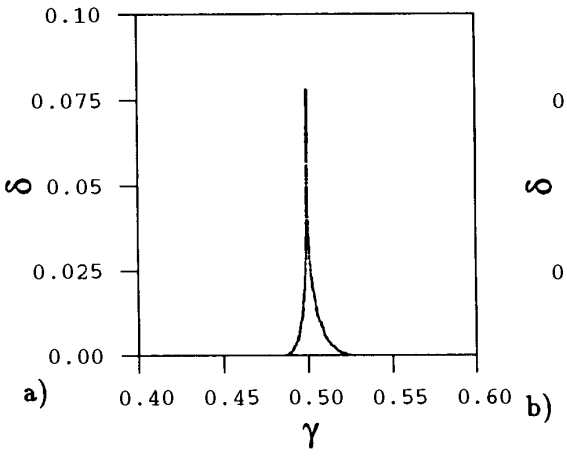

Figure 7.8: The tangent pruning front for the 3-disk scattering system $r = 2.02$.

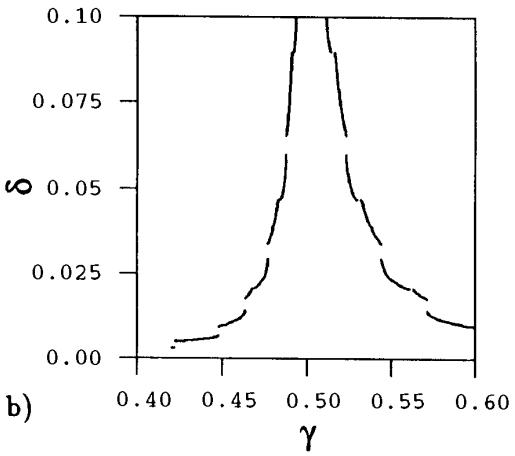

Figure 7.9: The tangent pruning front for the closed 3-disk system $r = 1.97$.

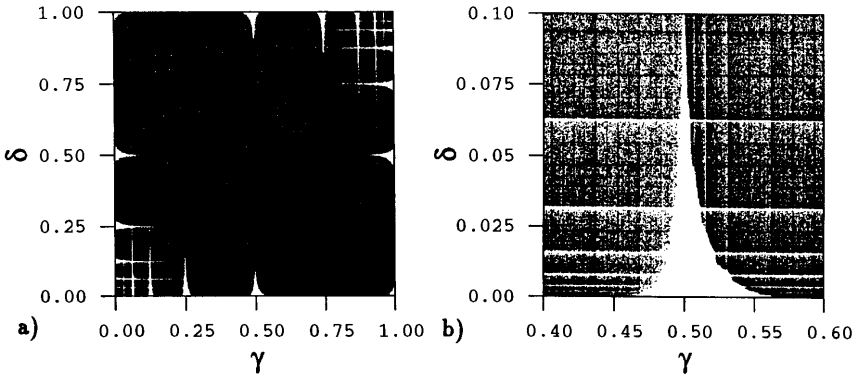

Figure 7.10: Bounces of a typical chaotic orbit plotted in (γ, δ) plane for the 3-disk system for touching disks, $r = 2$. b) Magnification of the primary pruned region.

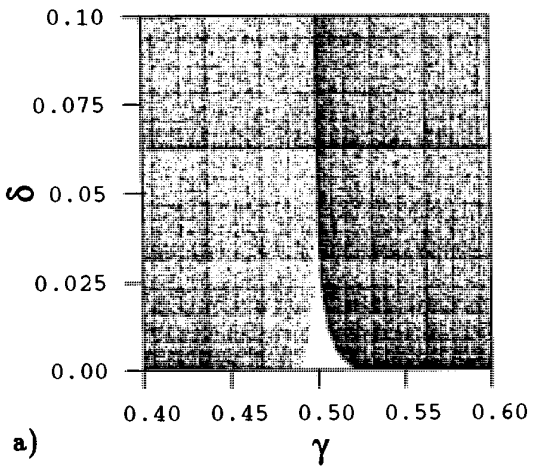

Figure 7.11: Bounces of a typical chaotic orbit plotted in (γ, δ) plane for the scattering 3-disk system, $r = 2.02$.

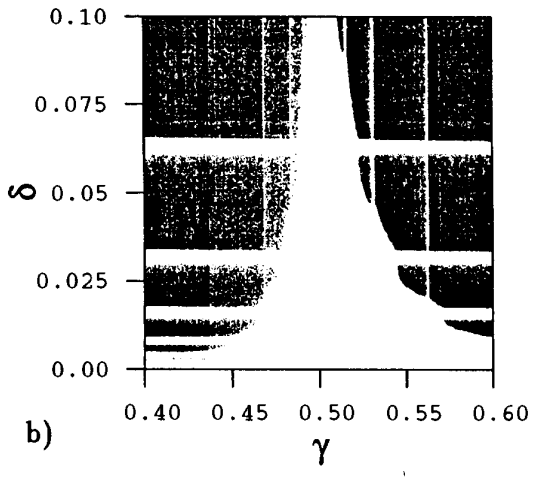

Figure 7.12: Bounces of a typical chaotic orbit plotted in the (γ, δ) plane for the closed 3-disk system, $r = 1.97$.

the same time the area is squeezed by a factor 2 in one direction and enlarged by a factor 2 in the other direction. As pointed out by Troll [193], this kind of well-ordered symbols has a more complicated time shift than the corresponding symbols s_t. For the s_t symbols the time shift is only a shift of the "present dot", that is all indices t change to $t + \tau$ after τ iterations. In the (γ, δ) plane the time iteration is both a shift operation, and an inversion $\gamma \to 1 - \gamma'$ and $\delta \to 1 - \delta'$. This follows from the algorithm (6.7).

The more complicated time iteration is the price one has to pay to get symbols that have a simple spatial ordering. All systems for which there is a change in direction under the folding cannot be ordered in space and time simultaneously.

The area of the primary pruned region grows as the parameter r decreases in the symmetric 3-disk system. As the distance between the disks becomes smaller, more and more orbits become forbidden, and the pruning front moves enlarging the pruned region. The topological entropy then decreases as r decreases.

7.2.2 Overlapping disks

In the 3-disk system with $r < 2$ the disks overlap each other. This leads to an additional pruning front mechanism. As long as the disks are not overlapping each other an orbit can bounce an arbitrarily number of times close to the period 2 cycle $\overline{s_1 s_2} = \overline{12}$ or $\overline{23}$ or $\overline{31}$, in the well-ordered symbols close to either $\overline{w_1} = \overline{0}$ or $\overline{w_1} = \overline{1}$. When the disks touch each other, $r = 2$, the cycle $\overline{s_1 s_2} = \overline{10}$ disappears, and for overlapping disks, $r < 2$, an orbit can only have a finite number of bounces

in a corner where two disks intersect. How many times a particle can bounce in the corner depends on the angle at which it arrives to the corner. The corner pruning front is obtained by bouncing out from the corner at all allowed angles, and determining the corresponding symbolic values (γ, δ).

The corner pruning front is drawn in figure 7.13 for $r = 1.9$. The tangential pruning front for the same parameter value is drawn in figure 7.14. In figure 7.15 we have drawn the two pruning fronts and some of their images together; we note that the corner pruning front ends where the tangent pruning front starts. A long chaotic orbit, figure 7.16, stays below the pruning front and never crosses into the forbidden white regions.

The corner pruning front moves down and gives a larger forbidden region as the disks move together. Figure 7.17 shows the corner pruning front for the parameter value $r = 1.8$, and figure 7.18 shows the tangent pruning front for the same parameter value. The corner pruning front becomes more important as r decreases and the tangent pruning front becomes smaller as r decreases.

In the limit where the area of the domain in which the particle bounces vanishes $(r \to \sqrt{3} = 1.732\ldots)$ the domain approaches a triangle, and the tangential pruning front shrinks to a point, the point common to the two pruning fronts. As we show in chapter8, the corner pruning front becomes a straight line.

7.2.3 Approximating the pruning front

The pruning front is an exact solution to the problem of "which orbits are forbidden in the billiard system", limited only by the numerical accuracy of calculating an orbit.

This picture is neither less nor more useful than the kneading sequence of the logistic map. To be useful in calculations of average values of physical interest the primary forbidden region has to be transformed into a description of admissible orbits in such a way that one can construct the Markov diagrams and the associated zeta function expansions for the new symbolic alphabet.

There may be several ways to do this but, we have chosen to follow the same procedure that we have used for one-dimensional maps. The forbidden region can be split into rectangles described by finite symbol strings which corresponds to paths of finite length down the symbolic tree, and we construct an approximate sequence of finite Markov graphs or automata. In the unimodal map this procedure works very well, and for the Hénon map it will converge rather well. The procedure also works in the billiards studied here, but the convergence has to be less good as the pruning front does not have a staircase structure as the Hénon map, with

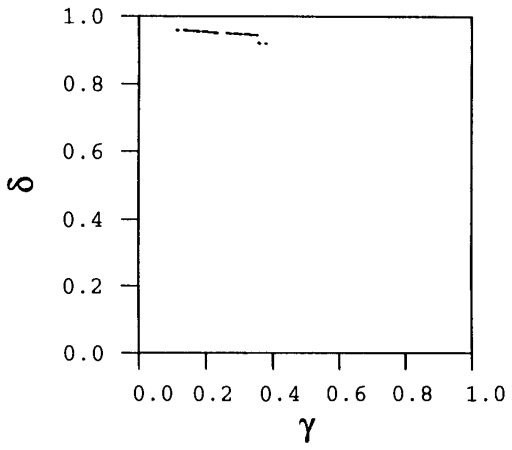

Figure 7.13: The corner pruning front for 3 overlapping disks, $r = 1.9$.

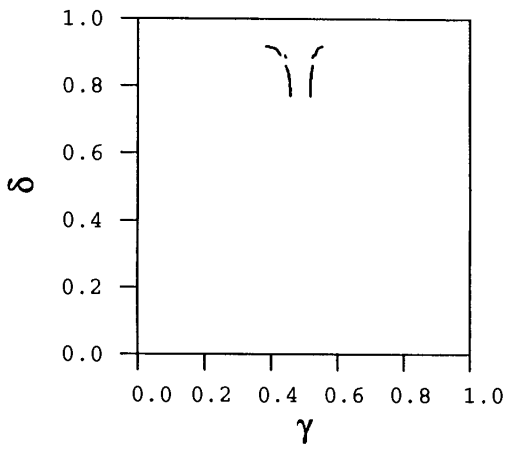

Figure 7.14: The tangent pruning front for 3 overlapping disks, $r = 1.9$.

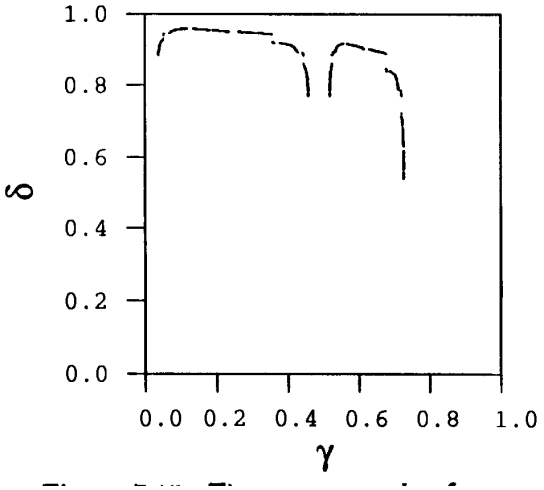

Figure 7.15: The corner pruning front, the tangent pruning front, together with some of their images, $r = 1.9$.

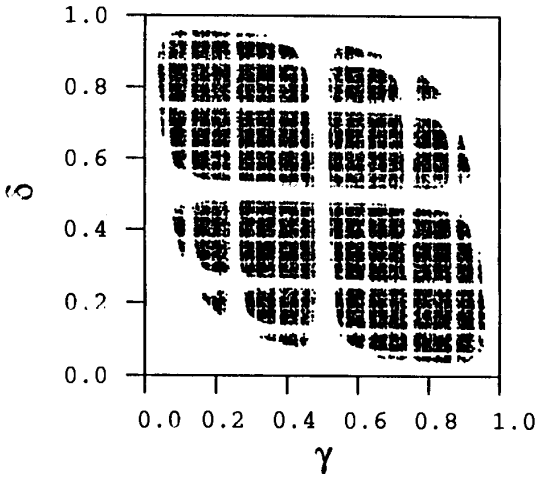

Figure 7.16: Bounces of a long chaotic orbit for the 3 overlapping disks, $r = 1.9$.

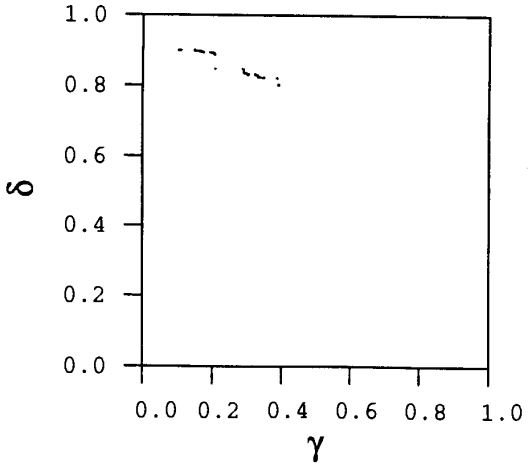

Figure 7.17: The corner pruning front for 3 overlapping disks, $r = 1.8$.

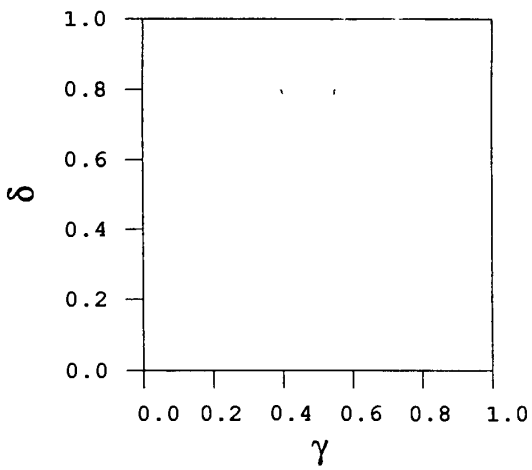

Figure 7.18: The tangent pruning front for 3 overlapping disks, $r = 1.8$.

a few large steps and smaller steps organized in a hierarchy. For a staircase-like pruning front where the steps become small very fast, a few rectangles cover most of the forbidden regions. If the pruning front is more like a smooth curve, the approximation with rectangles converges slowly. This suggests that we should use some kind of trapezoidal approximation, but at present we do not know how to implement this.

The first step is to find the forbidden rectangles in the symbol plane (γ, δ). In figure 7.19 we draw the pruning front together with a staircase approximation with steps at all rational values $p/2^7$. If we make an "under-pruning" ("under-counting") approximation where we let the approximating curve be entirely inside the forbidden region. We then take away too few of the forbidden orbits, but we are guaranteed that any orbit that exists in the system will be included in the new alphabet we construct. Alternatively we can choose to "over-prune" and let the approximation be on the other side of the pruning front. This implies that there are orbits in the system which cannot be represented in the alphabet we construct but every symbol sequence generated is realized by the dynamics. The third possibility is to chose a "closest" curve which partly over-prunes and partly under-prunes the system.

The approximation curve in figure 7.19 is an under-pruning curve, including some squares which are completely in the forbidden region. Each square with the side length 2^{-k} corresponds to a symbol string of length $2k$ in the symbolic description. The forbidden symbol strings of lengths 12, 14, 16, and 18 are given in table 7.1.

As an example, we implement this by taking the shortest forbidden string which

$\_w_{-5} \ldots w_6\_$	$\_w_{-6} \ldots w_7\_$	$\_w_{-7} \ldots w_8\_$
$000000 \cdot 100000$	$0000000 \cdot 1000011$	$00000000 \cdot 10001010$
	$0000000 \cdot 1000010$	$00000000 \cdot 10001001$
	$0100000 \cdot 1000001$	$00000000 \cdot 10001000$
	$0100000 \cdot 1000000$	$01000000 \cdot 10000101$
	$1100000 \cdot 1000000$	$01000000 \cdot 10000100$
	$0010000 \cdot 1000000$	$11000000 \cdot 10000100$
	$1000000 \cdot 0111111$	$01100000 \cdot 10000010$
	$0000000 \cdot 0111111$	$11100000 \cdot 10000010$
	$0000000 \cdot 0111110$	$01010000 \cdot 10000001$
	$0100000 \cdot 0111111$	$01010000 \cdot 10000000$
		$11010000 \cdot 10000000$
		$00110000 \cdot 10000000$
		$10110000 \cdot 10000000$
		$01110000 \cdot 10000000$
		$11110000 \cdot 10000000$
		$00001000 \cdot 10000000$
		$01010000 \cdot 01111111$
		$10010000 \cdot 01111111$
		$00010000 \cdot 01111111$
		$11100000 \cdot 01111111$
		$01100000 \cdot 01111111$
		$01000000 \cdot 01111101$
		$00000000 \cdot 01111011$

Table 7.1: The forbidden orbits in 3 discs, $r = 2$. "Under-counting" approximation to level 9.

$\_w_{-8} \ldots w_9\_$		
000000000 · 011110011	110101000 · 100000000	001000000 · 100001110
000000000 · 011110100	010101000 · 100000000	001000000 · 100001111
000000000 · 011110101	100101000 · 100000000	110000000 · 100010000
100000000 · 011110101	000101000 · 100000000	010000000 · 100010000
010000000 · 011110111	111001000 · 100000000	010000000 · 100010001
001000000 · 011111000	011001000 · 100000000	000000000 · 100010110
001000000 · 011111001	101001000 · 100000000	000000000 · 100010111
011000000 · 011111011	001001000 · 100000000	000000000 · 100011000
111000000 · 011111011	110001000 · 100000000	000000000 · 100011001
000100000 · 011111011	010001000 · 100000000	
001100000 · 011111101	000110000 · 100000010	
101100000 · 011111101	111010000 · 100000010	
011100000 · 011111101	011010000 · 100000010	
111100000 · 011111101	011010000 · 100000011	
011010000 · 011111110	010010000 · 100000100	
011010000 · 011111111	100010000 · 100000100	
111010000 · 011111111	000010000 · 100000100	
000110000 · 011111111	000010000 · 100000101	
100110000 · 011111111	001100000 · 100000110	
010110000 · 011111111	010100000 · 100001000	
110110000 · 011111111	100100000 · 100001000	
001110000 · 011111111	000100000 · 100001000	
101110000 · 011111111	000100000 · 100001001	
011110000 · 011111111	111000000 · 100001010	
111110000 · 011111111	011000000 · 100001010	
000001000 · 011111111	001000000 · 100001100	
100001000 · 011111111	001000000 · 100001101	

Table 7.1: Continue.

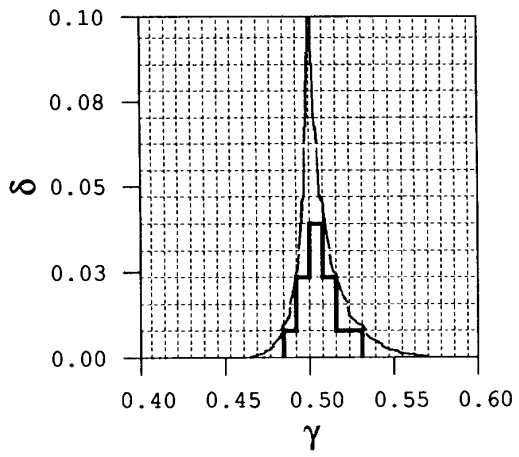

Figure 7.19: The pruning front for the 3 disk system for touching disks, $r = 2$, and a rational rectangles approximation.

has length 12, together with the time reversed version of the string and the conjugate strings (0 and 1 interchanged) as the forbidden strings which we remove from the binary tree. The corresponding Markov diagram is too complicated to implement by hand, and we use a computer program that generates an automaton from a list of forbidden strings. In order to handle the tree structure this program has to be relatively complicated; because of the object oriented structure of the data we have programmed it in C. The nodes with pointers to other nodes are programmed as *struct* variables, with pointers containing the address of the variables. The construction of the automaton is quite fast, but going through all loops and finding all possible combinations of non self-intersecting loops can be time consuming. We find that when the number of nodes in the automaton is larger than a number between 50 and 100, the time the program needs to scan all loops is too large for practical calculations. This may however vary a lot depending on the number of symbols and the structure of the automaton.

The result of this calculation is the fundamental part of the zeta function with all the terms that are not shadowed by shorter orbits but usually also a number of orbits that are shadowed together with the shadowing combinations. We will return to this problem in chapter 11. If we were only interested in determining the topological entropy, section 1.3, we could simply find the average number of symbol strings of a given length starting at one node in the tree. In practice this converges rather quickly with the length of the string to the correct entropy and can be applied to rather large trees.

With the 4 pruned symbol strings of length 12; 000000100000, 000001000000,

111111011111, 111110111111, we obtain an automaton with 35 nodes and the longest loop of length 22. The topological polynomial is

$$\begin{aligned} p(z) &= (-1+z)^2\,(1+z)\left(1-z+z^2\right) \\ &\quad \left(1+z+z^2\right)\left(1+z^6+z^7+z^8+z^9+z^{10}+z^{11}\right) \\ &\quad \left(1-z-z^2-z^3-z^4-z^5-z^6-z^8-2\,z^9-3\,z^{10}\right. \\ &\quad \left.-4\,z^{11}-3\,z^{12}-4\,z^{13}-3\,z^{14}-2\,z^{15}-z^{16}\right) \end{aligned} \tag{7.1}$$

The 4 forbidden strings are symmetricunder time reversal and $0 \leftrightarrow 1$ interchanged so we expect that the polynomial can be factorized [48]. The leading zero belongs to the 16th order polynomial, and yields $h = \ln 1.99856\ldots$.

The automaton can also be constructed with all the length 12 and 14 forbidden symbol strings, table 7.1. Some of the forbidden strings can be reduced to shorter strings; e.g. the two strings of length 14, $0000000 \cdot 1000011$ and $0000000 \cdot 1000010$, can be combined to one length 13 string 0000000100001, and both the two strings $0100000 \cdot 1000000$ and $1100000 \cdot 1000000$ contain the forbidden length 12 string 000001000000 and can be left out from the list. All strings up to length 14 are pruned by the following list of forbidden strings

$$\begin{array}{l} 000000100000 \\ 0000000100001 \\ 0100000100000 \\ 0000000111111 \\ 0000000011111 \\ 00100001000000 \\ 01000000111111 \end{array} \tag{7.2}$$

together with the time reversed strings and the strings with 0 and 1 interchanged. These forbidden strings yield an automaton with 171 nodes, too large for determination of all non-intersecting loops and their combinations. Counting all possible paths from the root node gives a topological entropy estimate $h = \ln 1.99575\ldots$.

That the calculation exceeds our computational skills after just a few approximations may seem discouraging, but the touching disk example is a bit special among the pruned systems because it has very few forbidden strings, or more precisely; there are no short orbits which are pruned. The average number of symbols is around 1.99 which is rather close to 2, and the pruning is not so important as in many other systems. The method works much better in the cases whith heavy pruning and where one really needs to control pruning in order to apply the theory to problems such as evaluation of semiclassical resonances.

For the overlapping three disk problem, e.g. $r = 1.9$, we find more interesting results. We can draw the pruning front for the corner and tangent pruning together with a 2^{-k} lattice and find the symbols corresponding to squares outside the pruning front in the forbidden region. By combining the forbidden strings we obtain the following list of forbidden orbits up to length 12:

$$\begin{array}{l} 11111 \\ 1101111 \\ 11110000 \\ 11100000 \\ 110111011 \\ 101111010 \\ 111011101 \\ 1111010111 \\ 11011011101 \\ 001111010111 \\ 101111001111 \end{array} \tag{7.3}$$

Pruning the two strings 11111 and 00000 of length 5 yields an automaton with 9 nodes and the characteristic polynomial

$$p(z) = \left(1 - z - z^2 - z^3 - z^4\right)\left(1 + z + z^2 + z^3 + z^4\right) \tag{7.4}$$

with a topological entropy $h = \ln 1.927561\ldots$.

Pruning the strings of length 5 and 7 yields an automaton with the characteristic polynomial

$$\begin{aligned} p(z) &= (-1 + z + z^2 + z^3 + z^4 - z^5 + z^6 - z^7 - z^{10}) \\ &\quad (-1 - z - z^2 - z^3 - z^4 - z^5 - z^6 + z^7 + 2\,z^8 + 2\,z^9 + z^{10}) \end{aligned} \tag{7.5}$$

giving a topological entropy $h = \ln 1.893040\ldots$. Including also the length 8 forbidden strings yields an automaton with 31 nodes with

$$\begin{aligned} p(z) &= (1 + z + z^2 + z^3 - 2\,z^7 - 2\,z^8 - 2\,z^9 - z^{10}) \\ &\quad (1 - z - z^2 - z^3 - 2\,z^6 + z^{10}) \end{aligned} \tag{7.6}$$

which yields the topological entropy $h = \ln 1.889286\ldots$. The value of e^h as a function of the maximal length of the forbidden strings included is plotted in figure 7.20 a). The topological entropy seems to converge to $h = \ln 1.862\ldots = 0.62\ldots$. We can plot the values $\ln(z - z_{l=12})$ as a function of the length as we did for the logistic map in figure 1.23. For the logistic map we found that this plot was linear with a slope $-h$. In figure 7.20 b) the convergence of the entropy seems to be faster as a function of the length of the forbidden strings. If the few points plotted are approximated by a line the slope is around -1.

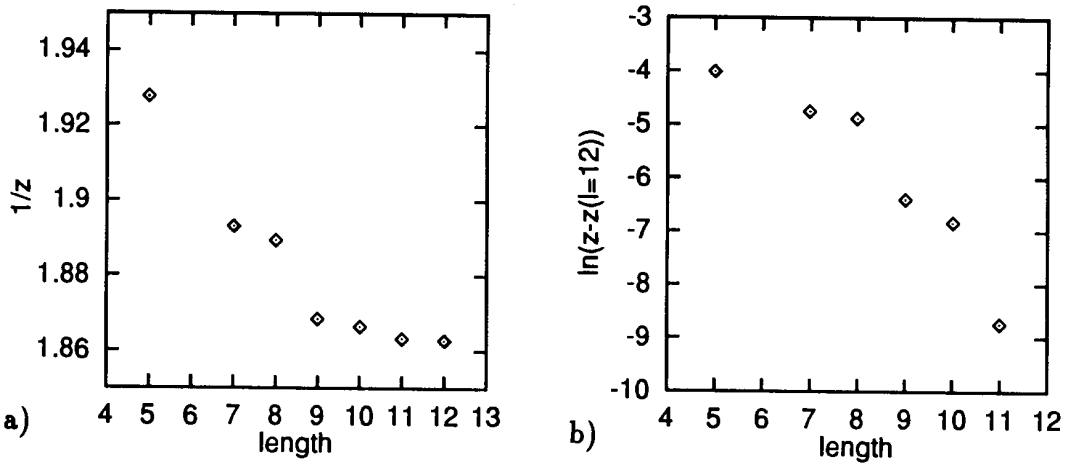

Figure 7.20: The values a) $a/z = e^h$ and b) $\ln(z - z_{l=12})$ as a function of the length of the forbidden strings for 3 disk $r = 1.9$.

7.3 4-disk

The analysis of the symmetric four disk system is very similar to the three disk system. We construct pruning fronts from the tangential and the corner orbits, and find the forbidden regions in the symbolic value plane (γ, δ). The alphabet s_t has 4 symbols, and the well-ordered alphabet, eq. (6.12), has 3 symbols. Hence the symbolic values are base-3 numbers, and the shift operations looks slightly different from the binary 3-disk case.

As for the three-disk system, the pruning starts at a critical disk separation r_c, where a point in the non-wandering set attains $\theta = \pi/2$. This outermost point is the hetroclinic point where the unstable manifold of one period-2 orbit, e.g. $\overline{s_1 s_2} = \overline{12}$, crosses the stable manifold of another period 2 orbit, e.g. $\overline{s_1 s_2} = \overline{23}$. We find numerically $r_c = 2.20469453\ldots$. Hence for the 4-disk system the pruning starts when the distance between the disks is approximately 20% of the radius, while in the 3-disk system pruning started at the distance approximately 5% of the radius.

For $2 \leq r < r_c$ the forbidden regions are limited by the tangential orbit pruning fronts. Figure 7.21 shows the pruning front for the touching disk case, $r = 2$.

As for the three-disk system, we make a grid in the symbol plane, and read off the forbidden strings listed in table 7.2.

The shortest forbidden string is the length 6 string 000100 (in terms of the w_t symbols) and letting this sting and the symmetric strings 001000, 222122 and 221222 be forbidden we obtain an under-pruned Markov graph with a new alphabet

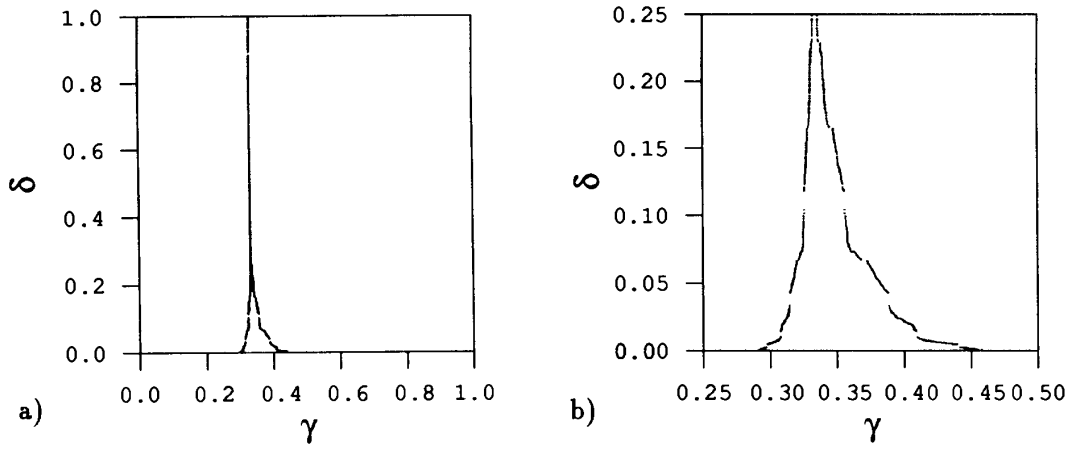

Figure 7.21: The pruning front for the touching 4-disk system, $r = 2$. b) Magnification.

and the characteristic polynomial

$$p(z) = (-1+z)^2\,(1+z)\left(1+z+z^2\right)\left(-1+z-z^2-z^4\right) \tag{7.7}$$

$$\left(-1+2\,z+2\,z^2+2\,z^3+z^4+3\,z^5+3\,z^6+3\,z^7+z^8\right) \tag{7.8}$$

with the topological entropy $h = \ln 2.986497\ldots$

We can also approximate the pruning front with the symbol strings from the squares which are mostly in the forbidden region. This gives the strings 00100, 000022 and 000101 and the symmetric ones of these and we obtain an automaton with 34 nodes and with topological entropy $h = \ln 2.95302\ldots$.

We can find all completely forbidden strings of length less or equal 8 and by combining the forbidden strings in table 7.2 we get the list of forbidden strings

$$\begin{array}{l} 000100 \\ 0000101 \\ 0000222 \\ 0001010 \\ 0010010 \\ 0010011 \\ 00000221 \\ 00010110 \\ 01000222 \\ 01001010 \\ 11000222 \\ 10001011 \end{array} \tag{7.9}$$

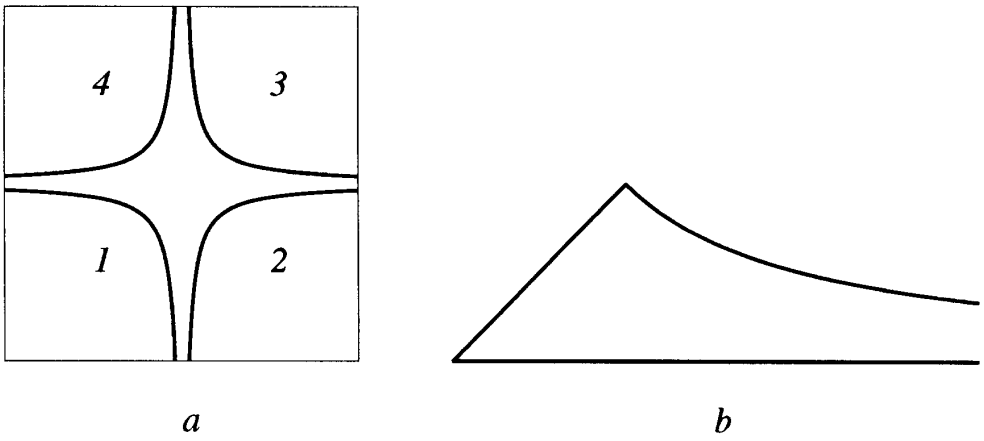

Figure 7.22: The hyperbola billiard. a) The full configuration space. b) The fundamental domain.

Including stings up to length 7 gives $h = \ln 2.96914\ldots$ and also including the strings of length 8 gives $h = \ln 2.96519\ldots$. The automaton in this case has 135 nodes and it is very time consuming to find all loop combination in the graph.

The topological entropy is close to the topological entropy of a three letter alphabet $h = \ln 3$, but the pruning is larger for the 4 disk touching system than in the 3 disk touching system.

7.4 Hyperbola billiard

The hyperbola billiard is a system similar to the 4 disk system where a point particle bounces elastically between the four hyperbola branches

$$y = \pm\frac{1}{x} \tag{7.10}$$

drawn in figure 7.22 [15, 176, 177, 178]. The symmetry in this billiard is the same as for the 4 disk system and the walls are dispersing. A pruning front for this system can be obtained in the same symbol plane as the 4 disk system. The four hyperbolas are enumerated s_t counterclockwise and (6.12) and (6.13) gives the well ordered symbols and the coordinate (γ, δ). As for the touching 4 disks the periodic orbit $\overline{w} = \overline{0} = \overline{1}$ does not exist. The walls does not overlap giving a corner and the tangent orbits are the only singular orbits in the system. The tangent pruning fronts give the pruned regions in (γ, δ) and are drawn in figure 7.23.

The tangent pruning fronts are the same two fronts as for the disk systems; one for the primary pruned region of orbits bouncing in the wall from the wrong

$\_w_{-2} \ldots w_3\_$	$\_w_{-3} \ldots w_4\_$
$000 \cdot 100$	$0000 \cdot 0221$
	$0000 \cdot 0222$
	$1000 \cdot 0222$
	$2000 \cdot 0222$
	$0100 \cdot 0222$
	$1100 \cdot 0222$
	$0100 \cdot 1000$
	$1100 \cdot 1000$
	$2100 \cdot 1000$
	$0200 \cdot 1000$
	$1200 \cdot 1000$
	$2200 \cdot 1000$
	$0010 \cdot 1000$
	$1010 \cdot 1000$
	$2010 \cdot 1000$
	$0110 \cdot 1000$
	$0200 \cdot 1001$
	$2100 \cdot 1001$
	$1100 \cdot 1001$
	$0100 \cdot 1001$
	$1100 \cdot 1002$
	$0100 \cdot 1002$
	$0100 \cdot 1010$
	$2000 \cdot 1010$
	$1000 \cdot 1010$
	$0000 \cdot 1010$
	$1000 \cdot 1011$
	$0000 \cdot 1011$
	$0000 \cdot 1012$

Table 7.2: The forbidden orbits in 4 discs, $r = 2$. Under counting approximation to level $k = 4$.

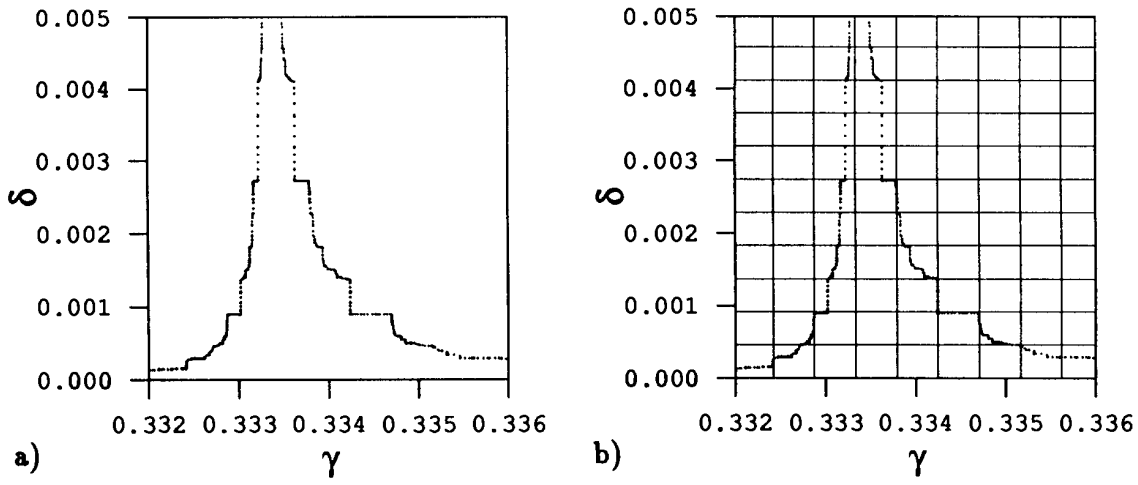

Figure 7.23: A magnification of the pruning front of the hyperbola billiard. b) with a lattice of size 3^{-7}

side and one region for orbits going through a wall without bouncing. We find in figure 7.23 that the primary pruned region is small compared with the touching 4 disk system. Qualitatively the shape of the front is slightly different than what we find in the disk billiards; the front has a more visible step-like shape. This may be because compared to the disk systems here more of the pruning is close to the origin and there is less pruning out in the tails $x \to \pm\infty$ and $y \to \pm\infty$.

To obtain lists of forbidden orbits of finite length we draw a lattice with length 3^{-k} between the lattice lines as in figure 7.23 b) and find the symbolic description of the rectangles in the forbidden region. This gives the following list of forbidden

orbits with symbol strings w_t shorter or equal 15.

$$
\begin{array}{l}
0000001000000 \\
0000001000001 \\
0000000100000 \\
1000000100000 \\
00000000222222 \\
00000001000010 \\
10000001222222 \\
00000000100001 \\
10000002222222 \\
00000002222222 \\
00000002222221 \\
000000000222221 \\
000000002222210 \\
010000010000010
\end{array}
\tag{7.11}
$$

and the strings symmetric to these. The shortest forbidden string is of length 13 and the pruning is very small in this system. By pruning these strings we get an automaton with 270 nodes and a topological entropy

$$h = \ln 2.999972\ldots$$

This entropy is very close to $h = \ln 3$ as for a complete three letter alphabet. It was also noticed by Sieber [176] that the number of periodic orbits missing in a three letter alphabet is very small. In practical calculations a three letter alphabet can be used with small errors even thought a random infinite string of symbols has a probability 1 that it is forbidden because a random string would sooner or later contain one of the forbidden strings in the list.

7.5 6+1 Disk system

We can also construct the pruning fronts for the system with one disk surrounded by 6 disks in figure 7.24. In this system the pruning starts already when the distance between the disc centers is $r_c = 3.59148407\ldots$, and we expect large pruning when the disks are close. There are two different tangent pruning fronts; one from orbits tangent to the center disk and one from orbits tangent to one of the other disks. The center-disk pruning front gives the largest pruned region. When the disks touches each other for $r = 2$ the system is reduced to 6 independent closed 3 disk systems and we do not have any corner pruning front for $r \geq 2$.

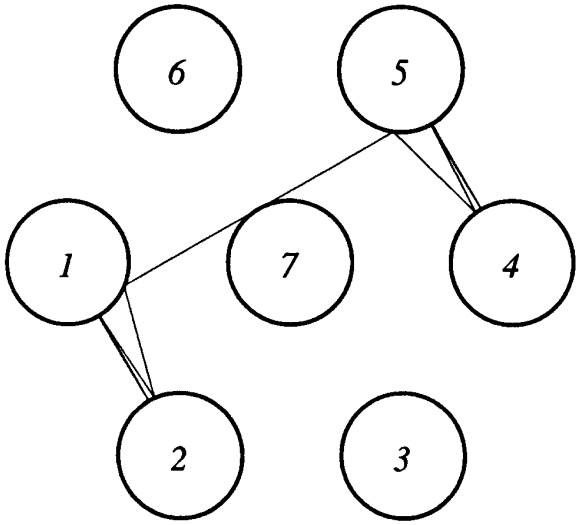

Figure 7.24: The 6+1 disk system and a hetroclinic orbit at the critical parameter value $r_c = 3.59148407\ldots$.

The well ordered symbols and the symbolic coordinate (γ, δ) are given by (6.18) and (6.19). The (γ, δ) space we use are the one corresponding to the phase space of a bounce in one of the 6 surrounding disks. The phase space for the center disk is different and we choose not to work in (γ, δ) for this disk. The pruned regions looks different in this space because the regions here are complicated shifts of the regions in the other symbol space.

The symbolic values γ and δ are base 5 numbers and a lattice with length 5^k between the lattice lines gives squares corresponding to symbol strings of length $2k$. The pruning fronts for the 6+1 disk system with parameter $r = 2.2$ are drawn in figure 7.25. From this picture we get the following list of forbidden strings:

$$\begin{array}{llll} 31 & 420 & 4220 \\ 41 & 320 & 3220 \\ & 421 & 1213 \\ & 321 & 1214 \\ & 221 & 0213 \\ & 113 & 0214 \\ & 114 & 1010 \\ & 013 & 0010 \\ & 014 & 0011 \end{array} \tag{7.12}$$

and the time reversed and $4 - w$ reversed of these stings.

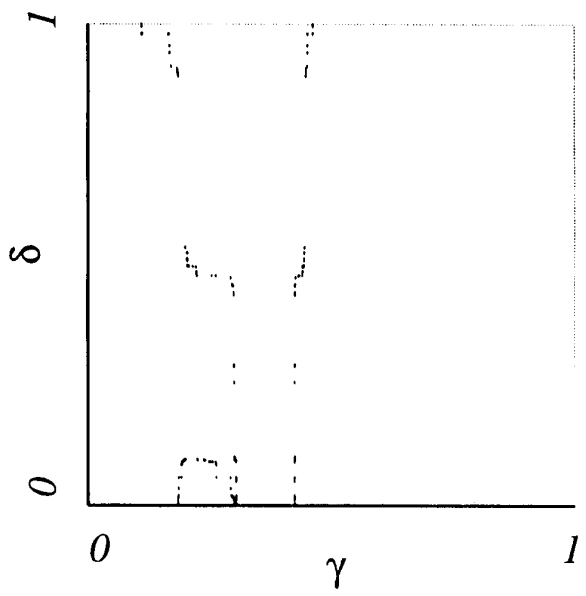

Figure 7.25: The pruning front of the 6+1 disk system for $r = 2.2$.

The forbidden stings up to length 4 gives an automaton with 33 nodes and a topological entropy

$$h = \ln 3.131\ldots \tag{7.13}$$

which is much lower than the well separated 6+1 disk system where $h = \ln 5$. This is an example where the pruning is very important for the description of the system.

7.6 Stadium billiard

We have different well ordered alphabets describing the stadium billiard and a corresponding symbols plane (γ, δ) for each alphabet as discussed in section 6.5. In each (γ, δ) we will have a monotone pruning front and we can identify forbidden strings of increasing length. All different symbol planes will in principle give pruned regions consisting of the same strings when translated into the same alphabet. The approximation to a given length k of the strings w_t for the pruned region may yield slightly different results for the different alphabets. When constructing the new alphabets the different combinations of symbols imply that a square of the symbol plane may correspond to different lengths of the strings in the different alphabets.

In the non overlapping disk systems there were two kind of forbidden orbits, orbits going into the disk and bouncing from the wrong side and orbits going through a disk without bouncing. By including these unphysical orbit we have a complete

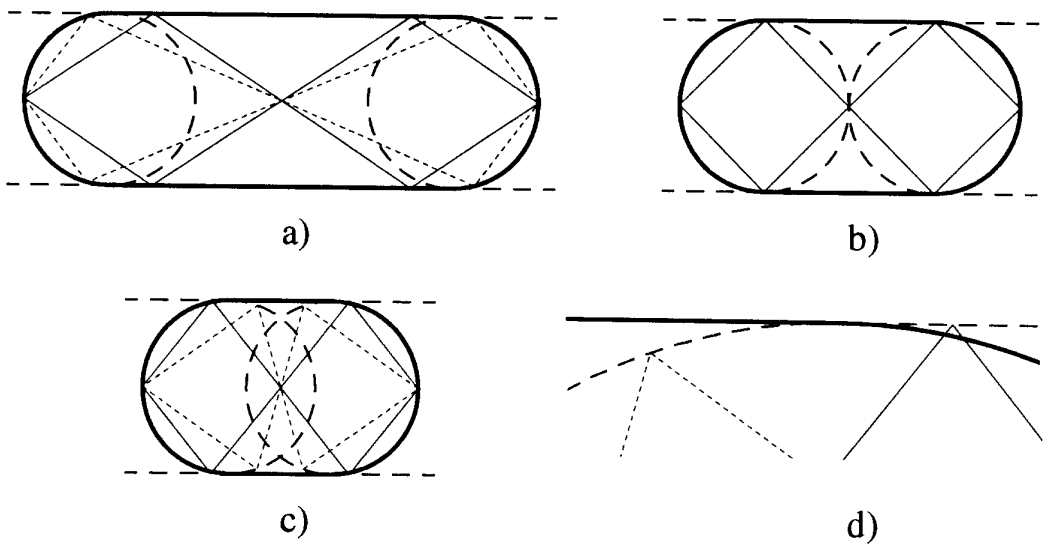

Figure 7.26: The orbits with s^a symbols $\overline{111333}$ and $\overline{012032}$ for a) $a = 2$, b) $a = 1$, c) $a = 0.6$. d) is a Blow-up of c).

n-ary symbolic description of all orbits. It is shown by Biham and Kvale [25] that in a similar way one can find unphysical orbits in the stadium billiard. These are the orbits that bounce in the straight line outside the singular point where the straight line joins the semi-circle, and the orbits which bounce in the circle inside the billiard domain. By including these unphysical orbits we can find all orbits described by the symbols obtained from the Markov graphs in section 6.5.

When we decrease the length a of the straight line in the billiard we have bifurcations. The bouncing points of an orbit with a given symbolic description may move as a decreases, and a points where the particle bounces off a wall moves closer to the closest singular point. In figure 7.26 we show one example of two orbits that become forbidden when a decreases below a critical parameter value; $a_c = 1.0$.

The orbit drawn with dashed lines in figure 7.26 is the orbit described with symbols s^a: $\overline{111333}$ or $\overline{444555}$ with s^b: $\overline{111333}$ or $\overline{444555}$ with s^c: $\overline{022011}$ and with s^d: $\overline{eac}$. The orbit drawn with solid lines is the orbit described with symbols s^a: $\overline{012032}$ or $\overline{240250}$ with s^b: $\overline{012032}$ or $\overline{210230}$ with s^c: $\overline{404303}$ and with s^d: $\overline{ghf}$.

These strings can be found as paths in the Markov graphs in figures 6.23, 6.24 and 6.25 and exist in the limit of an infinite long stadium $a \to \infty$. In figure 7.26 a) we find that the two orbits also exist when $a = 2$ but for $a = 0.6$ in figure 7.26 c) and d) these two orbits bounces off the illegal part of the stadium. The orbit $\overline{eac}$ bounces off the circle on the wrong side of the singular point inside the stadium where the semi-circle does not exist and the orbit $\overline{ghf}$ bounces off the straight line

outside the singular point where a physical orbit would bounce in the semi-circle. Figure 7.26 b) shows that for $a = 1$ the two orbits bounce exactly off the singular point and are on the limit of being illegal. These orbits are on the pruning front for $a = 1$. Biham and Kvale have numerically found periodic orbits and checked if each orbit is bouncing off the legal or forbidden part of the walls of the stadium.

We can draw the pruning front by finding the symbolic description of all orbits bouncing in the singular point with different outgoing angles. We record the symbol string as the symbols s^a and can translate these to the symbol space we want to use. The pruning front is drawn in (γ^a, δ^a) for the parameters $a = 5$, $a = 1$ and $a = 0.5$ in figure 7.27. The pruning front is also drawn in the (γ^b, δ^b) plane in figure 7.28 for these parameter values. As a check of the pruning front we have drawn the symbolic values of $1.5 \cdot 10^6$ bounces of chaotic orbits in the stadium with $a = 1$ in figure 7.29 for (γ^a, δ^a) and in figure 7.30 for (γ^b, δ^b). The pruning fronts are exactly the border of the points in these figures.

We can make a lattice with separation 5^{-k} between the lattice lines and read off the symbol strings that are forbidden in the primary pruned region which is not forbidden for $a \to \infty$. This gives the list in table 7.3 for $k = 2$ where we give all strings w^b and some of the corresponding strings s^b. In addition there is the strings of s^b symmetric to the given ones. The choice of approximating the pruning front in either symbol plane (γ^a, δ^a) or (γ^b, δ^b) does not make any other difference than changing the order in which we find the forbidden substrings when increasing k.

7.7 Wedge billiard

The pruning front in the wedge billiard is obtained by the symbol plane representation of the singular orbits from the tip of the wedge. For the two bouncing ball system these orbits are the points where the balls bounces together and in the floor simultaneously. In the map (6.22) the singular orbits are point on the line $(x_t - 2y_t)^2 \cos^2\theta + y_t^2 \sin^2\theta = 1$ which is the border between map T_0 and map T_1.

The pruning front is drawn in figure 7.31 for parameter values a) $\theta = 50°$, b) $\theta = 60°$, c) $\theta = 70°$ and d) $\theta = 80°$. The pruning fronts can be compared with figure 7.32 where we have plotted each bounce of a chaotic orbit with 10^6 iterations. The bounces are plotted in the symbol plane (γ, δ). These figures show that the pruning front is the border of the primary pruned region.

The primary pruned region changes as the parameter changes, but in contrast to the examples above there is not a monotone increase in the area of the region. In the limit $\theta = 45°$ most of the forbidden orbits are obits in the upper left corner.

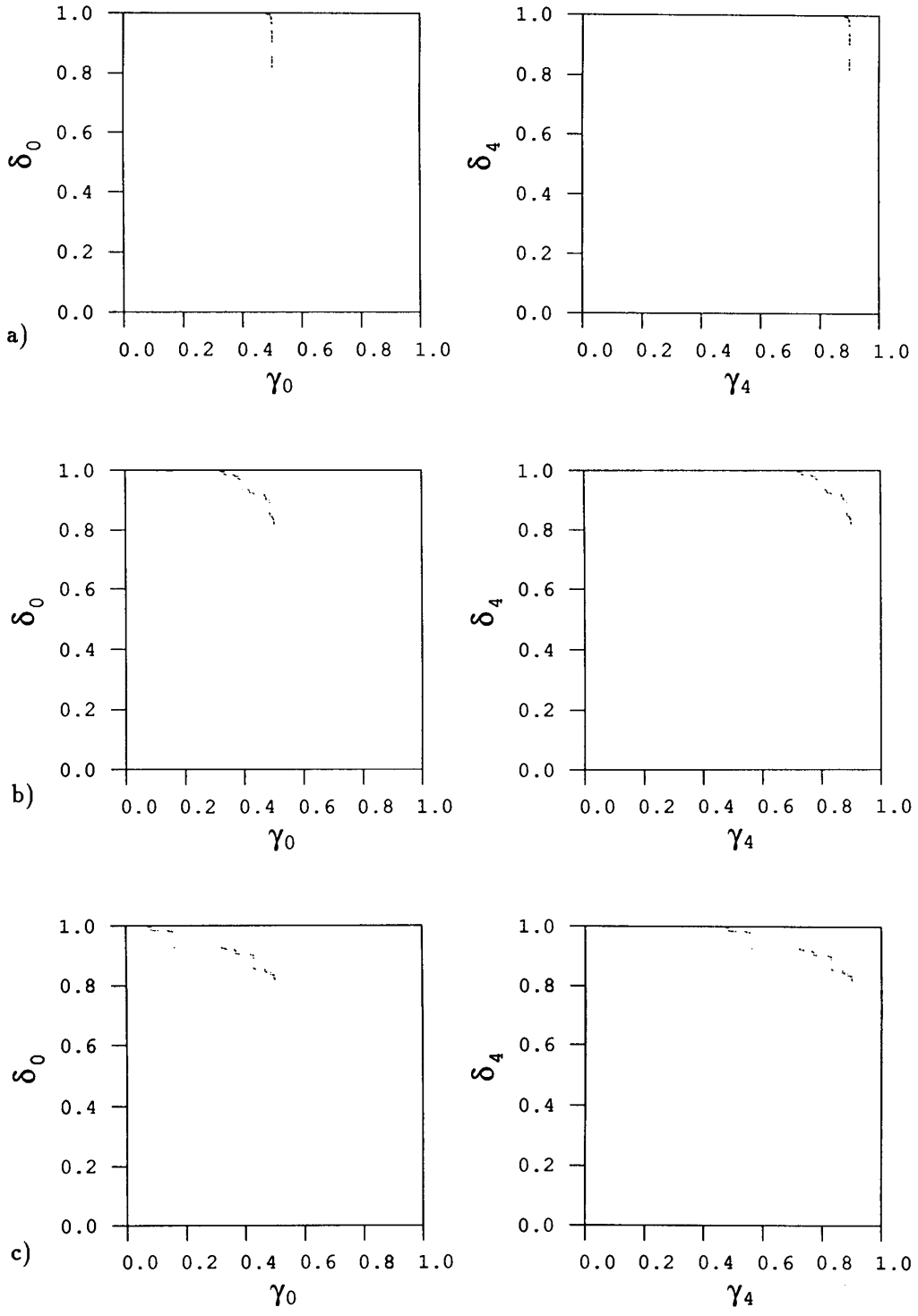

Figure 7.27: The pruning front for the stadium in the (γ^a, δ^a) symbol plane a) $a = 5$, b) $a = 1$, c) $a = 0.5$.

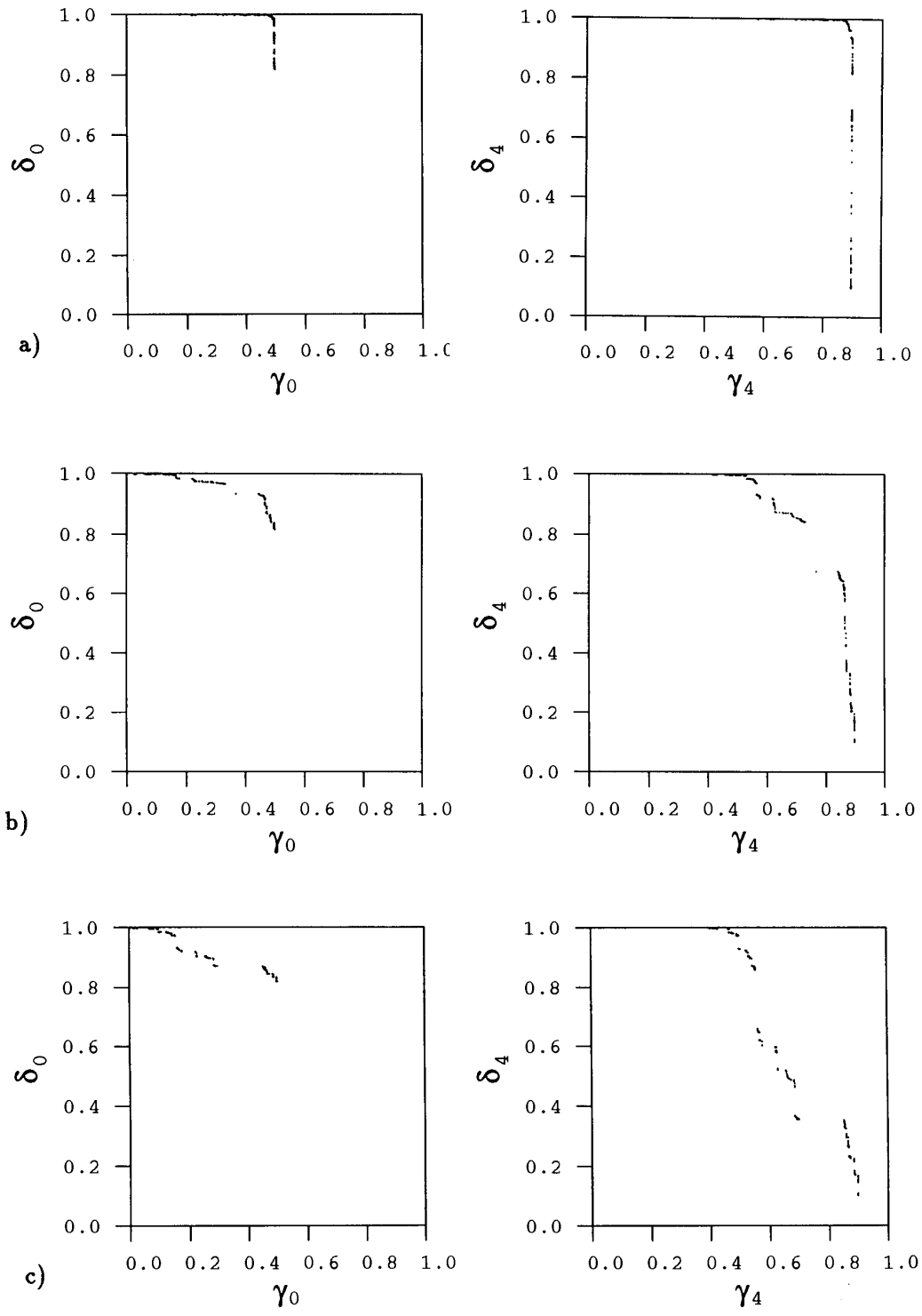

Figure 7.28: The pruning front for the stadium in the (γ^b, δ^b) symbol plane a) $a = 5$, b) $a = 1$, c) $a = 0.5$.

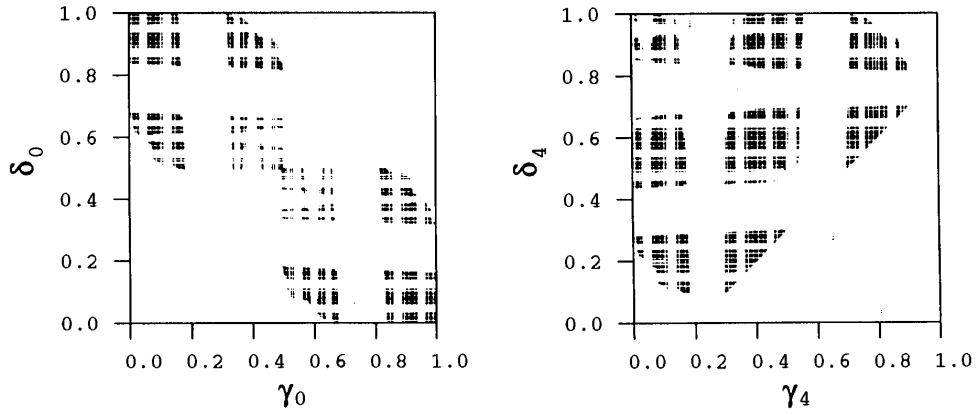

Figure 7.29: Bounces of a chaotic orbit in (γ^a, δ^a) for $a = 1$.

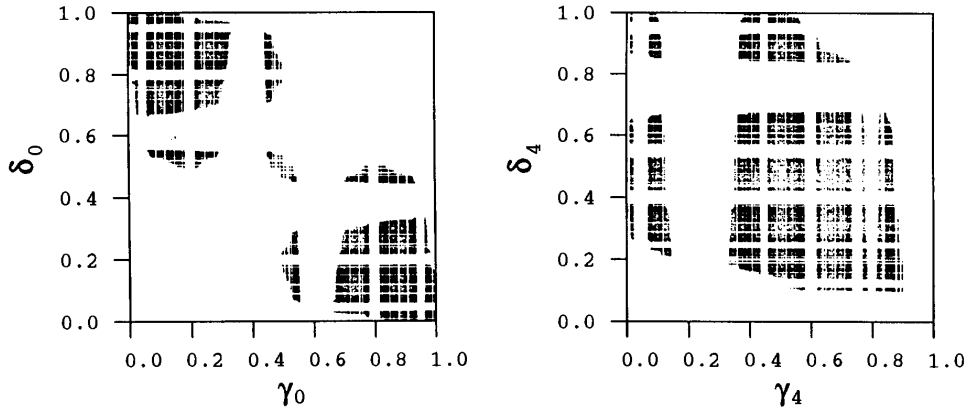

Figure 7.30: Bounces of a chaotic orbit in (γ^b, δ^b) for $a = 1$.

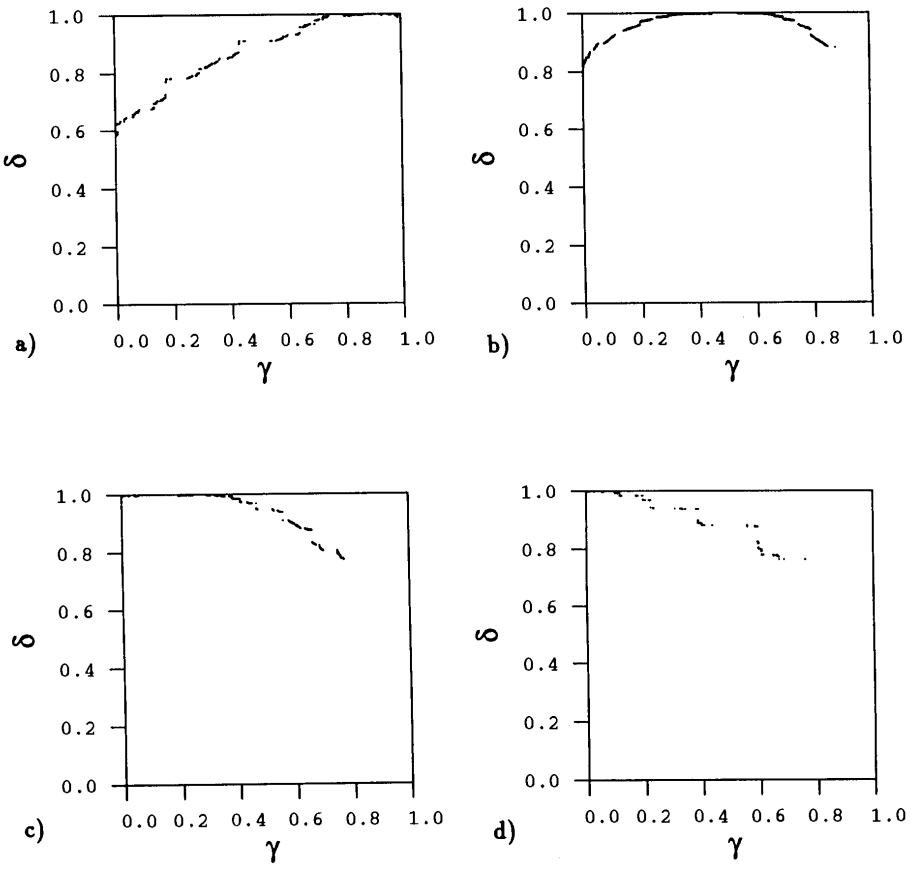

Figure 7.31: The pruning front for the wedge billiard. a) $\theta = 50°$, b) $\theta = 60°$, c) $\theta = 70°$ and d) $\theta = 80°$.

$w^b_{-1}w^b_0 \cdot w^b_1w^b_2$
$44 \cdot 3$
$34 \cdot 3$
$24 \cdot 31$
$24 \cdot 32$
$24 \cdot 33$
$24 \cdot 34$
$14 \cdot 34$
$04 \cdot 34$
$23 \cdot 4$
$3 \cdot 42$
$2 \cdot 42$
$41 \cdot 42$

a)

$s^b_ts^b_{t+1}\ldots$
444455
244455
34445544
3444551
3444550
3444555
55444555
0444555
02442
24420
34420
2554420

b)

Table 7.3: The parameter dependent completely pruned stings of length ≤ 4 for w^b for parameter $a = 1$. a) Symbols w^b_t. b) Some symbols s^b_t.

This corner is orbits having one symbol $s_t = 1$ with a long string of $s = 0$ symbols on each side of this symbol. A physical interpretation for the wedge billiard is that the orbits bouncing a number of times on one tilted wall then jumps over to the other tilted wall and bounces a number of times there are forbidden. This dynamics is difficult for the particle if the angle is close to $\theta = 45°$ because then usually the particle will return immediately to the first wall giving a $s_ts_{t+1} = 11$ string. For the two ball system this dynamics is orbits where the down-most ball bounces a number of times off the floor, then bounces *once* into the uppermost ball and then continues to bounce off the floor a number of times. When the masses of the two balls are similar then this is an unlikely event because the balls tend to bounce twice. The dynamics for this limit is discussed further in section 8.1.

In the limit of $\theta = 90°$ most of the forbidden orbits are obits in the upper right corner. This corner gives the symbol strings where there is a symbol string $s_ts_{t+1} = 11$ surrounded by strings of symbol 0. In the wedge this is orbits crossing the tip twice which is difficult in the limit where the tip vanishes. In the two ball system this is a sequence of ball-ball; ball-floor; ball-ball collisions which is unlikely if the uppermost ball is much smaller than the downmost ball.

We find that the first region decreases and the second region increases as θ increases from $\theta = 45°$ to $\theta = 90°$. All parameters between $\theta = 45°$ and $\theta = 90°$

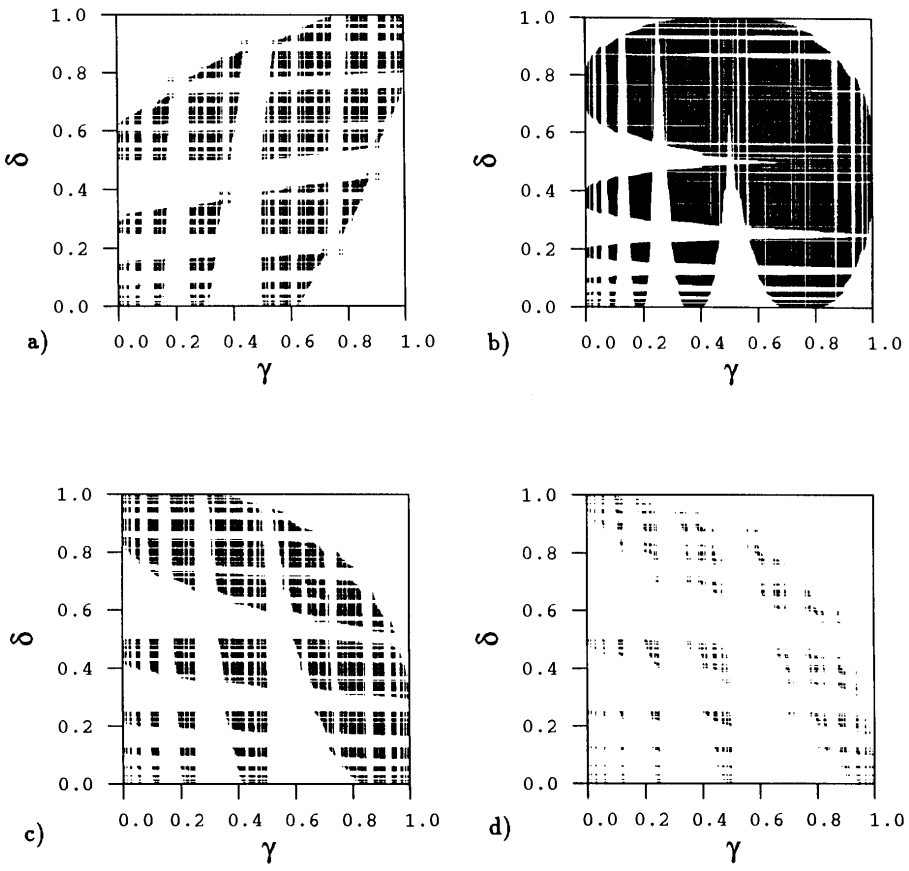

Figure 7.32: A chaotic orbit in the wedge billiard plotted in the symbol plane. a) $\theta = 50°$, b) $\theta = 60°$, c) $\theta = 70°$ and d) $\theta = 80°$.

$s_t s_{t+1} \dots$	
001100	000010011
0000110	110010000
0110000	011000110
0001000	001101100
00011011	0110011011
11011000	1101100110
00000100	1100110110
00100000	0110110011

Table 7.4: The forbidden strings up to length 10 of the wedge billiard; $\theta = 60°$.

have a primary pruned region including both the upper left and the upper right corner.

As for the other systems we can approximate the pruning front by rectangles and get an approximate description of the admissible orbits for a given parameter value. For $\theta = 60°$ we get the forbidden strings in table 7.4. Including strings up to length 10 gives the topological entropy $h = -\ln(0.522097\dots) = 0.64990\dots$. All the zeroes in the complex plane for this polynomeal is drawn in figure 7.33. The zeroes seems to build up a wall of convergence at the unit circle similar to the chaotic unimodal map in figure 1.24.

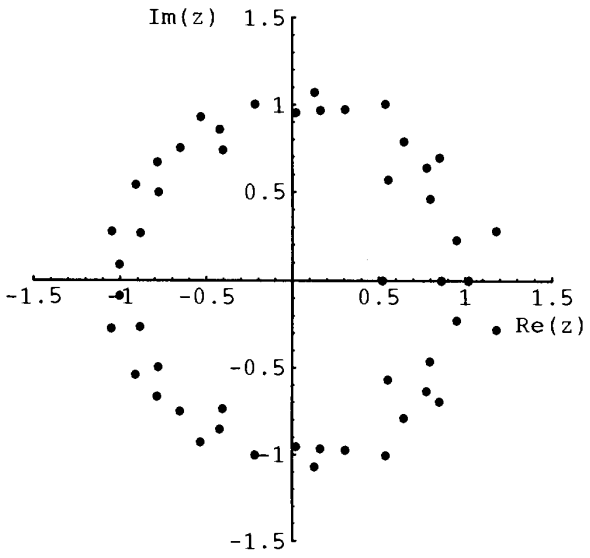

Figure 7.33: The zeroes of the characteristic polynomial for the wedge billiard; $\theta = 60°$, with forbidden strings up to length 10.

Chapter 8

Symbolic dynamics in special limits

In some limit cases of billiard systems the symbolic dynamics is special and can be found exact. Even if these cases are limits of the alphabets we can derive from a pruning front, the symbolic dynamics of the limit may have very different number theoretical properties than for the typical description. The limit we discuss in this chapter is the integrable limit of the billiards where the orbits are stable and exist in continuous families. The symbolic dynamics is in most cases mapped into a simple rotation which is the description of how a straight line crosses a lattice. The symbolic description of the rotation is a problem with old roots considered by Bernoulli (1772), Markov (1882), Christoffel (1875) and Smith (1877) (for historical notes see ref. [179]). The results as we use it was showed first by Morse and Hedlund [157]. Generalizations to higher dimensions can also be done [18].

Our simplest billiard, the 3 disk system, turns out to be slightly more complicated than the 4 disk billiard and the wedge billiard, so we choose here to first present the method for the later billiards.

In figure 8.1 a square lattice is drawn together with a line crossing the lattice. Denote a crossing of the line with a vertical lattice line 0 and a crossing of the line with a horizontal lattice line 1 . The symbol string $\ldots l_{-2}l_{-1}l_0l_1l_2\ldots$ is the symbolic representation of the different crossings of the line with the lattice lines. The line in figure 8.1 is described by the symbolic string $\ldots 0100100100100010\ldots$. A given infinite symbolic string define uniquely the slope of the line, but a periodic orbit has an interval of starting points giving the same symbolic dynamics. The admissible strings are not constructed from a finite alphabet or from a Markov graph as we have done in other examples, but can be constructed from a Farey tree expansion. The symbolic Farey tree is drawn in figure 8.3.

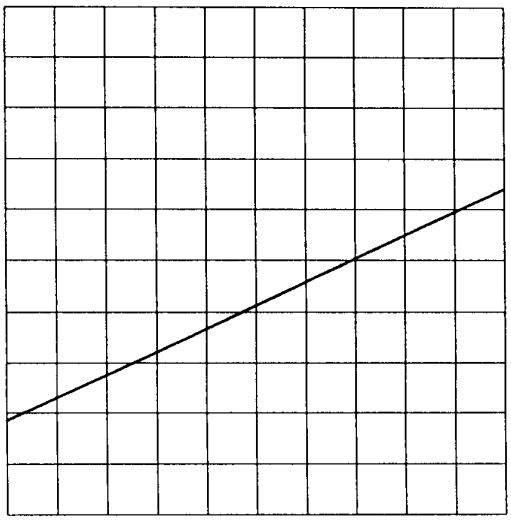

Figure 8.1: The crossing of a straight line with the lines of a square lattice.

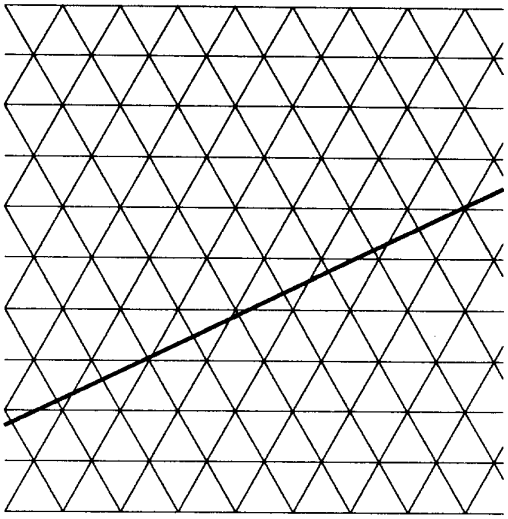

Figure 8.2: The crossing of a straight line with the lines of a triangular lattice.

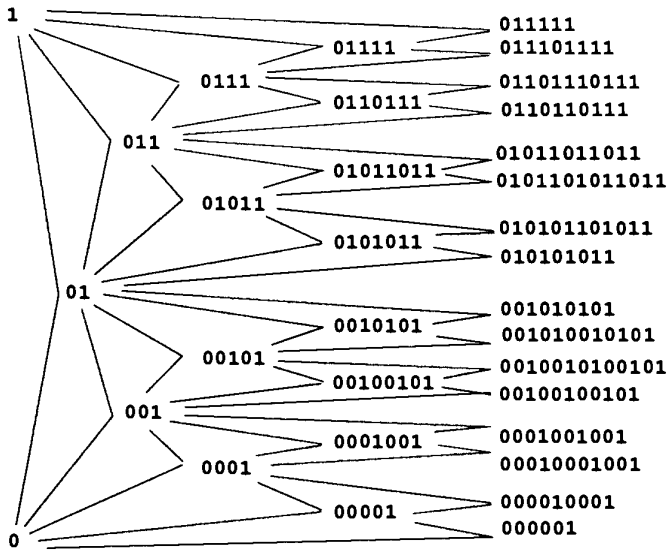

Figure 8.3: The construction of admissible symbolic sequences for the crossings in figure 8.1 by a Farey tree.

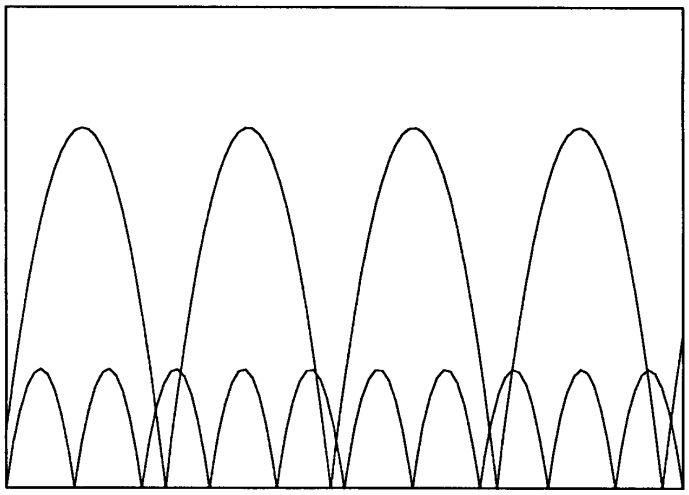

Figure 8.4: Two independent balls bouncing and crossing each others path. The symbolic description of this orbit is ...00110110011011....

To apply this for the billiard examples we have to translate the symbols for vertical and horizontal lines into the symbols in the different billiards.

8.1 Wedge billiard

In the limit where the angle in the wedge billiard goes to 45° the system is integrable and corresponds to a simple rotation. The corresponding system with two bouncing balls is when the two masses are equal $m_1 = m_2$. In this two ball system it is easy to see why a simple rotation is the correct dynamics of the system. An elastic collision between two point particles with equal masses is identical to the system where the two particles pass through each other without any interaction. We then have a crossing of balls instead off bouncing between two balls. If the two balls bounce in the floor independent of each other only the initial position and velocity matters and there are two independent, never changing bouncing patterns. In figure 8.4 two independent bouncing balls are drawn. One ball bounces with a time T_1 between each bounce and the second ball with time $T_2 \geq T_1$. The two times correspond to the vertical and horizontal distances in figure 8.1 and determine the slope of the line. We can associate the crossing of the straight line with a vertical lattice line with the motion where the lower most ball is bouncing twice off the floor without crossing (=bouncing) with the other ball. A symbol 0 in the lattice description corresponds to a symbol 0 in the two ball symbols. The crossing of the straight line with a horizontal line can be related to the sequence from one ball bouncing off

the floor, the two balls cross and the the second ball bounces off the floor, then the balls cross again and the first ball bounces off the floor. This symbol 1 in the lattice symbols corresponds to the symbolic string 11 in the two ball symbols. Figure 8.4 shows that the two ball symbols always appears in pairs.

Interpreted this way the symbols 0 and 1 for crossing vertical and horizontal lines are identical to the symbols 0 and 11 for the two ball system and therefore also the wedge billiard. The strings in figure 8.3 can be translated into the wedge symbols giving the symbols s_t

11				
			011111111	01111111111
		0111111		0111111011111111
			011110111111	011110111111011111111
	01111			01111011110111111
			0110111101111	011011110111101111
		01101111		0110111101101111011
			01101101111	011011011101101111
011				01101101101111
			0011011011	0011011011011
		0011011		00110110011011011
			00110011011	001100110110011011
	0011			001100110011011
			000110011	0001100110011
		00011		00011000110011
			000011	00001100011
0				0000011

(8.1)

This Farey tree is the description of admissible orbits in the integrable wedge in terms of symbolic dynamics. In the well ordered symbols we have to take care of the flipping process but this is simple since all symbol 1 which flip the ordering always come in an even number so the only difference from the symbols above is

that every second symbol 1 is turned into a symbol 0. This gives the symbols w_t

$$
\begin{array}{lllll}
10 & & & & \\
 & & & 010101010 & 01010101010 \\
 & & & & 0101010010101010 \\
 & & 0101010 & & \\
 & & & 010100101010 & 0101001010100101010 \\
 & & & & 010100101001010 \\
 & 01010 & & & \\
 & & & 0100101001010 & 0100101001010010 \\
 & & & & 0100100101001001010 \\
 & & 01001010 & & \\
 & & & 01001001010 & 0100100101001001010 \\
 & & & & 01001001001010 \\
010 & & & & \\
 & & & 0010010010 & 0010010010010 \\
 & & & & 0010010010010010 \\
 & & 0010010 & & \\
 & & & 00100010010 & 0010001001001010 \\
 & & & & 001000100010010 \\
 & 0010 & & & \\
 & & & 000100010 & 0001000100010 \\
 & & & & 00010000100010 \\
 & & 00010 & & \\
 & & & 000010 & 00001000010 \\
 & & & & 0000010 \\
0 & & & &
\end{array}
\tag{8.2}
$$

and the symmetric ones with 0 and 1 interchanged.

We can show that in the symbol plane this gives as the limit of the pruning front the straight line

$$\delta = \frac{1}{2}\gamma + \frac{1}{2} \tag{8.3}$$

Let a line go through one of the crossings between the horizontal and the vertical lattice lines which corresponds to a singular orbit. The line will cross the vertical and the horizontal lattice lines exactly the same way in both directions along the line from the crossing point. The pruning front is given by the symbolic description of all orbits having a double collision between the two balls and the floor simultaneously an this is the point where the vertical and horizontal lattice lines crosses. All points on the pruning front then has the form

$$\ldots l_3 l_2 l_1 l_0' l_0 l_1 l_2 l_3 \ldots$$

The symbol string $l_0' l_0$ describes the crossing of the line with the lattice cross and the string is either 01 or 10. If we choose $l_0' l_0 = 01$ we get the two ball symbol string describing the line

$$\ldots s_5 s_4 s_3 011 s_3 s_4 s_5$$

and the well ordered symbols

$$\ldots w_5 w_4 w_3 010 w_3 w_4 w_5$$

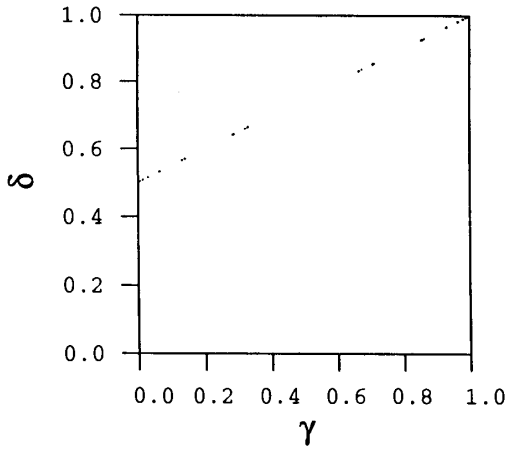

Figure 8.5: The pruning front for the wedge billiard in the integrable case $\theta = 45°$.

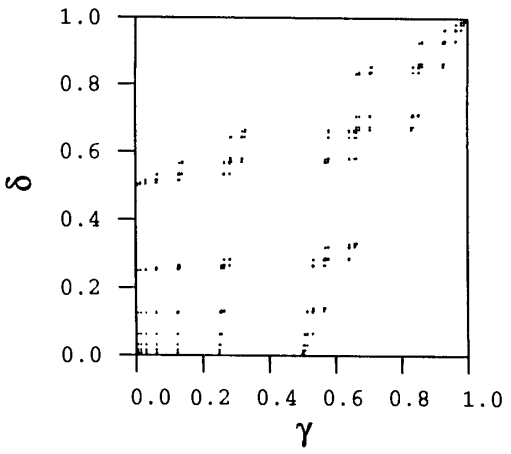

Figure 8.6: The symbolic values for a number of orbits in the wedge billiard in the integrable case $\theta = 45°$.

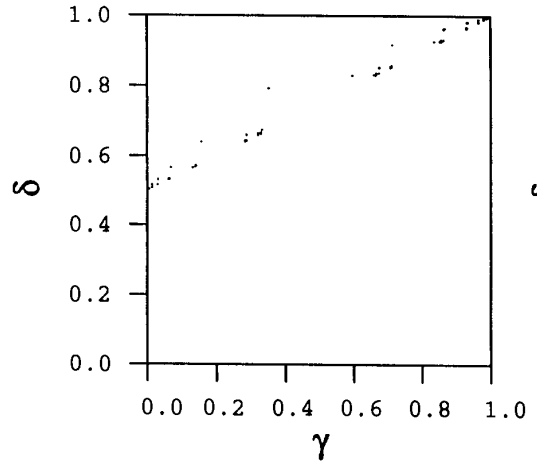

Figure 8.7: The pruning front for the wedge billiard for $\theta = 45.01°$.

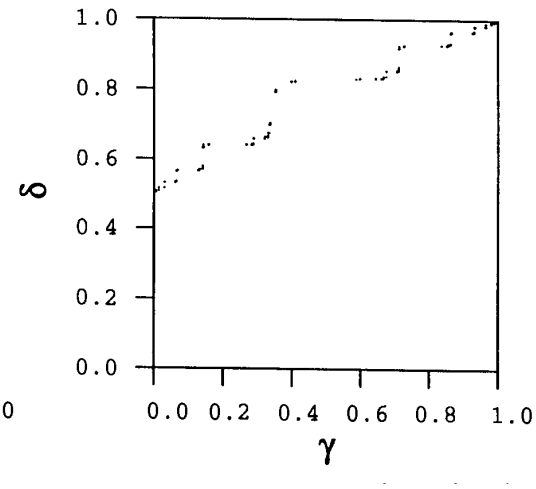

Figure 8.8: The pruning front for the wedge billiard for $\theta = 45.1°$.

which gives the symbolic values

$$\begin{aligned} \delta &= 0.10w_3w_4w_5\ldots \\ \gamma &= 0.0w_3w_4w_5\ldots \end{aligned}$$

From these equations we get (8.3). The other choice of $l_0'l_0$ gives the symmetric line $\gamma = \delta/2 + 1/2$.

Figure 8.5 shows the numerical pruning front obtained for the wedge billiard at 45° and figure 8.6 shows the symbolic values of a number of different (not chaotic) orbits in this wedge. Parameters close to 45° should give pruning fronts close to this straight line and in figures 8.7 and 8.8 we find for wedge angles $\theta = 45.01°$ and $\theta = 45.1°$ many points on the pruning front are close to the line $\delta = \gamma/2 + 1/2$ but some points are far above this line and gives a staircase like curve with the line as an envelope under the points.

8.2 4-disk

When the four disks are so close that the area of the domain where the particle bounces goes to 0 the walls of the domain approaches straight lines and the system becomes a particle in a square box. A particle bouncing inside a square is equivalent to a particle moving freely on a square lattice and again we get the symbolic description from the Farey tree construction. Here the translation from the rotation to the symbol plane is slightly more complicated because the alphabet in the 4-disk case is a four letter alphabet or a three letter alphabet.

We may choose to identify the four disk symbols $s_t \in \{1, 2, 3, 4\}$ with the lattice such that the symbols 1 and 3 correspond to horizontal lattice lines and the symbols 2 and 4 correspond to vertical lattice lines. Every second lattice line is then 1 and 3 (or 2 and 4) and every crossing of one of these lines gives these symbols alternating. We also immediately see that a clockwise bounce followed by a number of bounces between opposite disks gives a clockwise or anticlockwise bounce depending of whether the number of bounces was even or odd.

We can use the Farey tree in figure 8.3 to construct the symbolic strings for this system. As the well ordered symbols are of grater interest than the symbols s_t we only give the symbols w_t. Since the system is symmetric in the vertical and the

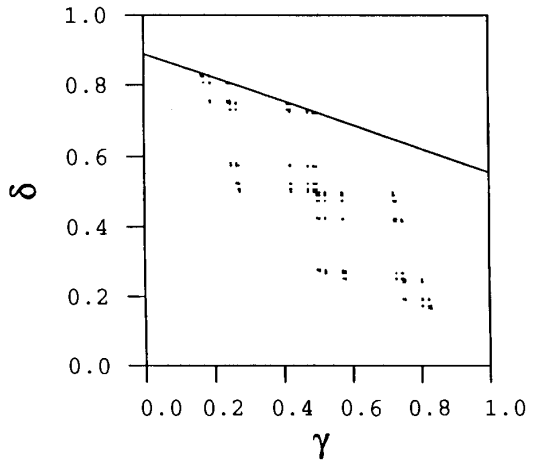

Figure 8.9: The symbolic values for a number of orbits in the overlapping 4-disk billiard close to the integrable limit with parameter $r = 1.416$ and the line $\delta = 8/9 - \gamma/3$.

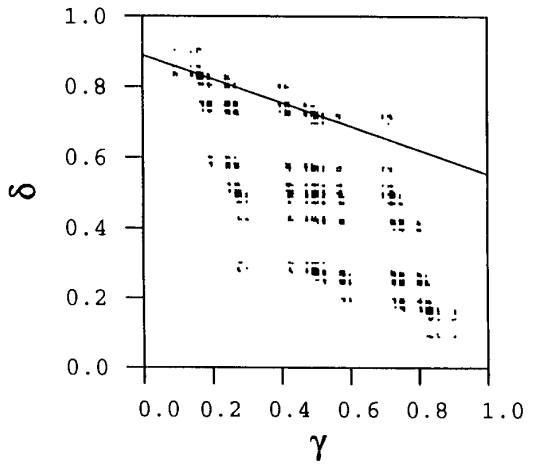

Figure 8.10: The symbolic values for a number of orbits in the overlapping 4-disk billiard with distance $r = 1.5$ between the disk centers and the line $\delta = 8/9 - \gamma/3$.

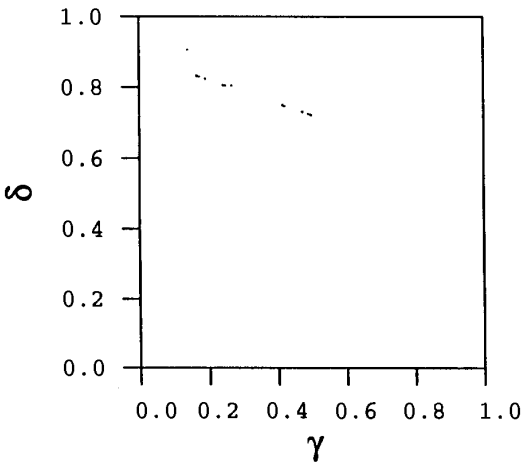

Figure 8.11: Corner pruning front for the overlapping four disk billiard close to the integrable limit with parameter $r = 1.416$.

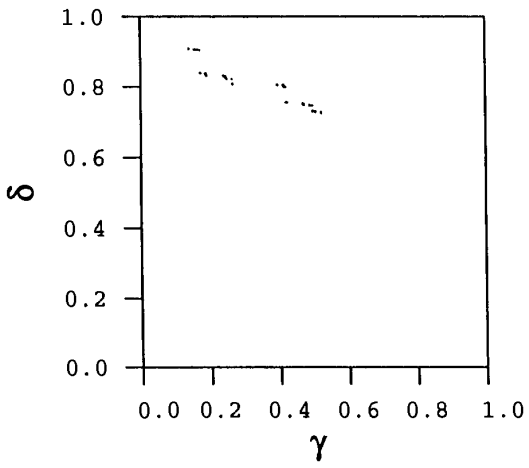

Figure 8.12: Corner pruning front for the overlapping four disk billiard with distance $r = 1.5$ between the disk centers.

horizontal direction we only have to use half the Farey tree to get w_t

$$
\begin{array}{lllll}
 & 20 & & & \\
 & & & 1202020 & 120202020 \\
 & & & & 120201202020 \\
 & & 12020 & & \\
 & & & 12012020 & 1201202012020 \\
 & & & & 12012012020 \\
 & 120 & & & \\
 & & & 1120120 & 1120120120 \\
 & & & & 11201120120 \\
 & & 1120 & & \\
 & & & 11120 & 111201120 \\
 & & & & 111120 \\
1 & & & &
\end{array}
\tag{8.4}
$$

In addition to these we have the strings where symbols 0 and 2 are interchanged.

The pruning front from the tangent orbits only becomes a point in these limit as there is no curvature left. As for the wedge the limit of the pruning front originating from the orbits starting in the corners is a straight line. Since the construction of well ordered symbols are different and have base 3 symbol values wee get a different line. Following an argument as above we find the line

$$\delta = \frac{8}{9} - \frac{1}{3}\gamma \tag{8.5}$$

to be the limit of the pruning front.

Figures 8.9 and 8.10 show the symbolic values of all bounces for chaotic orbits close to the limit $r = \sqrt{2} = 1.4142\ldots$. For the parameter $r = 1.416$ there is hardly any point above this line while for $r = 1.5$ there is some points above it. The figures 8.11 and 8.12 show the corner pruning fronts for the same parameter values. Close to the limiting parameter value the points of the pruning front are almost all very close to the line (8.5).

8.3 3-disk

In the limit when the three disks are so close that the domain turns into a triangle the orbit is equivalent to the straight line in a triangular lattice as showed in figure 8.2. The symbolic description of this can be found from the Farey tree in the following way; The line is always crossing in an angle between 60° and 120° to one of the three directions in the lattice. Every second crossing between the line and the lattice lines is a lattice line which has this direction. The non trivial dynamics is only the crossing between the line and the lattice lines in the other two directions. If we call the crossing of the line with a lattice line in one direction 0 and the crossing with a lattice line in the other direction 1 and skip the crossings

with the trivial lattice lines, then the Farey tree in figure 8.3 gives the grammar. There is no mathematical work on this triangular lattice proving that this is the correct procedure [192] but as it turns out to be very similar to the square lattice we state the result as a conjecture.

In figure 8.13 the triangular lattice is drawn and the labeling l_t is given as 1 for horizontal lines, 0 for lines going right-up and 2 for lines going right-down. In the lattice we have drawn a line going from left-down to right-up. This line crosses the lattice lines no 2 every second time it crosses a lattice line and analogous to the square lattice we can construct the Farey tree with these lattice line symbols l_t assuming every second crossing is 2. This gives the following tree for l_t

$$
\begin{array}{llll}
21 & & & \\
 & & 20212121 & 2021212121 \\
 & 202121 & & 20212120212121 \\
 & & 2021202121 & 2021202121202121 \\
2021 & & & 20212021202121 \\
 & & 2020212021 & 20202120212021 \\
 & 202021 & & 2020212020212021 \\
 & & 20202021 & 20202021202021 \\
20 & & & 2020202021
\end{array}
\tag{8.6}
$$

The orbit in figure 8.13 has the labeling in symbols $l_t \ldots 2120212120 \ldots$ and we find that this is a substring of the string 2021202121202121 in the Farey tree (8.6).

The three symbols s_t in the 3-disk system are not identical with the three directions of the lattice lines, but the disk symbols can be identified with the parts of the lattice lines as showed in figure 8.14. This unfolding of the domain to the lattice gives the new symbols and we obtain a Farey tree for the symbol s_t which is rather awkward to use because the symbols are not repeated the same way. Assuming we first cross the line with symbol 2 as in the figures we obtain the tree for s_t

$$
\begin{array}{llll}
21 & & & \\
 & & 23132132 & 2313213213 \\
 & 231321 & & 23132131213213 \\
 & & 2313231321 & 2313231321312132 \\
2313 & & & 23132313231321 \\
 & & 2312321232 & 23123212321232 \\
 & 231232 & & 2312321231213121 \\
 & & 23123121 & 23123121312313 \\
23 & & & 2312312313
\end{array}
\tag{8.7}
$$

It is simpler to directly work with the well ordered symbols w_t. In this alphabet

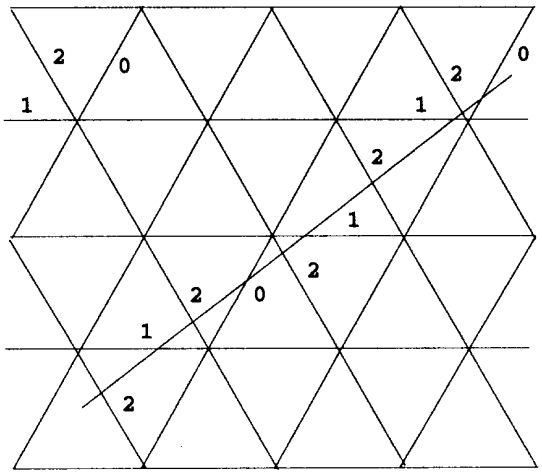

Figure 8.13: The triangular lattice with a symbol l_t for each direction and a line giving the sequence $\ldots 2120212120\ldots$.

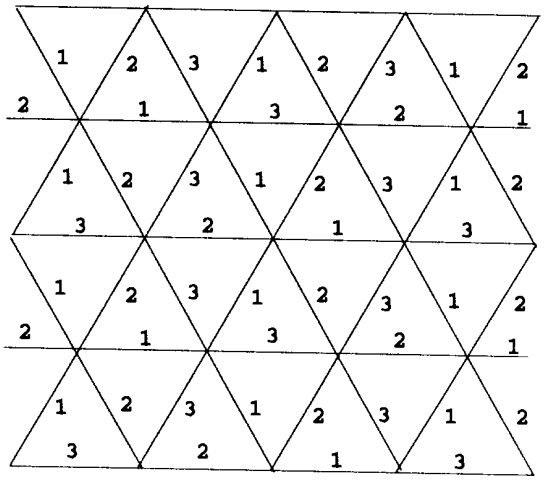

Figure 8.14: The triangular lattice with the symbols s_t for the 3-disk system folded out in the lattice.

we obtain the tree for symbols w_t

$$
\begin{array}{lllll}
10 & & & & \\
 & & & 01101010 & 0110101010 \\
 & & & & 01101001101010 \\
 & & 011010 & & \\
 & & & 0110011010 & 0110011010011010 \\
 & & & & 01100110011010 \\
 & 0110 & & & \\
 & & & 0101100110 & 01011001100110 \\
 & & & & 0101100101100110 \\
 & & 010110 & & \\
 & & & 01010110 & 01010110010110 \\
 & & & & 0101010110 \\
01 & & & &
\end{array}
\tag{8.8}
$$

We can get the limit of the corner pruning front by observing the well ordered symbols w_t for a line going through a lattice cross. We choose the symbols for going through the cross as three symbols for crossing close to the cross and obtain

$$
\begin{aligned}
\gamma &= .0w_2w_3w_4\ldots \\
\delta &= .110(1-w_2)(1-w_3)(1-w_4)\ldots
\end{aligned}
$$

which gives the line

$$\gamma = \frac{7}{8} - \frac{1}{4}\delta \tag{8.9}$$

In figure 8.15 this line is plotted together with a number of bounces in the 3-disk billiard for the center-center distance $r = 1.7325$ which is close to the critical

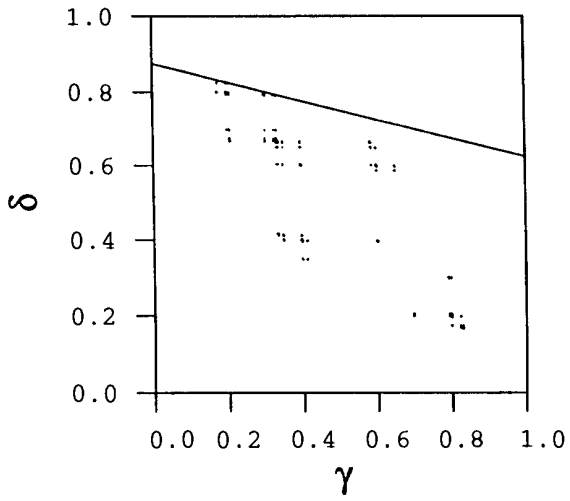

Figure 8.15: The symbolic values for a number of orbits in the overlapping 3-disk billiard close to the integrable limit with parameter $r = 1.7325$ and the line $\delta = 7/8 - \gamma/4$.

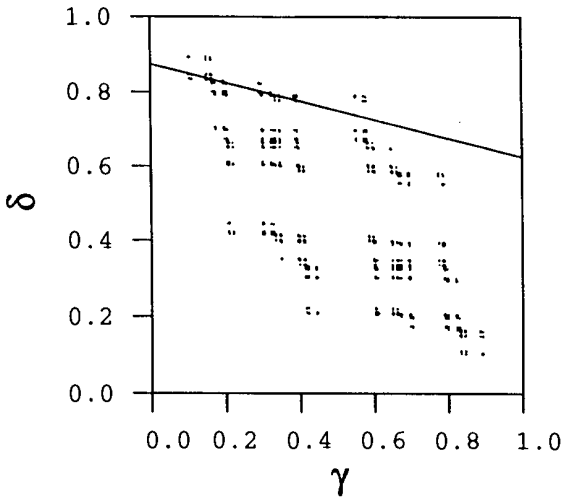

Figure 8.16: The symbolic values for a number of orbits in the overlapping 3-disk billiard with distance $r = 1.738$ between the disk centers and the line $\delta = 7/8 - \gamma/4$.

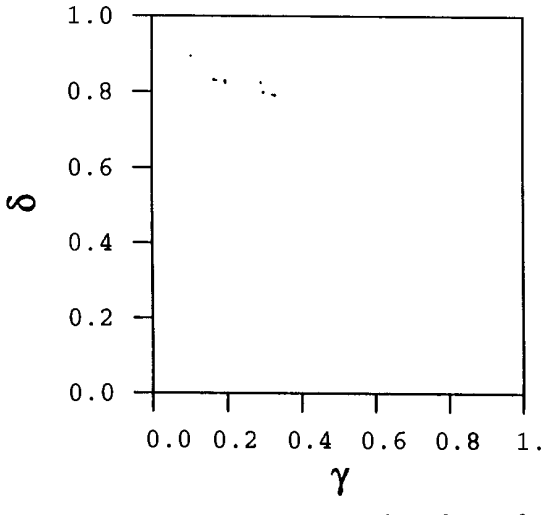

Figure 8.17: Corner pruning front for the overlapping 3-disk billiard close to the integrable limit with parameter $r = 1.7325$.

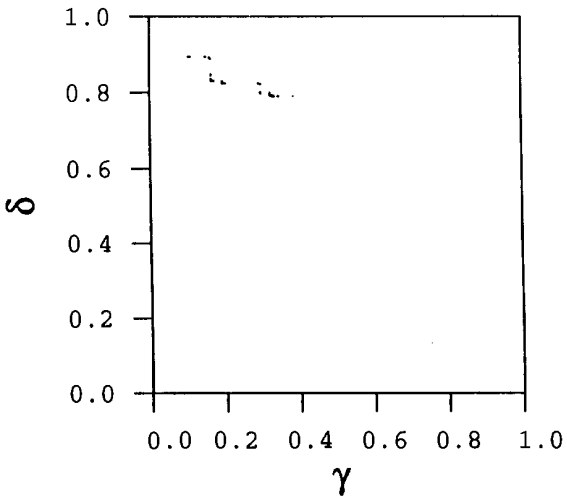

Figure 8.18: Corner pruning front for the overlapping 3-disk billiard with distance $r = 1.738$ between the disk centers.

distance $r = \sqrt{3} = 1.73205\ldots$. In this numerical experiment we do not get any points above the line. A slightly larger parameter value $r = 1.738$ gives figure 8.16 where a few of the points are above the line. The corner pruning fronts for these two parameter values are drawn in figures 8.17 and 8.18. The pruning front becomes points on the line (8.9) in the limit $r \to \sqrt{3}$.

8.4 Approaching the integrable limit from the mixed chaos-order side

The limit of orbits organized in a Farey tree gives a signature which is a pruning front that becomes a straight line. In a phase space plot of a chaotic orbit there is no clear signature of this organization.

We can however in these cases approach the integrable limit tuning the parameter from the opposite side of the critical parameter value. We then have a system with mixed chaos and stable islands. This is the dynamics for the wedge billiard (the two ball system) for $\theta < 45°$ ($m_1 < m_2$) and for the disc systems where the walls are slightly convex instead of concave. We can to study a disc system as a particle bouncing inside the convex domain limited by the focusing side of the disk walls for the 3-disk system with center-center distance less than $\sqrt{3}$.

The dynamics we observe in the wedge billiard and in the 3 disk system is that all stable islands close to the limit of the critical parameter value are islands surrounding each periodic orbit from the Farey tree construction. Approaching the limit, the islands become squeezed out into horizontal lines in the phase space. In the integrable system the orbits are degenerated and are lines instead of points in the phase space.

Pictures of the island structure for the wedge billiard was drawn by Lehtihet and Miller [131] and discussed in several articles [167, 197]. In figure 6.9 b) we find that in the limit $\theta \to 45°$ there is a hierarchy of islands with an island surrounding each periodic orbit from the Farey tree (8.1). For a θ finitely smaller than 45°, the smallest islands have disappeared in a chaotic sea. In smooth dynamical systems like the standard map [134], the KAM theory gives that quasiperiodic orbits with irrational winding number survive a perturbation depending on how irrational they are in a Farey tree sense. The Last surviving KAM tory has the golden mean as winding number. In these billiard systems it seems that the creation of chaotic regions also follows a Farey organization but here we do not have the unstable periodic orbit which give the chaotic regions and the mechanism of creating chaos is different. It seems that the stable periodic orbits furthest down in the Farey

tree disappear and create a chaotic region first. This imply that the orbits with most irrational winding numbers first disappear in the chaotic sea. This is in a way opposite to the KAM-scenario. The numerics indicate that the transition to chaos is different in these discontinuous systems than in the smooth flows and maps.

As the value of the parameter θ in the wedge billiard decreases the system "forgets" the Farey tree organization, and in the limit of a very narrow wedge $\theta \to 0$ the dynamics is dominated by one stable orbit.

We may compare the wedge billiard scenario with a disk system to examine how general the wedge billiard transition from integrability is. We know that the dispersive 3 disc billiard is completely chaotic and in the integrable limit it has the orbits organized in a Farey tree. The phase space picture of a number of different orbits in the focusing 3-disk system is plotted in figure 8.19 for different parameter values from close to the triangle shape, $r = \sqrt{3}$, to almost a circle, $r = 1$. In figure 8.19 a) there are islands which are very narrow and hard to distinguish but in figure 8.19 b) it is possible to distinguish a number of islands which surrounds the shortest of the periodic orbits from the Farey tree. When r decreases as for figure 8.19 c) we find that only the largest of the islands in figure 8.19 b) remain. As the value of r decreases further we find that the picture changes into new structures and only the stable period 3 orbit $\overline{s_1 s_2 s_3} = \overline{123}$ survive to $r \to 0$ and is here dominating the dynamics. This dynamics is qualitatively similar to the wedge for $\theta \to 0^\circ$ where the orbit bouncing back and fort between the two tilted walls dominates and to the two ball system where the dominating orbit for $m_1 << m_2$ is when the down-most ball bounces off the floor and bounces in the upper most ball every time.

We have not proven that the islands in figure 8.19 are surrounding the periodic orbits of the Farey tree, but this seems to be a reasonable conjecture from the numerical pictures. The different examples suggest that there is a number of systems that have this kind of transition to chaos, and this may be generic for non-smooth billiards.

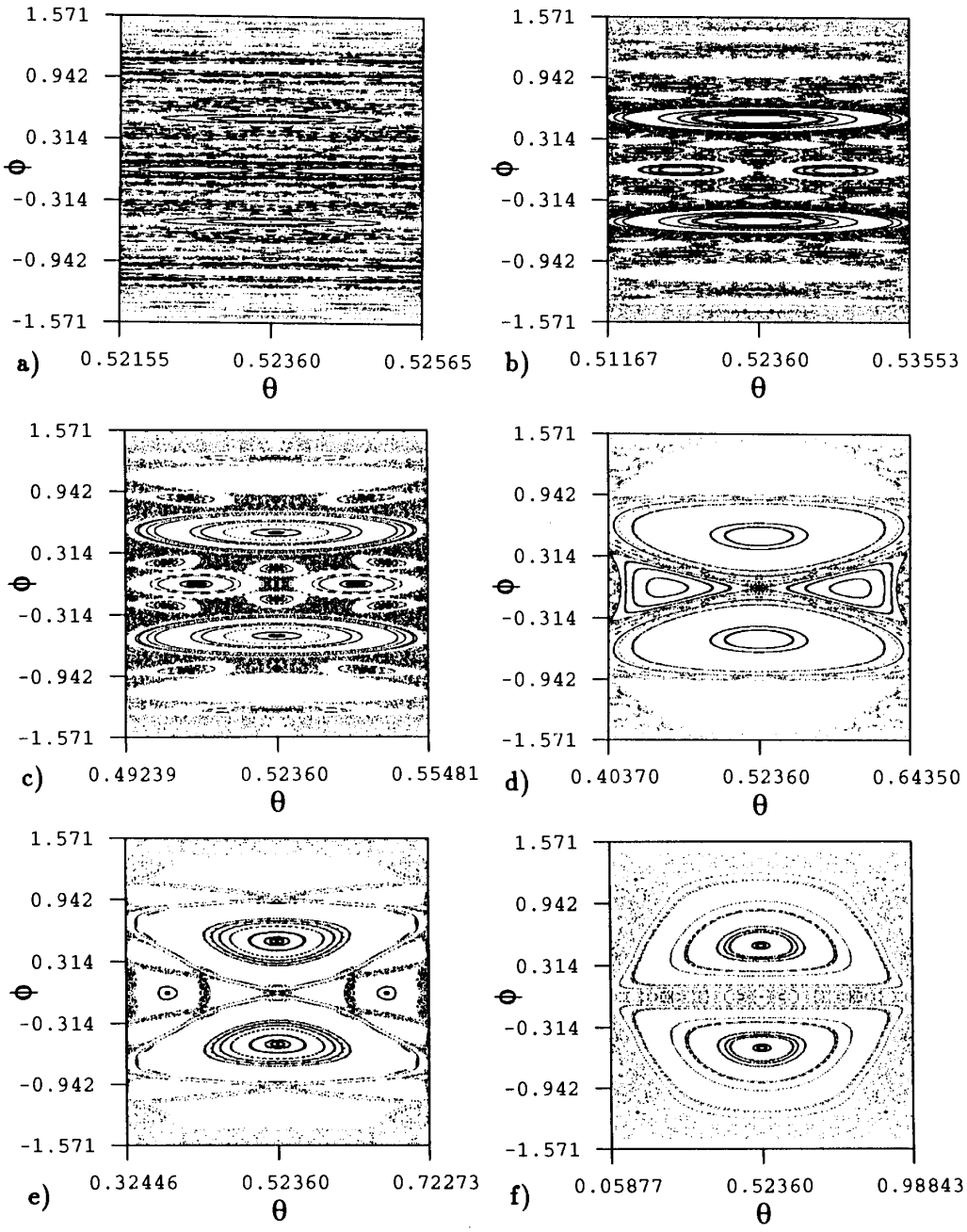

Figure 8.19: The phase space plot of orbits in the mixed stable-chaos 3 disk system. a) $r = 1.73$, b) $r = 1.72$, c) $r = 1.7$, d) $r = 1.6$, e) $r = 1.5$, f) $r = 1.1$,

Chapter 9

Bifurcation in billiards

Chapter 5 described bifurcations and forbidden orbits in billiard systems by introducing a pruning front. An orbit was forbidden if its symbolic value was in the forbidden region and the orbit bifurcated if its symbolic value was on the pruning front. We will in this chapter investigate the bifurcation process in billiard systems; the structure in the phase space and how the bifurcations are organized in families. This will enable us to connect bifurcations in a hard billiard system with the bifurcations in a soft Hamiltonian system even if it is difficult to obtain a pruning front for a smooth potential.

The bifurcations in billiard systems have received very little attention in the literature. It has even been claimed that there are no bifurcation structure in billiards; "...the E-τ plots [phase space as function of parameter] for this problem [anisotropic Kepler] has no interesting structure and shows no branching. The same is true of the various 'Billiards' problems." [23]. I disagrees with the statement on the billiard systems. The lack of interest in bifurcations in billiards should not be because these billiards are too artificial, because the billiards are very popular to use in e.g. quantum chaos calculations. It may be that the problems with symbolic dynamics have discouraged studies of bifurcations in billiards, but that is unlikely since bifurcations in the more complicated smooth potentials are much studied. Anyway I find these problems an interesting and a not too complicated exercise.

9.1 Tent map revisited

The best way to understand bifurcations in billiards is first to study the one dimensional tent map. In chapter 1 we made some remarks on bifurcations in the tent map. In the one parameter tent map a family of orbits is born at one critical parameter value. In the one dimensional phase space x the orbit at the bifurcation

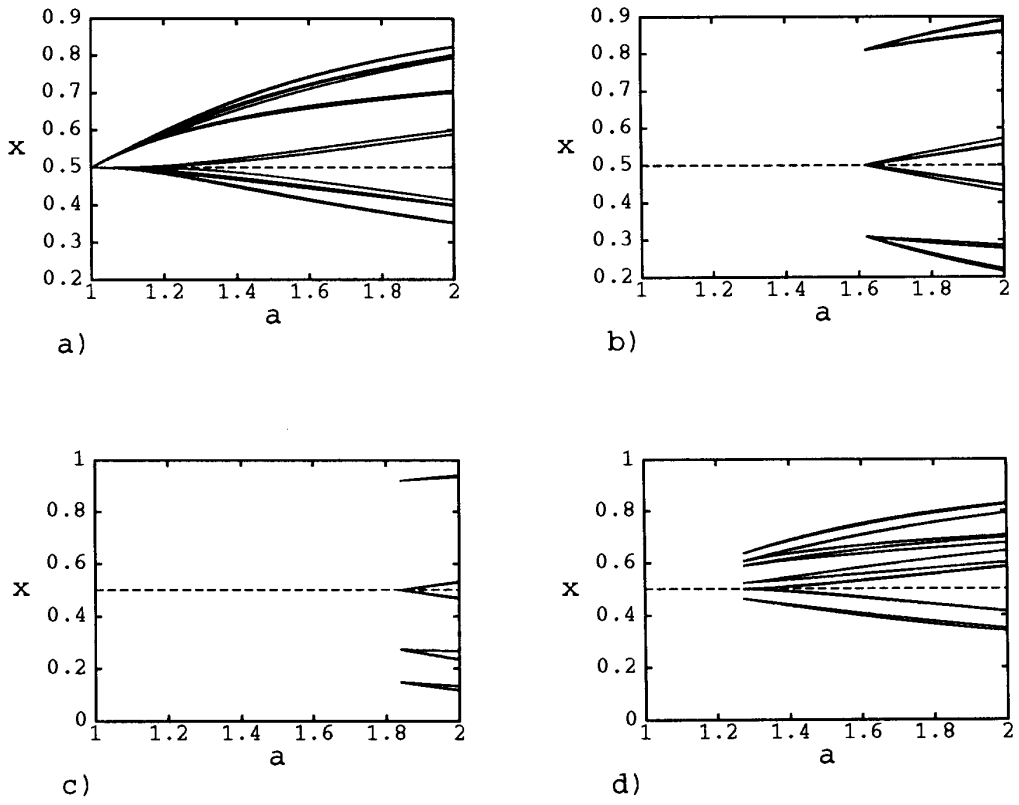

Figure 9.1: Bifurcation of families of periodic orbits in the tent map. a) $\overline{1}$, b) $\overline{100}$, c) $\overline{1000}$, d) $\overline{101111}$.

has one point at $x_c = 1/2$ and moves away as the parameter a increases. Some examples of bifurcating orbits are given in figure 9.1. We define the bifurcation family of orbits to be the period doubling family. This is all orbits of the form

$$\begin{aligned}
&\overline{S(1-\epsilon)} \\
&\overline{S\epsilon} \\
&\overline{S\epsilon S(1-\epsilon)} \\
&\overline{S\epsilon S(1-\epsilon)S\epsilon S\epsilon} \\
&\overline{S\epsilon S(1-\epsilon)S\epsilon S\epsilon S\epsilon S(1-\epsilon)S\epsilon S(1-\epsilon)} \\
&\vdots
\end{aligned} \tag{9.1}$$

with $S = s_1 s_2 s_3 \ldots s_{n-1}$ and $s_i \in \{0,1\}$, $\epsilon_i \in \{0,1\}$, the number of symbol 1's in $S\epsilon$ is odd, $S\epsilon$ can not be written as $S'(1-\epsilon)S'\epsilon$ and finally $\overline{S\epsilon}$ has to be the cyclic permutation giving $\tau^{\max}$. This corresponds to all harmonics of an orbit in the MSS terminology [147].

With this definition is it only the critical parameter $r_c = 1$ in eq. (1.3) that gives a bifurcation of only one family. This is the family of the fixed point $\overline{1}$ where the

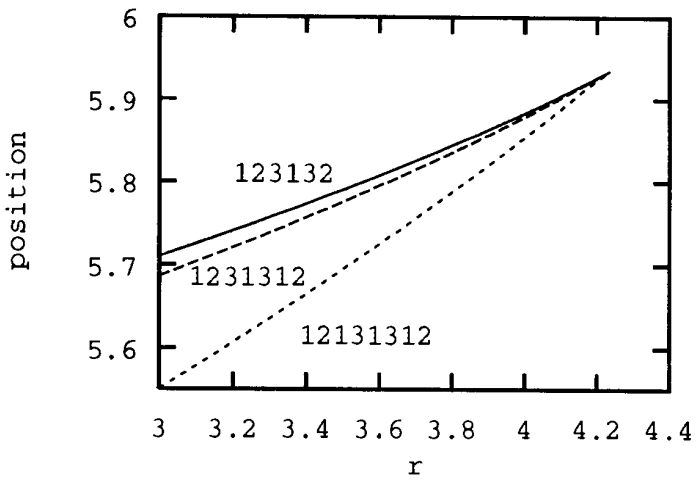

Figure 9.2: The position of one point of the orbits $\overline{123132}$, $\overline{12131312}$ and $\overline{1231312}$ as a function of the parameter $\tilde{r}$ close to the bifurcation in the non-symmetric 3 disk system.

string S consists of no symbols (here $\overline{S(1-\epsilon)} = \overline{0}$ does not bifurcate together with the family). All the other critical parameter values give the bifurcation of several families. The topological entropy increases linearly with the parameter and the map is called *not full* since not all kneading sequences can be obtained. In a more general map with a none-smooth critical point and no stable orbits, the different families may split up and bifurcate at different parameter values, while the different orbits belonging to the same family (9.1) always bifurcate at the same parameter value. The different families bifurcate in the MSS order but with critical parameter values where many orbits are created simultaneously.

In the tent map we find that the period 3 orbit family $\overline{S\epsilon} = \overline{100}$ bifurcates together with all other families with $\tau(\overline{101}) < \tau(\overline{S'\epsilon}) < \tau(100\overline{101}) = 0.111\overline{010}$ which is all orbits in the resonance of the logistic map. In general the orbits $\overline{S'}$ which bifurcate together with the primary family $\overline{S\epsilon}$ have $\tau(\overline{S(1-\epsilon)}) < \tau(\overline{S'}) < \tau(S\epsilon\overline{S(1-\epsilon)})$

The shortest orbits in the families $\overline{1}$, $\overline{100}$, $\overline{1000}$ and $\overline{101111}$ are drawn in figure 9.1 as a function of the parameter a.

9.2 Dispersing billiards

The bifurcation of a whole family of orbits at one parameter value is also happening in the billiards, but an important difference is that the billiards have a one

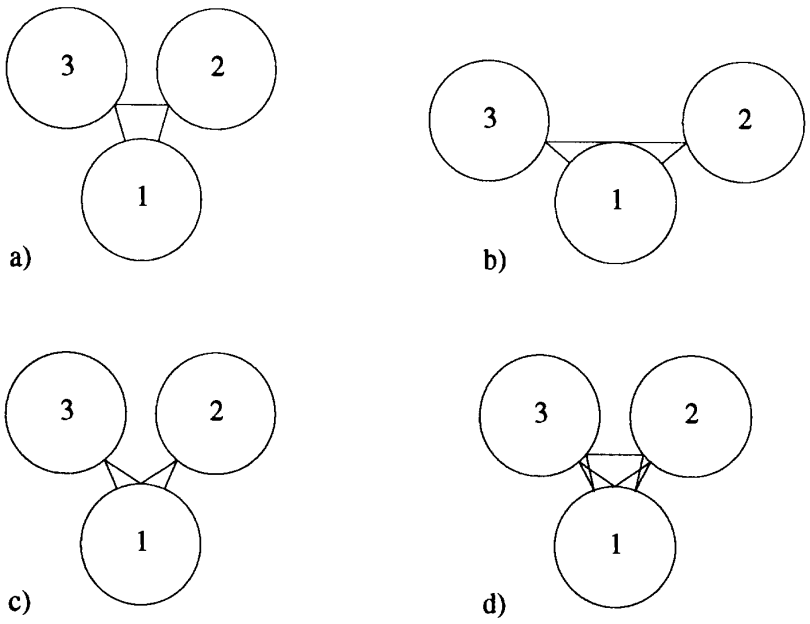

Figure 9.3: The orbits: a) and b) $\overline{123132}$, c) $\overline{12131312}$ and d) $\overline{1213132}$ for the parameter values: a), c) and d) $\tilde{r} = 2.5$ and b) $\tilde{r}_c = 4.212\ldots$.

dimensional family of critical orbits while the tent map only has one critical orbit.

9.2.1 The bifurcation family

Figure 9.2 shows a point in some orbits as a function of the parameter $\tilde{r}$ in a 3 disk system with the center-center distances $d_{12} = d_{13} = 2.5$, $d_{23} = \tilde{r}$, and with radius equal to 1. These orbits are the orbits in the family

$$\ldots 313 s_{-1} 212 s_0 313 s_1 212 s_2 313 \ldots \tag{9.2}$$

with s_i either empty or the symbol 1. An equivalent definition of this family is that it consists of the orbits constructed by using the alphabet

$$\hat{s}_i \in \{313, 3131, 212, 2121\} \tag{9.3}$$

We see that this family has more members than the period doubling family of the one dimensional map.

The reason why this is the correct symbolic description of the family is understood by the description of the singular orbits in figure 9.3. We know that an orbit in a dispersing billiard without corners bifurcates; that is changes between admissible and not admissible, because either

1) a free flight of the particle becomes tangential to the border

or

2) a bounce off the wall has the outgoing angle $\phi = \pi/2$.

In the configuration space at the bifurcation parameter r_c, these two cases look the same. From the figure 9.3 b) it is not possible to tell if the straight line between disk 2 and 3 is case 1) or 2). The parameter value r_c therefore has to be the bifurcation value of both the orbit where this straight line does not bounce and have no symbol, and for the orbit where it bounces and has the symbol 1. The orbit is infinite in future and in past and each time it passes the tangent point it may have a bounce or not. The descriptions (9.2) and (9.3) are exactly the descriptions of these orbits using symbols.

If we study an orbit which is tangent at one point but never returns to this point tangentially, there are only two orbits that bifurcate together for this parameter value. This is the case for hetroclinic orbits.

The argument for why the orbits bifurcate at the same parameter value does not depend on the details of how the billiard changes with a parameter. The only necessary knowledge is which straight line that becomes tangential to the wall, or which angle that becomes $\pi/2$. Figure 9.4 shows the same orbits in a 3-disk system as a function of a parameter $\hat{r}$ when we choose different radiuses of the disks

$$\text{radius(disk 1)} = 2, \quad \text{radius(disk 2)} = 1/2, \quad \text{radius(disk 3)} = 1$$

with the center-center distances

$$d_{12} = d_{13} = d_{23} = \hat{r}$$

The positions and the parameter change from the previous example but the same orbits (9.2) belong to the bifurcation family. The ordering along $\hat{r}$ for when the different families bifurcate may however change. This ordering is not fixed here as it is for the unimodal map (the MSS ordering).

An other example of a dispersing billiard is the symmetric 4 disk system and in figure 9.5 the position of one bounce of some long orbits is drawn as a function of the parameter r. The orbits are drawn in figure 9.6 and this family of orbits are described by the string

$$\ldots 1s_{-1}(32)^4 t_{-1} 4 t_0 (23)^4 s_0 1 s_1 (32)^4 t_1 4 t_2 (23)^4 s_2 \ldots \tag{9.4}$$

with s_i either 2 or no symbol, and t_i either 3 or no symbol. Because of the symmetry of this family there is a bifurcation two places in the orbit simultaneously. The critical parameter value is $r_c = 2.0312\ldots$.

We will return to this example later when we discuss the smooth potentials.

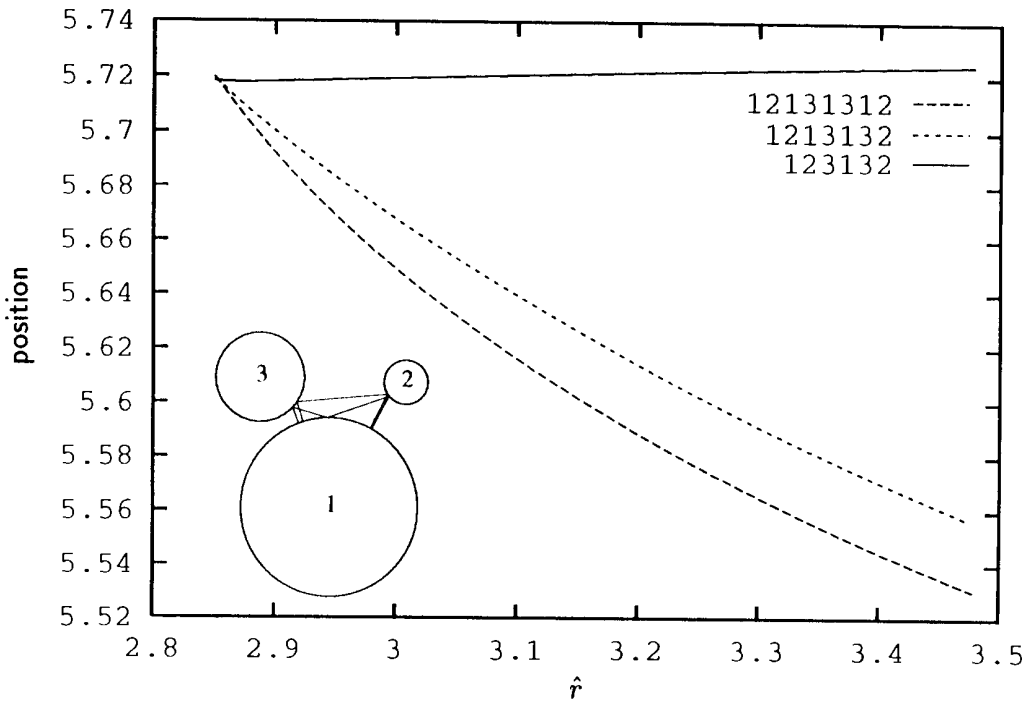

Figure 9.4: Bifurcation of the orbit $\overline{123132}$ and its family in a not symmetric 3-disk system. The position of the bounce on disk 3 as a function of $\hat{r}$.

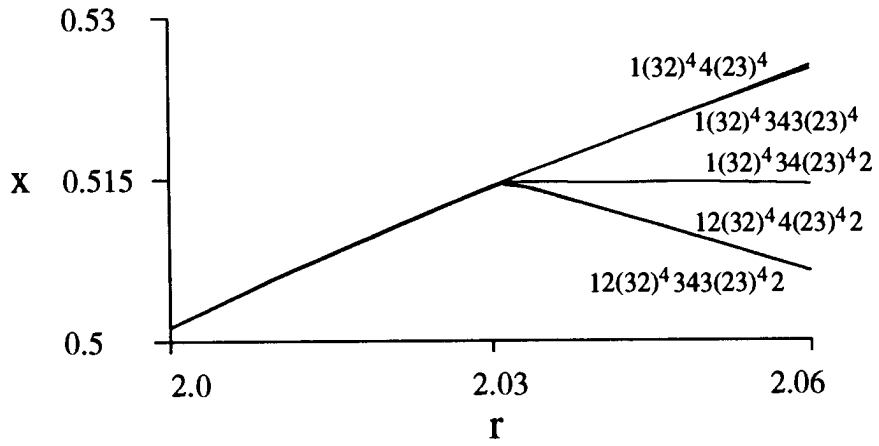

Figure 9.5: Bifurcation of the orbit $\overline{1(32)^4 4(23)^4}$ and its family in the 4-disk system. The position of the bounce on disk 1 as a function of r.

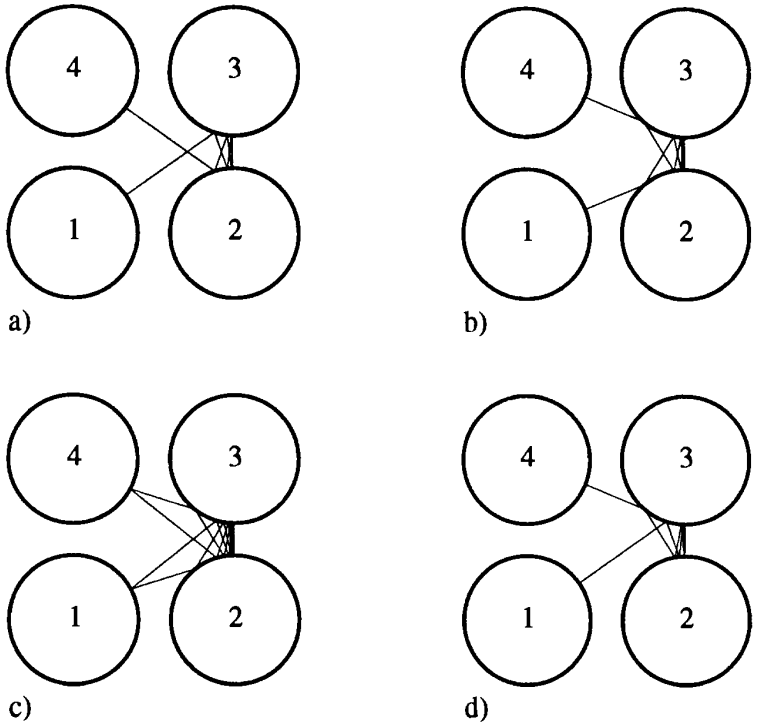

Figure 9.6: The orbits a) $\overline{1(32)^4 4(23)^4}$, b) $\overline{12(32)^4 343(23)^4 2}$, c) $\overline{1(32)^4 34(23)^4 2}$ and d) $\overline{1(32)^4 343(23)^4}$ in the 4 disk system for $r = 2.5$.

9.2.2 The parameter space

In the tent map each bifurcating orbit has one point equal to the critical point $x_c = 1/2$. In the dispersing billiards the critical points are a function of one parameter x which is the position of the tangent bounce. We call the orbit tangential to the border at x for $x_c(x)$ if this orbit is in the non-wandering set of the system. If the dispersing billiard is closed then $x_c(x)$ is continuous in the phase space. In an open billiard $x_c(x)$ is a point set, possibly a Cantor set, or it is empty.

The different families bifurcate at different positions on $x_c(x)$ and if we choose two different ways to parameterize the billiard with two parameters r_1 and r_2 then the different families with different $x_c(x)$ are not necessarily ordered the same way in contrast to the unimodal map. The only ordering between the families follows from the requirement that the pruning front is monotone.

The number of parameters necessary for describing all possible ways the system may bifurcate is infinite. We can deform a small part of the wall without destroying the dispersive properties. This will change the orbits that bounce in this part of the wall but not the other orbits. By making this deformation we can change the bifurcation point of one orbit without changing the bifurcation point of another.

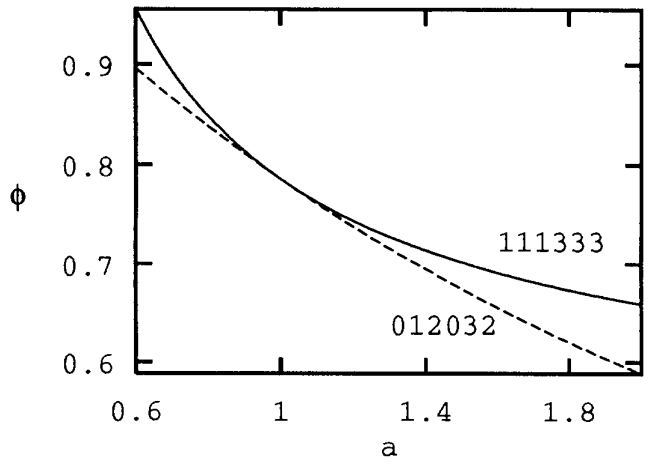

Figure 9.7: The angle of a bounce in the orbits $\overline{111333}$ and $\overline{012032}$ as a function of a for the stadium billiard.

These different local deformations may be considered as the different parameters in the system. Another point of view on the parameters is to understand each point of the pruning front as one parameter. This also gives an infinite number of parameters equivalent to the discussion above. In the folding maps of the Hénon type the pruning front has large steps, and we found a natural hierarchic structure of the infinite parameter space which gave a good way of describing the bifurcations of the map. We have not been able to find a similar ordering into more and less important parameters for the billiards because the pruning front does not have any large steps but is rather smooth.

9.3 Stadium billiard

The focusing stadium billiard also has the same kind of singular bifurcations of families as the dispersing billiards. Figure 7.26 shows some orbits for different parameter values. The outgoing angle ϕ of one bounce of the orbits as a function of the half length of the straight line, a, is plotted in figure 9.7. The structure of the singular bifurcations is similar to the dispersive billiards where all orbits belonging to one bifurcation family bifurcate at one parameter point. The family for the example in figures 7.26 and 9.7 is given by the symbol strings in symbols s^a

$$\ldots c_0 1 d_0 e_0 3 f_0 c_1 1 d_1 e_1 3 f_1 \ldots \tag{9.5}$$

with

$$c_i \in \{0,1\},\ \ d_i \in \{1,2\},\ \ e_i \in \{2,3\} \text{ and } f_i \in \{0,3\}.$$

An orbit in the stadium billiard becomes not admissible because either

1) The point where the particle bounces in the semi-circle moves to the end of the semi-circle

or

2) The point where the particle bounces in the straight line moves to the end of the straight line.

Assume an orbit bounces exactly off the singular point on the border where the straight line and the semi-circle join. In the configuration space is it not possible to decide whether this orbit is bouncing in the semi-circle or in the straight line. The symbol of this bounce is then given by either the semi-circle symbol or the symbol for the straight line. If the orbit is periodic then the orbit bounces off the singular point every n-th bounce and therefore a whole family bifurcates at this parameter value. The family of orbits is described by an alphabet

$$s_i = S\epsilon \tag{9.6}$$

where S is a fixed symbol string and ϵ is either a semi-circle or a straight line symbol. If there are symmetries of the orbit such that it bounces several times in a singular point before it closes, then the alphabet may be more complicated as the example above shows.

9.4 Corner bifurcations

We have a corner bifurcation in the wedge billiard where the singularity is the tip between the planes and in the corners of the overlapping disk systems. An orbit becomes illegal because a bouncing point on the wall moves from bouncing legally outside the corner until until it hits the corner at the bifurcation parameter. The only other orbit with a point that hits the corner for the same parameter value is the orbit which bounces off the other wall in a symmetric system. Because of the symmetry this is the orbit that is a mirror image of the first orbit or it is the same orbit if this orbit also is symmetric. In a fundamental domain is it only one orbit bifurcating. The bifurcation family is only the trivial family consisting of the orbit, its reflection and the time reversed orbit.

One exception is the orbits bifurcating for $\theta = 60^\circ$ in the wedge billiard. As observed by Smilansky [185, 189] there are several orbits bifurcation simultaneously

for this parameter value. One may expect this for some special parameter values but generically it does not seem to be true. Typically will the size of the family depend crucially on the smoothness of the singularity in the system.

Part IV

Hamiltonian systems

Chapter 10

Smooth Hamiltonian systems

In this chapter we will discuss the difficult problem of analyzing a smooth Hamiltonian system. It is not proven for any nontrivial example that there exist a partition of the non-wandering set, and there is no theory analog to the MSS theory which explains the ordering of different bifurcations in these systems. We will show some examples where we can understand bifurcations better than before by using the results we have obtained on folding maps and on billiard systems. These examples support the conjectures and speculations we present below concerning the smooth Hamiltonian systems and we suggest future investigations of these problems.

In an area preserving smooth system, e.g. a Hamiltonian system, there is a non-wandering set of stable and unstable orbits. The major difference from the smooth dissipative system is that the stable orbits are not attracting neighboring orbits but are surrounded by KAM tori [134]. The determinant of the Jacobian of a dissipative system is less than 1 while for the area preserving map the determinant is 1.

From a two-dimensional Hamiltonian we can find the Jacobian for the canonical variables (I, θ) [134] (also called the monodromy matrix) and since the determinant is 1 a period n orbit is hyperbolic (unstable) if

$$|\mathrm{Tr}\,\mathbb{J}| > 2 \tag{10.1}$$

and the orbit is elliptic (stable) if

$$|\mathrm{Tr}\,\mathbb{J}| < 2 \tag{10.2}$$

If $|\mathrm{Tr}\,\mathbb{J}| = 2$ we have a bifurcation point. If the periodic orbit is elliptic then the eigenvalues are

$$\lambda_{1,2} = e^{\pm i\sigma} \tag{10.3}$$

$$\sigma = \arccos\left(\frac{\mathrm{Tr}\,\mathbb{J}}{2}\right) \tag{10.4}$$

and there is a bifurcation of a periodic orbit for all rational values of $\sigma/2\pi$ [148, 8, 94]. The typical bifurcation for $\sigma/2\pi = p/q$ is the creation of two period $q \cdot n$ orbits in the Poincaré map where one orbit is elliptic and one is hyperbolic and the orbits have q points in a chain surrounding each point of the period n orbit in the Poincaré plane. If $q \leq 5$ the orbits may have a different bifurcation depending on the system. The general classification of bifurcations is given by Meyer [148] and is used to show general scaling behavior of bifurcations [94].

This general theory does not predict neither the shape of the bifurcated orbit in the configuration space nor how many times a given periodic orbit has the same value of σ scanning a parameter line.

10.1 Hamiltonian Hénon maps

The once folding maps are for some parameter values area preserving maps and could in principle be constructed as a Poincaré map of a Hamiltonian flow. The Hénon map has $\det \mathbb{J} = -b$ and is area preserving for $|b| = 1$ and also the Lozi map is area preserving for $|b| = 1$.

In chapter 4 we found that some cusp bifurcations have to be exactly at $b = 1$ or $b = -1$ because of symmetries in the symbol strings describing the orbits. In a 2^n-dimensional symbolic parameter space the area preserving maps seem not to correspond to a simple line or surface but to points characterized by a special symmetry in the strings giving the values $\kappa_0, \kappa_1, \kappa_{10}, \kappa_{00}, \kappa_{01}, \kappa_{11}, \ldots$. Similarly in the pruning front language it is not obvious which pruning fronts that give an area preserving map, but the points (δ, γ) on the pruning front must have special symmetries in the symbol strings.

That we at all can describe bifurcations e.g. the period 4 cusp $\{\overline{1011}, \overline{1000}, \overline{1001}\}$ in the symbolic parameter space $(\kappa_{10}, \kappa_{00}, \kappa_{01}, \kappa_{11})$ indicates that the non-wandering set at $|b| = 1$ can be described by the binary symbolic dynamics. However conjecture 1 which gave a continuous partition curve of the Hénon map in the (x_t, x_{t+1}) space assumed that the unstable manifold is not dense in (x_t, x_{t+1}) which is not necessarily true for $|b| = 1$. When there is a bifurcation of a turning points the partition curve may break up into not connected parts. A not connected partition curve may be acceptable if it goes through the unstable manifold in a unique way, but the partition of the area conserving Hénon map is not understood and further investigations is needed.

10.2 The $(x^2y^2)^{1/a}$ potential

One group of smooth Hamiltonians which seem to be promising candidates for a good symbolic description is the two-dimensional potentials $V(x, y)$ that have a shape which can be compared with a billiard system. We can consider these systems to be created by starting with a billiard potential which is 0 in the domain accessible to the particle and $+\infty$ in the forbidden regions and then smoothen this hard potential to a soft potential.

One example of this is the potential

$$V(x, y) = \left(x^2y^2\right)^{\frac{1}{a}} \tag{10.5}$$

which was investigated by Dahlqvist and Russberg [57, 58] and other authors. In the limit $a \to 0$ this potential becomes the hyperbola billiard (7.10) which we in section 7.4 found was described by a slightly pruned trinary alphabet. Dahlqvist and Russberg adiabatically followed periodic orbits starting at the hyperbola billiard $a = 0$ and letting the parameter a increase slowly. They found that an unstable periodic orbit in the hyperbola billiard smoothly changes and is hyperbolic when a increases, and some orbits have a parameter interval (a window) where the orbit is elliptic, and then the orbit disappears in a bifurcation and does not exist for larger values of a. Other orbits bifurcate and disappear without becoming stable. They described a number of bifurcations and found that the symbolic description of the orbits merging into each other is similar. They conjectured [58] that all orbits pruned during one bifurcation cascade, have a symbolic description consisting of combinations of two symbolic strings.

Figure 10.1 shows Dahlqvist and Russbergs calculation of $\mathrm{Tr}\,\mathbb{J}$ as a function of a for some periodic orbits. The symbols they use are slightly different than those used here. In figure 10.2 the same bifurcations are drawn with dashed lines indicating hyperbolic orbits and solid lines indicating elliptic orbits. For clarity the parameter axis is not at correct scale and the vertical axis is a sketch of a possible point in a Poincaré map.

Dahlqvist and Russberg showed that the orbit $\overline{S} = \overline{1(32)^434(23)^42}$ is stable in a window that includes the parameter value $a = 1$, and therefore that an earlier conjecture claiming that the potential $V = x^2y^2$ is completely chaotic was wrong [57].

We are now interested in the symbolic description of the orbits bifurcating in one bifurcation scenario. Dahlqvist and Russbergs conjecture is that all orbits in the cascade in figure 10.2 a) are described by the symbol strings of the form

$$\ldots 2t_{-1}434t_0232t_1434t_223\ldots \tag{10.6}$$

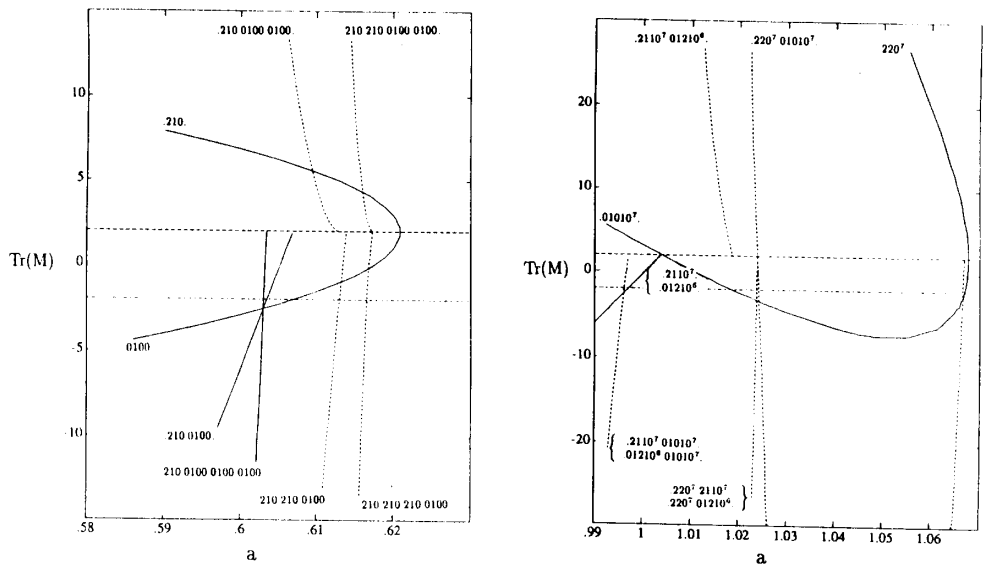

Figure 10.1: The Tr $\mathbb{J}$ as a function of a for some periodic orbits. From [58].

with t_i either symbol 3 or no symbol, and that the orbits in figure 10.2 b) are described by the strings

$$\ldots 1s_{-1}(32)^4 t_{-1} 4 t_0 (23)^4 s_0 1 s_1 (32)^4 t_1 4 t_2 (23)^4 s_2 \ldots \tag{10.7}$$

with s_i either 2 or no symbol, and t_i either symbol 3 or no symbol.

We now compare these bifurcations to the bifurcation families for the billiard systems in chapter 9 and we find that the strings describing a billiard family of orbits are the same strings that give the orbits bifurcating in the bifurcation trees of the potential (10.5). The 4 disk system with $r_c = 2.104231\ldots$, figure 10.4, is the bifurcation point of the orbits with symbolic description (10.6) and for $r_c = 2.0312\ldots$ there is a singular bifurcation of the orbits (10.7), figures 9.5 and 9.6.

We now state a general conjecture of bifurcations of "billiard like" smooth potentials.

Conjecture 2 *In a billiard like smooth Hamiltonian system the orbits bifurcating in one bifurcation cascade are the orbits of one family bifurcating at a singular parameter r_c for a corresponding billiard system.*

We can also state an other interesting conjecture.

Conjecture 3 *The symbolic description of the bifurcation family of the billiard system predicts the minimum number of times a periodic orbit has to bifurcate with the same complex eigenvalues $\lambda_{1,2} = e^{\pm i\sigma}$ for any one-dimensional parameter path from the complete horseshoe repellor to the parameter value where the orbit disappear.*

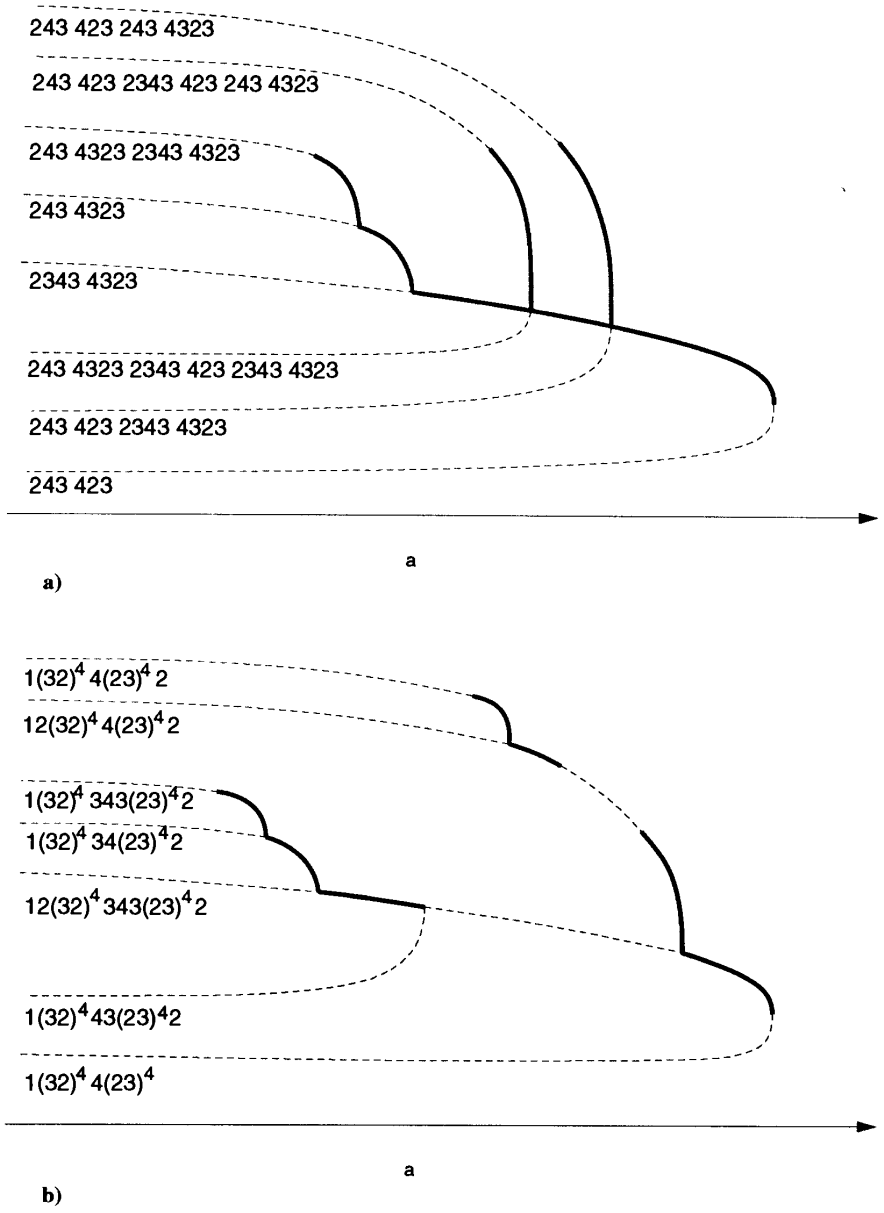

Figure 10.2: A sketch of the bifurcation trees of the orbits in figure 10.1. Solid lines are elliptic orbits while dashed lines are hyperbolic orbits.

One major difficulty in these conjectures is that we have not precisely defined a "billiard like" Hamiltonian and which billiard one associates with a specific potential. A guiding line may be that a smooth slope is represented as a hard billiard wall, convex and concave walls in the billiard are similarly shaped in the smooth potential and the symmetries in configuration space have to be the same.

The potential (10.7) has four hills which we identify with the 4 disks in the 4-disk system. We could have studied the hyperbola billiard (7.10) and changed the hard hyperbola walls to find the bifurcations, but the bifurcation families would be the same in these two billiards and the 4-disk system is more convenient. In some cases the 4-disk system may give problems because it has the corner pruning which is not present in the potential (10.7). The singular bifurcation of a billiard is when the orbit is tangent to the disk. In the smooth potential there is no sharp wall to be tangent to, but in Dahlqvist and Russbergs plot of orbits in the configuration space, figure 10.3, we find that orbits that are going to bifurcate together, move closer such that the curves corresponding to the tangent line in figure 10.4 straighten out and move closer to each other. We then get a kind of tangent curve off a soft wall. This kind of curve is what we have to identify as a singular orbit or a turning point in the smooth potential. The orbit is tangential to a constant energy line but the position is not given as simple as for the billiard system. To find this orbit in general is an open question.

We can illustrate the conjectures 2 and 3 by the two examples in figure 10.2. In figure 10.2 a) the orbit $\overline{2343\,4323}$ becomes elliptic in a bifurcation where the orbit $\overline{243\,4323}$ disappears and then the elliptic orbit changes once through each winding numbers σ and then the orbit disappears together with the unstable orbit $\overline{243\,423}$. The bifurcation where the elliptic orbit becomes hyperbolic is a symmetry breaking bifurcation which in some Poincaré map is a bifurcation from a fixed point to a period two orbit. In the 4-disk system all orbits in the family (10.6) bifurcate for $r_c = 2.104231\ldots$ where one line is tangent to a disk, figure 10.4.

The family $\ldots 1s_0(32)^4t_04t_1(23)^4s_1\ldots$ in the 4-disk system, figure 9.5, has one more tangent line do the disks than the $\ldots 2t_0434t_123\ldots$ family. If the symmetric orbit $\overline{12(32)^4343(23)^42}$ bifurcates in a similar way as the orbit $\overline{2343\,4323}$ then $\overline{12(32)^4343(23)^42}$ has to bifurcate two times to bifurcate together with the different symmetry broken orbits. For these two examples we find that the number of tangent lines of the billiard orbit at r_c is equal to the number of stable windows of the orbit. We may conjecture that this is a general feature such that the number of tangent lines in the singular bifurcation gives the number of times the short orbit has to go through a stable window.

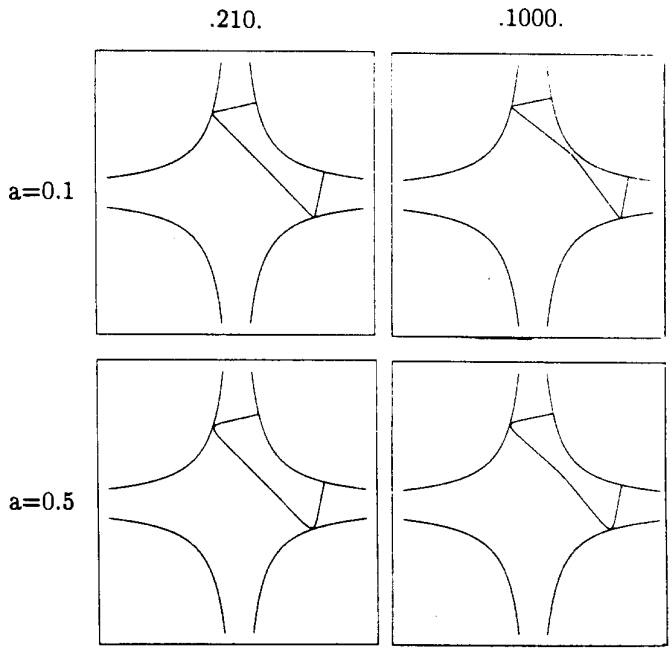

Figure 10.3: The orbits $\overline{243\,423}$ and $\overline{2343\,4323}$ in potential (10.7) for two different parameter values. From [58].

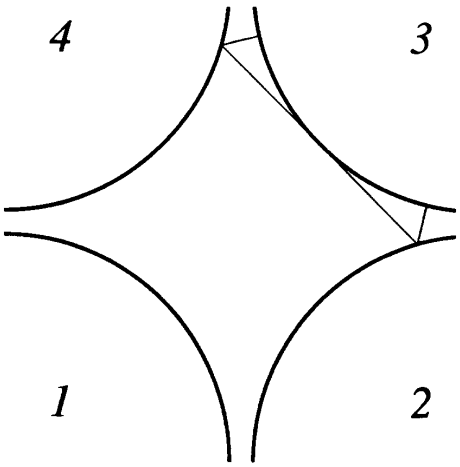

Figure 10.4: The orbit $\overline{243\,423}$ in the 4 disk system for $r_c = 2.104231\ldots$.

In figure 10.2 a) we also find that orbits bifurcating in the stable window at rational values of $\sigma/2\pi$ are described by the symbol string (10.6). The length of the symbol string gives approximately the length of the orbit in the potential.

The non-periodic symbol strings from (10.6) and (10.7) may be orbits from the accumulation point of n-tuplings of stable periodic orbits or from quasiperiodic orbits created between the creation of periodic orbits at irrational values of $\sigma/2\pi$

In the two examples shown here the shortest critical billiard orbit is tangent to the wall 2 or 4 times. If the orbit is tangent only one time we expect the bifurcation where the shortest elliptic orbit turns hyperbolic to be a period doubling bifurcation instead of the symmetry breaking bifurcation.

10.3 Parabola shaped potentials

We will sketch here how an investigation of bifurcations in a smooth potential can be interpreted in terms of symbolic dynamics of a corresponding billiard.

10.3.1 NELSON

Baranger and Davies [23] have carefully studied bifurcations in a potential

$$V(x,y) = \left(y - \frac{x^2}{2}\right)^2 + \frac{x^2}{20} \tag{10.8}$$

which they called NELSON, and other more complicated potentials [1]. They studied the bifurcations of periodic orbits as a function of the energy for this potential. Figure 10.5 shows equipotential contours of potential (10.8). This system without any other parameters does not have a limit of a hard billiard system and Baranger and Davies did not try to give a symbolic description of orbits but denoted them different names according to how they look and how they bifurcate. The potential is just chosen as one typical system of a parabolic shape and it is no reason to expect that the increasing energy , E, should be a more special parameter path than a change of a parameter in the potential as in the $(x^2y^2)^{1/a}$ potential.

We will now try to give the periodic orbits as a symbolic description by replacing the soft walls with hard billiard walls and find singular bifurcations which corresponds to a bifurcation tree in the smooth potential. In addition to the billiard bifurcation where the singular orbit is tangent to a dispersing wall we also find it necessary to allow two consecutive bounces in a focusing wall to merge into one bounce.

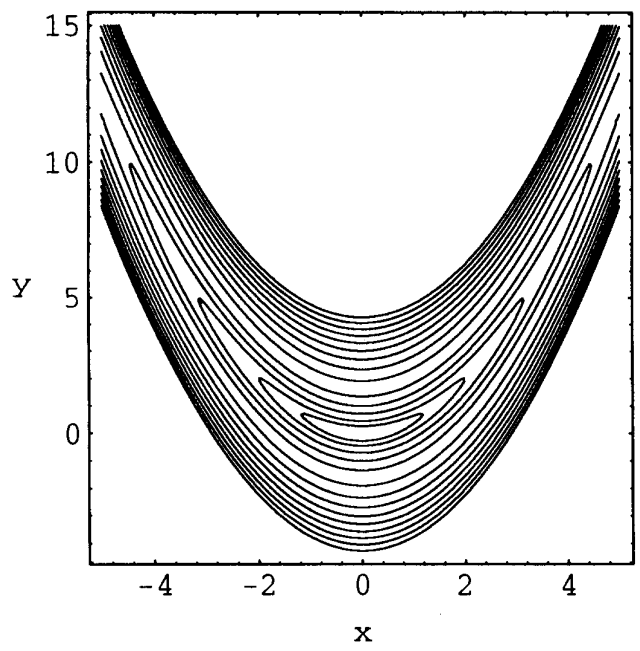

Figure 10.5: Equipotential contours of the potential (10.8).

Baranger and Davies have chosen to plot the bifurcations in the (E, τ) plane where E is the energy and τ is the length of the periodic orbit. Some of their bifurcation diagrams are given in figure 10.6. In these diagrams orbits are denoted by different letters and the plots of some of the periodic orbits in (x, y) are given in figure 10.7.

We will define a billiard system with a symbolic dynamics and identify the orbits in figure 10.7 with a symbol string. A "smiling billiard" is drawn in figure 10.8. This is just a hand-drawn billiard which is not ergodic and the periodic orbit is also just sketched by hand. A change of parameter is a change in the shape of the walls. We define the symbols:
$s = 1$ for a bounce off the dispersing wall,
$s = 2$ for a counterclockwise bounce off the focusing wall,
$s = 3$ for a clockwise bounce off the focusing wall and
$s = 4$ for a normal bounce off the focusing wall.
If the normal bounce $s = 4$ is on the symmetry line $x = 0$ we denote it $4'$. We assume this is a covering (and heavily pruned) alphabet. A number of periodic orbits of the billiard are drawn in figures 10.8 and 10.9 together with the symbol string $\overline{S}$ and the Baranger–Davies name for the corresponding smooth orbit.

In figure 10.6 we find that when the smooth orbit **A**; $\overline{133122}$ changes from elliptic to hyperbolic then the orbit **q2**; $\overline{13131212}$ is born. In our smiling billiard there exists

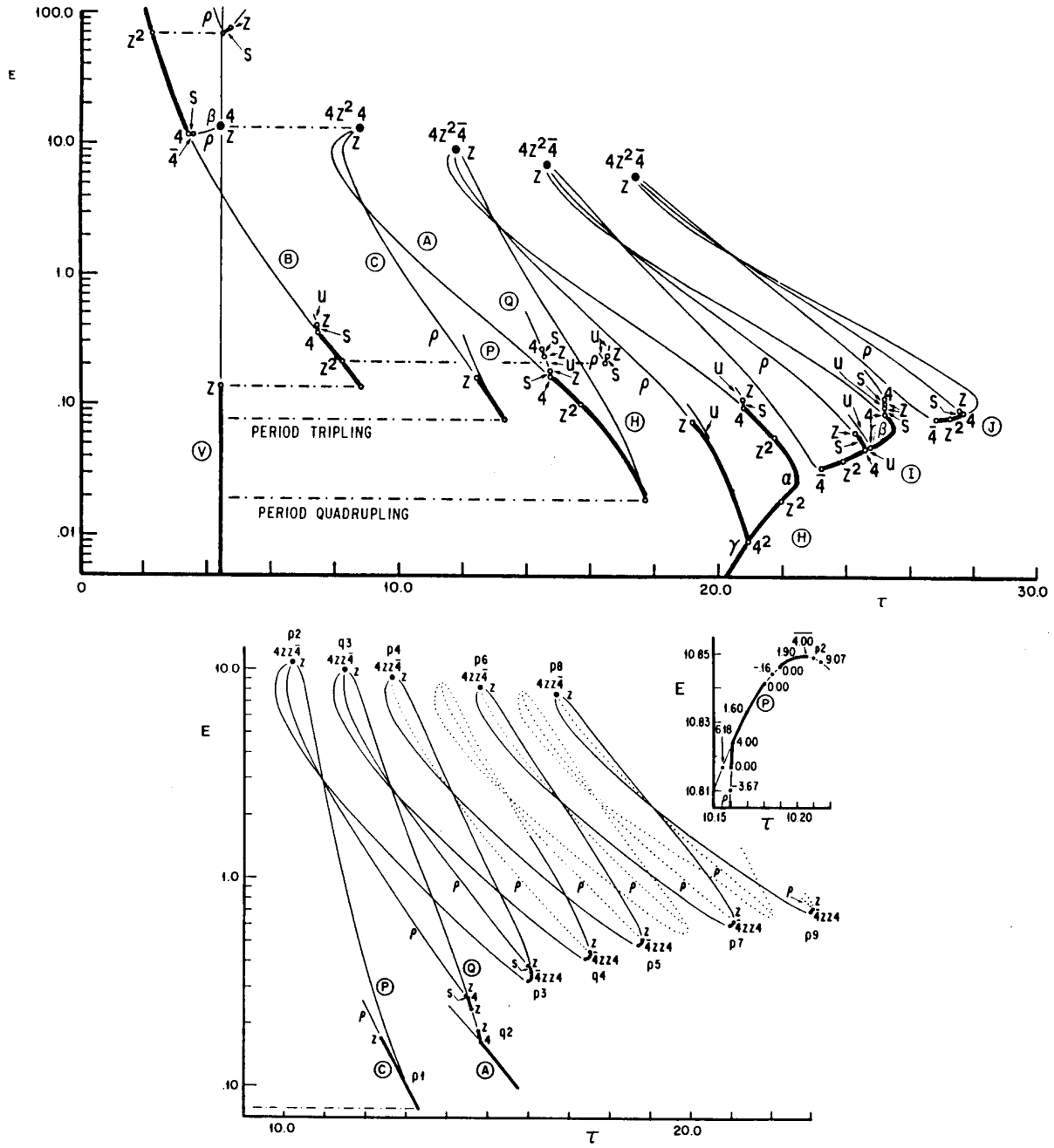

Figure 10.6: The bifurcation diagram (E, τ) of the potential (10.8). From [23].

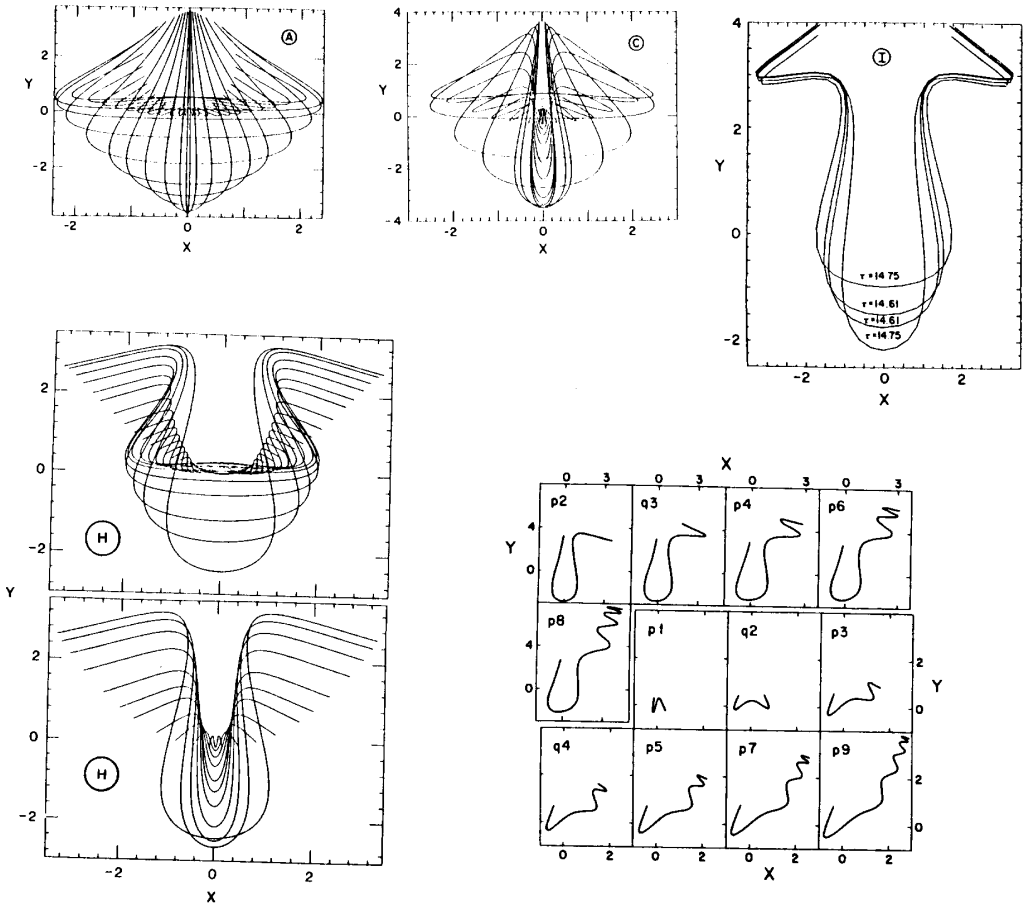

Figure 10.7: Some periodic orbits in the potential (10.8). From [23].

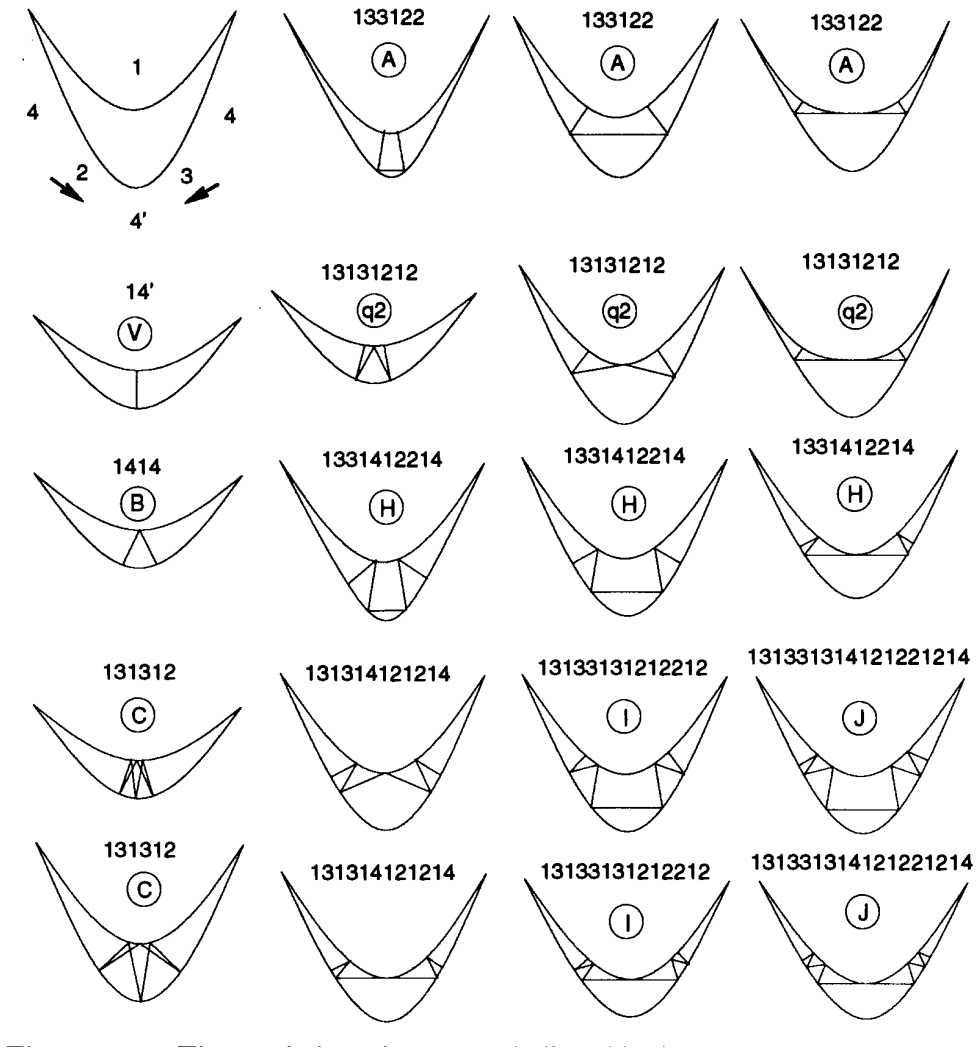

Figure 10.8: The symbols and some periodic orbits in the "smiling billiard".

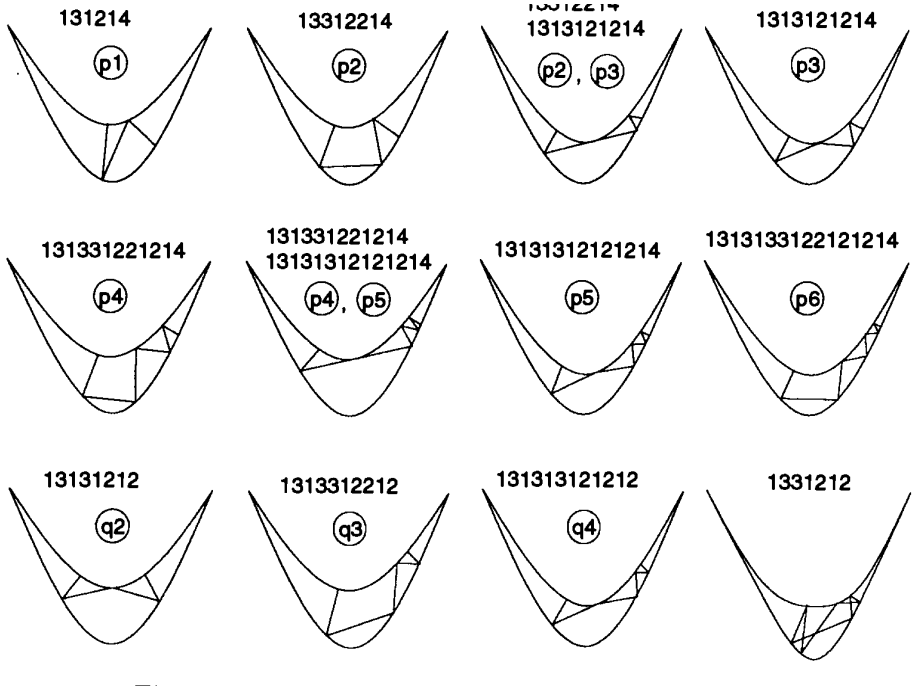

Figure 10.9: Periodic orbits in the "smiling billiard".

a singular bifurcation of these two orbits where the orbits have a line tangential to the dispersive wall. This orbit is drawn in figure 10.8. The singular bifurcation gives a change of symbols $33 \leftrightarrow 313$ or $22 \leftrightarrow 212$. The singular bifurcation family of orbits have the symbolic description

$$\ldots 13t_{-1}312t_0213t_1312t_22\ldots \tag{10.9}$$

with t_i either 1 or no symbol. One other periodic orbit in this bifurcation family is $\overline{1331212}$ which is drawn in figure figure 10.9 and which we identify with an orbit bifurcating from **q2**; $\overline{13131212}$ in figure 10.6.

An other example of a tangent type of a singular orbit in the billiards is the family

$$\ldots 1313t_{-1}312t_021413t_1312t_2214\ldots \tag{10.10}$$

with t_i either 1 or no symbol. In figure 10.9 the singular orbit is drawn and the two orbits **p2**; $\overline{13312214}$ and **p3**; $\overline{1313121214}$ are drawn for a different parameter values. The orbits **p2** and **p3** bifurcate together in the (E, τ) plane in figure 10.6.

It seems to be necessary to make an ad. hoc. assumption of a second bifurcation in the smiling billiard. We allow one bounce in the focusing wall close to $x = 0$ to split into two bounces. This bifurcation implies the change of symbols $3 \leftrightarrow 33$ or $2 \leftrightarrow 22$. This is not an bifurcation that are a singular bifurcation in a billiard but in

the region below origin in the smooth potential a path changes very smoothly and a billiard model may not be a good approximation here. An example of a family from this bifurcation is

$$\ldots 13r_0 12s_0 1413r_1 12s_1 14\ldots \tag{10.11}$$

with r_i either 3 or no symbol and with s_i either 2 or no symbol. The symbol 4 can turn into 2 or 3 if the combination of r_i and s_i gives an orbit that is not symmetric. The two orbits **p1**; $\overline{131214}$ and **p2**; $\overline{13312214}$ in figure 10.6 are members of this family. A periodic orbit may be member of both these two kind of singular bifurcations and this gives the zig-zag structure in figure 10.6 b) which Baranger and Davies calls a "duet of asymmetric librations". The orbit $\overline{1331212}$ in figure 10.9 is a member of the family (10.9) and of the family (10.11) and is the hard version of the smooth orbit Baranger and Davies calls the "first rotational bridge". Figure 10.10 a) shows Baranger and Davies' rotational bridge for different parameter values connecting the orbits **q2** and **p2**. Figure 10.10 b) is the billiard orbit $\overline{1331212}$ connecting the orbits $\overline{13131212}$ and $\overline{13312214}$. The symbolic description of all bifurcation families in this zig-zag structure is

$$\begin{aligned}
&\ldots(13)^{k+1}t_0 312 t_1 2(12)^k\ldots\\
&\ldots(13)^{k+1}t_0 312 t_1 2(12)^{k-1}14\ldots\\
&\ldots(13)^{k+1}r_0 12 s_0 (12)^k\ldots\\
&\ldots(13)^{k+1}r_0 12 s_0 (12)^k 14\ldots
\end{aligned} \tag{10.12}$$

with $t_i \in \{1,\emptyset\}$, $s_i \in \{2,\emptyset\}$ and $r_i \in \{3,\emptyset\}$.

It seems possible to describe all bifurcations in this system in terms of a symbolic alphabet but more investigations of the bifurcations in this and similar systems should be done to test this conjecture. The family of orbits obtained by splitting one bounce in the focusing wall into two bounces is made ad. hoc. to fit the description of the smooth system and are not directly motivated from the billiard suggested as a hard model of the potential. From a symbolic dynamics point of view is this a simple creation of symbol strings but from a physical point of view we would like to have a better billiard model that also had this family of orbit as a singular bifurcation.

10.3.2 Størmers problem

A physical problem which has a kind of parabola shaped potential is the motion of a charged particle in a magnetic dipole field. Pioneering numerical investigations of this problem was started by Carl Størmer 1903 [187] who probably was the first to numerically calculate complicated chaotic orbits [122, 123].

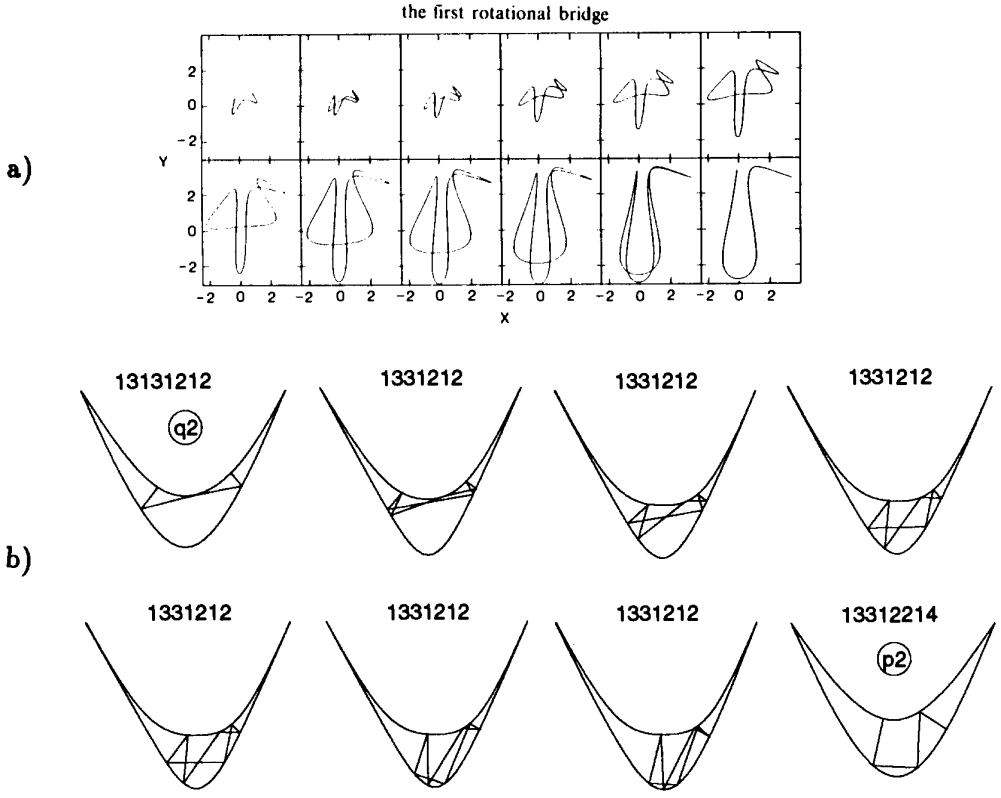

Figure 10.10: a) The "first rotational bridge" of the potential (10.8). From [23]. b) The orbit $\overline{1331212}$ in the "smiling billiard".

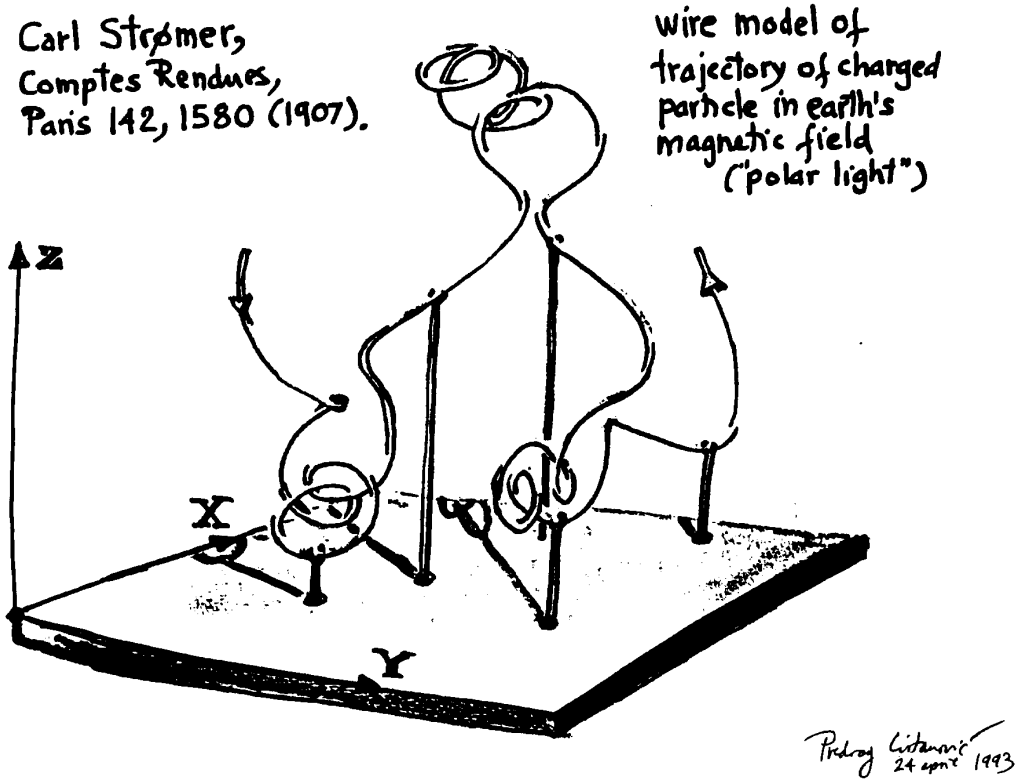

Figure 10.11: The path of a particle in a magnetic dipole field. Drawing by P. Cvitanović after C. Stormer [187]

The problem can be reduced to a two dimensional problem with the Hamiltonian

$$H = \frac{1}{2}(p_\rho^2 + p_z^2) + \frac{1}{2}\left(\frac{1}{\rho} - \frac{\rho}{r^3}\right)^2 \tag{10.13}$$

where ρ, ϕ, z is the cyclical coordinates around the magnetic dipole and r is the distance from the particle to the origin. For low energies the potential is near integrable with KAM tory and it has a shape similar to a parabola but with one path going into the dipole. For slightly larger values of the energy the problem is a scattering problem with a structure comparable to the three-disk problem. For large enough values of the energy the system is a complicated but not chaotic scatter. This system is investigated in several works [31, 38, 62, 64, 123, 124] but a careful study of the bifurcation structure has not been done. We expect that we can describe the bifurcation diagrams for the Størmer problem by a symbolic dynamics obtained from a corresponding billiard system as we could do for the potential (10.8). Figure 10.11 shows one path of a scattered particle in the dipole field.

Part V

Quantum Chaos and Zeta Functions

An important application of the theory of symbolic dynamics and pruning discussed in the chapters above is the semi-classical quantization of classical chaotic systems. A control of the geometrical structure of the classical system is essential for controlling the convergence of the semi-classical expansions, as showed in several examples by Cvitanović [42, 43, 46, 48], Artuso, Aurell and Cvitanović [10, 11, 14], Ezra, Richter, Tanner and Wintgen [70] and others. Gutzwiller [103] states: "Finding the appropriate code seems the most important task when facing a dynamical system with hard chaos".

Chapter 11

Quantum Chaos

11.1 Semi-classical methods

The semi-classical Bohr-Sommerfeld theory, or the first quantum theory described successfully the quantum spectrum of hydrogen. However, this method failed in describing even the ground level of the helium atom, the calculation which was the first triumph triumph of the new quantum mechanics [120]. Before the introduction of the quantum mechanics of Heisenberg, Born, Jordan, Dirac, Pauli and Schrödinger, Einstein noticed that the Bohr-Sommerfeld quantization rested on the construction of action-angle variables and would fail for systems which are not integrable [69]. Understanding of the geometrical phase factors Morse [156] and Maslov indices [145, 6, 37] came much later and the ground level of helium was calculated with semi-classical methods by Percival and Leopold as late as 1980 [132].

Lately there has been much interest in applying semi-classical methods to determine spectra of systems whose classical dynamics is chaotic, both because semi-classical methods are a useful tool for obtaining numerical results, and because they offer a classical intuitive picture of the quantum system. Fundamental work was done by Gutzwiller around 1970 [102, 103], with the Gutzwiller trace formula which connects a sum over periodic orbits in a completely chaotic classical system to the eigenvalues of the corresponding quantum mechanical system

$$g_c(E) = \frac{1}{i\hbar} \sum_{\text{p.o.}} \frac{T_p}{|\det(M_p - I)|^{\frac{1}{2}}} e^{\frac{i}{\hbar} S_p(E) - i\pi\sigma_p/2} \tag{11.1}$$

where $g_c(E)$ is the trace of the semi-classical Green's function. M_p is the monodromy matrix, T_p the time of the primitive periodic orbit p, S_p the classical action along the periodic orbit and σ the Maslov index for the orbit. The poles in $g_c(E)$ give eigenvalues of the quantum system; energy levels, resonances, decay times, correlations, etc. There are several different ways to formulate this result; the

zeta-function formulation from thermodynamic theory, see below, gives a slightly different formula.

The classical dynamical zeta function in thermodynamics was introduced by Ruelle [170, 171, 172] and applied to chaotic quantum systems by Cvitanović [42] and others. The classical dynamical zeta function is given by

$$1/\zeta = \prod_p (1 - t_p) \quad ; \quad t_p = \frac{z^{T_p \gamma}}{|\Lambda_p|} \tag{11.2}$$

and the corresponding quantum zeta function can be written as

$$1/\zeta = \prod_p (1 - t_p) \quad ; \quad t_p = \frac{1}{\sqrt{\Lambda_p}} e^{\frac{i}{\hbar} S_p(E) + i\pi\sigma_p/2} \tag{11.3}$$

where Λ the leading eigenvalue of the Jacobian matrix. The zeros of the zeta functions corresponds to the semiclassical eigenvalues of the system. (11.3) is a truncation of the Gutzwiller-Voros zeta function [196, 195]

$$Z_{qm} = \prod_p \prod_{k=0}^{\infty} \left(1 - \frac{e^{\frac{i}{\hbar} S_p(E) + i\pi\sigma_p/2}}{|\Lambda_p|^{1/2} \Lambda_p^k} \right) \tag{11.4}$$

or the recently introduced "quantum Fredholm determinant" of Cvitanović and Rosenqvist [55]

$$Z_{qm} = \prod_p \prod_{k=0}^{\infty} \left(1 - \frac{e^{\frac{i}{\hbar} S_p(E) + i\pi\sigma_p/2}}{|\Lambda_p|^{1/2} \Lambda_p^k} \right)^{k+1} \tag{11.5}$$

and even more recent determinants constructed suggested by Vattay et.al. [194].

These different formulations are expected to give the same leading eigenvalues, but they differs in the domain of analyticity and the speed of convergence. Formally the sums or products in such formulas are divergent, and only a "clever" expansion will yield a good result. The trace formula (11.1) will usually give very few eigenvalues, while the quantum Fredholm determinant is claimed to have the largest domain of analyticity, and yelds most eigenvalues [55, 56]. The classical Fredholm determinant is entire for an axiom A system [173, 16, 17], and this fact motivates the belief that quantum Fredholm also has good analytic properties.

A fast convergence for these formulas depends on a good expansion, usually ordered according to the length of the periodic orbits. If we have a complete binary symbolic description the expansion can be done according to the symbolic description.

The dynamical zeta function is formally given by the sum

$$\begin{aligned} 1/\zeta &= \prod_p (1 - t_p) = 1 - \sum_{p_1 p_2 \dots p_k} t_{p_1 + p_2 + \dots + p_k} \\ t_{p_1 + p_2 + \dots + p_k} &= (-1)^{k+1} t_{p_1} t_{p_2} \dots t_{p_k} \end{aligned} \tag{11.6}$$

where the product and sum is over all distinct non-repeating combinations of prime periodic orbits. If the orbits are given by a complete binary symbolic description, we can reorder of the terms as follows:

$$\begin{aligned} 1/\zeta &= (1-t_1)(1-t_0)(1-t_{10})(1-t_{100})(1-t_{101})(1-t_{1000}) \\ &\quad (1-t_{1001})(1-t_{1011})(1-t_{10000})(1-t_{10001}) \\ &\quad (1-t_{10010})(1-t_{10011})(1-t_{10101})(1-t_{10111})\dots \\ &= 1-t_1-t_0-[t_{10}-t_1t_0]-[(t_{100}-t_{10}t_0)+t_{101}-t_{10}t_1] \\ &\quad -[(t_{1000}-t_{100}t_0)+(t_{1110}-t_1t_{110}) \\ &\quad +(t_{1001}-t_{100}t_1-t_{101}t_0+t_{10}t_0t_1)]\dots \end{aligned} \tag{11.7}$$

The terms in square brackets are called the n-th curvature correction c_n by Cvitanović [43], and the first part of the expansion is called the fundamental part. If all orbits with the same symbolic description have approximately the same weight the terms in the curvatures almost cancel each other, and the convergeness of the expansion is fast. This near cancelationcan be understood as a shadowing effect, as shown numerically for 1-dimensional repellors and the well-separated 3-disk system [50].

The weight of the term t_p may be different for some orbits and the simple shadowing might fail. One example is the unimodal Farey map

$$T = \begin{cases} x/(1-x) & \text{if } x < 1/2 \\ (1-x)/x & \text{if } x > 1/2 \end{cases} \tag{11.8}$$

discussed by Artuso, Aurell and Cvitanović [10]. Here the fixed point $\overline{0}$ is marginally stable while all other orbits are unstable. The term t_0 cannot shadow any of the other orbits but Artuso et.al. found that one can resum the unstable terms in such a way that different infinite sums shadow each other, with the fundamental part of the zeta-function given by a geometrical series

$$\begin{aligned} 1/\zeta &= 1-(t_1+t_{10}+t_{100}+t_{1000}+\cdots) \\ &\quad -[(t_{110}+t_{1100}+t_{11000}+\cdots)-t_1(t_{10}+t_{100}+t_{1000}+\cdots)] \\ &\quad -[(t_{1110}+t_{11100}+\cdots)-t_1(t_{110}+t_{1100}+\cdots)] \\ &\quad -[(t_{10100}+t_{101000}+\cdots)-t_{10}(t_{100}+t_{1000}+\cdots)] \\ &\quad -\cdots \end{aligned} \tag{11.9}$$

this sum can be written as [10]

$$1/\zeta = 1-\hat{t}_1-[\hat{t}_{12}-t_1\hat{t}_2]-[\hat{t}_{112}-t_1\hat{t}_{12}]-[\hat{t}_{23}-t_2\hat{t}_3]-\cdots \tag{11.10}$$

where the index of t_k for $k>1$ denotes a string 10^{k-1} and $\hat{t}_{klm\dots n}$ is the infinite sum starting with $t_{klm\dots n}$ and increasing the number of 0's in the end of the symbol

string; $\hat{t}_{klm\ldots n} = t_{klm\ldots n} + t_{klm\ldots(n+1)} + t_{klm\ldots(n+2)} + \ldots$. We then have to evaluate an infinite sum to obtain the fundamental part of the zeta function. The terms in this sum will in typical examples converge as a power law, and the sum can be estimated from just a few terms.

This kind of orbits seems to be common in chaotic systems. In the stadium billiard an orbit bouncing infinitely many times successively in one semi-circle does not exist, but the whispering gallery orbits bouncing an arbitrary number of times do. The length of these orbits converges to a finite length as the number of bounces goes to infinity, and the fundamental part of a zeta function has to include at least one such infinite sum. In the wedge billiard there are the orbits bouncing n times successively on one tilted plane, denoted 0^n. The length (and action) of these orbits with increasing n converges to a finite length (action), but the fixed point $\overline{0}$ orbit does not exist. In smooth Hamiltonian systems with stable islands we expect this type of orbits to be generic. The orbits inside islands are stable, but there always exist unstable orbits wandering arbitrarily close to the outermost KAM torus. These orbits have to be included in the zeta function expansions as infinite sums.

11.2 Markov diagrams

Given a finite Markov diagram for the admissible orbits, one can easily read off the terms in the fundamental part of the zeta function. As we did when finding the topological entropy in section 1.3 we fidentify all non-self-intersecting loops and non-intersecting combinations of these loops. We record the symbol string corresponding to each such loop in the diagram and this is the index for each fundamental term t_k. Combinations of loops with no common node give products of terms $t_k t_l \cdots t_m$, with the indices corresponding to the different loops. The self-intersecting loops, combinations of these, and intersecting combinations of non-intersecting loops give the curvature terms of the zeta-function. A few examples of getting the terms from a diagram illustrate the procedure.

The loops in the binary graph 1.11 gives t_0 and t_1, no combination of loops, and the zeta function is

$$1/\zeta = 1 - t_0 - t_1 + (\text{curvatures}).$$

The graph in figure 1.17 b) describing the repellor when the period 3 orbit of the unimodal map is stable gives the loops t_1 and t_{10}

$$1/\zeta = 1 - t_1 - t_{10} + (\text{curvatures}). \tag{11.11}$$

An example of the zeta function from a graph describing the bimodal map is given in figure 2.12. The zeta function has the fundamental orbits

$$\{\overline{1}\}, \{\overline{01}\}, \{\overline{20}\}, \{\overline{200}\} \tag{11.12}$$

and in addition the combination of the orbits $\overline{1}$ and $\overline{200}$ is not a shadow of any orbit in the expansion of the ζ–function. The ζ–function is now expanded and gives

$$\begin{aligned} 1/\zeta \;=\; & 1 - t_{\overline{1}} - t_{\overline{10}} - t_{\overline{20}} - t_{\overline{200}} + t_{\overline{1}} t_{\overline{200}} && (11.13) \\ & -[t_{\overline{201}} - t_{\overline{20}} t_{\overline{1}}] - [t_{\overline{101}} - t_{\overline{10}} t_{\overline{1}}] \\ & -[t_{\overline{2010}} - t_{\overline{20}} t_{\overline{10}}] - [t_{\overline{1011}} - t_{\overline{101}} t_{\overline{1}}] - [t_{\overline{2011}} - t_{\overline{201}} t_{\overline{1}}] \\ & -[t_{\overline{10111}} - t_{\overline{1011}} t_{\overline{1}}] - [t_{\overline{10020}} - t_{\overline{10}} t_{\overline{020}}] && (11.14) \\ & -[t_{\overline{20020}} - t_{\overline{200}} t_{\overline{20}}] - [t_{\overline{10101}} - t_{\overline{101}} t_{\overline{01}}] \\ & -[t_{\overline{20101}} + t_{\overline{20110}} - t_{\overline{201}} t_{\overline{01}} - t_{\overline{2010}} t_{\overline{1}} - t_{\overline{20}} t_{\overline{110}} + t_{\overline{20}} t_{\overline{10}} t_{\overline{1}}] - \ldots \end{aligned}$$

where for smooth flows the shadowing terms become small compared with the fundamental orbits.

If a loop in the Markov diagram corresponds to a forbidden orbit or an orbit isolated from all other orbits then we can find a fundamental part of the zeta function with infinite sums as in the above Farey map example of Artuso, Aurell and Cvitanović [10, 11]. Instead of the forbidden orbit in the diagram we choose the series of non-selfintersection loops in the diagram running n times through the loop of the forbidden orbit. Examples of this are the stadium billiard and the wedge billiard.

In the billiard systems we have made an approximation of the pruning front to obtain the Markov graphs. The zeta functions we obtain from these graphs will then be an approximation, but we expect this zeta function to have good convergence properties since we have an approximation both to the fundamental parts and the shadowing parts of the expansion.

Chapter 12

Conclusions and new challenges

The long and detailed analysis of symbolic dynamics in a variety of systems developed above, shows that symbolic dynamics may be a powerful tool for solving various problems in chaotic systems. Possibly this kind of detailed analysis of chaotic systems overshoots, and becomes too complex for a practical application to physical problems such as of finding the energy levels of a bound quantum system. Only future investigations can decide whether such a detailed description of the geometry of orbits is really necessary for practical calculations in different systems. If this turns out to be necessary, we believe that the symbolic description given here is a natural and effective way implementing this description.

Regardless of what the applications might turn out to be, we believe that the symbolic description of bifurcations and the pruning fronts discussed above is important for theoretical understanding of dynamical systems. In mathematical literature the discussion is usually centered around unimodal one-dimensional maps and the renormalization of bifurcations. For two-dimensional diffeomorphisms and flows the literature deals mostly with the problems of the existence of complete Smale horseshoe non-wandering sets, bifurcations creating homoclinic tangency points, the Newhouse theorem, and the different bifurcations of stable orbits [100, 198]. Not much has been done in systematically describing the resonance structure in the parameter space for multi-modal one-dimensional endomorphisms, and chaotic two-dimensional diffeomorphisms. For billiards the interest in mathematical literature has been on proving the ergodicity [32, 39, 181, 182, 200] and not on the understanding of bifurcations. For some billiards the existence of countable Markov partitions has been showed [34, 128, 129], but not how to obtain useful approximations to this partition. We think that the methods developed here to generalize the MSS and Milnor-Thurston theory lead to a better understanding of bifurcation structures in the parameter space, but this thesis does not pretend to be mathemat-

ically rigorous. The conjecture of the existence of a unique way to assign symbols to a pruned folded map is one important case where a proof, a counterexample or an improved conjecture is needed. The existence of pruning fronts in the billiard systems may be turned into theorems without too much effort, but the conjecture of existence of a pruning front for smooth Hamiltonian systems may be very difficult to prove. The main difficulty is constructuion of a "singular orbit" in a smooth potential that would be analog to the singular orbit in the billiard. We have pointed out the close connection between the bifurcation trees in the billiards and in the smooth potentials. We expect a "singular orbit" in a smooth potential to be at, or close to, a homoclinic/hetroclinic tangency with a geometric shape in the configuration space similar to a singular billiard orbit, e.g. an orbit tangent to a wall or bouncing off a singular point of the billiard wall. This is an important question which requires further investigation. Also it will be nontrivial to prove that the well-ordered symbols of the billiard are ordered the same way in the phase space of a smooth potential, a necessary prerequisite for construction of a monotone pruning front.

The transformation of a pruned region into an expansion of the zeta function is obtained by constructing a Markov transition graph and finding loops in this graph. This is faster than a direct construction of a matrix from the symbol plane, but finding all combinations of loops is time consuming for large graphs. The diagrams we construct are also not necessarily the smallest possible and their form may depend on the order in which the forbidden strings are implemented as we construct the graph. This implies that the "fundamental part" of our the zeta function expansions may be unnecessarily large. Our approximations to the pruning front are implemented by removing rational rectangles, and for billiard systems this seems not very efficient. An approximation with triangles would converge much better, but we do not know how to implement this to get the admissible orbits. In addition Markov graphs might have symmetries which should be removed. Symmetry decomposition for complete alphabets has been discussed in detail by Cvitanović and Eckhardt [49], but should also be implemented for the pruned systems.

Another question receiving interest lately is the question of the monotonicity of bifurcations in different maps. Recent work by Milnor, Tresser and others [59, 149, 151, 168] has shown that in bimodal maps with bifurcation diagrams similar to the symbolic parameter planes discussed in section 2.1, there are simple paths along which the topological entropy increases monotonically, and regions with constant entropy are connected in the parameter plane. Numerics indicate that these results also hold for the parameter spaces of polynomial maps [151]. The

question of anti-monotonicity has been discussed by Yorke and coworkers [60, 125], who claim that bimodal and more complicated maps are anti-monotone. There has not been further work for higher modal maps following the aproach of by Milnor and Tresser, but the bifurcation diagrams obtained here, figures 2.13, 2.17 and 2.20, indicate that the results for bimodal maps also apply to three-modal and possibly higher-modal maps. However, in the higher modal maps bifurcations can change the modality and make the picture more complicated. We have also obtained similar symbolic parameter spaces for the once-folding maps, and we hope that this will enable us to prove monotonicity for once-folding maps as well. This however appears to disagree with the results of Kan, Koçak and Yorke [125]. The folding maps are complicated systems with an infinite-dimensional parameter spaces. Much more work is required before we can claim this problem to be solved, but we hope the work presented here is a step in the right direction.

Another problem of interest is the description of the parameter values for which the entropy changes from 0 to a positive number called the "border of chaos" [140]. By using symbolic parameter spaces this border may be described for the N-modal one-dimensional maps and for folding two-dimensional maps. This border may then also be understood in an ordinary parameter space. This is also a question for further studies.

The question of a chaotic attractor for a finite measure of parameter values has been addressed, and positive results have been obtained for the logistic map [21] and for the Hénon map with very small values for the parameter b [22]. Nothing is known about this question in bimodal and other more complicated maps.

The construction of symbols for an arbitrary smooth dynamical system is not understood. We believe that in a number of Hamiltonian systems we can use symbols defined for a corresponding billiard, but there currently exists no method for constructing symbols for any system. This is a difficult problem but progress here will be very interesting. See also ref. [68].

The method of Biham and Wenzel [26, 27] for finding periodic orbits in the Hénon map is interesting, and could be generalized to other once-folding maps and maybe to n-folding maps. With more than one folding the method will depend on the starting conditions, and an investigation of such methods may be interesting. We have shown here how the convergence of the BW method is closely related to the modality of the 1-dimensional approximation, and we expect this also for a generalized BW method.

In the field of quantum chaos there is a number of interesting questions under investigation. The quantum verions of our classical chaotic billiard systems are

"particle in box" problems and the systems studied most. The semi-classical work on the three-body problem in atomic systems is very promising, and the results already obtained for these systems under special conditions are impressive [70, 199]. Further studies along this path may be the most exciting projects of the near future. The question of diffusion in classical and quantum systems is an interesting, but difficult problem [9], and application to astrophysical problems are interesting [20, 64].

Index

Bibliography

[1] M. A. M. de Aguiar, C. P. Malta, M. Baranger and K. T. R. Davies, *Ann. Phys.* **180**, 167 (1987).

[2] G. D'Alessandro, S. Isola and A. Politi, *Prog. Theor. Phys.* **86**, 1149 (1991).

[3] G. D'Alessandro and A. Politi, *Phys. Rev. Lett.* **64**, 1609 (1990).

[4] G. D'Alessandro, P. Grassberger, S. Isola and A. Politi, *J. Phys.* **A 23**, 5285 (1990).

[5] K. T. Alligood and T. Sauer, *Commun. Math. Phys.*, 105 (1988).

[6] V. I. Arnold, *Functional Anal. Appl.* **1**, 1 (1967).

[7] V.I. Arnold,*Mathematical Methods in Classical Mechanics* (Springer-Verlag, Berlin, 1978).

[8] V.I. Arnold, *Geometrical Methods in the Theory of Ordinary Differential Equations* (Springer, New York 1983).

[9] R. Artuso, *Phys. Lett.* **A 160**, 528 (1991).

[10] R. Artuso, E. Aurell and P. Cvitanović, *Nonlinearity* **3**, 325 (1990).

[11] R. Artuso, E. Aurell and P. Cvitanović, *Nonlinearity* **3**, 361 (1990).

[12] R. Artuso, P. Cvitanović and G. Casati, eds., *Chaos, Order and Patterns* (Plenum, New York 1992).

[13] D. Auerbach, P. Cvitanović, J.-P. Eckmann, G.H. Gunaratne and I. Procaccia, *Phys. Rev. Lett.* **58**, 2387 (1987).

[14] E. Aurell, *J. Stat. Phys.* **58**, 967 (1990).

[15] R.Aurich, M.Sieber and F.Steiner, *Phys. Rev. Lett.* **61**, 483 (1988).

[16] V. Baladi, J.-P. Eckmann and D. Ruelle, *Nonlinearity* **2**, 119 (1989).

[17] V. Baladi and G. Keller *Comm. Math. Phys.* **127**, 459 (1990).

[18] V. Baladi, D. Rockmore, N. Tongring and C. Tresser *Renormalization on the n-dimensional torus*, Preprint 1992.

[19] J. Belair and L. Glass, *Physica* **16 D**, 143 (1985).

[20] N.J. Balmforth, P. Cvitanović, G.R. Ierley, E.A. Spiegel and G. Vattay, *Proceed. 8th Florida Workshop in Nonlinear Astronomy: Noise*, (New York Academy of Sciences, New York 1993).

[21] M. Bennedicks and L. Carleson, *Ann. of Math.*, **122**, 1 (1985).

[22] M. Benedicks and L. Carleson, *IXth Int. Congr. on Mathematical Physics*, B. Simon *et al.*, eds., 489 (Adam Hilger, Bristol, 1989).

[23] M. Baranger and K. T. R. Davies, *Ann. Phys.* **177**, 330 (1987).

[24] M. Barnsley, *Fractals Everywhere* (Academic Press, New York 1988).

[25] O. Biham and M. Kvale, *Phys. Rev.* **A 46**, 6334 (1992).

[26] O. Biham and W. Wenzel, *Phys. Rev. Lett.* **63**, 819 (1989).

[27] O. Biham and W. Wenzel, *Phys. Rev. A* **42**, 4639 (1990).

[28] G.D. Birkhoff, *Acta Math.* **50**, 359 (1927), reprinted in ref. [139].

[29] G. D. Birkhoff, *Dynamical systems*, Amer. Math. Soc. Colloq. Publ., vol. **9**, (Amer. Math. Soc., Providence R. I., 1955).

[30] B. Branner and J. H. Hubbard, *Acta Math.*, **160**, 143 (1988).

[31] M. Braun, *J. Diff. Eq.* **8**, 294 (1970).

[32] L. Bunimovich, *Funkts. Anal. Ego Prilozh.* **8**, 73 (1974).

[33] L. Bunimovich, *Comm. Math. Phys.* **65**, 295 (1979).

[34] L. Bunimovich and Y. G. Sinai, *Comm. Math. Phys.* **78**, 247 (1980).

[35] N.I. Chernov, *Physica* **D 53**, 233 (1991).

[36] P. Collet and J. P. Eckmann, *Iterated Maps on the Interval as Dynamical Systems* (Birkhauser, Boston, 1980).

[37] S. C. Creagh, J. M. Robbins and R. G. Litteljohn, *Phys. Rev. A* **42**, 1907 (1990).

[38] G. Contopoulos and L. Vlahos, *J. Math. Phys.* **16**, 1469 (1975).

[39] I.P. Cornfeld, S.V. Fomin and Ya.G. Sinai, *Ergodic Theory*, (Springer, Berlin, 1982).

[40] D.M. Cvetković, M. Doob and H. Sachs, *Spectra of Graphs* (Academic Press, New York, 1980).

[41] *Universality in Chaos*, P. Cvitanović, ed., (Adam Hilger, Bristol, 1989).

[42] P. Cvitanović, *Phys. Rev. Lett.* **61**, 2729 (1988).

[43] P. Cvitanović, in E. Moss, ed., *Noise and Chaos in Nonlinear Dynamical Systems,* (Cambridge Univ. Press, Cambridge, 1989).

[44] P. Cvitanović, in *Nonlinear Physical Phenomena, Brasilia 1989 Winter School*, À. Ferraz, F. Oliveira and R. Osorio, eds. (World Scientific, Singapore 1990).

[45] P. Cvitanović, *Physica* **D 51**, 138, (1991).

[46] P. Cvitanović, *CHAOS* **2**, 1 (1992).

[47] P. Cvitanović and F. Christiansen, *CHAOS* **2**, 61 (1992).

[48] P. Cvitanović and B. Eckhardt, *Phys. Rev. Lett.* **63**, 823 (1989).

[49] P. Cvitanović and B. Eckhardt, *Nonlinearity* **6**, 277 (1993).

[50] P. Cvitanović, B. Eckhardt, P.E. Rosenqvist, G. Russberg and P. Scherer, in G. Casati and B. Chirikov, eds., *Quantum Chaos*, (Cambridge University Press, Cambridge 1993).

[51] P. Cvitanović, P. Gaspard and J.-P. Eckmann, *Transport properties of the Lorentz gas in terms of periodic orbits*, preprint (May 1991).

[52] P. Cvitanović, P. Gaspard, and T. Schreiber, *CHAOS* **2**, 85 (1992).

[53] P. Cvitanović, G. H. Gunaratne, I. Procaccia, Phys. Rev. A **38**, 1503 (1988).

[54] P. Cvitanović, I. Percival, and A. Wirzba, eds. *Quantum Chaos - Quantum Measurement*, (Kluwer, Dordrecht, 1992).

[55] P. Cvitanović and P.E. Rosenqvist, in G.F. Dell'Antonio, S. Fantoni and V.R. Manfredi, eds., *From Classical to Quantum Chaos, Soc. Italiana di Fisica Conf. Proceed.* **41**, 57 (Ed. Compositori, Bologna 1993).

[56] P. Cvitanović, P.E. Rosenqvist, H.H. Rugh, and G. Vattay, *A Fredholm determinant for semi-classical quantization*, submitted to *CHAOS* (1993).

[57] P. Dahlqvist and G. Russberg, *Phys. Rev. Lett.* **65**, 2837 (1990).

[58] P. Dahlqvist and G. Russberg, *J. Phys. A* **24**, 4763 (1991).

[59] S. P. Dawson, R. Galeeva, J. Milnor and C. Tresser, to appear.

[60] S. P. Dawson, C. Grebogi, J. Yorke, I. Kan and H. Koçak, *Phys. Lett. A*, **162**, 249 (1992).

[61] R.L. Devaney, *An Introduction to Chaotic Dynamical Systems* (The Benjamin/ Cummings Publishing Co., Inc., California, 1986).

[62] A. J. Dragt and J. M. Finn, *J. Geophysical Res.* **81**, 2327 (1976).

[63] A. Douady and J. H. Hubbard, *Ann. Sci. Ec. Norm. Sup., Paris*, **18**, 287 (1985).

[64] P. B. Dusenbery, R. F. Martin and G. R. Burkhardt, *Chaos* **2**, 427 (1992).

[65] B. Eckhardt and G. Ott, *Periodic orbit analysis of the Lorentz attactor*, preprint (1993).

[66] B. Eckhardt, *J. Phys.* **A 20**, 5971 (1987).

[67] B. Eckhardt and G. Russberg, *Phys. Rev.* **E 47**, 1578 (1993).

[68] B. Eckhardt, and D. Wintgen, *J. Phys.* **A 24**, 4335 (1991).

[69] A. Einstein, *Verh. Dtsch. Phys. Ges.* **19**, 82 (1917).

[70] G. S. Ezra, K. Richter, G. Tanner and D. Wintgen, *J. Phys.* B **24**, L413 (1991).

[71] K.M. Falconer, *The Geometry of Fractal Sets* (Cambridge Univ. Press, Cambridge, 1985)

[72] M. J. Feigenbaum, *J. Stat. Phys.* **19**, 25 (1978); **21**, 669 (1979).

[73] M. J. Feigenbaum, *Phys. Lett.* **74A**, 375 (1979).

[74] M.J. Feigenbaum, *Comm. Math. Phys.* **77**, 65 (1980).

[75] D. Fournier, H. Kawakami and C. Mira, *C.R. Acad. Sci. Ser. I,* **298**, 253 (1984).

[76] D. Fournier, H. Kawakami and C. Mira, *C.R. Acad. Sci. Ser. I,* **301**, 223 (1985).

[77] D. Fournier, H. Kawakami and C. Mira, *C.R. Acad. Sci. Ser. I,* **301**, 325 (1985).

[78] S. Fraser and R. Kapral, *Phys. Rev.* **A 25**, 3223 (1982).

[79] S. Fraser and R. Kapral, *Phys. Rev.* **A 30**, 1017 (1984).

[80] J. Frøyland, *Chaos and coherence*, (Inst. of Phys. publ., Bristol, 1992).

[81] J. Frøyland and K. H. Alfsen, Phys. Rev. A, **29**, 2928, (1984).

[82] P. Gaspard and D. Alonso Ramirez, *Phys. Rev.* **A 45**, 8383 (1992).

[83] P. Gaspard and S.A. Rice, *J. Chem. Phys.* **90**, 2225 (1989); **90**, 2242 (1989); **90**, 2255 (1989).

[84] N. K. Gavrilov and L. P. Šilikov, *Math. USSR Sb.*, **88**, 467 (1972); *Math. USSR Sb.*, **90**, 139 (1973).

[85] F. Giovannini and A. Politi, *Phys. Letters* **A 161**, 333, (1992).

[86] L. Glass and R. Perez, *Phys. Rev. Lett.* **48**, 1772 (1982).

[87] D.A. Goodings and T. Szeredi, *Am. J. Phys.* **59**, 924 (1991).

[88] P. Grassberger, *J. Stat. Phys.* **26**, 173 (1981).

[89] P. Grassberger, *Int. J. Theor. Phys* **25**, 907 (1986).

[90] P. Grassberger, *Z. Naturforsch. A* **43**, 671 (1988).

[91] P. Grassberger, R. Badii and A. Politi, *J. Stat. Phys.* **51**, 135 (1988).

[92] P. Grassberger and H. Kantz, *Phys. Lett. A* **113**, 235 (1985).

[93] P. Grassberger, H. Kantz and U. Moening, *J. Phys.* **A 43**, 5217 (1989).

[94] J. M. Greene, R. S. MacKay, F. Vivaldi and M. J. Feigenbaum, *Physica* **D 3**, 468 (1981).

[95] J.M. Greene, *J. Math. Phys.* **20**, 1183 (1979).

[96] C. Grebogi, E. Ott and J.A. Yorke, *Phys. Rev.* **A36**, 3522 (1987).

[97] C. Grebogi, E. Ott and J. Yorke, *Physica* **D 7**, 181 (1983).

[98] C. Grebogi, E. Ott and J. Yorke, *Phys. Rev. A* **37,** 1711 (1988).

[99] J. Guckenheimer, *Inventions. Math.* **39**, 165 (1977).

[100] J. Guckenheimer and P. Holmes, *Non-linear Oscillations, Dynamical Systems and Bifurcations of Vector Fields* (Springer, New York, 1986).

[101] G. Gunaratne, M.H. Jensen and I. Procaccia, *Nonlinearity* **1**, 157 (1988).

[102] M.C. Gutzwiller, *J. Math. Phys.* **8**, 1979 (1967); **10**, 1004 (1969); **11**, 1791 (1970).

[103] M.C. Gutzwiller, *Chaos in Classical and Quantum Mechanics* (Springer, New York, 1990).

[104] T. D. H. Hall and N. B. Tufillaro, *Braid analysis of (low-dimensional) Chaos*, Preprint 1993.

[105] Hao Bai-Lin, *Chaos* (World Scientific, Singapore, 1984).

[106] Hao Bai-Lin, *Elementary symbolic dynamics and chaos in dissipative systems* (World Scientific, Singapore, 1989).

[107] K. T. Hansen, Phys. Lett. A **165**, 100 (1992).

[108] K. T. Hansen, *CHAOS* **2**, 71 (1992).

[109] K. T. Hansen, *Symbolic dynamics I, Finite dispersive billiards*, Nonlinearity **5** in press.

[110] K. T. Hansen, *Symbolic dynamics II, Bifurcations in billiards and smooth potentials*, Nonlinearity **5** in press.

[111] K. T. Hansen, *Symbolic dynamics III, The stadium billiard*, submitted to Nonlinearity.

[112] M. Hénon, *Comm. Math. Phys.* **50**, 69 (1976).

[113] F. Hofbauer, *Ergod. The. and Dynam Sys.* **5**, 237 (1985).

[114] F. Hofbauer, *Prob. Th. Rel. Fields* **72**, 359 (1986).

[115] P. J. Holmes, *Phys. Rev. Lett.* **104A**, 299 (1984).

[116] P. J. Holmes and D. Whitley, *Phil. Trans. Roy. Soc.* **A 311**, 43 (1984).

[117] E. Hopf, *Ergodentheorie* (Chelsea Publ. Co., New York, 1948).

[118] E. Hopf, *Abzweigung einer periodischen Lösung*, Beriech. Sächs. Acad. Wiss. Leipzig, Math. Phys. Kl. **94**, 19 (1942), 15-25.

[119] J.E. Hopcroft and J.D. Ullman, *Introduction to Automata Theory, Languages, and Computation* (Addison-Wesley, Reading MA, 1979)

[120] E. A. Hylleraas, *Z. Phys.* **48**, 469, (1928); *Z. Phys.* **54**, 347, (1929).

[121] S. Isola and A. Politi, *J. Stat. Phys.* **61**, 259 (1990).

[122] E. Atlee Jackson, *Perspectives of nonlinear dynamics*, (Cambridge University Press, Cambridge, 1989).

[123] E. Atlee Jackson, private communications.

[124] C. Jung and H.-J. Scholz, *J.Phys. A* **21**, 2301 (1988).

[125] I. Kan, H. Koçak and J. Yorke, *Anals of Math.*, **136**, 219 (1992).

[126] H. Kantz and P. Grassberger, *Physica* **D 17**, 75 (1985).

[127] E. J. Kostelich and J. A. Yorke *Phys. Rev.* **A38**, (1988)

[128] T. Krüger, P. Sibt and S. Troubetzkoy, *Complexity and Randomness of Recursive Discretizations of Dynamical Systems*, Preprint (1992).

[129] T. Krüger and S. Troubetzkoy, *Ergod. Th. and Dynam. Sys.* **12**, 487 (1992).

[130] J. H. Lefebvre, T. Szeredi and D. A. Goodings, to be published.

[131] H. E. Lehtihet and B. N. Miller, *Physica* **D 21**, 93 (1986).

[132] J. G. Leopold and I. Percival, *J. Phys. B*, **13**, 1037 (1980).

[133] T. Y. Li and J. A. Yorke, *Amer. Math. Monthly*, **82**, 985 (1975).

[134] A. J. Lichtenberg and M. A. Liebermann, *Regular and Stochastic Motion* (Springer-Verlag, New York, 1981).

[135] R. Livi, A. Politi and S. Ruffo, *J. Stat. Phys.* **65**, 73 (1991).

[136] E.N. Lorenz, *J. Atmos. Sci.* **20**, 130 (1963).

[137] H. A. Lorentz, *Amst. Acad.*, **7**, 438 (1905).

[138] R. Lozi, *J. de Phys.* (Paris) **39**, Colloq. **C5**, 9 (1978).

[139] R.S. MacKay and J.D. Meiss, *Hamiltonian Dynamical Systems* (Adam Hilger, Bristol, 1987).

[140] R.S. MacKay and C. Tresser, *Physica* **D 19**, 206 (1986).

[141] R.S. MacKay and C. Tresser, *Physica* **D 27**, 412 (1987).

[142] R.S. MacKay and J. B. J. van Zeijts, *Nonlinearity* **1**, 253 (1988).

[143] B.B. Mandelbrot, *The Fractal Geometry of Nature* (Freeman, San Francisco, 1983).

[144] R. M. May, *Nature*, **261**, 459, (1976).

[145] V. P. Maslov, *Théorie des Perturbations et Métodes Asymptotiques* (Dunod, Paris, 1972).

[146] F.A. McRobie, *Proc. R. Soc. Lond.* **A 438**, 545 (1992).

[147] N. Metropolis, M.L. Stein and P.R. Stein, *J. Comb. Theo.* **A15**, 25 (1973).

[148] K. R. Meyer, *Trans. AMS* **149**, 95 (1970).

[149] J. Milnor, *Experimental Math.*, **1**, 5 (1992).

[150] J. Milnor, *Remarks on Iterated Cubic Map* Preprint # 1990/6, SUNY Stony Brook, Institute for Mathematical Sciences (1990). (Included in ref. [149])

[151] J. Milnor, *Lecture at "Real and Complex dynamical systems", Hillerød, Denmark June 20 - July 2, 1993.*

[152] J. Milnor and W. Thurston, "On iterated maps of the interval", *Lec. Notes in Math.* **1342,** 465 (Springer, Berlin, 1988).

[153] C. Mira, *Chaotic Dynamics* (World Scientific, Singapore, 1987).

[154] M. Misiurewicz, *Publ. Math. IHES* **53**, 17 (1981).

[155] M. Misiurewicz, p 348 in R.H.G. Helleman ed., *Nonlinear dynamics*, (New York Academy of Sciences, New York, 1980).

[156] M. Morse, *The Calculus of Variations in the Large.* New York: Am. Math. Soc. Colloquium Publ. **18** (1934).

[157] M. Morse and G. A. Hedlund, *Am. J. Math.*, **62**, 1 (1940).

[158] J. Moser, *Stable and Random Motions in Dynamical Systems* (Princeton University Press, Princeton 1973).

[159] P.J. Myrberg, *Ann. Acad. Sc. Fenn., Ser. A,* **256**, 1 (1958); **259**, 1 (1958).

[160] S. E. Newhouse, *Topology* **13**, 9 (1974).

[161] S. E. Newhouse, *Publ. Math. IHES* **50**, 101 (1979).

[162] M. Nordahl, private communication.

[163] E. Ott, C. Grebogi and J.A. Yorke, *Phys. Lett. A* **135**, 343 (1989).

[164] A.M. Ozorio de Almeida, *Hamiltonian Systems: Chaos and Quantization* (Cambridge University Press, Cambridge, 1988).

[165] A. Politi, R. Badii and P. Grassberger, *J. Phys. A* **15**, L763 (1988).

[166] H. Poincaré, "Remarques sur une expérience de M. Birkeland" *C. R. Acad. Sci.,* Paris, **123**, 930 (1896).

[167] P. H. Richter, H.-J. Scholz and A. Wittek, *Nonlinearity* **3**, 45 (1990).

[168] J. Ringland and C. Tresser, *A Genealogy for finite kneading wequences of bimodal maps on the interval*, Preprint (1993).

[169] O. Rössler, Phys. Lett. **57A**, 397 (1976).

[170] D. Ruelle, *Bull. Amer. Math. Soc.* **82**, 153 (1976); *Inventiones math.* **34**, 231 (1976).

[171] D. Ruelle, *Thermodynamic Formalism* (Addison-Wesley, Reading, 1978).

[172] D. Ruelle, *Commun. Math. Phys.* **125**, 239 (1989).

[173] H. H. Rugh, *Time Evoluation and Correlations in Chaotic Dynamical Systems*, (Ph.D. Thesis, Univ. of Copenhagen, 1992).

[174] H.G. Schuster, *Deterministic Chaos* (Physik-Verlag, Weinheim, 1984).

[175] A. N. Sarkovskii, *Ukranian Math. J.* **16**, 61 (1964).

[176] M. Sieber *The Hyperbola Billiard: A model for the semiclassical Quantization of chaotic systems*, (Thesis, Hamburg, 1991).

[177] M. Sieber and F. Steiner, Physica D **44**, 248 (1990); Phys. Lett. A **148**, 415 (1990).

[178] M.Sieber, CHAOS **2**, 35 (1992).

[179] R.M. Siegel, C. Tresser and G. Zettler, *CHAOS* **2**, 473 (1992).

[180] S. Simo, *J. Stat. Phys.* **21**, 465 (1979).

[181] Ya.G. Sinai, *Russ. Math. Surveys* **25**, no 2, 137 (1970).

[182] Ya.G. Sinai, *Russ. Math. Surveys* **27**, no 4, 21 (1972).

[183] S. Smale, *Ann. Math.*, **74**, 199, (1961).

[184] S. Smale, *Bull. Am. Math. Soc.* **73**, 747 (1967).

[185] U. Smilansky, unpublished (1992).

[186] C. Sparrow, *The Lorenz Equations: Bifurcations, Chaos, and Strange Attractors*, (Springer-Verlag, 1982).

[187] Carl Størmer, *Comptes Rendus, Paris* **142**, p 1580; **143**, p 140, p 408 and 460. *Archiv for Mathematik og naturvidenskab, Christiania*, **B 28, nr. 2**, 3(1906). *Arch. Sci. phus. nat., Genève* 4 period, **24**, p 5, p 113, p 221, p 317 (1907). *The Polar Aurora* (Oxford Univerity Press, 1955).

[188] T. Szeredi and D.A. Goodings, *Phys. Rev. Lett.* **69**, 1640 (1992).

[189] T.Szeredi and D.A.Goodings, Phys. Rev. **E 1**, to appear (1993).

[190] T. Szeredi, Ph.D. thesis, McMaster University (1992).

[191] T. Tél, *J. Stat. Phys.* **49**, 157 (1982).

[192] C. Tresser, private communication.

[193] G. Troll *Physica* **D 50**, 276 (1991).

[194] G. Vattay, unpublished.

[195] A. Voros, *Comm. Math Phys.* **110**, 439 (1987).

[196] A. Voros, *J. Phys. A* **21**, 685 (1988).

[197] N.D. Whelan, D.A. Goodings and J.K. Cannizzo, *Phys. Rev.* **A 42**, 742 (1990).

[198] S. Wiggins, *Global Bifurcations and Chaos* (Springer-Verlag, New York, 1988).

[199] D. Wintgen, K. Richter and G. Tanner, *CHAOS*, **2**, 19 (1992).

[200] M.P. Wojtkowski, *Commun. Math. Phys.* **126**, 507 (1990).